

Evaluation of the Corrosion Behaviour of Continuously Galvanized Rebar

by

Ibrahim Ogunsanya

A thesis

presented to the University of Waterloo

in fulfilment of the

thesis requirement for the degree of

Master of Applied Science

in

Mechanical Engineering

Waterloo, Ontario, Canada, 2016

© Ibrahim Ogunsanya 2016

I hereby declare that I am the sole author of this thesis. This is a true copy of the thesis including any required final revisions, as accepted by my examiners.

I understand that my thesis may be made electronically available to the public.

Abstract

De-icing/anti-icing salts used during the winter season are the major culprit in limiting the durability of reinforced concrete structures. The salts induce corrosion of rebar, by penetrating the concrete and breaking down the protective film formed on the steel in the high alkaline environment of the concrete. Since the corrosion products occupy a volume larger than that of the corroded steel, they crack the concrete. The use of more corrosion resistant alloys is one method of improving the durability of reinforced concrete structures.

Conventional hot-dipped galvanized steel (HDG) is an economical alternative to black steel mainly because: the zinc coating has a higher chloride threshold and, when the bar eventually corrodes, it provides additional protection to the base steel through its sacrificial anode effect, its corrosion products are soluble and do not crack the concrete, and it forms a stable protective film even in low pH concrete. However, its major drawback is the brittle and less corrosion resistant (than pure Zn) Fe-Zn intermetallic compounds (IMC) formed in the coating. To remedy this, a ductile pure zinc coating produced by a continuously galvanizing process has recently been developed. Small amounts of aluminum are added to the zinc bath with the goal of forming an Fe-Al inhibition layer between the steel and the zinc coating.

In this project, three prototypes of the continuously galvanized rebar (CGR) grades, C1, C2 and C3 were electrochemically assessed, using galvanostatic pulse (GP) and linear polarization resistance (LPR) techniques, to evaluate and compare the corrosion behaviour of these bars against HDG and black steel. A second goal of the project was to identify the characteristic electrochemical potentials of HDG steel and CGR coatings to provide similar guidelines to those provided by ASTM C876 for assessing the probability of corrosion of uncoated carbon steel rebar in the field. All bars were cast in both non-cracked and cracked concrete, and exposed to a multi-chloride brine solution locally available and used across Ontario, Canada.

Metallographic examination performed on the galvanized bars showed the non-uniformity of all coatings, particularly the CGR grades - some regions which were significantly less than the specified thickness, and some others were too thin to be detected. The coating thickness on the

tested HDG, C1 and C2, and C3 bars were in the range of 105 – 250 μm , 15 – 60 μm , 5 – 33 μm respectively. The aluminum content of the C3 bars, ~9%, was similar in range to “Galvan” steel.

After weekly electrochemical testing for 64 weeks, the results showed that the C3 performed the same as black steel in both passive and active state. The C1 and C2 bars performed the same as HDG bars in the passive state and three to five times better than black steel in the active state. The HDG bars exhibited ten times better “corrosion performance” than black steel in both passive and active state. The time to corrosion initiation was not determined in the present project, as a result, “corrosion performance” is defined as the active corrosion rate after initiation. The electrochemical behaviour of galvanized bars has been attributed to their zinc thickness and/or the presence of significant aluminum content in the coatings. The corrosion product of the high Al containing bar, C3, appeared to affect the bonding between the bar and its concrete, which then negatively affected the electrochemical behaviour of the bar.

To characterize the corrosion potentials of these galvanized bars, the passive and active corrosion potential values of all galvanized bars were in the range of -266 to -382 mV vs SCE and -345 to -686 mV vs SCE, respectively. Moreover, the HDG and C3 rebar grades are in the upper and lower end of the ranges, respectively. The potential guideline developed for accessing probability of corrosion of black steel in concrete suggests that when the potential is more positive than -335 mV vs SCE (or -410 mV CSE), there is low probability of corrosion, when it is more negative than -385 mV vs SCE (or 460 mV vs CSE), there is high probability of corrosion, and an uncertain region exists between these potentials.

Acknowledgements

All thanks to God for the grace. Thanks to my parent, wife, family and friends for their support.

I would like to especially thank my supervisor Prof. Carolyn M. Hansson for giving me the opportunity to work under her supervision. Thanks for the encouragement and always looking to get the best out of me. Words cannot express how grateful I am.

Special thanks to my past and present colleagues: Dr. Nermein Khattab, Tim Bandura; Victoria Sirega/Strong, Colin Van Niejenhuis; for their support and advice.

The project would not have been possible without the generous grant from our sponsors, International Zinc Association (IZA).

A big thank you to the University's departmental technical staffs; Richard Morrison, Doug Hirst, Yuquan Ding, Mark Griffet, for their help.

Table of Contents

Abstract.....	iii
Acknowledgements.....	v
Table of Contents.....	vi
List of Figures.....	x
List of Tables.....	xv
List of Equations.....	xvi
List of Abbreviations and Variables.....	xvii
Chapter 1 Introduction.....	1
1.1. Background.....	1
1.2. Statement of the problem.....	4
1.3. Objectives.....	4
1.4. Scope and Importance of the study.....	4
Chapter 2 Literature Review.....	6
2.1. Overview of impact on the corrosion of rebar in concrete.....	6
2.2. Conventionally hot-dipped galvanized (HDG) steel.....	11
2.2.1. Overview.....	11
2.2.2. Metallurgy of HDG Rebar.....	13
2.3. Continuously Galvanized (CG) steel.....	17
2.3.1. Overview.....	17
2.3.2. Metallurgy of CG rebar.....	20
2.4. Behaviour of Zn in high alkaline environment.....	29
2.5. Long term use of galvanized rebar.....	31
2.6. Electrochemical test equipment.....	34

Table of Contents

2.6.1.	Linear Polarization Resistance (LPR) Technique.....	36
2.6.2.	Galvanostatic Pulse (GP) Technique	37
Chapter 3	Experimental Procedure.....	38
3.1.	Design set up	38
3.1.1.	Sound Concrete Specimens.....	39
3.1.2.	Transversely Cracked Specimens	40
3.1.3.	Longitudinally Cracked Specimens	41
3.2.	Rebar sample preparation.....	42
3.3.	Specimen cast and concrete mixture design.....	43
3.4.	Preparation for brine exposure	47
3.4.1.	Specimen Cracking.....	47
3.4.2.	Cutting and epoxy coating of cracked specimens and measurement of initial OCP 48	
3.5.	Exposure of specimens to brine	49
3.6.	Electrochemical measurements	51
3.7.	Microstructural and Compositional Analysis of Steel Coatings	51
3.8.	Autopsy of Corroded Bar	51
Chapter 4	Experimental Results and Discussion.....	53
4.1.	Materials properties.....	53
4.1.1.	Characterization of coatings	53
4.1.2.	Rebar weight and crack width.....	57
4.1.3.	Concrete properties	57
4.2.	Electrochemical Measurement Results	58
4.2.1.	Sound Concrete.....	59
4.2.2.	Transversely Cracked Concrete	63

Table of Contents

4.2.3. Longitudinally cracked concrete.....	67
4.3. Autopsy Results.....	70
4.3.1. Concrete and rebar analysis for corrosion product	71
4.3.2. Recalculated electrochemical result of the cracked specimens	73
4.4. General discussions	75
4.5. Observations during electrochemical testing	84
Chapter 5 Summary and Conclusion.....	86
5.1. Influence of cracks in concrete.....	86
5.2. Behaviour of the coatings.....	86
5.3. Corrosion potential characterization	87
Chapter 6 Recommendation	89
6.1. Recommendations for application of the experimental results	89
6.2. Recommendations for Future Research	89
Reference	91
Appendix A – Specimen averages for both GP and LPR	95
A1. Corrosion potential (E_{corr}).....	95
A2. Corrosion current density (i_{corr})	96
A3. Concrete resistance.....	98
Appendix B – Steel and concrete properties.....	99
B1. Steel weight, crack peak load, and crack width.....	99
B2. Compressive strength – individual concrete cylinder.....	101
B3. Pore solution recipe	101
Appendix C – Electrochemical results.....	102
C1. Ecorr for individual specimens.....	102

Table of Contents

C2. Icorr for individual specimens	111
C3. Concrete resistance for individual	120
Appendix D– Micrographs	128
D1. Micrograph of specimen C1	128
D2. Micrograph of specimen C2	129
D3. Micrograph of specimen C3	130
D4. Micrograph of specimen HDG	131
D5. Micrograph of galvanized specimen	132
Appendix E – Autopsy specimens	133
E1. Initial autopsy	133
C1.....	133
C2.....	138
C3.....	143
HDG.....	148
E2. Final autopsy.....	154
C1.....	154
C2.....	156
C3.....	158
HDG.....	160

List of Figures

Figure 1-1: ASTM C876 Half-cell potential guideline for black steel. 3

Figure 2-1: Corrosion cycle [56]..... 6

Figure 2-2: Equilibrium E/pH diagram for Iron (Fe) [4]. The a and b line represent hydrogen evolution and oxygen reduction respectively. 8

Figure 2-3: Carbonation (top) and chloride attack (bottom) of reinforced concrete [6]..... 9

Figure 2-4: Mechanism of passivity breakdown on steel in the presence of chloride [7]. 10

Figure 2-5: Cross section of a reinforced structure attacked by chloride, left [8]. Expansive nature of corrosion product, right [9]..... 10

Figure 2-6: Hot dipped galvanizing process [12]. 12

Figure 2-7: HDG rebar coating (from IZA) and Fe-Zn phase equilibria [18]. 1 = Γ and Γ_1 (gamma 1 & 2), 2 = δ (delta), 3 = ζ (zeta), 4 = η (eta)..... 14

Figure 2-8: Comparison between HDG coating from the literature [47] (left) and that used in this experiment (right). The numbers refer to that in Table 2-3. 15

Figure 2-9: Nucleation and growth of phases in a HDG coating (left) and phase layer thickness variation with immersion time (right) [21]. 16

Figure 2-10: Coating alternatives in terms of corrosion resistance versus black steel [46]. 18

Figure 2-11: CGR production line [46] 19

Figure 2-12: Micrograph of a CGR (1- Inhibition layer, 2- pure Zn eta layer) (left) and HDG coating (right) both bent after galvanizing [47]..... 21

Figure 2-13: Micrograph of CGR specimen 1 and 2 respectively used in the present work. Layer 1 and 2 is the Fe-Al-Zn layer and the pure zinc layer respectively. 22

Figure 2-14: Ternary phase diagram of Fe-Al-Zn. Left – overall section of the Zn rich corner at 460°C. Right – Al corner of the Zn-rich corner. [34]. 22

List of Figures

Figure 2-15: Variation of Al content with immersion time [18].	25
Figure 2-16: Micrographs of a typical Fe-Zn outburst (left) [41], and outburst in 85um grain size steel immersed in 0.2 wt.% Al-Zn bath (right) [43].	26
Figure 2-17: Mechanism of Fe-Zn outburst [18].	27
Figure 2-18: Zn diffusion path (left) and grain size influence on outburst (right) [31].	28
Figure 2-19: E/pH diagram of Zn [4] (left) and influence of pH on Zn corrosion [19] (right). ...	29
Figure 2-20: Pure Zn overlay dissolution during passivation (left) and selective dissolution of Zn in Fe-Zn IMC (right) [15].	30
Figure 2-21: Randle's circuit (left) [55], Helmholtz double layer (middle and right) [56].	34
Figure 2-22: Polarization curve [54].	36
Figure 2-23: A typical linear polarization resistance curve. $R_T = R_C + R_P$	37
Figure 2-24: A typical Galvanostatic pulse curve.	37
Figure 3-1: Sound specimen formwork design.	39
Figure 3-2: Transversely cracked specimen formwork design.	40
Figure 3-3: Longitudinally cracked formwork design.	41
Figure 3-4: Sound beam formwork. Note: cross bars were straightened before placing concrete.	45
Figure 3-5: Formwork for transversely cracked specimens with rebar in place.	45
Figure 3-6: Formwork for longitudinally cracked specimens with rebar in place.	46
Figure 3-7: Inducing cracks in the transversely cracked (left) and longitudinally cracked beams (right).	48
Figure 3-8: Measurement of corrosion potential before exposure to brine (left); and epoxy of all but cracked side of the prisms (right). Closer view of individual prism (insert).	49

List of Figures

Figure 3-9: Specimen exposure to brine solution. Cracked specimens are placed in tubs containing brine solution while ponding well is filled with brine.	50
Figure 3-10: Cracked specimens closed in tubs (left), and sound beams closed with ply wood (Right).	50
Figure 4-1: Comparison of the HDG sample from the literature [47] with one used in the present work (right). Note for the picture on the right that: a) layer 1 is too thin to be detected or absent, b) the arrows points at defects in the coating.	54
Figure 4-2: Comparison of C1 and C2 specimens with CGR [47]. Note the thicker layer 1 in C1 and the obscure or absent layer 1 in C2. Insert shows the broken layer 1 in C1 bar.	54
Figure 4-3: Comparison of C3 with Galvan coating from [62]. The Zn-rich nodule and eutectic structure of aluminum and zinc can be seen in both photos.	55
Figure 4-4: Regions analysed for coating thickness.	55
Figure 4-5: Average corrosion potential (E_{corr}) values of bars in sound concrete beam specimens.	60
Figure 4-6: Average corrosion current density (i_{corr}) values of bars in sound concrete beam specimens.	61
Figure 4-7: Average concrete resistance value of sound beam specimens.	62
Figure 4-8: Average corrosion potential (E_{corr}) values of bars in transversely cracked concrete specimens.	63
Figure 4-9: 1-week test showing the non-protective nature of CHZ crystals in water.	64
Figure 4-10: 1-week test showing the non-protective nature of CHZ crystals in 3% NaCl.	65
Figure 4-11: Correlation of crack width and corrosion current density of bars in the transversely cracked concrete specimens at 450 days of brine exposure.	66
Figure 4-12: Average corrosion current density (i_{corr}) value of bars in transversely cracked concrete specimens.	66

Figure 4-13: Average corrosion potential (E_{corr}) values of bars in longitudinally cracked concrete specimens..... 68

Figure 4-14: Average corrosion current density (i_{corr}) values of bars in longitudinally cracked concrete specimens. 69

Figure 4-15: Salt crystals on the surface and in the cracked region. Such crystals in the crack could block further ingress of salt..... 70

Figure 4-16: Concrete specimen of autopsied transversely cracked C2 specimen..... 71

Figure 4-17: Exposed surface (to concrete crack) of bars in transversely- (left) and longitudinally- (right) cracked HDG steel specimen 1 to 5..... 72

Figure 4-18: Non-exposed surface (to concrete crack) of bars in transversely- (left) and longitudinally- (right) cracked HDG steel specimen 1 to 5..... 72

Figure 4-20: XRF analysis of autopsied transversely cracked C3 concrete specimen. The detection of aluminum in the autopsied concrete confirms the $\text{Ca}_2\text{Al}(\text{OH})_7 \cdot 3\text{H}_2\text{O}$ product suggested by [65]. 73

Figure 4-21: Average corrosion current density (i_{corr}) in the corroded area of transversely cracked specimens. Insert are the i_{corr} values averaged over the exposed surface. 74

Figure 4-22: Average corrosion current density (i_{corr}) in the corroded area of longitudinally cracked specimens. Insert are the i_{corr} values averaged over the exposed surface..... 74

Figure 4-23: Definition of “corrosion performance”. t_i = corrosion initiation time, t_p = corrosion propagation time, t_s = service life time..... 75

Figure 4-24: Corrosion current density (i_{corr}) of galvanized steel in OPC concrete with cast in chloride kept at 100% R.H. [51] (left) and OPC concrete submerged in artificial sea water [45] (right). Note: cement/sand ratio of 1/3 is similar to one used in the present work. 76

Figure 4-25: Average corrosion potential (E_{corr}) values on a 30 years old bridge deck reinforced with HDG steel [48]. The figure also shows the corrosion current density values and degree of delamination found at years where the E_{corr} values began to rise again. 77

List of Figures

Figure 4-26: Average depth loss over time of the corroded area on all galvanized bars (left) and total depth loss (at the end of 64 weeks' exposure to brine) of the corroded area on each of the 5 replicate bars (right), both in the transversely cracked concrete specimens.	78
Figure 4-27: Corrosion potential (E_{corr}) of galvanized steel in OPC concrete with cast in chloride kept at 100% R.H. [51] (left) and OPC concrete submerged in artificial sea water [45] (right). Note: cement/sand ratio of 1/3 is similar to one used in the present work.	79
Figure 4-28: Potential guideline for assessing the probability of corrosion of galvanized steels in concrete.	81
Figure 4-29: Correlation of corrosion- potential and rate of 100% R.H concrete [51].	82
Figure 4-30: Correlation of corrosion- potential and current density (averaged over the entire exposed rebar area) at 150, 300 and 450 days of exposure to brine solution.	83
Figure 4-31: Correlation of corrosion- potential and current density (averaged over the entire corroded rebar area) at 150, 300 and 450 days of exposure to brine solution.	83
Figure 4-32: Recovery time for potential and current controlled system [66].	84
Figure 4-33: Outlier in a galvanostatic pulse weekly test.	85
Figure A1 & A2: Average E_{corr} and i_{corr} from both GP and LPR test.	104 - 106
Figure A3: Average concrete resistance from GP test.	107 - 108
Figure C1 & C2: Individual E_{corr} and i_{corr} from both GP and LPR test.	111 - 129
Figure C3: Individual concrete resistance from GP test.	129 - 136
Figure D1 - D5: Micrographs of untested rebar specimens.	137 - 141
Figure E1 & E2: Initial and final autopsy photos.	142 - 170

List of Tables

Table 2-1: Cathodic reactions. Note that the mentioned line “a” and “b” are present in Figure 2-3.
..... 7

Table 2-2: Comparison between reinforcing materials [11]. 11

Table 2-3: Characteristics of the Zn coating. Note: numbers are based on Figure 2-13 [18]. 14

Table 2-4: Varying Al content in formation of the inhibition layer [Tang, 1998]. 23

Table 2-5: NRC recommended guideline for assessing HDG through its half-cell potential. 34

Table 3-1: Dimensions and schematic of concrete specimens. 41

Table 3-2: Tested rebar grades. 43

Table 3-3: Highway bridge mixture design used for casting. 44

Table 4-1: Compositional analysis determined by x-ray fluorescence. Note that the percentages do not equal 100 because other minor elements are not presented. 53

Table 4-2: Coating thickness around rebar samples. 56

Table 4-3: Range of E_{corr} , steel weight, crack width for five replicate specimens. 57

Table 4-4: Average concrete compressive strength (MPa). 58

Table 4-5: Corrosion potential values of the bars in cracked and non-cracked concrete after 450 days exposure to brine containing 21% Cl^- 80

List of Equations

Equation 1: Fe Active corrosion 7

Equation 2: Below pH=7 (Between line “a” and “b”) 7

Equation 3: Fe Active corrosion 7

Equation 4: Below pH = 7 (Below line “a”) 7

Equation 5: Passive corrosion 7

Equation 6: Above pH=7 (Between line “a” and “b”) 7

Equation 7: Passive corrosion 7

Equation 8: Above pH = 7 (Below line “a”) 7

Equation 9: Formation of Calcium hydroxyzincate (CHZ) [13]. 30

Equation 10: Equation used to calculate the corrosion current density of the rebar (i_{corr}). 36

List of Abbreviations and Variables

Abbreviation	Name
ASTM	American Society for Testing and Materials
Ba and Bc	Anodic and cathodic tafel constant
CE	Counter electrode
CGR	Continuously galvanized rebar
CHZ	Calcium hydroxyzincate
CP	Cyclic polarization
C-S-H	Calcium-silicate-hydrate
CSE	Copper-copper sulfate electrode
E_{corr} or E_c	Corrosion potential
ECR	Epoxy-coated rebar
EDS	Energy-dispersive X-ray spectroscopy
EIS	Electrochemical impedance spectroscopy
E/pH	Potential versus pH
GP	Galvanostatic Pulse
HDG	Hot-dipped galvanized
HPC	High performance concrete
I_{corr}	Corrosion current
i_{corr}	Corrosion current density
IMC	Intermetallic compound
IZA	International zinc association
LPR	Linear polarization to resistance
MTO	Ministry of Transportation Ontario
NRC	National Research Council
OPC	Ordinary Portland Cement
PS	Potentiostatic
R_c	Concrete resistance
RE	Reference electrode
Rebar	Reinforcing bars
R_p	Resistance polarization
SCE	Saturated calomel electrode
SHE	Standard hydrogen electrode
SEM	Scanning electron microscope
w/c	Water to cement (ratio)
w/cm	Water to cementitious materials (ratio)
WE	Working electrode (typically the rebar)
XRF	X-ray fluorescence

Chapter 1 Introduction

1.1. Background

Concrete can be cast into complex shapes at ambient temperature. This reason has seen concrete emerging as one of the most widely used material today. Concrete is basically a ceramic and, therefore, strong in compression but not in tension. As a result, concrete is generally reinforced with metals such as plain carbon (or black) steel.

Every metal wants to revert to their combined ore form and, depending on how 'favourable' the surrounding environment is, corrosion could be a major concern. Fortunately for most reinforced structures, the high pH in concrete is a favourable environment for the use of black steel - because the steel forms a protective thin layer (passive film) that significantly reduces the corrosion rate of the reinforcing bar (rebar) [1,2]. Unfortunately, this passive film can break down if the alkalinity of the concrete environment around the steel drops or in the presence of chlorides [2].

Carbonation causes the alkalinity of concrete to drop when carbon dioxide (CO_2) in air combines with hydroxides, mainly calcium hydroxide ($\text{Ca}(\text{OH})_2$), present in concrete to form limestone (CaCO_3) and lowers the pH to about ~9 [5]. There has been little report regarding failure of infrastructure due to carbonation in Canada – mainly because of the wet climate condition which takes longer for CO_2 to successfully reach the rebar surrounding. A second cause of deterioration of infrastructure, which is a major concern because of the harsh winter season experienced in Canada, is chloride contamination. The brine solutions applied to Ontario outdoor concretes during this season penetrate the concrete to the rebar and breaks down the protective film formed on the bar, resulting in higher rate of corrosion.

Concretes are cast containing fine pores that serve as channels for chlorides to travel to the rebar surface. As a result, the durability of reinforced structures in and around the marine area in coastal regions and in countries with harsh winter season is of concern. Furthermore, today's concretes are designed for higher strength - since they are made to carry more load than in the past, and such high strength concretes are more susceptible to shrinkage resulting from varying weather condition. Continuous weather changes lead to a corresponding volume change of

concrete through expansion and contraction and, this can easily cause micro- and macro- cracks to be present in the concrete, making corrosion of the rebar of greater concern. In addition, when black rebar corrodes, the corrosion products fill a volume larger than that of the corroding steel [9]. This can result in cracking and spalling of the concrete cover (distance between the embedded rebar and concrete surface). The use of a more corrosion resistant rebar is one method of improving the durability of our infrastructure.

Conventionally (hot-dipped) galvanized steel, a zinc-coated steel with $\sim 75\text{-}135\ \mu\text{m}$ thickness, was introduced as an alternative reinforcing material mainly because: 1) it forms a stable protective film even in carbonated concrete, 2) the coated Zn possess higher chloride threshold than black steel and, when it corrodes, it has added benefit of protecting the base steel as a sacrificial anode, 3) the zinc corrosion product is soluble and do not crack the concrete.

Despite these benefits of HDG steel, there are few major drawbacks of using it for reinforcing concrete. The first is the initial corrosion of Zn when placed in the high pH environment of the fresh concrete. In this high pH, >13.6 , zinc is highly unstable and corrodes vigorously in the first few days before a crystalline film called calcium hydroxyzincate (CHZ) is formed [15]. As a result, the rebar loses some of its Zn layer even before carbonation or chloride contamination of the concrete. The other drawback is the nature of the iron-zinc (Fe-Zn) intermetallic compounds (IMC) present in the coating, which were formed by interaction between the steel substrate and Zn bath. Due to the brittle nature of the IMC, cracks may form in the coating during forming (e.g. bending), and those regions would be preferential sites for localized corrosion. Lastly, a larger part of the HDG coating contains these IMCs which [15] reported to be less corrosion resistant compared to the outer pure Zn layer.

To remedy this, a new technology of continuously galvanizing (CG) is aimed at producing a more ductile corrosion resistance coating. The ductility of this coating is achieved by small aluminum addition to the zinc bath to produce a nanometre thick Fe-Al-Zn (known as inhibition layer) adjacent to the steel substrate that inhibits the formation of the IMCs and results in the remainder of the layer being the almost pure zinc layer. Furthermore, this new method of galvanizing allows less residence time of rebar in the molten bath to prevent reactions between Fe and Zn. As a result, continuously galvanized rebar (CGR) comes with thinner coatings,

typically about half that on HDG steels. The project reported here involves evaluation of three prototypes of continuously galvanized rebar.

In accessing the condition of reinforcing bars in field concretes, the half-cell potential (also known as open circuit potential, OCP, or corrosion potential, E_{corr}) measurement is the most common method. On this account, American Standard Testing and Materials (ASTM C876) provides a guideline for assessing the probability of corrosion of rebar. However, this guideline, shown in Figure 1-1, is only sufficient for uncoated rebar in concrete and cannot be used for galvanized steel reinforced structures. As a result, there is considerable uncertainty in interpreting half-cell potentials collected on galvanized reinforced structures in the field. Thus, a more detailed study of the potentials of galvanized bars in various stages of degradation is essential. The first such study, published as recently as 2014, by the National Research Council of Canada (NRC) provided guidelines specifically for galvanized reinforced structures. These guidelines are based on single author's results performed on HDG steel and require validation for both the HDG steel and the new CGR.

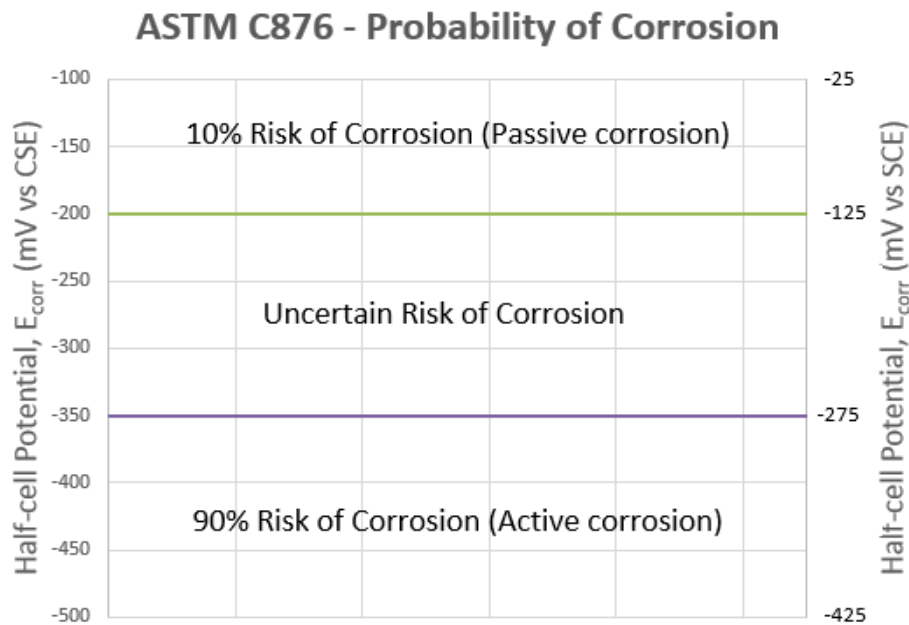


Figure 1-1: ASTM C876 Half-cell potential guideline for black steel.

1.2. Statement of the problem

As a general contribution from the international zinc association (IZA) towards providing an alternative economical corrosion resistance reinforcing material, the new CGR needed to be assessed for its ability to meet the 75 year' service life specified by Canadian Building Code. Thus, a comparative metallurgical and electrochemical assessment was carried out on the prototypes of continuously galvanized steel and conventionally hot-dipped galvanized steel to evaluate the long term effectiveness of the reinforcing bars.

1.3. Objectives

Based on the aforementioned, the objectives of this project were:

- 1) To evaluate the effectiveness of the inhibition provided by the alloyed coating of the CGR in improving corrosion performance of galvanized steel in concrete. A metallographic and electrochemical assessment were performed with an attempt to answer the following:
 - a. Is the inhibition layer continuous and crack free?
 - b. Does it suppress the formation of the IMC or just delay it, possibly leading to Fe-Zn outburst and cracks in the coating, as suggested by reference [18]?
 - c. Is there sufficient thickness of coating remaining after the initial corrosion of zinc, for the formation of a stable protective CHZ film and to provide long term service life to the structure?
- 2) To identify characteristic corrosion potentials and current densities corresponding to:
 - a. Passive & chloride-induced active, corrosion of the galvanized rebar in non-cracked/sound concrete;
 - b. Galvanized rebar partially exposed to chloride solution through cracks in the concrete.

1.4. Scope and Importance of the study

Electrochemical methods were utilized in determining the corrosion behaviour of the reinforcing bars in both non-cracked (sound) and cracked concretes exposed to brine solution. The sound beam specimens contained built-in ponding well for holding multi-chloride brine solution. The cracked concrete specimens were set up such that: cracks were initiated perpendicular (transverse) to the rebar in some concrete prisms; while others had cracks parallel (longitudinal)

to the rebar, simulating concrete bridge deck. Afterwards, all cracked specimens were placed in a tub filled with multi-chloride brine solution.

Furthermore, since alloying elements and their amount, immersion and quenching time, bath temperature, etc. can all influence the metallurgy of galvanized coatings, and subsequently their performance in concrete. This study utilizes CGR produced on trials from China and Dubai, thus their results should be carefully compared. In addition, since the concrete environment in which these bars are placed greatly influences their corrosion performance, the concrete mixture design and proportion (i.e. water-to-cement ratio, supplementary cementitious used, wet curing time etc.) should be taken into account in comparing results. This study utilized a typical Canadian highway bridge mixture design.

Overall, the electrochemical tests yielded corrosion potential and corrosion current density for both passive and active conditions. The results from this study are comparative but should not be considered absolute in making decisions on service life or in creating maintenance schedule without putting into account the variability in environments and weather conditions. Nonetheless, this result will assist the producers in assessing the parameters which require more stringent control in order to ensure a consistent quality of the CG rebar.

Chapter 2 Literature Review

This section highlights the background research on corrosion of rebar in concrete; corrosion behaviour of zinc in concrete; the metallurgy of conventionally hot-dipped galvanized (HDG) and continuously galvanized rebar (CGR) coating, and the long term use of galvanized rebar in concrete structures.

2.1. Overview of impact on the corrosion of rebar in concrete

Metals will generally try to revert to their ore form; therefore, in most of the environments in which they are used, corrosion is a concern. **Error! Reference source not found.** shows a typical corrosion cycle; where metals, existing in their ore form, are extracted and, when used in service, corrode over time and revert to their stable ore form. Fortunately for practical use, this process is slow and steel, because of its ductile nature, typically yield (i.e. give some warning) before any catastrophic failure.

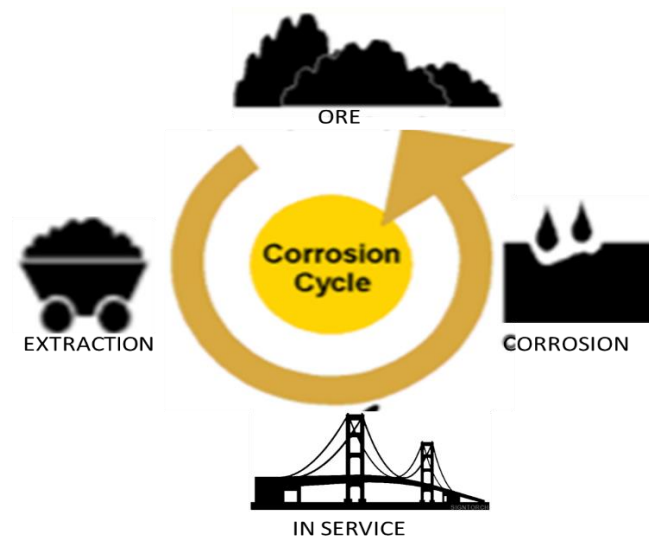


Figure 2-1: Corrosion cycle [56]

For an electrochemical cell to be complete, an anodic and a cathodic reaction are required. **Error! Reference source not found.** shows typical anodic and cathodic reactions that occur for iron (Fe). In some cases, the product of the anodic and cathodic reactions combines to form a thin oxide or hydroxide film (passive film) that protects the metal against further rapid corrosion [2,3]. In other cases, a soluble non-protective oxide or hydroxide ion is formed, known as rust.

Table 2-1: Cathodic reactions. Note that line “a” and “b” are present in Figure 2-3.

Anodic reactions	Cathodic reaction
$Fe \rightarrow Fe^{2+} + 2e^{-}$ Equation 1: Fe Active corrosion	$O_2 + 4H^{+} + 4e^{-} \rightarrow 2H_2O$ Equation 2: Below pH=7 (Between line “a” and “b”)
$Fe + 2H_2O \rightarrow HFeO^{2-} + 3H^{+} + 2e^{-}$ Equation 3: Fe Active corrosion	$2H^{+} + 2e^{-} \rightarrow H_2$ Equation 4: Below pH = 7 (Below line “a”)
$2Fe + 3H_2O \rightarrow Fe_2O_3 + 6H^{+} + 6e^{-}$ Equation 5: Passive corrosion	$O_2 + 2H_2O + 4e^{-} \rightarrow 4(OH^{-})$ Equation 6: Above pH=7 (Between line “a” and “b”)
$3Fe + 4H_2O \rightarrow Fe_2O_3 + 8H^{+} + 8e^{-}$ Equation 7: Passive corrosion	$2H_2O + 2e^{-} \rightarrow H_2 + 2(OH^{-})$ Equation 8: Above pH = 7 (Below line “a”)

One of the most benign environments for plain carbon steel is the high pH (~12.6 - 13.8) environment of concrete [1, 2]. In this environment, carbon steel readily forms a protective oxide or hydroxide that decreases the corrosion rate significantly as shown in the E/pH diagram - a thermodynamic map of potential (E) versus pH showing the equilibrium products of corrosion of iron, Figure 2-1.

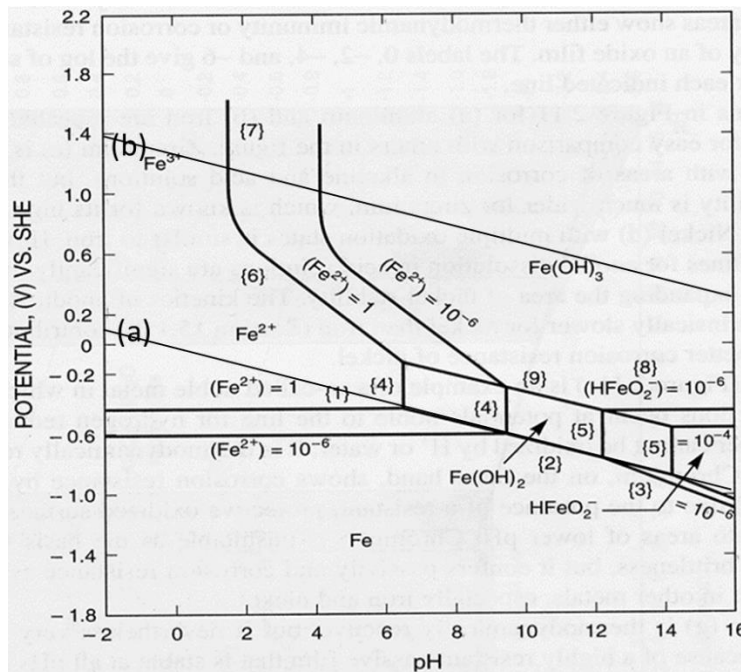


Figure 2-2: Equilibrium E/pH diagram for Iron (Fe) [4]. The a and b line represent H^+/H_2 equilibrium and O_2/H^- equilibrium respectively.

This passive film, typically formed within the first week of hydration of the concrete [5], can break down after some time depending on the exposure condition of the concrete. Concrete is porous and seldom crack-free. As a result, the components of the surrounding environment of the concrete can diffuse through these pores over time and, more easily, through the cracks. Carbon dioxide (CO_2) from the atmosphere will react with $Ca(OH)_2$ in the concrete, lowering the pH. Consequently, a decrease in pH of the rebar's surroundings creates instability and breakdown of the passive film on the rebar, Figure 2-3. This process is called carbonation and, it is one cause of deterioration of reinforced concretes. However, it is not much of a problem in Canada because of the wet climate condition - it typically takes longer for CO_2 to reach the rebar surrounding when the concrete is wet. The focus of this report is chloride contamination - a more common and faster medium of deterioration of reinforced concrete in North America.

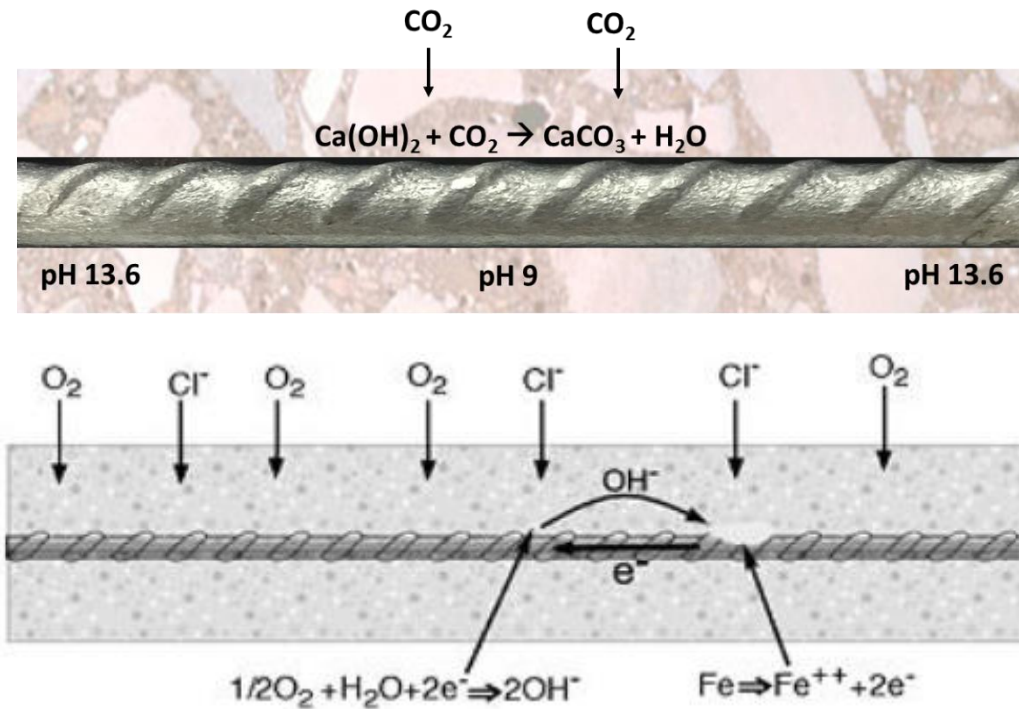


Figure 2-3: Carbonation (top) and chloride attack (bottom) of reinforced concrete [6].

For a country like Canada that experiences a harsh winter season, salts are typically sprayed on walk-ways, bridges, parking lots etc. to melt the ice, securing the safety of road users. As a result, susceptibility of concretes in this part of the world to chloride attack is a major concern. Marcus et al. [7] proposed two mechanisms for passive film breakdown in the presence of chloride: local thinning and anion diffusion. They hypothesized that passive films are polycrystalline in nature and the grain boundaries act as sites for thinning and diffusion. In the local thinning model, diffused Cl^- and OH^- in the concrete compete for adsorption on the passive metal surface, with Cl^- being more superior due to its higher affinity towards Fe. This forms aqueous chloride compound that dissolves after a while, leaving the chloride free for continued reaction, and the process becomes autocatalytic. In the anion diffusion model, the diffused Cl^- penetrates the passive film to form a compound at the steel/passive film interface that exert pressure on the film and delaminates it, Figure 2-4.

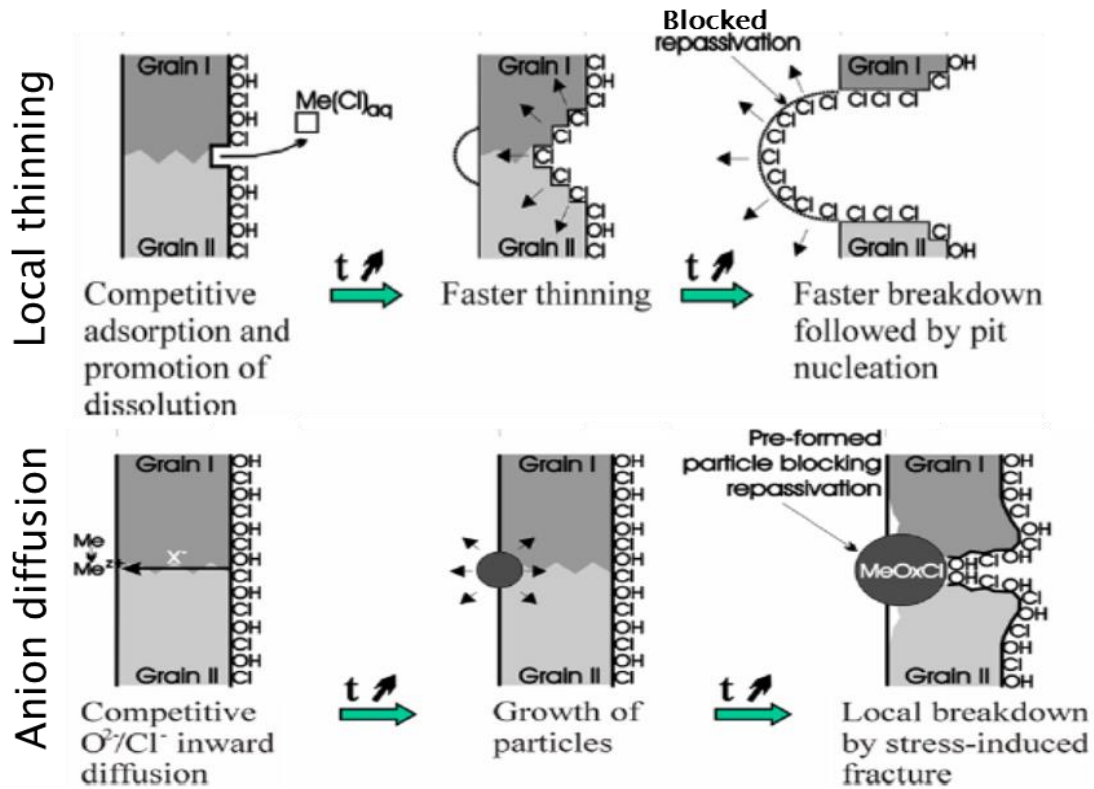


Figure 2-4: Mechanism of passivity breakdown on steel in the presence of chloride [7].

During the electrochemical reaction, corrosion product from the anode (Fe^{2+}) and the cathode (typically OH^-) react to form numerous expansive compounds that exerts pressure in the surrounding concrete. These compounds are typically 2 - 3.5 times larger than the corroded steel, and can result in cracking and spalling of the concrete cover, exposing the rebar [8], Figure 2-5. This, often enough, is the main mode of reinforced concrete deterioration.

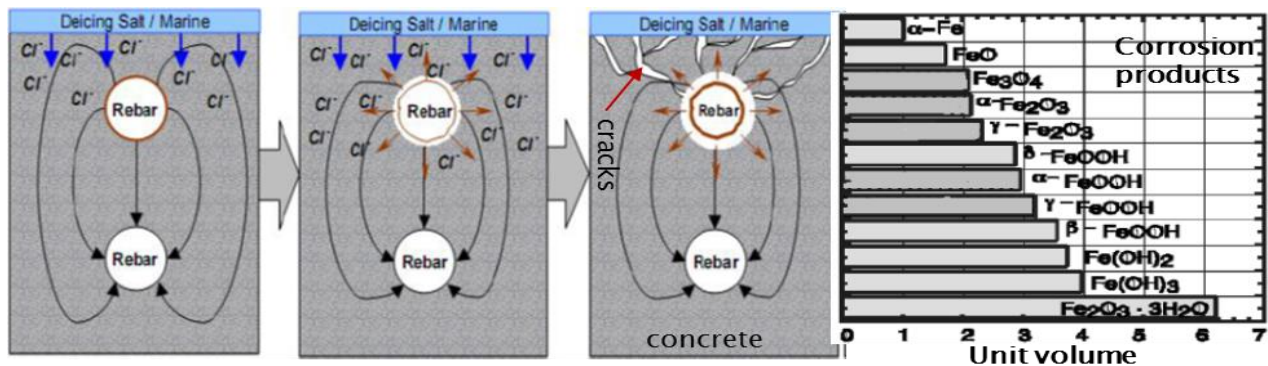


Figure 2-5: Cross section of a reinforced structure attacked by chloride, left [8]. Expansive nature of corrosion product, right [9].

2.2. Conventionally hot-dipped galvanized (HDG) steel

This section briefly describes the general overview of the conventionally used hot-dipped galvanized rebar, the advantage of using HDG rebar over plain carbon steel, and metallurgy of HDG coating.

2.2.1. Overview

In the past few decades, the use of galvanized rebar has become an economical option for the replacement of regular plain carbon steel as reinforcement [10]. Table 2-2 shows comparison between HDG and other kinds of corrosion resistance reinforcing materials.

Table 2-2: Comparison between reinforcing materials [11].

Type of rebar	Times more corrosion resistant than black rebar	Scratch and chip resistance	Bending	Cutting	Welding	Chloride threshold	Cost, \$/lb ¹
Epoxy-coated ■ Damage level 0.5% ■ Damage level 0.004%	150 to 1,175 69 to 1,762	Easily damaged, requiring field repairs	Allowed but can damage epoxy coating	Allowed; coating of cut end required	Allowed; coating of weld required	Same as black rebar Very high	0.32
Galvanized (zinc-coated)	38	Very tough; hard to damage	Allowed but may weaken coating	Allowed; coating of cut end required	Allowed; coating of weld required	4 to 10 times higher than black steel	0.50
GFRP	Won't corrode	Fairly tough; difficult to damage	Field bends not allowed	Allowed; sealing of cut end may be required	Nonweldable	Immune to chloride attack	3.00 to 4.00 ²
Solid stainless steel	800 to 1,500	Not an issue	Allowed	Allowed	Allowed; special welding procedures apply	15 to 24 times higher than black rebar	1.60
Stainless-steel-clad	Same as solid stainless-steel rebar	Very tough; nearly impossible to damage	Allowed	Allowed; coating of cut end may be required	Allowed; special welding procedures apply	Same as solid stainless-steel rebar ³	0.60

This zinc coated rebar, typically 75-135 μm (ASTM A767), is produced by hot dipping of ribbed plain carbon steel in a molten zinc bath at a temperature approximately 450 – 500°C. The galvanizing process includes several stages before the zinc-coated bar is achieved, as illustrated in Figure 2-2. Prior to immersion, the steel undergoes multiple surface preparation stages where it is degreased in an alkali solution, rinsed, pickled in an acid solution (typically HCl or H₂SO₄) and rinsed again. Afterwards, it is fluxed in ammonium chloride (NH₄Cl) to remove impurities, oxidized iron and mill scale that may react in the Zn bath. The fluxed bar is then immersed in Zn bath and, after a short period, it is withdrawn and cooled.

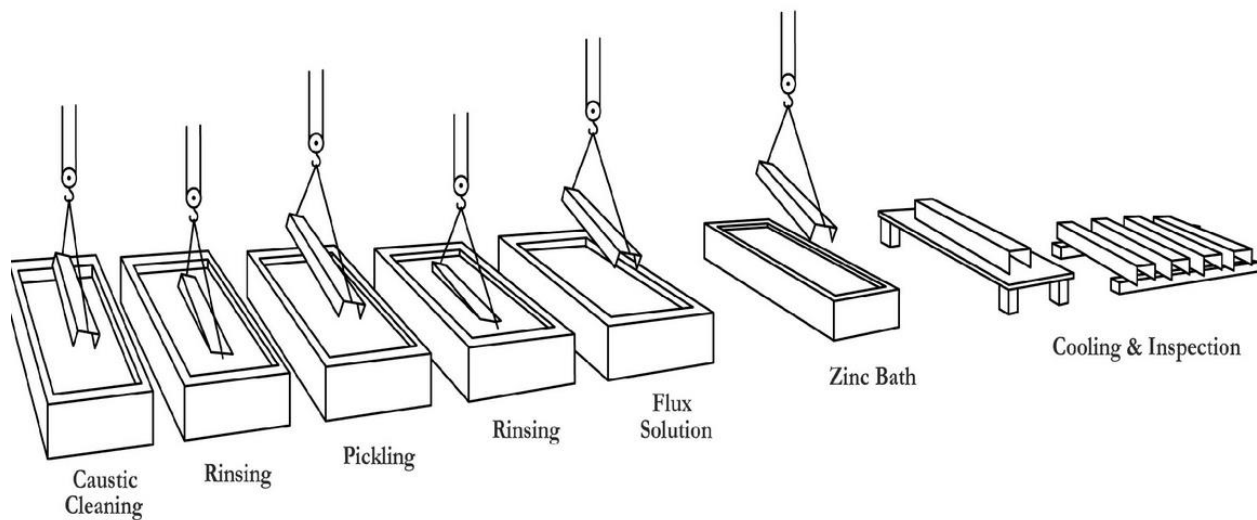


Figure 2-6: Hot dipped galvanizing process [12].

Galvanized rebar in concrete possesses a few advantages over the conventional plain carbon steel (also known as black steel) because of its ability to provide:

- Barrier protection – the Zn coating acts as a shield for the underlying rebar against its environment;
- Galvanic protection – the Zn acts as a sacrificial anode by corroding and cathodically protecting the base steel [5,11], after a higher chloride threshold has been surpassed [5,11,13,17];
- Passive film protection – the Zn is able to form a stable protective film in a low pH environment (up to ~9) found in carbonated concrete, Figure 2-3. Several authors [14,15,16] found that galvanized steel produces a protective crystalline layer of calcium

hydroxyzincate ($\text{Ca}(\text{Zn}(\text{OH})_3)_2$) (CHZ) at high pH levels, which significantly reduces the corrosion rate of the zinc;

- Aqueous corrosion product – when the Zn corrodes, it produces a soluble corrosion product that diffuses into the concrete and, therefore, exerts significantly less pressure on the surrounding concrete than do iron corrosion products [17].

2.2.2. Metallurgy of HDG Rebar

In 2000, Marder [18] performed an extensive review and update to Mackowiak and Short's review in the 1970's on the metallurgy of Zn coating. Marder [18] addressed both the scientific and practical aspects of galvanized coatings by considering: 1) the thermodynamics - Fe-Zn equilibrium phase diagram, comparing the expected phases with those actually found in a galvanized coating; 2) the kinetics of each phases; 3) the effect of steel and Zn bath composition on the intermetallic compounds (IMC) formed in the coating. Unless otherwise stated, all references in this section are obtained from the review and, since the amount of work reported is extensive, only the more important references have been included.

2.2.2.1. Overview

Anatomy of a conventional HDG rebar consists of three sections: the outer layer (pure zinc layer); the underlying steel substrate and; the IMC (formed by reaction between Fe and Zn reaction) between the overlay and the steel substrate. The formation of these IMC layers is affected by galvanizing procedure and parameters like bath temperature and chemistry, steel chemistry and surface roughness, immersion and withdrawal/quenching time/rate, etc. [19]. Generally, when forming (e.g. bending) a HDG steel, the brittle nature of the IMC is a concern – because they may lead to cracked regions in the coating (Figure 2-7) that could result in localized corrosion, or worse delamination [47]. However, it is expected that delamination may not be a problem when HDG rebar is used as reinforcement since there is usually enough compaction from the surrounding concrete to keep the coating intact. Nonetheless, the cracked region remains a preferential site for localized corrosion.

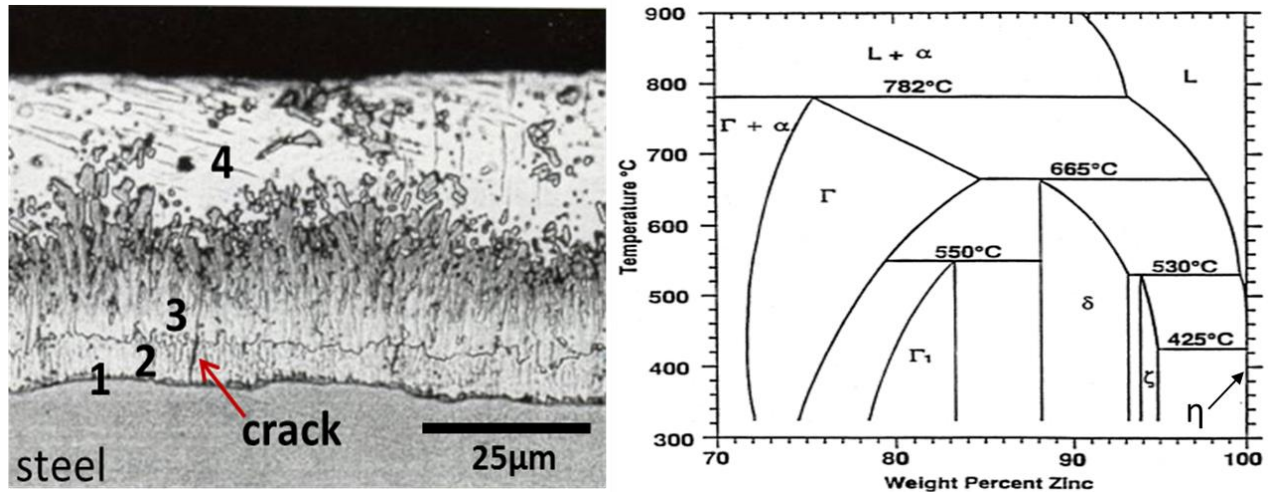


Figure 2-7: HDG rebar coating (from IZA) and Fe-Zn phase equilibria [18]. 1 = Γ and Γ_1 (gamma 1 & 2), 2 = δ (delta), 3 = ζ (zeta), 4 = η (eta).

2.2.2.2. Iron-Zinc (Fe-Zn) Equilibria and Kinetics

As mentioned earlier, the reactions between Fe and Zn give rise to brittle IMCs that increase in Zn and decrease in Fe content with distance from the substrate to the outer surface of the coating. The name and characteristics of these phases are listed in the Table 2-3 below:

Table 2-3: Characteristics of the Zn coating. Note: numbers 1, 2, 3 and 4 in the table are based on Figure 2-3 [18].

	No.	Phases	Name	Formular	% Fe	Crystal structure
Substrate	Steel	Fe	Iron	Fe (Zn)	96.1	BCC
INTERMETALLIC COMPOUNDS	1	Γ	Gamma	$FeZn_3$	23.5-28	BCC
		Γ_1	Gamma ₁	$Fe_{20}Zn_{80}$	17-19.5	FCC
	2	δ	Delta	$Fe_{10}Zn_{90}$	7-11.5	Hexagonal
	3	ζ	Zeta	Fe_5Zn_{95}	5-6	Monoclinic
Outer layer	4	η	Eta	Zn(Fe)	0.03	HCP

The eta (η) almost pure Zn layer is typically formed during withdrawal of the rebar from the molten Zn bath. The zeta (ζ) layer, lower in Zn content, can consist of two layers depending on the supersaturation of Fe in the melt; a columnar crystal grows first and after saturation, nucleation of tiny crystals separated by pure Zn begins [22]. Furthermore, Marder reported that crack can begin to form in the basal plane of the delta phase and can extend below and above to the delta and gamma phase respectively. Generally, both gamma layers are very thin ($<1\mu\text{m}$ [21]) and are often seen as a single layer, Figure 2-8 (left), or are hardly visible as in the coating from the current work, Figure 2-8 (right). Note the presence of a defect in the eta layer of the coating in Figure 2-8 (right), which could be a preferential site for localized corrosion.

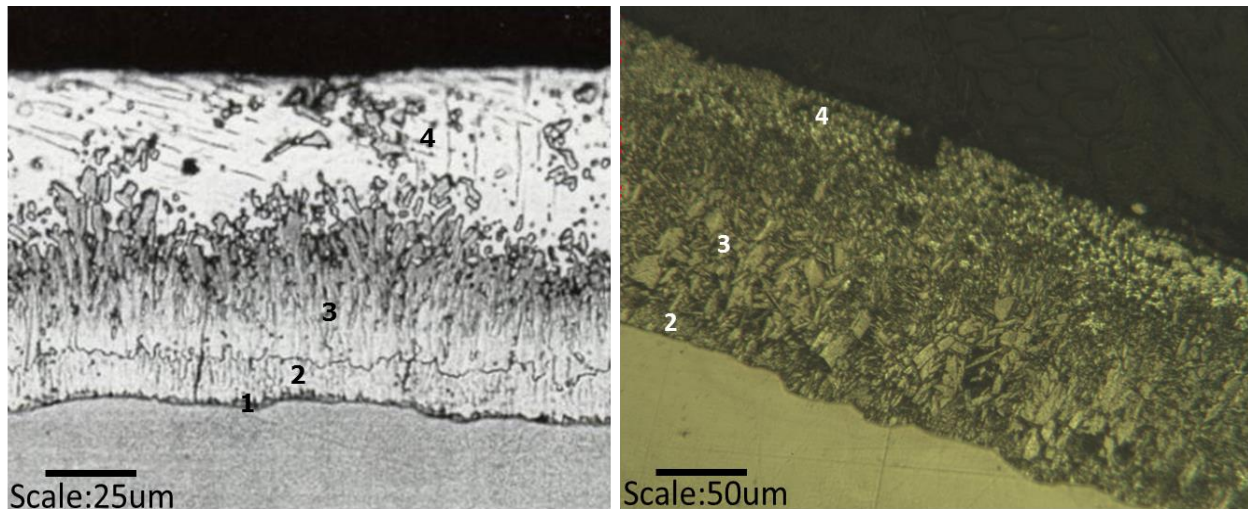


Figure 2-8: Comparison between HDG coating from the literature [47] (left) and that used in this experiment (right). The numbers refer to that in Table 2-3.

Figure 2-9 (left) [21], provides a schematic representation of the sequence of nucleation and growth of these IMCs, starting with the phase with the lowest amount of iron, zeta ζ . Thereafter, delta δ phase, with a higher Fe content, forms underneath the zeta ζ , with both phases forming only after 5s immersion time. Lastly, after some incubation time ($\sim 30\text{s}$), the gamma phases possessing the highest amount of Fe then forms underneath the δ phase. Figure 2-9 (right) shows the influence of immersion time on the growth thickness of each IMC. A lower immersion time during production could explain why the gamma phases are absent in the HDG used in the current study, Figure 2-8 (right).

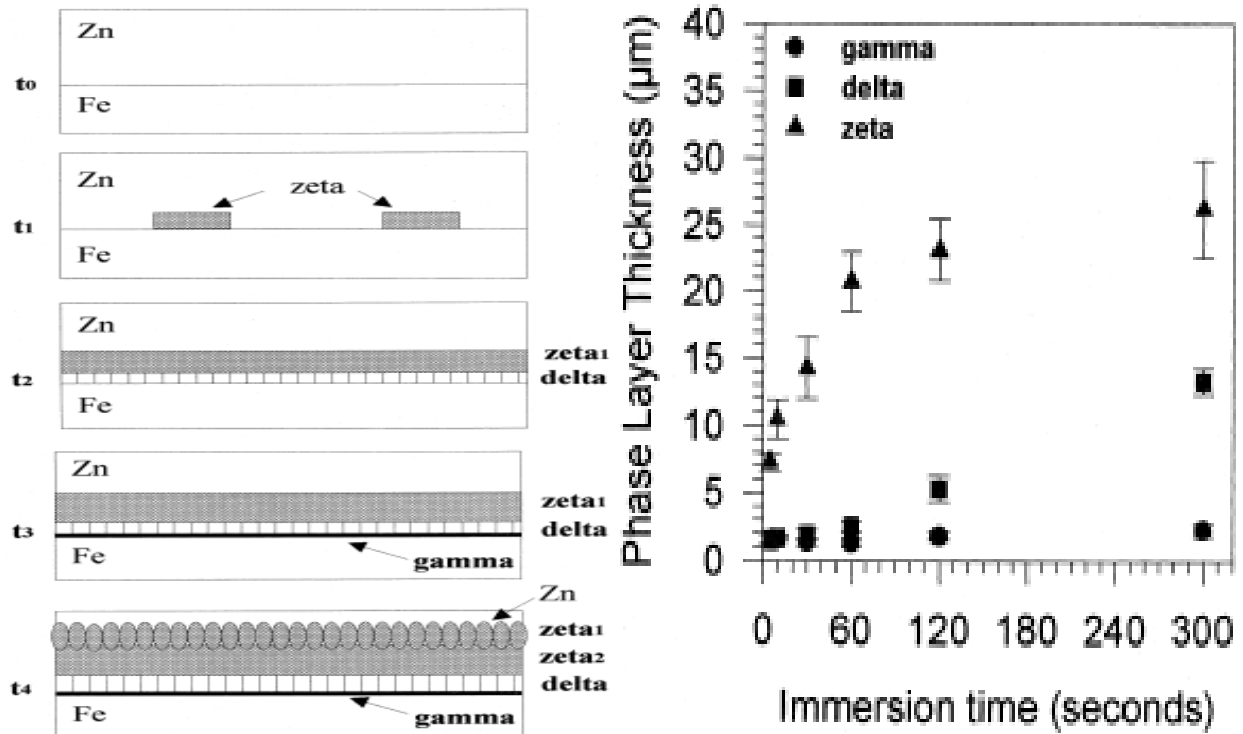


Figure 2-9: Nucleation and growth of phases in a HDG coating (left) and phase layer thickness variation with immersion time (right) [21].

The mechanisms of growth of the IMCs are different with most being diffusion controlled, i.e. diffusion of Zn into the steel substrate. Iron also diffuses into the Zn melt, but at a much slower rate [25]. In the diffusion mechanism of growth, there is inward growth movement of the gamma phase towards Fe, zeta phase grows towards the Zn melt and, the delta phase grows in both direction - but generally towards Zn. As the gamma phase grows inward, it is consumed by the growing delta that also consumes the growing zeta phase, causing an indistinct interface between the phases [22].

2.2.2.3. Factors affecting coating chemistry

Apart from the immersion time discussed earlier, temperature and substrate chemistry are other major influencing factors affecting the phases formed in an HDG coating. Onishi et al. [25] showed there is a general lower and upper parabolic growth of the IMC at 495°C and 520°C respectively and, between these temperatures, the growth was mentioned to be linear. Individually, these phases showed different growth behaviour at different temperatures. At

450°C and above, zeta layer was found to have high initial growth that decreases over time up to 300s until 495°C, when it is no longer possible to form a continuous phase. The opposite was observed for the delta layer and the gamma phase grows over a longer period at the same temperature. Between 550°C – 665°C, only gamma and delta layers were found to be stable. At higher temperatures, delta becomes unstable and is not present [22].

The phases formed in HDG coating are also affected by the substrate chemistry. Hisamatsu [26] found carbon, when added in small amount, segregate to the grain boundaries of the substrate, impeding Fe-Zn reaction. On the other hand, when silicon is present in greater amounts in the steel, an alloyed coating of only Fe-Zn may form [30]. This may not be good in terms of corrosion behaviour, since “pure” Zn eta has been reported to be more corrosion resistance than the IMC layers [39]. Furthermore, Sebisty and Ruddle [27] found steel containing a small amount (1-2%) of manganese to have little effect on the coating microstructure. Marder [29] found phosphorus addition to an interstitial-free (IF) steels (produced by adding Ti + Nb to low carbon steel to precipitate carbon and nitrogen atoms) to retard the kinetics of the gamma layer by blocking the diffusion of Zn along the steel grain boundaries, but did not affect other phases.

2.3. Continuously Galvanized (CG) steel

This section describes the product of a new technology of galvanizing rebar, continuously galvanized rebar (CGR). It is important to mention here that, although the steel is only recently being produced in bars for concrete reinforcement, the metallurgy of the continuously produced coating has been studied far back as the 1970’s. This section briefly describes a general overview of the advantages of using a CGR, and metallurgy of the coating.

2.3.1. Overview

The CGR is being promoted by the IZA [47] as having ductile coating, an excellent property for steel forming, and a corrosion resistant coating that can give reasonable service years (~40 years) in marine and salt-water environments. Figure 2-10 shows how the CGR compares with other reinforced materials in terms of cost and, one can see that it is very competitive.

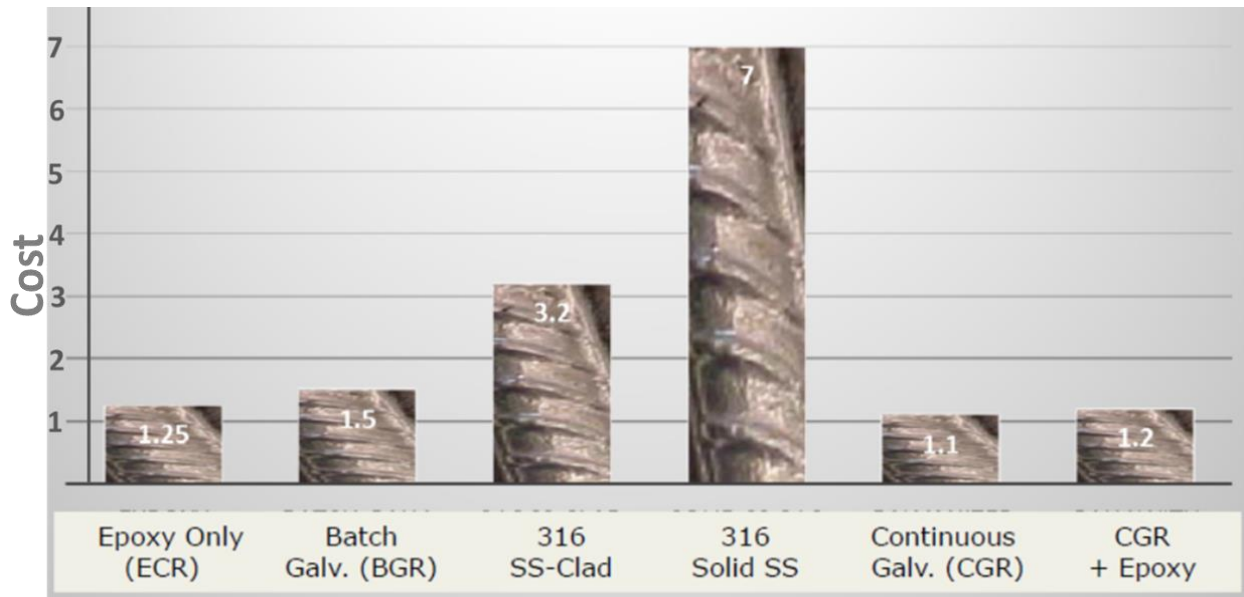


Figure 2-10: Coating alternatives in terms of cost versus black steel [46].

The CGR production process employs a set-up similar to continuous galvanizing of sheet used for automobiles, where there is uninterrupted passage of long length steel through the bath and which spends only few second in the molten Zn bath. Figure 2-11 is a schematic of a CGR production line, showing the surface preparation and galvanizing procedures are quite different from the HDG production line, Figure 2-6. For the CGR production, the Zn bath is alloyed with a small addition (typically 0.25 wt. %) of aluminum (Al), because of its higher affinity towards Fe, and the bar is passed through the alloyed bath within few seconds.

In describing the galvanizing process, the IZA is quoted in the CGR brochure released in 2015, “the bar passes through a flooded trough positioned above the bath. A metal pump maintains the zinc level in the trough above the submerged bar. Each end of the trough is sealed with an end-plate containing a hole for the bar to pass through. Excess zinc flows through the hole with the rebar and back into the bath. For the flux process, trough length must be sized to provide sufficient time (3 seconds) for flux release. The coated bar then passes through an air knife with a circular orifice which is used to control the coating weight”.

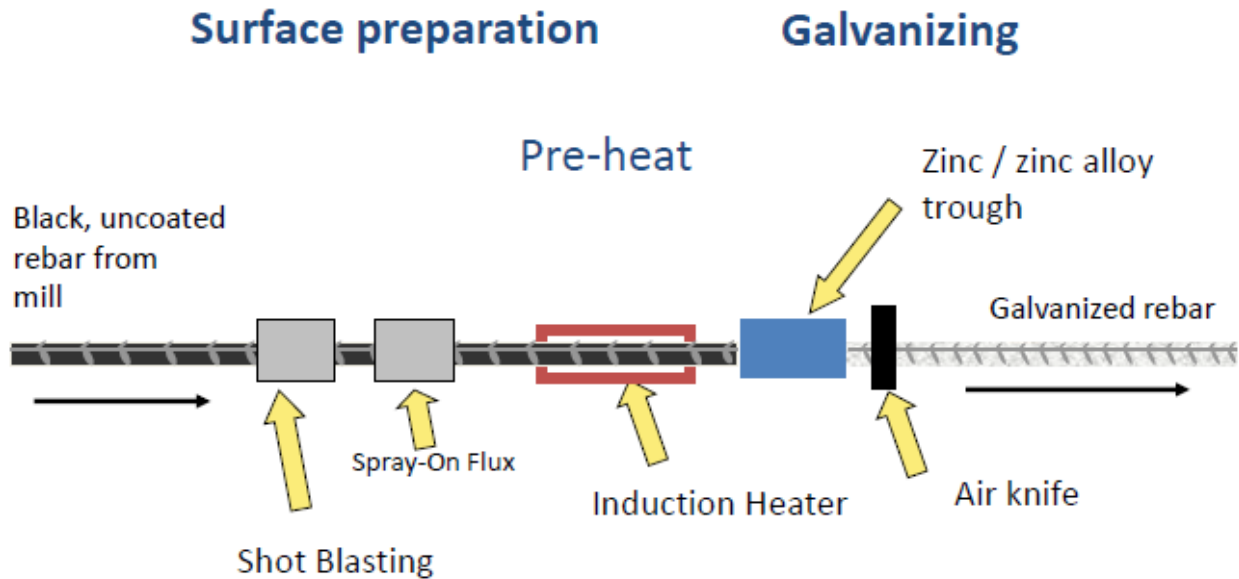


Figure 2-11: CGR production line [46]

According to IZA [47], this method of production and corresponding CGR produced is an advantage because:

- the Al addition to the bath produces a very thin layer (~100 nm) of ternary intermetallic Fe-Al-Zn, called the inhibition layer, in the coating which suppresses the formation of the brittle Fe-Zn IMCs. Unlike the HDG coating, bulk of which consists of the brittle IMCs, the thin inhibition layer in CGR allows the rest of the coating to be a “pure” ductile Zn layer that adheres very well.
- the adherent property, thinness and ductility of the CGR coating are particularly useful for forming purposes. For example, in building columns where onsite bending of rebar is required, cracking and flaking of the Zn coating will not be a concern for a CGR coating, unlike the HDG rebar that should be formed before coating.
- the galvanizing speed of this rebar (10 m/min line speed) minimizes exposure time in the high temperature bath (4-5 seconds) and results in: 1) production of a thinner coating (~50 μm) which reduces rebar weight; 2) significant cost saving due to reduced coating mass, 3) production time saving, and 4) possibility of galvanizing any rebar grade without risk of embrittlement.

This low cost, lightweight, highly formable, Zn-coated corrosion resistance rebar is now being produced and used in several countries including China and Dubai and, is under assessment in Canada at the interest of the IZA [46]. From a metallurgical and electrochemical point of view, for a thin-coated rebar like the CGR, quality assurance needs to be strict to ensure uniform coating thickness on all regions of the rebar. Although ASTM A1094 recommended a weigh-strip-weigh analysis to be performed in determining a CGR coating thickness, unless the coating is uniform, this test is not very helpful. This is because, a coating thickness determined to be on average 50 μm , can in fact be lesser in some regions in the coating and, such regions will act as preferential sites for localized corrosion.

Furthermore, processing and handling procedures need to be optimized to ensure a less defective coating, because damage to the $\sim 50 \mu\text{m}$ coating will significantly affect its corrosion resistance performance over the years. In addition, the processing parameters need to guarantee that a continuous inhibition layer is formed at the coating interface to prevent the brittle IMCs from forming in some regions in the bar.

For a galvanized rebar to be considered CGR, ASTM 1094/1094M recommends that the Al content should be in the range of 0.05 – 0.25 wt. %, supplied either as aluminum or as a compound containing aluminum, giving room for other elements to be present in the bath. Thus, a continuously galvanized coating may vary not only within the range of aluminum supplied to the bath, but with other elements present in the bath. This variation needs to be examined to see how it affects the coating. For example, it will be seen in the next section that at least 0.15 wt. % Al is needed for full inhibition of the Fe-Zn IMC.

2.3.2. Metallurgy of CG rebar

In CGR, coated at a high speed, the reaction(s) occurring at the substrate/coating interface is significantly different from the bulk of the coating. According to [35], this may not be surprising since thermodynamic equilibrium is seldom reached there due to the transient nature of the reactions. The consequence of alloying the molten bath in the production of a CGR is that understanding the interface reaction and its mechanism is further compounded due to the following reasons [31]:

- the rate of reaction is very fast, sometimes <1sec;
- reactions occur in parallel: wetting of the steel by molten Zn; dissolution of the substrate by the Zn; isothermal solidification of the inhibition layer (Fe-Al-Zn), solid state diffusional phase transformation; solidification of the molten Zn alloy on the coating etc.;
- the reaction is not governed by simple equilibrium thermodynamics of Fe and Zn, as in HDG. This is because the reaction can be seen as Fe-Al, Zn-Al, and Fe-Al-Zn.

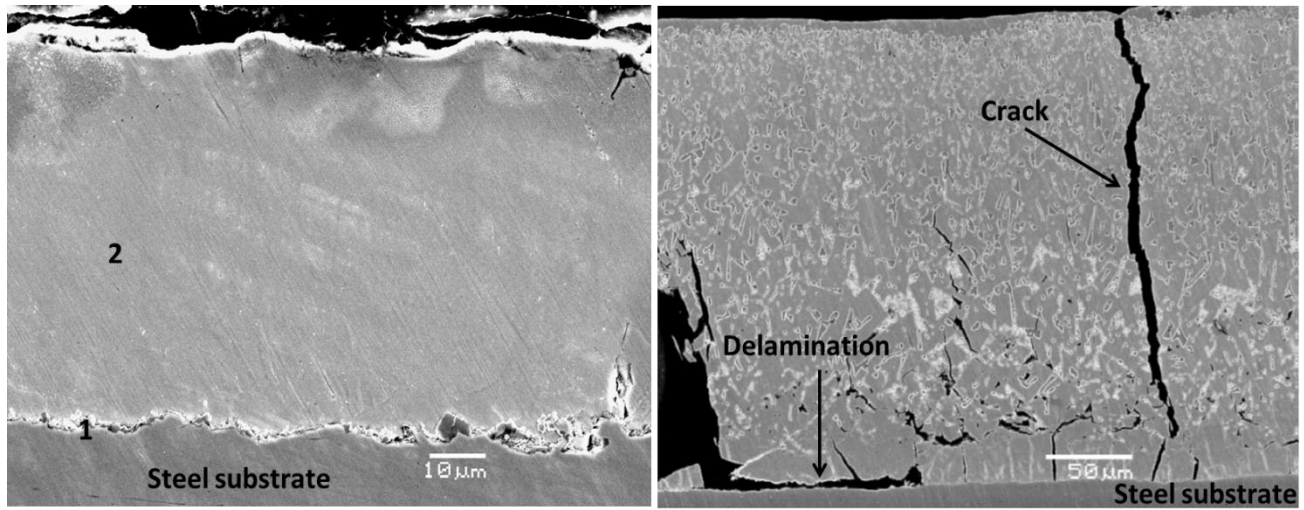


Figure 2-12: Micrograph of a CGR (1- Inhibition layer, 2- pure Zn eta layer) (left) and HDG coating (right) both bent after galvanizing [47].

Figure 2-12 compares the micrograph of a CGR and HDG coating bent after galvanizing and, the ductile and brittle behaviour respectively, of these coatings is clearly observed. In Figure 2-12 (left), a thin layer (1) separating the base steel from the pure Zn layer (2) can be seen in the coating. This layer, referred to as the inhibition layer, appear to be rough, broken in some part and non-uniform throughout the coating. From the specimens used in the present work, it also appears that this inhibition layer can be thicker, Figure 2-13 (left), or even absent in some coatings, Figure 2-13 (right). The effect of the rough, absent, broken or non-uniform nature of this inhibition layer on the performance of the CGR coating in reinforcement corrosion is yet to be covered in the literature. Typically, what seem to be of interest when considering the coating of a CGR is the absence of the brittle and lesser corrosion resistance IMC and the presence of a thicker ductile and more corrosion resistant ‘pure’ zinc, η layer.

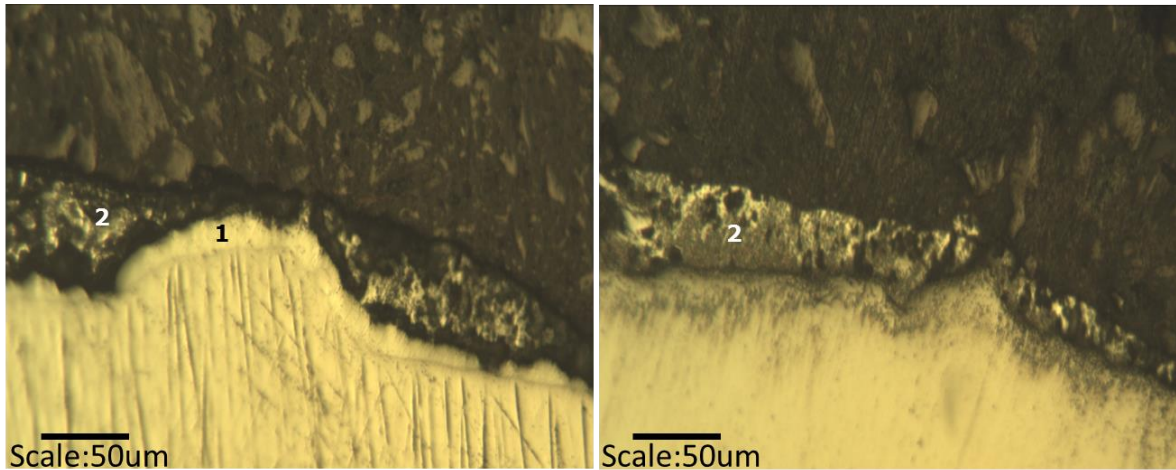


Figure 2-13: Micrograph of CGR specimen 1 and 2 respectively used in the present work.

Layer 1 and 2 is the Fe-Al-Zn layer and the “pure” zinc, η layer respectively.

2.3.2.1. Iron-Aluminum-Zinc (Fe-Al-Zn) phase equilibrium and kinetics

The Fe-Al-Zn ternary phase diagram is shown in Figure 2-14 to help understand the thermodynamics of the reaction.

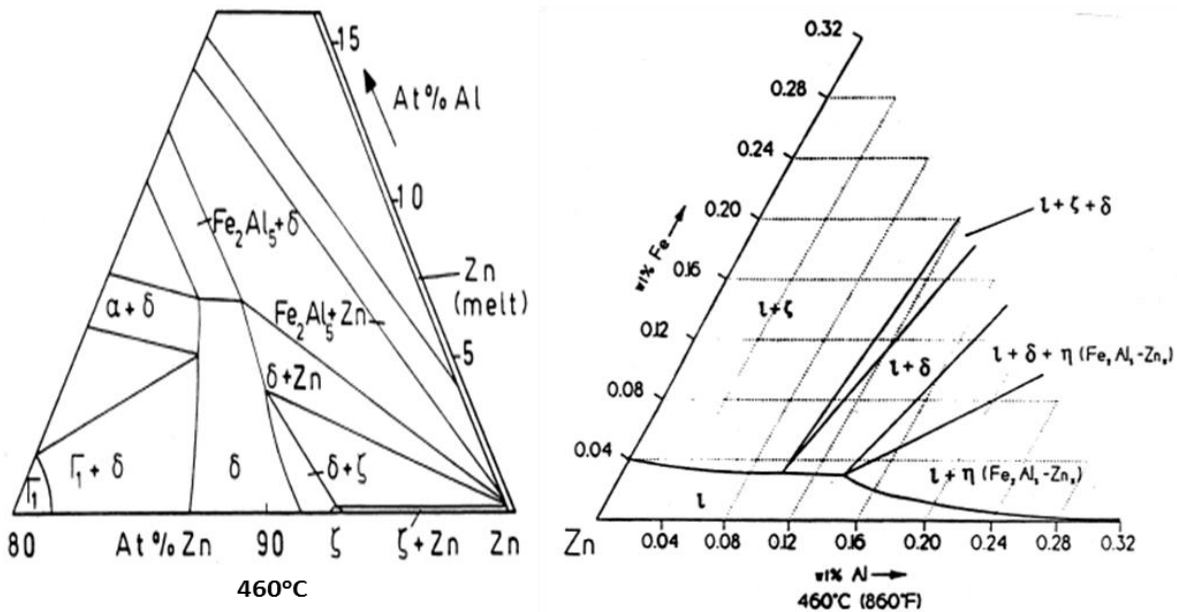


Figure 2-14: Ternary phase diagram of Fe-Al-Zn. Left – overall section of the Zn rich corner at 460°C. Right – Al corner of the Zn-rich corner. [34].

Figure 2-14 (left) shows the Zn-rich corner of Fe-Al-Zn ternary phase diagram and, the Al corner of Figure 2-14 (left) is shown in Figure 2-14 (right) to help determine the concentration of Al needed to produce a full inhibition layer. The varying Al concentrations involved in the interface reaction results in different “inhibition” layer formed (Table 2-4) and, varying solubility of Fe and Zn in those layers. Perrot et al., 1992 found the solubility of Zn in the different “inhibition” layers formed to vary depending on immersion time at typical galvanizing temperature ($\sim 450^{\circ}\text{C}$). At short immersion times: < 30 mins, Fe_2Al_5 has up to 23% Zn and FeAl_3 has up to 14% Zn; at < 2 mins (typical of CGR), the average composition begins with ZnFeAl_3 and afterwards the formation of Fe_2Al_5 saturated in Zn. For longer immersion time, Fe_2Al_5 has about 14-18% Zn.

Table 2-4: Varying Al content in formation of the inhibition layer [35].

Wt% Al	Equilibrium compound	Phases in coating	Alloy layer Characteristics
< 0.1	ζ	$\zeta/ \delta/ \Gamma_1/ \Gamma$	Continuous
$0.1 - 0.135$	δ	$\zeta/ \delta/ \Gamma_1/ \Gamma$	Gap exist
$0.135-0.14$	η	Mostly ζ	Discontinuous
$0.14-0.145$	η	ζ plus η	ζ dissolution
$0.145-0.15$	η	Mostly η	ζ dissolution
> 0.15	η	η	Full inhibition

Furthermore, from Figure 2-14 (right), the following can be seen for different bath Al contents;

- at $< 0.1\%$, the phase in equilibrium with the liquid is ζ phase ($\sim 6\%$ Fe);
- between $0.1-0.15\%$, the phase in equilibrium with the liquid is δ phase ($\sim 10\%$ Fe);
- at $> 0.15\%$, the phase in equilibrium with the liquid is $\text{Fe}_2\text{Al}_5\text{Zn}_x$ (η) phase.

This means that solubility of Fe increases continuously with increasing Al at a given temperature. Furthermore, Table 2-1 shows that approximately 0.15 wt.% minimum is needed

for the full inhibition effect of the Fe-Zn by the $\text{Fe}_2\text{Al}_5\text{Zn}_x$ (η) phase. This is interesting because, the lower range of Al content recommended by ASTM A1094/A1094M may not be able to produce a layer that gives full inhibition effect in a CGR coating. According to Marder, failure to give full inhibition will only delay Fe-Zn IMC formation, eventually leading to a Fe-Zn outburst in some part of the coating (details in section 2.3.2.3).

Tang [37] explained that formation of the inhibition layer is a two-stage process: the first stage, associated with a high rate of Al uptake, is controlled by continuous nucleation of Fe_2Al_5 ; followed by a second stage, diffusion-controlled, growth process. In Guttmann et al. [31] study, 0.15% Al bath produced a continuous inhibition layer, $\text{Fe}_2\text{Al}_5\text{Zn}_x$ (containing ~23% Zn), with a thickness of 250 nm made up of two distinct layers. These two layers confirm the two-stage growth kinetics and Al uptake mentioned in [37]. Interestingly, the IZA mentioned this layer to be ~100 nm [47], implying that the layer varies in thickness with processing parameters.

2.3.2.2. Factors affecting coating composition of low aluminum (0.1-0.3%) bath

Marder [18] explained that it is possible for the “inhibition” reaction taking place between the substrate and the Zn outer layer to only last a short time, resulting in some incubation period (time taken for Fe-Zn phase to form) that can increase with: 1) increasing bath Al content; 2) decreasing bath temperatures; 3) decreasing bath Fe content; 4) increasing bath agitation; 5) increasing substrate Si content; 6) decreasing substrate surface roughness.

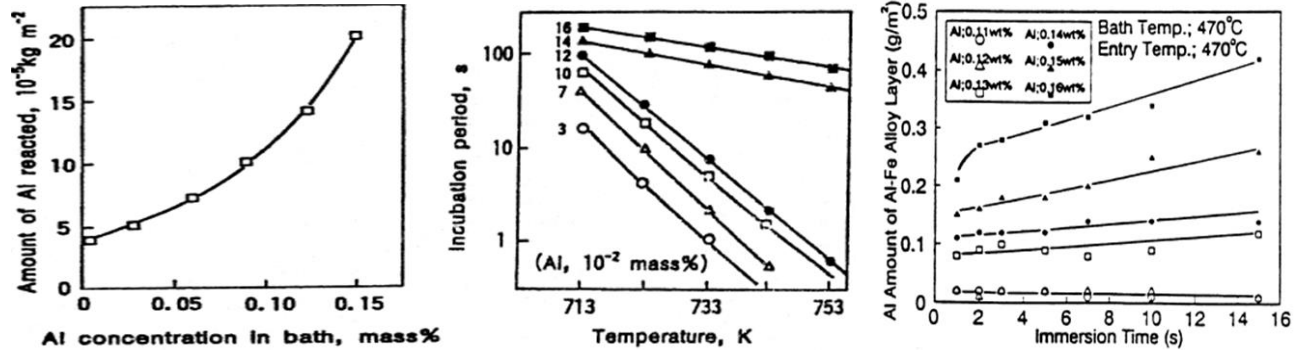


Figure 2-15: Variation of Al content with immersion time [18].

From

Figure 2-15: Variation of Al content with immersion time [18].

(left), as expected, the rate of Al uptake in the coating increases with bath aluminum content. Furthermore, the increasing Al content increases the incubation period, which decreases with bath temperature,

Figure 2-15: Variation of Al content with immersion time [18].

(middle). In addition, at typical galvanizing temperatures (450 - 470°C) and varying bath Al content, the rate of Al uptake in the Fe-Al inhibition layer changes significantly with time,

Figure 2-15: Variation of Al content with immersion time [18].

(right). However, in the time required for rebar to pass through a bath in a continuous galvanizing line (typically 4-5s), a significant amount of the bath Al uptake occurs.

2.3.2.3. Inhibition layer outburst

Even with sufficient bath Al content, traces of Fe-Zn IMC were occasionally found around the inhibition layer – which is not surprising since some part of the layer was earlier shown to be broken. However, Marder [18] mentioned that there was a debate whether Fe-Zn particles is also nucleated on top or underneath the Fe_2Al_5 layer or if both phases nucleate side-by-side on the substrate/coating interface. A study [41] with zinc bath containing 0.2% wt. % Al found both ζ and δ at the interface between Fe-Al inhibition layer and the liquid Zn, Figure 2-16. Relative amounts of the ζ , δ and Fe_2Al_5 phases formed was mentioned to be dependent on the substrate

reactivity, bath temperature and immersion time. On the other hand, [26] reported that lumps of Fe_2Al_5 was found scattered throughout an Fe-Zn outburst as if the outburst had caused Fe_2Al_5 to break apart by nucleating beneath the inhibition layer. In fact, the outburst was found to occur on substrate grain boundaries, Figure 2-17. This is interesting because, the thinner and more ductile coating of a CGR, thought to be pure Zn, could in fact contain some brittle Fe-Zn IMC, further questioning the effectiveness of the inhibition layer.

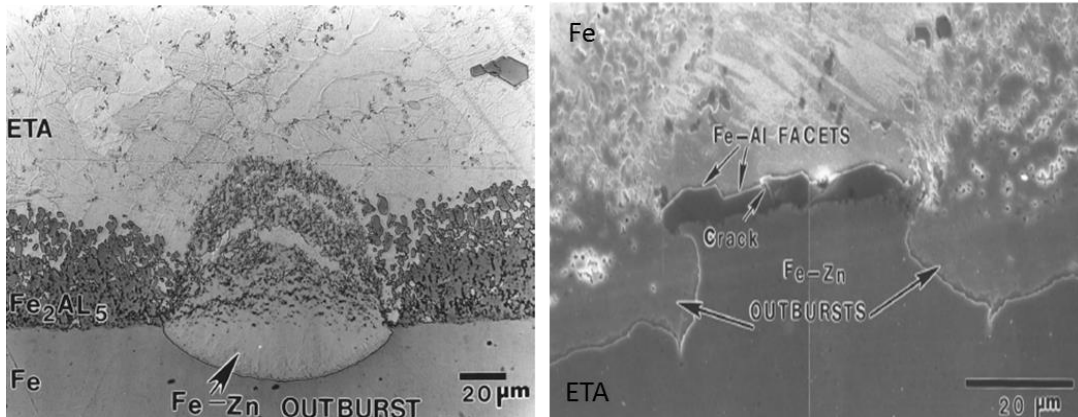


Figure 2-16: Micrographs of a typical Fe-Zn outburst (left) [41], and outburst in 85μm grain size steel immersed in 0.2 wt.% Al-Zn bath (right) [43].

According to Marder [18], inhibition of the IMC is always transient – as the Al addition often only delays the Fe-Zn reaction, rather than completely suppressing it, and eventually resulting in Fe-Zn ‘outbursts’ [41]. These outbursts were found to occur only when a fully inhibitive interface layer is formed. For example, no outburst was observed for low carbon steel dipped in a 0.12% Al bath (thermodynamically insufficient amount to form an ‘inhibition layer’) at 460°C at immersion time of up to 10 secs, but outbursts occurred after 3 secs in a 0.16% Al bath. Furthermore, it was reported that even thick layers of Fe_2Al_5 formed in a sufficiently high Al bath could be destroyed after sufficiently holding time. However, according to the ternary diagram, a Zn bath with more than 0.15% Al is in principle saturated with respect to Fe_2Al_5 and this phase should not redissolve in the liquid after forming. Thus, transient inhibition behavior cannot exactly be explained by thermodynamic equilibrium between Fe_2Al_5 and the liquid.

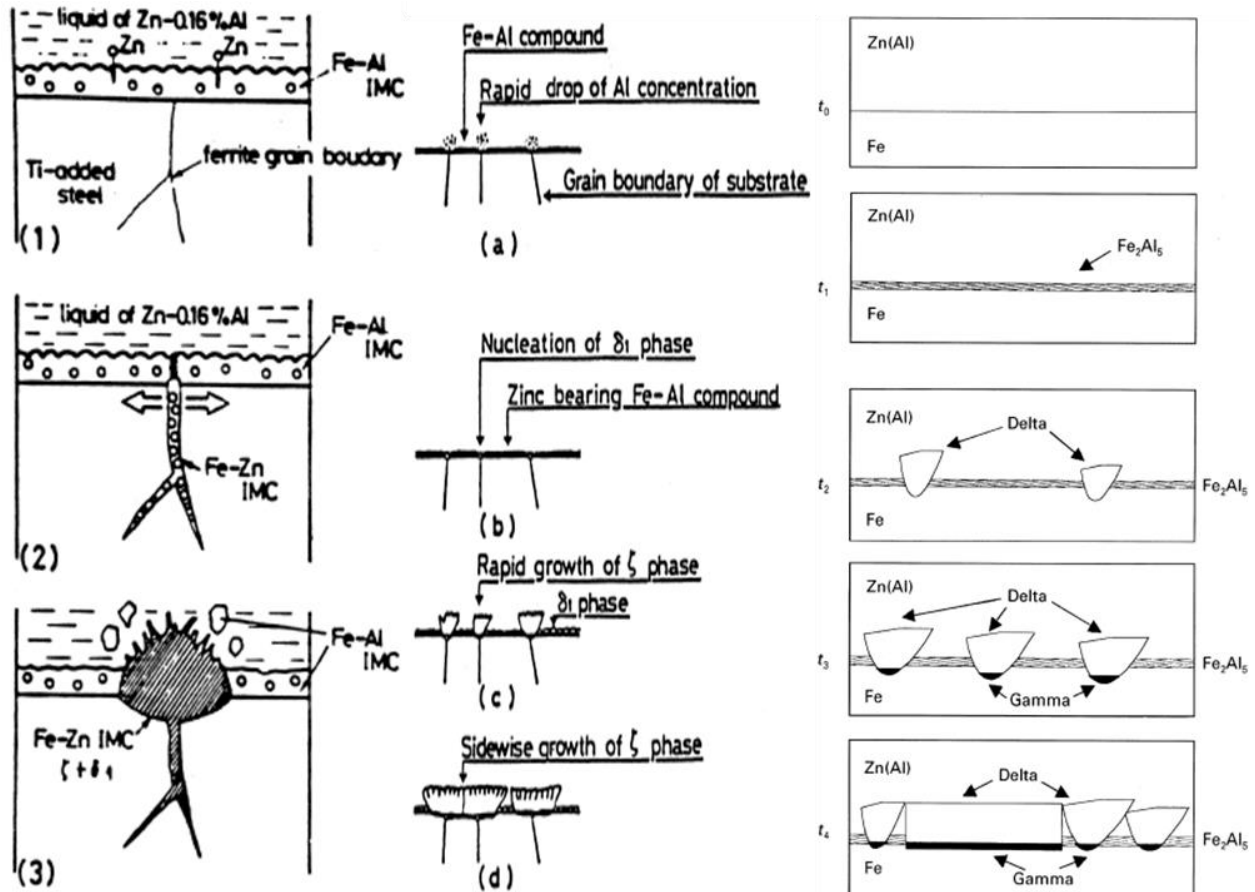


Figure 2-17: Mechanism of Fe-Zn outburst [18].

Several models were proposed for the breakdown of the inhibition layer. These include: 1) diffusion of Zn through the inhibition layer as illustrated in Figure 2-17 (left); 2) a drop in Al concentration in the inhibition layer and a subsequent formation of Fe-Zn IMC, Figure 2-17 (middle) and; 3) enrichment of the inhibition layer by Zn or Al until the solid solubility limit is reached Figure 2-17 (right). The first mechanism seems to be the most agreed upon mechanism of Fe-Zn outburst. In this mechanism, Zn atoms find its way through to the substrate via grain boundaries (GB) to react with Fe in the high-angle region - where a grain boundary of the inhibition layer aligns with that of the substrate, Figure 2-18 (left). This causes nucleation and growth of the Fe-Zn compounds at the substrate/ Fe_2Al_5 interface which burst the inhibition layer apart into the surrounding bath, making the rest of that region vulnerable to Fe-Zn formation. Guttmann et al., 1995 [31] found the average diffusion coefficient of Zn to be $5 \times 10^{-11} \text{ cm}^2/\text{s}$, making it possible for Zn to diffuse through a 70nm thick Fe_2Al_5 layer in a second and a 250nm

layer in 3s at 460°C galvanizing temperature. This is interesting because some side of a CGR coating (i.e. the high angle region) can actually possess a coating with an outburst.

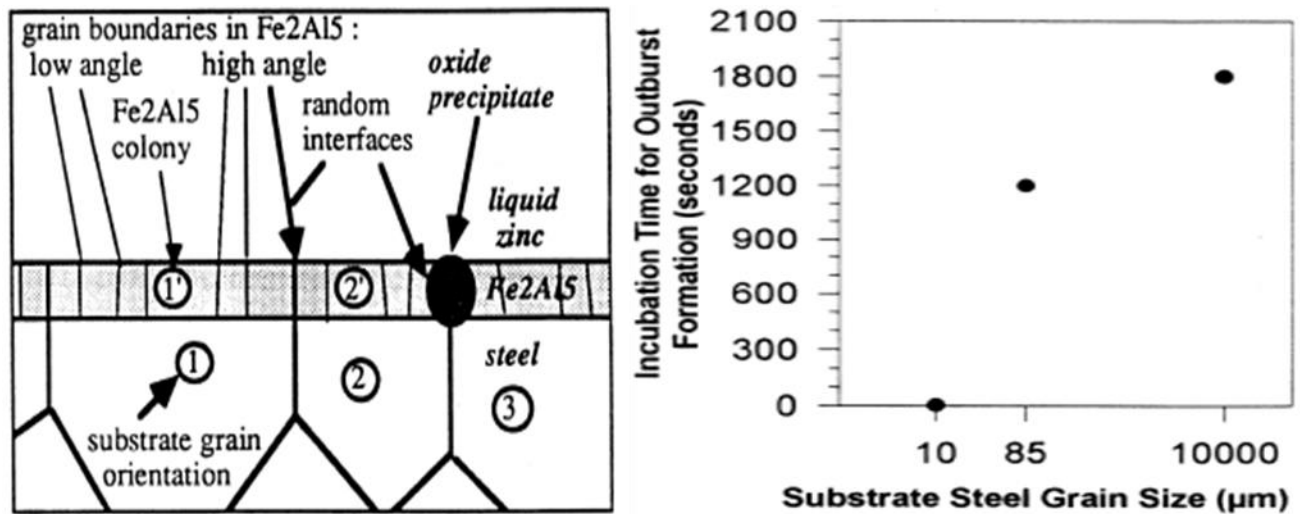


Figure 2-18: Zn diffusion path (left) and grain size influence on outburst (right) [31].

From the aforementioned mechanism, there is no doubt that substrate grain size will influence the Fe-Zn outburst – since the high angle region is where grain boundaries align. That is, a finer grain size substrate would be more reactive - since more grain boundary area is available for reaction, Figure 2-18 (right) [26]. In the study reported earlier by Jordan and Marder [42], with a 0.2 wt. % Al bath, outburst formation readily occurred; however, an increase in grain size led to a significantly increased incubation time.

Furthermore, one can also expect that substrate solute addition will also be an influencing factor to outburst formation, since reactivity at grain boundaries of the substrate will depend on the solute element segregation to these sites. These solute elements can be divided into two: those that segregate to the grain boundaries (e.g. C, P); and those that leave the boundaries clean (e.g. Ti, Nb) by forming compounds that precipitate in the grain. A clean grain boundary will have no barrier to Fe-Zn IMC formation, whereas a boundary containing segregated element could reduce the thermodynamic interactions at these sites, decreasing Fe-Zn outburst and breakdown of the Fe₂Al₅.

2.4. Behaviour of Zn in high alkaline environment

In the early minutes of mixing of the concrete, the pH of the pore solution is ~ 12.6 (due to saturation of $\text{Ca}(\text{OH})_2$) and increases over the next few hours to ~ 13.8 , due to the presence of KOH and NaOH [13]. In this high alkaline environment ($\sim 12.6 - 13.8$) Zn is thermodynamically unstable, resulting in a high initial corrosion when placed in concrete [13]. This is evident from the E/pH diagram of Zn, Figure 2-19 (left), showing Zn corrosion product in the pH range of less than 8.5 (although not of concern in this study) and greater than 12.5 to be an ion. In addition, in Figure 2-19 (right) the high corrosion rate of Zn at this high pH is also confirmed.

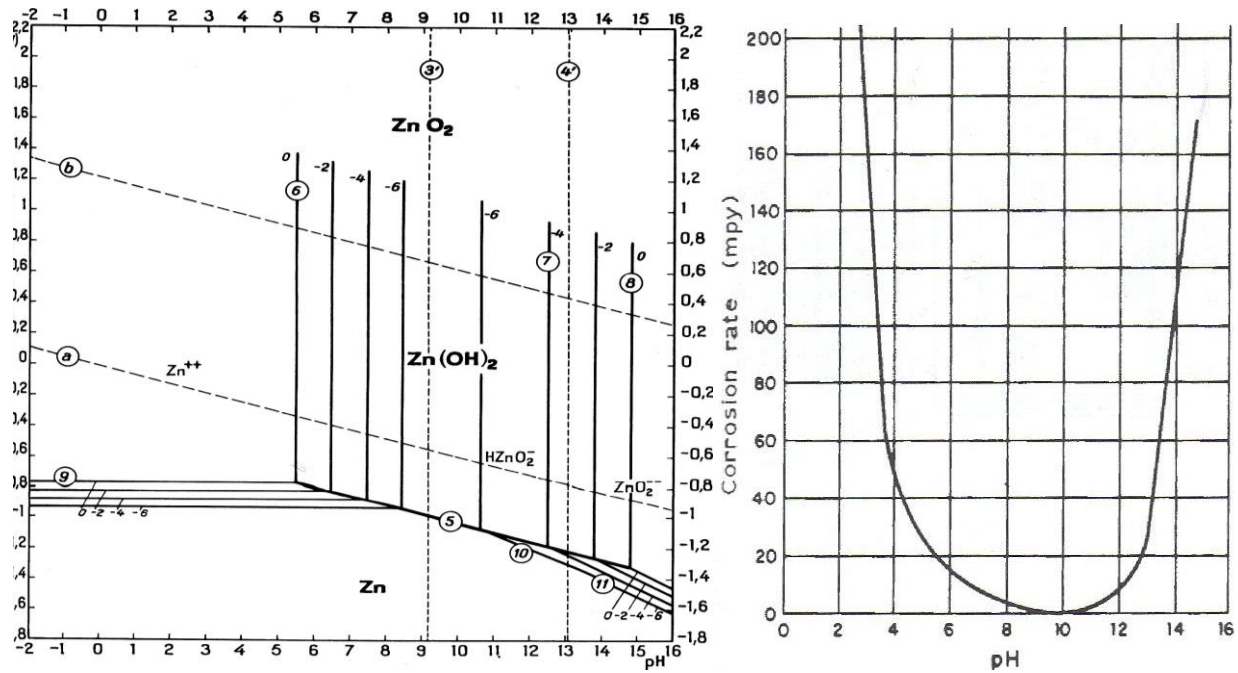
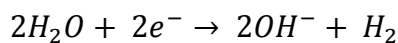
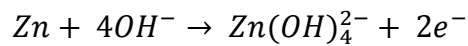
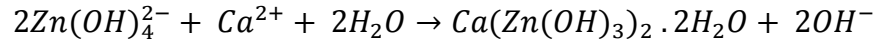
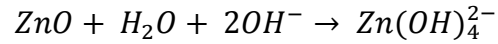
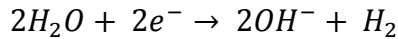
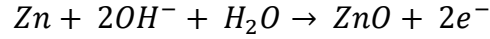


Figure 2-19: E/pH diagram of Zn [4] (left) and influence of pH on Zn corrosion [19] (right).

After this high initial corrosion rate (estimated to be $10-100 \mu\text{A}/\text{cm}^2$, [15]), a crystalline protective film, known as calcium hydroxyzincate (CHZ), $\text{Ca}(\text{Zn}(\text{OH})_3)_2$, that protects the rebar and reduce the corrosion rate to as low as $< 1 \mu\text{A}/\text{cm}^2$ is able to form after ~ 2 days [13]. Yeomans [13] reported that Equation 9 best describes the sequence of reactions leading to the formation of the CHZ.





Equation 9: Formation of Calcium hydroxyzincate (CHZ) [13].

According to Andrade and Marcinius 1987 [14], the pH around the rebar determines the level of protection offered by the CHZ crystals formed. They mentioned that a fine, continuous and compact CHZ crystal that gives great protection is formed at pH 12.5 – 13.3. However, this crystal was reported to increase with pH such that beyond pH > 13.3, a coarse CHZ crystal that is not compact enough to keep the Zn surface completely protected is formed. Furthermore, the coarse CHZ crystals may also grow in isolated areas on the Zn surface depending on the calcium content of the region. They added that pH increase has no further influence on stability of the layer once a protective CHZ has been formed in the specified pH range. Typically, the CHZ crystals create a good bond with the concrete because they grow into the concrete pores.

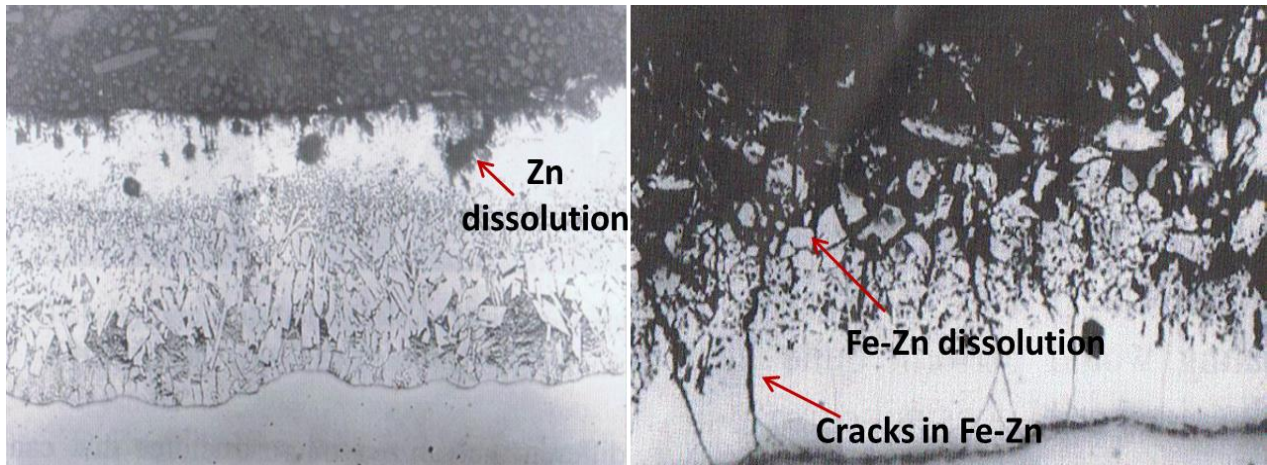


Figure 2-20: Pure Zn overlay dissolution during passivation (left) and selective dissolution of Zn in Fe-Zn IMC (right) [15].

The initial Zn corrosion causes some amount to be lost. With HDG rebar, which has a ~75-100 μm thick Zn coating, losing some (or all) of the pure Zn eta layer (Figure 2-20 (left)) means

some level of protection is still offered by the less corrosion resistant [15] Fe-Zn IMC (Figure 2-20 (right)). On the other hand, dissolution of the same amount of Zn in a CGR could actually mean that most of the $\sim 50\mu\text{m}$ coating is lost, putting the corrosion resistance of the CGR in question. In this sense, corrosion protection in both types of galvanized rebar will largely depend on the initial coating thickness, also supported by [15].

2.5. Long term use of galvanized rebar

Researchers and ministries, the Ministry of Transportation of Ontario (MTO) [48], and National Research Council (NRC) [51] have reported varying performances for the use of galvanized steel in reinforced concrete structures. Andrade and Macius [48] reported that depending on the alkali content of the cement used for casting, the corrosion rates of galvanized rebar may vary by an order of magnitude, and better corrosion performance is obtained in a lower alkali concrete. This is interesting because, several cement supplements like blast furnace slag, fly ash, and environmental regulation like the United States federal highway administration (F.H.W.A) [48] now makes it possible for alkali content of cement to increase, resulting in potential decrease in service life of a galvanized structure [48].

The galvanized industry reported a service life of up to 50 years with little or no maintenance for a galvanized bridge in Bermuda [48], where the major challenge is carbonation as opposed to chloride contamination in North America. However, the opinion of researchers on the use of galvanized rebar is less positive in comparison. Andrade et al., 1994 [48] mentioned that a galvanized structure attacked by chloride may only last about 15 years. K. Clear (48) stated that galvanized rebar would only give additional 2 years to a bridge deck, in comparison with black rebar. According to Kepler et al. [49], McCrumb and Arnold obtained a more positive result, stating that additional 5 years of service life can be obtained from a galvanized reinforced bridge structure. Furthermore, Bautista and Gonzalez [45] suggest that once active corrosion has initiated in a galvanized rebar, all of the Zn can be lost in the space of 5 years, making galvanized steel most suitable for moderately aggressive chloride environment.

Ministries and Committees also hold less positive and varying opinions regarding the use of galvanized rebar. In 1982, American Concrete Institute (ACI) Committee 345 [50] stated that galvanized rebar is no better than plain carbon rebar. Broomfield [48] quoted F.H.W.A to have

said that a galvanized structure in a chloride environment may only last about 15-year service life, even in a good quality concrete. In referencing a more recent field experience, in the same province as this report, with galvanized rebar, the rest of this section will look into reports from the Ministry of Transportation of Ontario (MTO) [48] and National Research Council (NRC) [51]. The MTO Bridge Durability Work Group carried out an assessment on three Ontario bridge decks constructed with galvanized steel in 1975 and 1976 to determine their long-term performance. These bridges were exposed to deicing salts sprayed in the winter season. The assessment included periodic visual surveys; half-cell potential and corrosion current measurement, degree of delamination and chloride content of the concrete.

The result of the 30-year old galvanized reinforced structures showed evidence of corrosion and resulting concrete delamination when the chloride threshold had been exceeded. The galvanized structure was also reported to be only marginally better than the conventional black reinforced structure. More interestingly, one of the structures surveyed showed evidence of deterioration by approximately 10% and needed rehabilitation to achieve even 20 years of service life. The MTO mentioned these structures to have been built using practices adopted in the year the concrete was cast. Since research has shown galvanized corrosion product to be soluble and no information was given regarding the concrete mixture design of these structures, it is difficult to explain the cause of deterioration of the galvanized structure. The conclusion of this Ontario highway bridge deck assessment was that, galvanized rebar did not provide the anticipated corrosion protection.

In 2015, NRC also published a comprehensive report on a 3-year assessment of galvanized rebar in concrete. The study included both laboratory evaluation and field survey and the report included 3 major parts: i) corrosion performance of galvanized concrete compared with black reinforced concrete; ii) corrosion potential of galvanized concrete similar to ASTM C876 guideline; iii) field concrete survey used to validate the developed corrosion potential guideline. The conclusion of this study was that galvanized rebar in concrete containing 2% Cl^- by mass of cement or 0.31% by mass of concrete was 5-10 times more corrosion resistant than black rebar concrete, depending on environmental exposure. At 80% R.H and temperature between 25 – 40°C, the corrosion rate of HDG reinforced concrete was 10 times lower than that of black steel.

At 100% R.H and room temperature, the corrosion rate of HDG reinforced concrete was 5 times lower than black steel. They also added that, due to the soluble corrosion product of Zn, it took longer (double the time when compared with black steel) for HDG corrosion product to induce cracks in the concrete.

A report by NRC in 1997 (referenced in the 2015 report) showed that lower corrosion rate of an HDG reinforced structure was obtained in the summer and, the same result was mentioned to be obtained in this recent report. Furthermore, they reported that no corrosion-induced cracking was found on columns of two 50 years old highway bridges structure examined by chloride content analysis and visual inspection. Also mentioned was that high performance concrete (HPC) was able to delay the onset of corrosion of HDG rebar and could potentially be an effective method of further preventing corrosion of the rebar. However once corrosion is initiated, the behavior is similar to an OPC structure. Interestingly, pre-cracking of concrete and severe artificial damage to the coating of galvanized rebar was found to have negligible impact on its corrosion performance, while black rebar in a pre-cracked concrete was adversely affected. The authors concluded that minor damage, resulting from handling and/or transport, to a galvanized coating would have less impact on its corrosion performance.

Similar to ASTM A876 on recommended interpretation of corrosion potential measurements for the assessment of black rebar in concrete, three levels of guidelines were developed by NRC for galvanized rebar from an assessment of the condition of eight columns of two highway bridges. The cumulative-probability-based Guideline 1 was developed from two columns with overall best and worse conditions, and Guideline 2 further ranked the condition of the columns based on the corrosion potential measured. Overall, Guidelines 1 and 2 offer four to five sets of probability of corrosion based on the measured corrosion potential. A third model, “an advanced Model-P that calculates the corrosion probability from a continuous function of corrosion potential by the establishment its probability density functions” was also presented, but will not be reported here. The summary of this corrosion potential assessment guidelines is given in Table 2-5 and, a comparison will be made with one obtained from the current work.

Table 2-5: NRC recommended guideline for assessing HDG through its half-cell potential [51].

Guideline 1			Guideline 2		
CSE	SCE	condition	CSE	SCE	condition
More +ve than -335	-260	90% no corrosion	More +ve than -335	-260	90% no corrosion
Between -335 to -500	-260 to -425	uncertain	Between -335 to -400	-260 to -325	70% no corrosion
Between -500 to -610	-425 to -535	85% active corrosion	Between -400 to -500	-325 to -425	30% passive 70% active
More -ve than -610	-535	90% active corrosion	Between -500 to -610	-425 to -535	85% active corrosion
			More -ve than -610	-535	90% active corrosion

2.6. Electrochemical test equipment

A Randles circuit is typically used to represent the electrochemical behaviour of steel in concrete, Figure 2-21 (left). R_s is the solution or ohmic resistance, which in the case of steel in concrete will be concrete resistance, R_C and, will vary with temperature and humidity inside of the concrete. The double layer capacitor, C_{dl} , is a capacitor layer that develops on any conducting solid in contact with a polar solution, which water is no exception. The layer between the negatively charged solid surface and hydrogen ions from water molecules forms the inner layer, and that between the oxygen ions and the solvated ions (i.e. cation of brine solution, Mg^{2+} , Na^+ , Ca^{2+}) forms the outer layer, Figure 2-21 (middle). These two layers are called the Helmholtz double layer capacitance, representing two plates of a capacitor, Figure 2-21 (right).

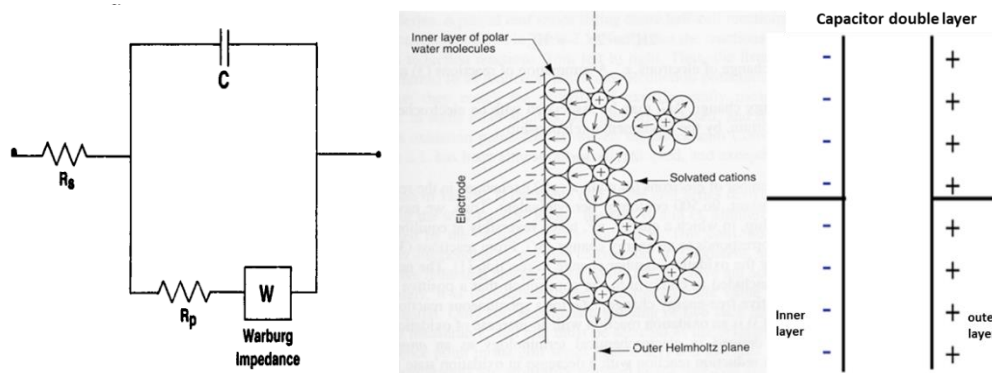


Figure 2-21: Randle’s circuit (left) [55], Helmholtz double layer (middle and right) [56].

The Warburg impedance (W) in parallel with the C_{dl} , is used to represent a diffusion controlled system. In concrete, oxygen needs to diffuse through to provide oxygen needed for cathodic reaction and, a corroding rebar also need to eject the ions (e.g. Zn^{2+}) into the surrounding concrete. In both cases, the diffusion coefficient of the concrete will play some part in fulfilling requirement for corrosion of the rebar. The polarization resistance, R_p , in parallel with the C_{dl} , represents the resistance of atoms of the material to ionize. Ionization is the process of stripping electron off an atom to become an ion (e.g. $Zn \rightarrow Zn^{2+} + 2e^-$), which requires a certain amount of energy (e.g. voltage). The rate of corrosion is proportional to ionization speed and, the rate of ionization depends on the amount of energy required/available to strip off electrons; which varies with material and environment.

In reality, the analogue circuit may appear more complicated in some cases – having multiple resistors and capacitors representing some other unit component the applied energy polarize before getting to the rebar. For example, when a certain amount of energy is applied to polarize a rebar in concrete, the energy is expended in polarizing: 1) brine solution in which the concrete is placed; 2) pore solution in the concrete; 3) C_{dl} developed on rebar surface; 4) passive film on rebar surface if any, and 5) the rebar.

Stern and Geary found a linear relationship between current (I) and potential (E) at an applied potential/current close to corrosion potential/current (E_{corr}/I_{corr}) of the rebar, Figure 2-22. In other words, at any potential applied within that linear region, a corresponding linear current can be obtained and, the slope is the R_p of the rebar. Furthermore, they determined an inverse relationship between R_p and I_{corr} connected by a Tafel constant, B , which generally varies between 13 – 52 mV [52]. However, it was reported to be 26 mV and 52 mV for active and passive rebar in concrete, respectively [54].

Based on this linear response, several electrochemical techniques were developed, two of which were used in the present work - linear polarization resistance (LPR) and galvanostatic pulse (GP). Both measurement techniques can determine the R_p of the rebar and, because of the low potential/current applied, are able to be essentially non-destructive, thereby allowing further testing.

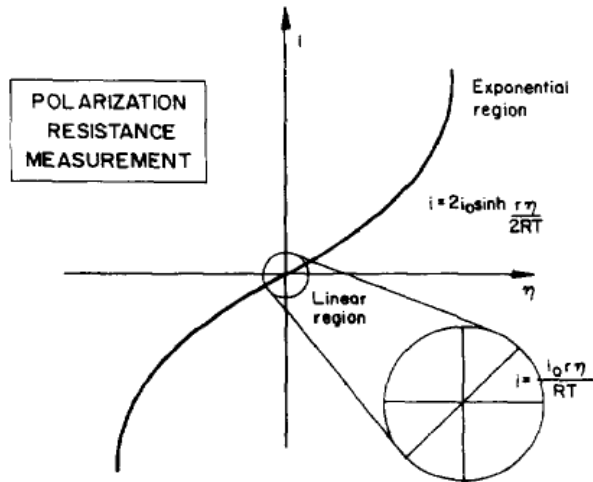


Figure 2-22: Polarization curve [54].

R_p = polarization resistance

E_{corr} and I_{corr} = corrosion potential and corrosion current

ΔE = change in potential from E_{corr} ($E_{applied} - E_{corr}$)

ΔI = change in current from I_{corr} ($I_{applied} - I_{corr}$)

β = Stern-Geary's constant

β_a and β_c = anodic and cathodic Tafel constant/slope.

2.6.1. Linear Polarization Resistance (LPR) Technique

The potentiostatic linear polarization resistance test [52] was used to determine the polarization resistance (R_p) of the rebar by applying a constant anodic and cathodic potential away from the corrosion potential and measuring the corresponding current. This applied potential is in the linear region of the Tafel curve, i.e. the region where potential applied results in a linear current response. This range typically falls within ± 10 – 20 mV for reinforced concrete, although up to ± 100 mV has been reported in the past [54]. A potential step of ± 20 mV for 150 secs per scan was used in the current research to allow current response to reach the steady state. A typical LPR curve is shown in Figure 2-23. When the voltage is applied, there is a current spike due to the concrete resistance (R_c). Subsequently, a gradual decrease in current is observed which indicates the charging of the C_{dl} and, the material is forced to polarize and either lose or gain electrons for the anodic or cathodic scan, respectively. The resistance to this polarization is termed R_p (polarization resistance) and can be determined from the applied potential and current response using Equation 10 (left). The corrosion current density (i_{corr}) can then be determined using the calculated R_p along with Tafel constant (β) and exposed area (A) of the rebar, Equation 10 (right).

$$R_p = \frac{\Delta E}{\Delta i} \qquad i_{corr} = \frac{B}{R_p \cdot A}$$

Equation 10: Equation used to calculate the corrosion current density of the rebar (i_{corr}).

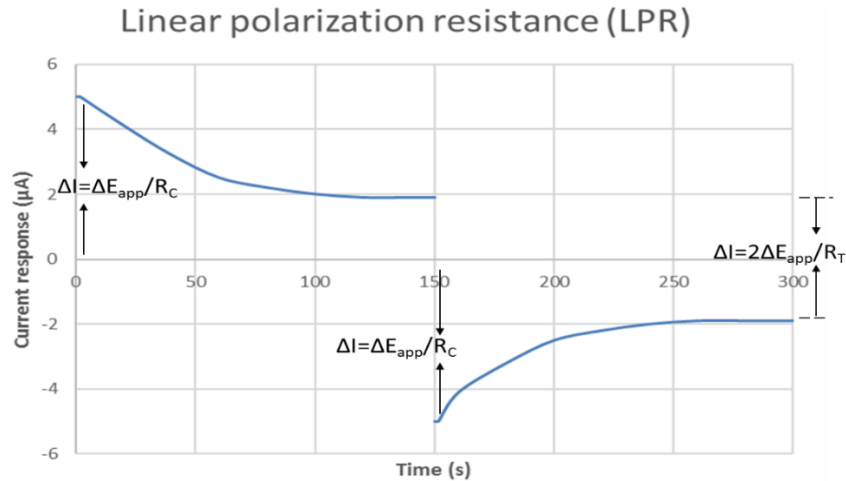


Figure 2-23: A typical linear polarization resistance curve. $R_T = R_C + R_P$.

2.6.2. Galvanostatic Pulse (GP) Technique

The galvanostatic pulse test [53] was used to determine the polarization resistance (R_P) of the bars by applying $\pm 10 \mu\text{A}$ for 200s and measuring the corresponding potential change, Figure 2-24. The first potential value on the graph represents the corrosion potential of the rebar, while the difference between the third and the second potential gives the potential/ohmic drop ($E_C = IR$) due to concrete resistance (R_C). The increase in potential from the third to the last point shows the charging of the double layer capacitor (C_{dl}) until it reaches a steady state (levelled horizontal top of the graph).

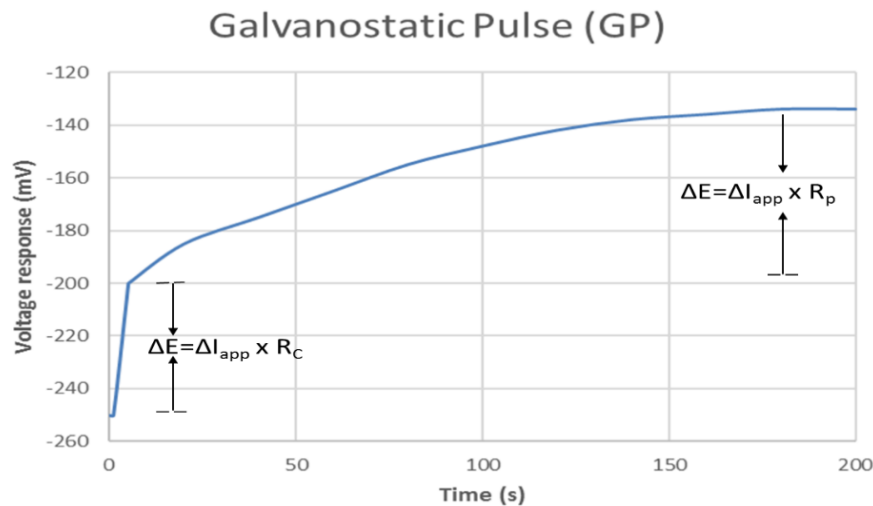


Figure 2-24: A typical Galvanostatic pulse curve.

Chapter 3 Experimental Procedure

This chapter describes the experimental procedure adopted in evaluating the electrochemical behaviour of the galvanized rebar from test set-up to autopsy. The chapter has been written in steps by which the experiment was set-up and tested for easy replication.

The following types of galvanized reinforced bars were supplied by the sponsor of this research, the International Zinc Association (IZA):

- 3 grades of the continuously galvanized rebar (CGR), denoted;
 1. C1 - CGR batch 1.
 2. C2 - CGR batch 2.
 3. C3 - CGR batch 3.
- A conventionally hot-dipped galvanized rebar (HDG).

A regular carbon steel rebar - Black steel – was also tested for comparison purposes.

Note that the HDG rebar was smaller in nominal diameter ($\phi 10$ mm) than the continuously galvanized and black rebar ($\phi 12$ mm).

These bars were cast into concrete and electrochemical tests were carried out on the concrete specimens. The specimens were tested in three different concrete conditions, based on what are thought to be the most common conditions of field concretes, namely: sound (non-cracked) concrete; concrete with a crack perpendicular to the rebar (transversely cracked specimens), and concrete with a crack parallel to, and located above, the rebar (longitudinally cracked specimens). The details of inducing cracks are described in subsequent subheadings. Five replicates of each type of specimen were prepared. Thus, 15 samples of a rebar type were cast in concrete.

3.1. Design set up

As earlier mentioned, the goal of these laboratory experiments is to yield results that can be used for assessing general field conditions of reinforced concrete. One of the best ways of achieving this is to set up specimens in manner similar to concretes used in the field. Although field concretes are cast intending no cracks present, however over time with; load variations, changing weather conditions (e.g. humidity), temperature variations and shrinkage cracks, some micro- and macro- cracks appear, exposing the rebar. The cracks reduce the time for the ingress of the

chloride from the environment into the concrete. Furthermore, they can vary in size and manner (i.e. parallel or perpendicular) to the embedded rebar surface, as can be found in bridge decks.

3.1.1. Sound Concrete Specimens

These specimens (Figure 3-1) were designed to represent the ideal condition (typical of laboratory test) of concrete containing no crack (i.e. non-cracked), which is seldom found in the field. Furthermore, it was also designed to contain a rebar-mat, where bars are placed over and perpendicular to each other, as installed in field structures such as bridge decks. The goal was to examine possibility of crevice corrosion at the intersection. The top bar of the mat was positioned 25 mm (1 inch) from the concrete surface – this distance being the concrete cover. This cover depth, below the surface of a 38 mm (1.5 inch) deep ponding well to be filled with brine, differs from that of field concretes with 60 – 75mm (2.5-3 inch) cover depth [CSA handbook, 2006]. The aim was to limit the time required to obtain result by allowing a small distance for chloride ingress to the rebar surface. A Styrofoam prism was glued into the bottom of the formwork to create the 1.5 inches (38 mm) ponding well in the concrete.

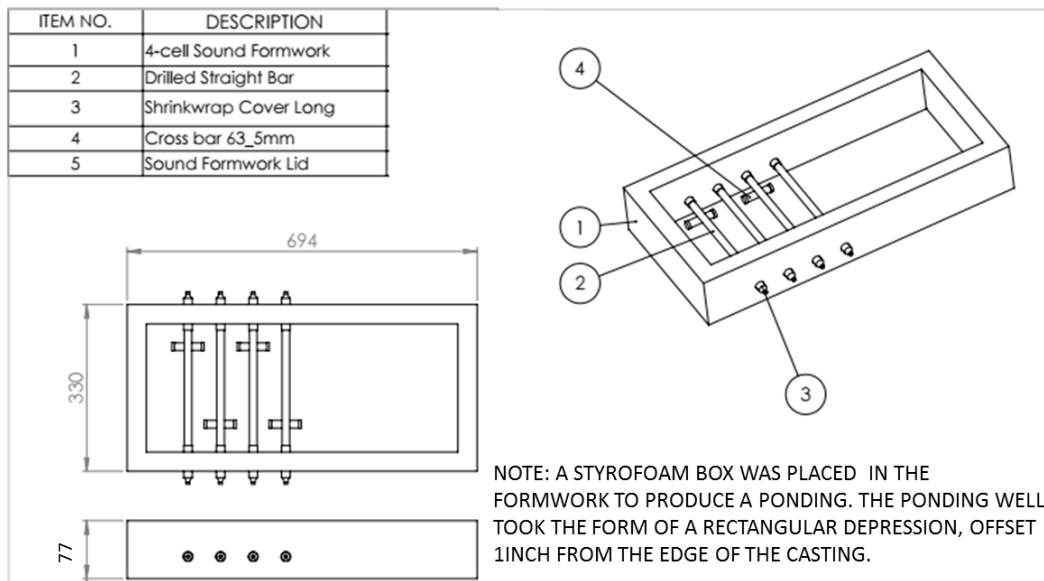


Figure 3-1: Sound specimen formwork design. The figure shows the plan, side-view and cross-section.

3.1.2. Transversely Cracked Specimens

The loading on a bridge deck cause cracks to initiate in some part of the structure. These cracks are usually perpendicular to the driving lanes and, therefore, to the longitudinal rebar and parallel to the transverse rebar in the mat. These set of specimens were designed to simulate the scenario experienced by the longitudinal rebar in a bridge deck. The specimens were designed as individual reinforced concrete prism of dimension 67 mm (~2.75 inch) width, 67 mm (~2.75 inch) base and 356 mm (14 inches) length, as illustrated in Figure 3-2. Similar to the sound beams, a 255 mm (10 inches) exposed length of the rebar with an inch (25 mm) cover depth is maintained in these specimens. As shown in Figure 3-3, a length of plexiglass, triangular in cross section, was used to create a notch transverse to the rebar and half-way along the length of the concrete prism for crack initiation. The concrete cover for these specimens were calculated from the root of this notch to the rebar surface – since the objective is to evaluate the influence of the crack. To better achieve this, the specimens were also cast upside down, similar to the sound specimens. Instead of using an assembly support shown in the diagram, a fishing line was used to centre the fully embedded end of the rebar in the concrete prism, to ensure a uniform cover depth.

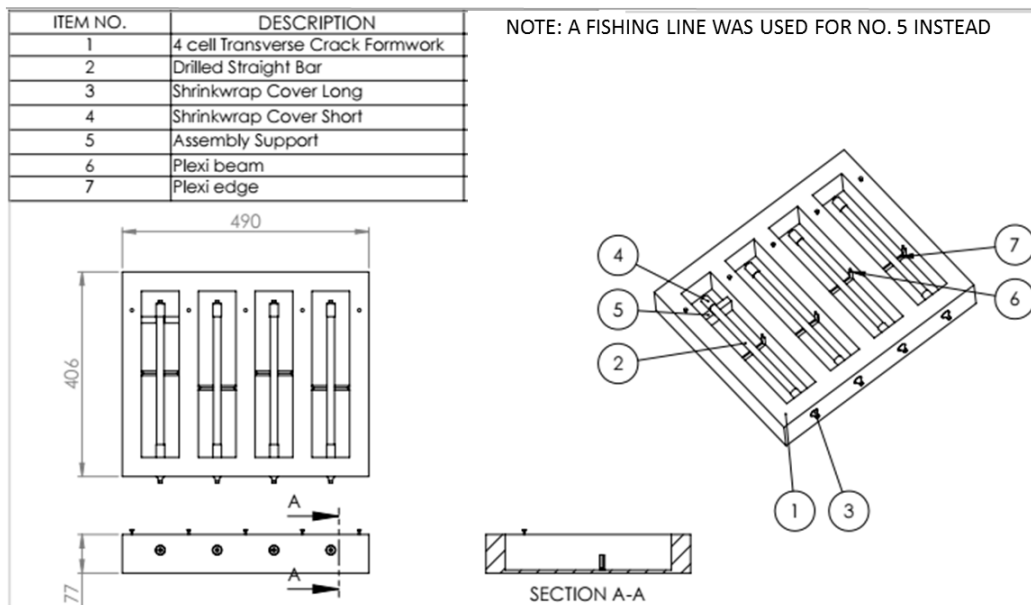


Figure 3-2: Schematic diagram of the layout for the transversely cracked specimen. The figure shows the plan, side-view and cross-section.

3.1.3. Longitudinally Cracked Specimens

These concrete specimens simulate the part of a concrete deck containing cracks parallel to and above the transverse rebar of a bridge deck. They were cast as a large concrete beam and, later cut to individual prism of dimension 67 mm (~2.75 inch) width, 67 mm (~2.75 inch) base and 356 mm (14 inches) height, Figure 3-4. These specimens were similar to the transverse specimen, in terms of the exposed length and concrete cover; however, a longer plexiglass rod was used to form a notch in the concrete prism parallel to the rebar surface. Two glass fibre reinforced polymer (GFRP) bars were used to reinforce the concrete to provide support when inducing cracks in specimen surface. The GFRP bars were made to extend through the length of the formwork, also long enough to help move the beam around. The choice of using GFRP was based on its electrical insulator properties.

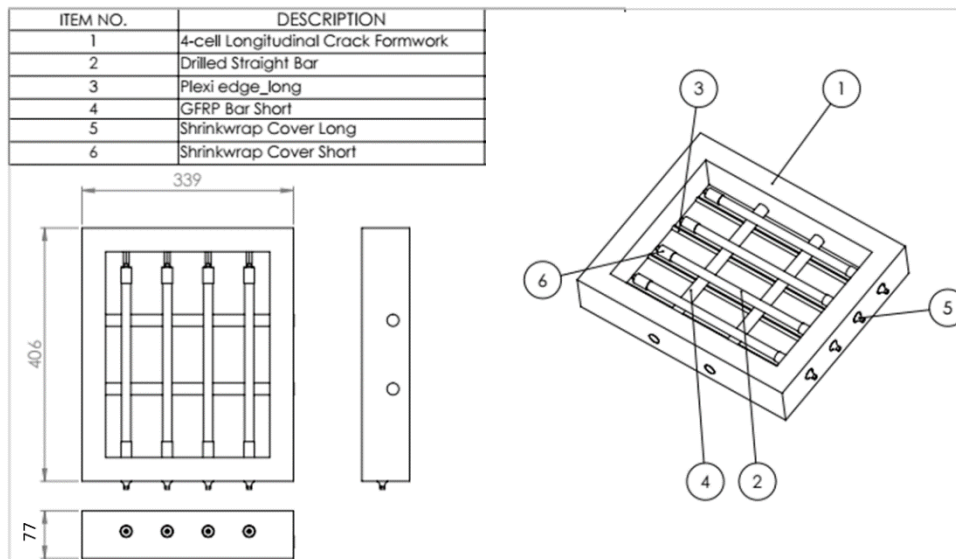
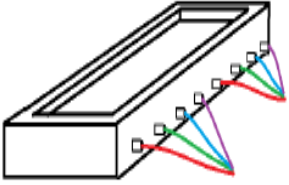
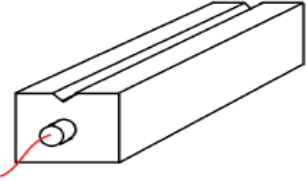
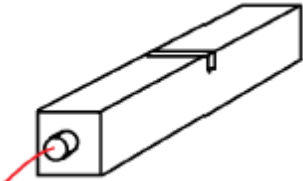


Figure 3-3: Schematic diagram of the layout for the longitudinally cracked specimen. The figure shows the plan, side-view and cross-section.

All concrete specimens were built according to Table 3-1 below. Note that different wiring color in the sound beam indicates the alternating arrangement of the various rebar grades.

Table 3-1: Dimensions and schematic of concrete specimens.

Formwork type	Concrete Dimension (inch)	Steel Specimens (13 inch)	Total steel in concrete	Schematic
Sound (non-cracked)	8-cell = 11.8 x 24.8 x 5.5, 4-cell = 5.9 x 12.4 x 2.8	B, C1, C2, C3, G	28	
Longitudinally cracked	12.8 x 4 x 3 per prism	B, C1, C2, C3, G	28	
Transversely cracked	12.8 x 3 x 3 per prism	B, C1, C2, C3, G	28	

3.2. Rebar sample preparation

According to ASTM A1094/1094M, each grade must follow certain processing method and meet certain coating thickness. This is intended to ensure the quality and consistency across the manufacturing process of different manufacturers of the rebar. It is important to mention that according to IZA, the closest rebar, in terms of processing and properties, to the ASTM A1094 CGR is the C2 rebar, Table 3-1.

All rebar samples were cut to 330 mm (13 inch) long and the burs were removed from the cut edge. The bars were tapped with $\phi 4$ mm drill to a depth of 12.7 mm (0.5 inch). After weighing and labeling each steel type, 20-gauge copper wire was soldered to each bar to create an electrical connection. Each rebar type was soldered with a specific wire colour for easy identification when cast in concrete.

Table 3-2: Tested rebar grades.

Rebar	Specified coating thickness from supplier	Supplier's comment
C1	~50 μm	~0.25% Al in Zn bath
C2	~50 μm	Closest in production to ASTM A1094 (~0.25% Al)
C3	~30 μm	Closer to galfan (~7% Al in Zn bath)
HDG	~75 – 135 μm	In specification with ASTM A767
B	No coating	Mild steel (400W)

The steels were then washed and rinsed (with water and ethanol) to remove as much heat bloom (resulting from the soldering) as possible, as well as grease and dirt from handling. Both ends of steel were lacquered with two coats of Watco lacquer (5 hours' interval between both and 24 hours after second coat), covered with epoxy-lined shrink tube, and hot glue to avoid any end effects. This left 254 mm (10 inches) exposed length of the rebar for testing. A smaller 64 mm (2.5 inch) long rebar was also cut and lacquered on both end for “transverse bars” concrete mat, as illustrated in Figure 3-1. These bars were tied perpendicular to the exposed area of the 254 mm (10 inch) tested rebar using UNS S31653 stainless steel tie wire.

3.3. Specimen cast and concrete mixture design

Premixed concrete ordered from Dufferin Concrete (mix code M3559310, which corresponds to MTO mixture design for 35 MPa at 28 days compressive strength - with, 25% slag replacement and 0.4 w/cm ratio) was used for the first cast. The maximum aggregate size was limited to 14 mm because of the small cover depth of the specimens, rather than the 19 mm aggregate specified by Ontario Provincial Standard Specification (OPSS) 1002 [60]. Upon arrival, the fresh concrete was examined to have 80 mm slump and 7% air content. A second cast was made in the laboratory due to the late arrival of the C3 rebar and the concrete mixture design is given in Table 3-2. The slump and air test was measured to be 90 mm and 8% respectively.

Table 3-3: Highway bridge mixture design used for casting.

Highway Bridge Mixture Design			Second Cast mix
Constituent	Amount (m ³)		Amount (m ³)
Gravel (14mm)	1045	Kg	173.65
Sand	705	Kg	117.15
GU Cement	297	Kg	65.64
Slag	98	Kg	19.69
Euclid Air Extra	237	mL	39.38
Superplasticizer	900	mL	149.55
Water	155	L + abs	27.92
w/c	0.40	Ratio	0.40

3.3.1.1. Slump test

This test enables one to know the workability of a fresh concrete mix. A concrete mixture must contain enough water to increase workability for easy handling and placement. However, the water-to-cementitious (w/cm) ratio must also be kept minimal to avoid detrimental effect (e.g. porosity) of other properties of the concrete when hardened. Procedure on this test can be found in ASTM C143/C143M – 15a Standard Test Method for Slump of Hydraulic-Cement Concrete.

3.3.1.2. Air content

This is an important property of a concrete mixture for this geographical area because, in cold climate region where temperature drops below 0° C, the solution in the pores of the hardened concrete can freeze, resulting in expansion and possible cracking of the concrete. To accommodate this behaviour, concretes are cast with large numbers of small air voids resulting from addition of an air entraining agent to the fresh concrete mixture. However, a balance has to be struck between having too little or too many small air bubbles as too high will reduce the strength of the concrete - hence the need for measuring the air content. ASTM C231/231 – 10 provides a guideline for measuring the air content of a fresh concrete by pressure method.



Figure 3-4: Sound beam formwork. Note: cross bars were straightened before placing concrete.



Figure 3-5: Formwork for transversely cracked specimens with rebar in place.

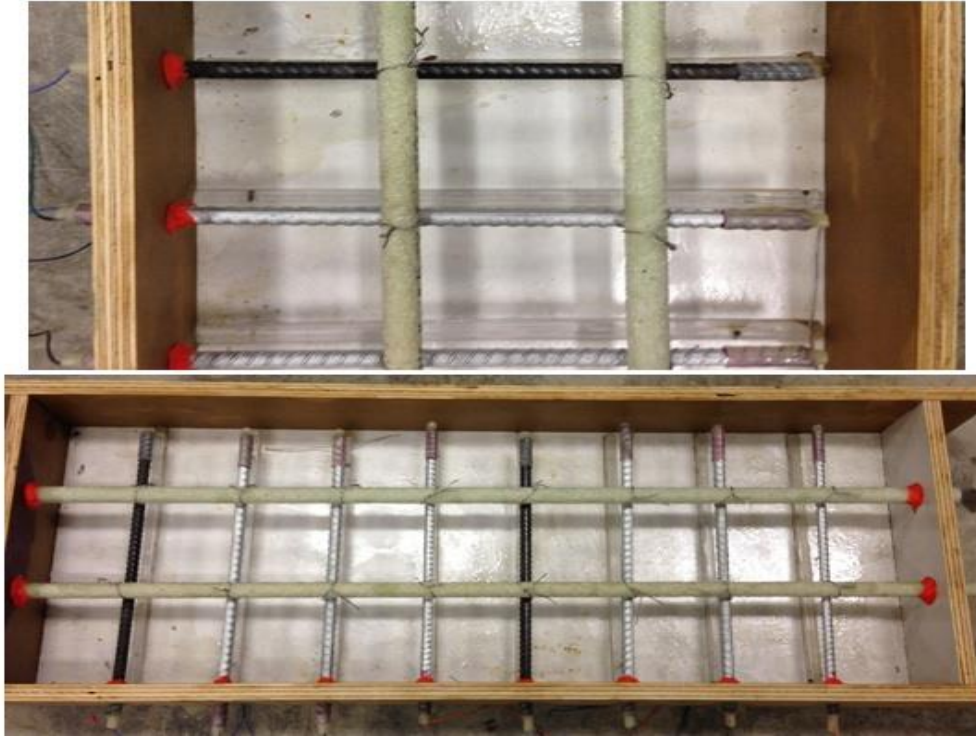


Figure 3-6: Formwork for longitudinally cracked specimens with rebar in place.

After slump and air testing, the fresh concrete was placed inside the moulds (shown in Figure 3-4 to 3-6), compacted on a vibrator table and finished with a rod. Fifteen concrete cylinders of dimension $\phi 100$ mm x 250 mm were also cast and placed in the humidity room for curing.

3.3.1.3. 28-day cylinder compressive strength

Compressive strength of a concrete at 28 days is one of the most important concrete properties to structural engineers. This test helps evaluate the soundness of field concrete and, to replicate a field scenario in the laboratory, the test also was also performed to understand the properties of concrete in which the rebar is embedded. However, the information from this test must be interpreted carefully, and should not be taken to indicate the durability of the concrete. This is particularly because the cylinders tested for strength are typically cured differently from the concrete beam. Consequently, the strength values are approximately 10% higher than those of field cored cylinders [ASTM intl. C873]. In this experiment, the cylinders were made and cured according to ASTM C873/C873M – 10, standard tests for concrete cylinders cast in cylindrical

molds, and ASTM C39/C39M – 12a standard test for compressive strength of cylindrical concrete specimens was followed for compressive strength test.

Fifteen concrete cylinders were made as mentioned above, and three replicates were tested for compressive strength gain with age at 7, 14, 21, 28 and 56 days using ELE international concrete tester. Prior to testing, cylinders were ground on both ends with a concrete grinder to provide smooth, parallel surfaces.

After casting, concrete specimens were covered with soaked burlap and topped with a layer of plastic bag for 14 days' wet cure. All through the wet curing period, daily soaking of the burlap was carried out by spraying with water to maintain constant relative humidity in the concrete. This differs in comparison with the 4 days minimum wet curing specified by the OPSS 904 for concrete structures cured above zero degrees Celsius [59]. Subsequently, concrete beams were demoulded and allowed to air dry for 2 months in laboratory atmosphere (approximately 50% RH, 25°C).

3.4. Preparation for brine exposure

Before finally exposing specimens to brine for electrochemical testing, several actions were taken. This section highlights the action of inducing cracks in some specimens, cutting of the longitudinally cracked beams to individual concrete prism, epoxy of cracked specimens, and measurement of initial corrosion potential of all specimens.

3.4.1. Specimen Cracking

Cracks were induced in the individual transversely cracked concrete prisms and the longitudinally cracked concrete beams with 3-point bending using the T220 load equipment Figure 3-7. The idea behind cracking before cutting the longitudinally cracked beams into individual prisms was based on the better precision/accuracy in inducing the cracks – because of the extra arm length provided by the concrete beam.

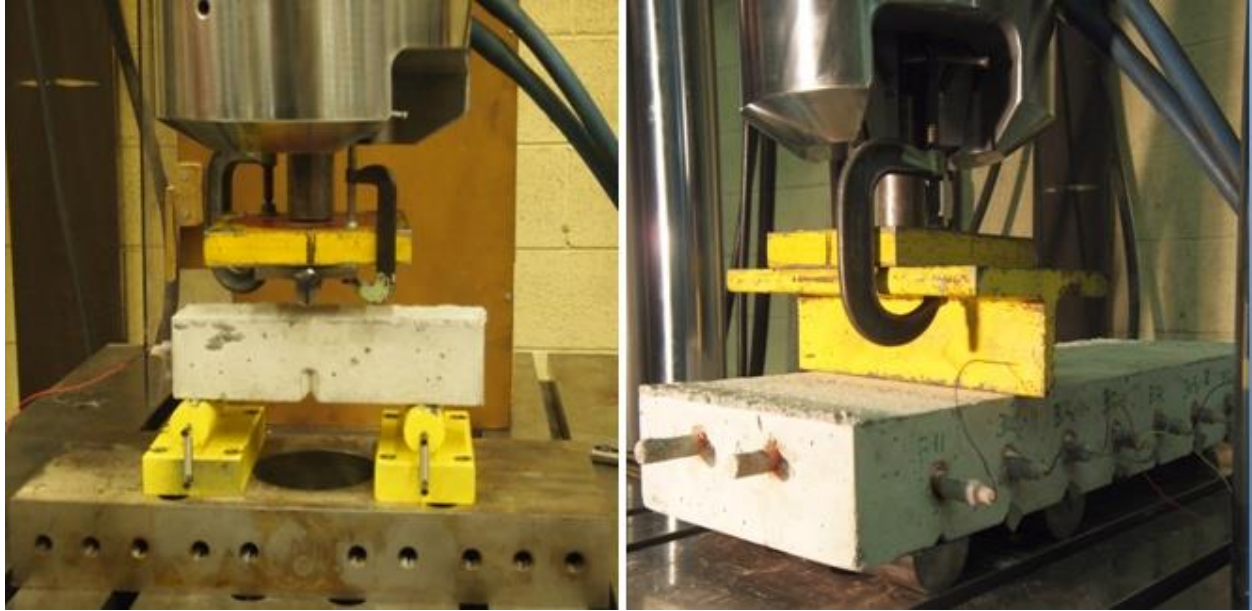


Figure 3-7: Inducing cracks in the transversely cracked (left) and longitudinally cracked beams (right).

After crack had been induced, a 10mm L x 10mm B x 0.3mm W 304 stainless steel shim was inserted at each end of the crack to prevent the crack from closing. The original intention was to simulate worst case condition of a structure containing crack width of at least the thickness of the shim (0.3mm) – the width above which the MTO requires sealing of the crack [58]. However, over the course of preparing the specimens for brine exposure, some of the shims removed and were unable to be placed back in the crack. A decision was then made to remove all shims to allow specimens retain their varying range of crack width, which is a more realistic occurrence for field structures.

3.4.2. Cutting and epoxy coating of cracked specimens and measurement of initial OCP

Once cracks were induced, the longitudinally cracked beams were cut into individual prisms and they and the transversely cracked specimens were epoxy coated on all but the cracked surface, Figure 3-8. The goal was to limit chloride ingress to one direction, simulating the chloride exposure of a bridge deck. Afterwards, the corrosion potential was measured for all 112 specimens using a voltmeter and a saturated calomel reference electrode (SCE) as done in the

field with a Cu/CuSO₄ reference electrode. This was to provide a baseline for each concrete specimen's corrosion potential before exposure to brine solution.



Figure 3-8: Measurement of corrosion potential before exposure to brine (left); and epoxy of all but cracked side of the prisms (right). Closer view of individual prism (insert).

3.5. Exposure of specimens to brine

Cracked specimens were placed upright in several tubs containing a commercial multi-chloride brine solution (applied to highway infrastructures in Ontario) containing 21% Cl⁻ solution up to approximately 25 mm (1 inch) below the top of concrete, **Error! Reference source not found.** Figure 3-9. The transversely- and longitudinally- cracked specimens were placed in separate tubs with specimens arranged in circle in both cases, to allow a stainless steel counter electrode (C.E) and reference electrode (R.E) be placed in their middle. Also, the arrangement was such that the cracked region faced the stainless steel C.E and the SCE R.E. This is to ensure electrons are transferred in relatively equal distance to all rebar in each concrete specimen.

The tubs were then covered to reduce evaporation of water and crystallization of the salt. C.E was also placed in the ponding well of the sound beam specimens before being filled with brine solution and also covered to reduce evaporation of water and salt crystallization, Figure 3-9.



Figure 3-9: Specimen exposure to brine solution. Cracked specimens are placed in tubs containing brine solution while ponding well is filled with brine.



Figure 3-10: Cracked specimens closed in tubs (left), and sound beams closed with plywood (Right).

3.6. Electrochemical measurements

To compare the corrosion behaviour of the various coatings, microcell corrosion rate of the specimens was measured using the galvanostatic pulse, GP and linear polarization resistance, LPR (discussed in Chapter 2) techniques. This is based on the idea that through cracks and pores in concrete, localized corrosion can occur on a single rebar, i.e. with anodic and cathodic regions present on the same rebar. Bi-weekly GP and LPR tests were performed on all the specimens for approximately 65 weeks (450 days).

3.7. Microstructural and Compositional Analysis of Steel Coatings

Rebar coating compositional analysis was performed using x-ray fluorescence analysis (XRF) and energy dispersive x-ray spectroscopy (EDS) feature in a scanning electron microscope (SEM). In the EDS, which was conducted on a polished surface of the rebar cross-section, different points or regions in the coating were chosen for analysis. The result, however, is semi-quantitative because a region or phase in the coating may be selected for analysis, but a larger volume including other phases may be included in the analysis. Furthermore, the EDS require one to have an idea of the coating composition in the case of overlapping peaks in the analysed spectrum. This may pose a problem for a rebar like the CG where other elements other than Al could be added to the Zn bath. On the other hand, XRF of the coating was performed on the rebar surface, rather than on a cross section of the bar, and is more quantitative. However, because of the depth of penetration of the x-ray beam, the accuracy of the data is influenced by contributions from the steel substrate if the coating is too thin. This is the case for the CGR. The mode of operations for both XRF and SEM/EDS can be found in [57] and [61] respectively.

Micrographs of the rebar coating were obtained using the optical microscope and SEM. While the SEM is able to give more details of a particular region in the coating, because of its higher resolution, the optical microscope is able to differentiate between phases in the coating - because of their contrast. As a result, optical microscopy images were obtained for most part of the microstructural analysis in this report.

3.8. Autopsy of Corroded Bar

After 365 days of bi-weekly GP and LPR testing, two replicate of both transversely- and longitudinally- cracked concrete prisms for all rebar grades were autopsied. The most corroded

specimens of each grade were chosen for autopsy to confirm the results from the electrochemical testing. Furthermore, a more precise corrosion current density (i_{corr} , A/cm²) value was also obtained by dividing the corrosion current values over the actual corroded area, as opposed to dividing over the entire exposed area.

In addition, photographs were taken before and after cutting the concrete prisms with concrete saw. The autopsied bars and both sides of the concrete adjacent to them were analysed for corrosion product and confirmation of Zn loss into the concrete using XRF. For the transversely cracked rebar specimens, only the region (top and bottom side) of the bar exposed to the crack and a little away was examined, while in the longitudinally cracked rebar specimens, the entire exposed rebar length and side adjacent to the crack was analysed.

After 450 days of specimen exposure to brine solution, the final autopsy was performed for the rest of the cracked specimen (three replicates) and two replicates of the sound specimens – to confirm the electrochemical results suggesting passive corrosion. All steps taken in the initial autopsy were also performed for the final autopsy.

Chapter 4 Experimental Results and Discussion

The chapter feature sections on material properties, metallography of coatings, electrochemical results obtained from bi-weekly GP testing, and results from specimen autopsy.

4.1. Materials properties

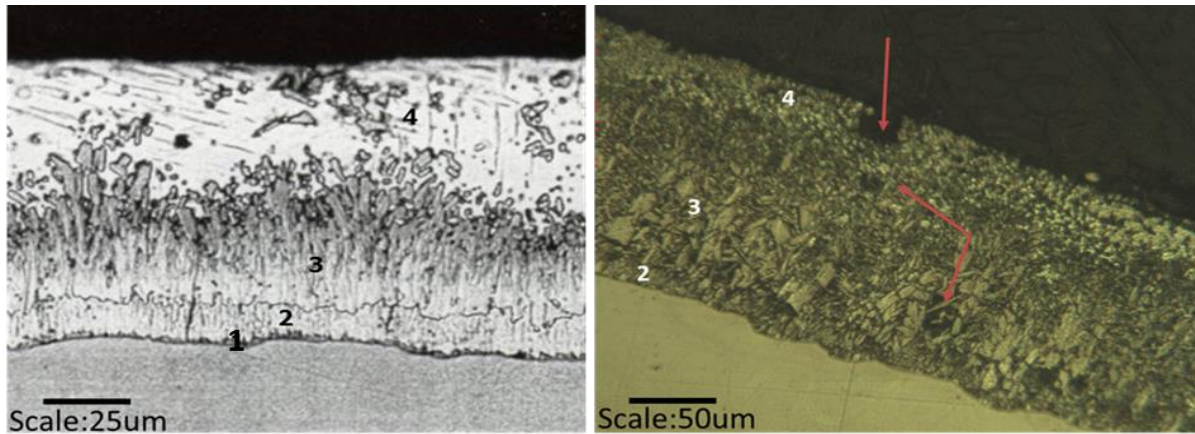
This section includes subsection that outlines the results from materials tested for their physical and chemical properties. This includes: analysis of coating composition and thickness, rebar weight, compressive strength of concrete, and corrosion potential (E_{corr}) of embedded rebar in concrete before exposure to brine solution. Note that only average values are presented here, the individual data can be found in Appendix A.

4.1.1. Characterization of coatings

The coating composition was analysed by XRF of the rebar surface and, the average result of no fewer than 50 measurements is presented in Table 4-1. It should be noted that XRF cannot detect elements lighter in atomic mass than aluminum (e.g. carbon, nitrogen) and, if coatings are too thin, the substrate element can also be detected. Although some coating programs are designed to measure only the coating, the values presented in Table 4-1 were obtained without these programs. As a result of these limitations of the XRF, the values in Table 4-1 should be considered semi-quantitative. Moreover, one can see that the equipment is able to detect more of the steel substrate in the C3 bar than in C1 and C2 bars, indicating that it has the thinnest coating. In addition, the lowest Fe content was detected in the HDG sample, confirming its much thicker coating than the C1, C2 and C3 bars. Also to note is that the C3 sample was found to have Al content in the range (although slightly higher) of ‘Galvan’ bar, typically between 5-7% Al [62].

Table 4-1: Compositional analysis determined by x-ray fluorescence. Note that the percentages do not equal 100 because other minor elements are not presented.

Rebar type	Wt% composition of elements		
	Fe	Zn	Al
HDG	1.0	97.8	<LOD
C1	4.5	92.5	0.5
C2	8.8	88.7	1.9
C3	16.1	74.2	8.9



1- Gamma Γ , 2- Delta δ , 3- Zeta ζ , 4- Eta η

Figure 4-1: Comparison of the HDG sample from the literature [47] with one used in the present work (right). Note for the picture on the right that: a) layer 1 is too thin to be detected or absent, b) the arrows points at defects in the coating.

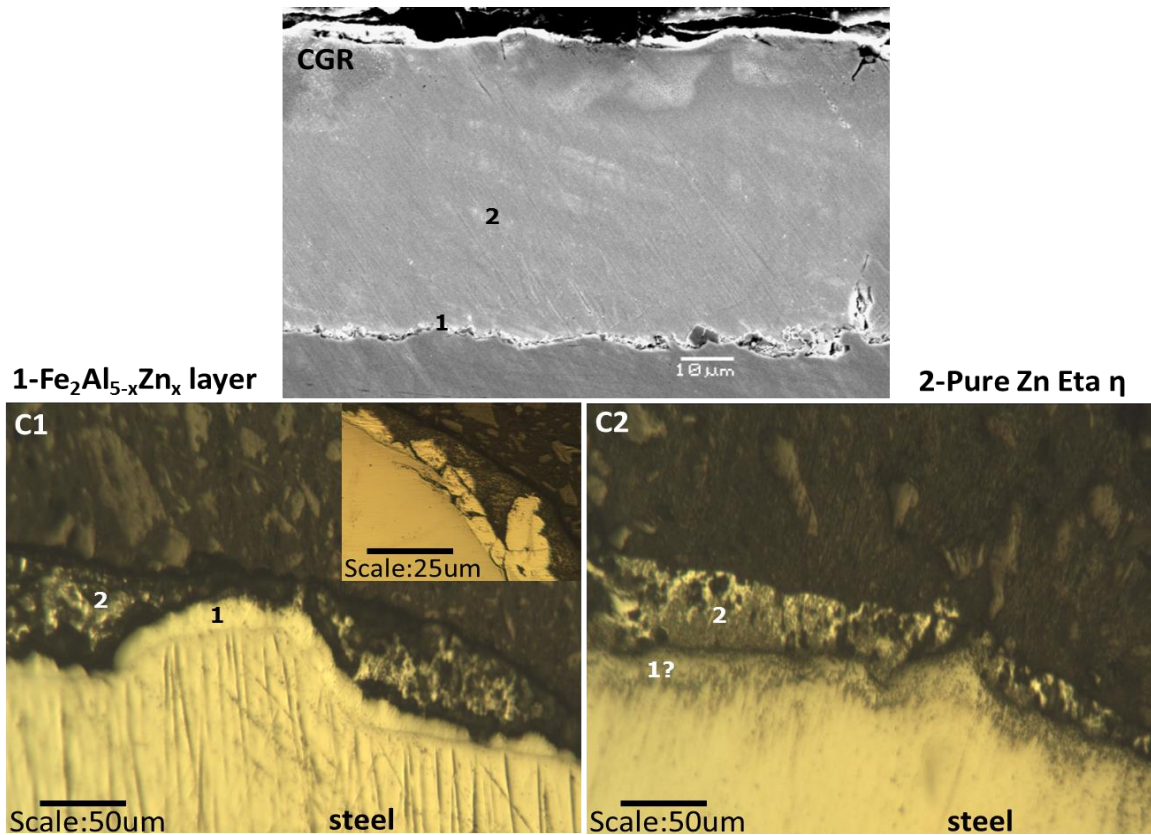


Figure 4-2: Comparison of C1 and C2 specimens with CGR [47]. Note the thicker layer 1 in C1 and the diffuse or absent layer 1 in C2. Insert shows the broken layer 1 in C1 bar.

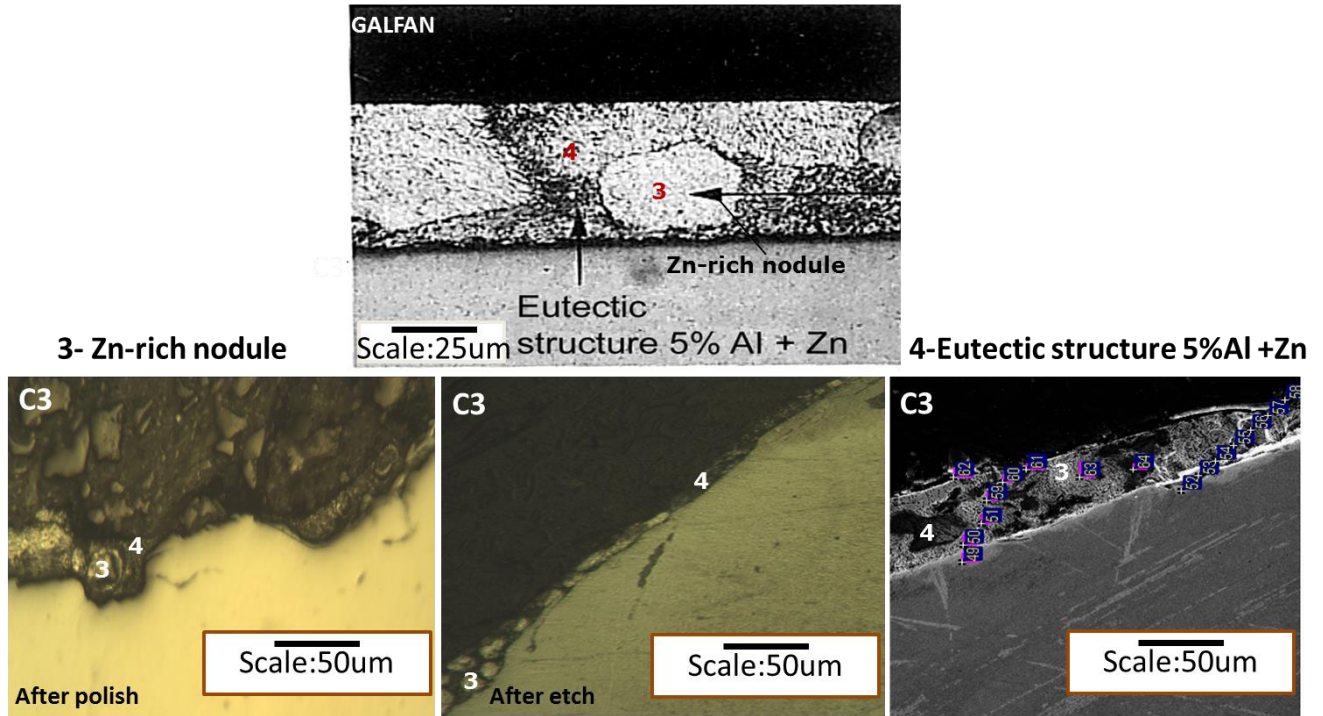


Figure 4-3: Comparison of C3 with Galfan coating from [62]. The Zn-rich nodule and eutectic structure of aluminum and zinc can be seen in both photos.

To further confirm the coating thickness, examine its uniformity around the bars, and assess the phases present, optical microscopy and scanning electron microscopy (SEM) were used to examine the cross-section of these bars. Representative micrographs are shown in Figure 4-1 to 4-3 and, the individual micrographs are presented in the Appendix D. Note that different samples were mounted to obtain the micrographs of the polished and the etched figures. After several trials, it was observed that the inhibition layer in the CGR samples is easily seen without etching, whereas the phases in the coating of an HDG rebar are better seen after etching.

Polished sample



Figure 4-4: Regions analysed for coating thickness.

The non-uniformity in the coatings around the bars can be seen in these micrographs and the rest in Appendix D. Also, notice the damage and pores (indicated by the arrows) in the right hand micrograph of Figure 4-1 and the broken/discontinuous layer 1 in the bottom left micrograph of Figure 4-2. In Appendix D, micrographs where top, bottom, left and right side of the rebar cross-section as shown in Figure 4-4 is presented for both polished and etched condition. These micrographs have been used to generate Table 4-2 that shows the coating thickness around the rebar samples. The data in the table confirm the observation from the XRF analysis that C3 bars have the thinnest coating, of about 26 μm on average. The suppliers of the rebar had indicated the C1 and C2 bars both had coating thickness of about $\sim 50 \mu\text{m}$, but, in fact the average Zn thickness on C1 and C2 were only 41 μm and 33 μm respectively with wide variations around the bars.

Table 4-2: Coating thickness around rebar samples.

Location (Figures from micrographs in Appendix D)		Thickness (μm)			
		HDG	C1	C2	C3
Top (1)	Polished figure	200	60	45	10
	Polished figure	160	30	20	10
	Etched figure	120	40	30	38
Bottom (2)	Polished figure	150	45	40	25
	Etched figure	120	35	30	40
	Etched figure	120	20	15	30
Left (3)	Polished figure	150	60	50	45
	Polished figure	150	50	25	5
	Etched figure	115	50	40	35
Right (4)	Polished figure	250	50	50	35
	Polished figure	160	25	20	15
	Etched figure	105	25	30	20
Average		150	41	33	26
Standard deviation		41	14	12	13

4.1.2. Rebar weight and crack width

Table 4-3 below shows the range of rebar weight, corrosion potential (E_{corr}) and crack width of all five replicates of each rebar grade in all types of concrete conditions. Note that for the longitudinally cracked specimens, the crack width in a particular concrete prism varies over a range because of inhomogeneity of the concrete. However, only the largest crack width is reported because it poses more threat in terms of corrosion of the rebar. Also to note is that the HDG bars weighed significantly less because it is slightly smaller in nominal diameter (11.3 mm) than the other bars (12 mm). Significant difference in potential values can already be seen between the black and galvanized bars, pointing out the importance of having a separate guideline for assessing the probability of corrosion of galvanized steels. The E_{corr} range of the C3 specimen is the most negative of all galvanized rebar, while the HDG is the most positive. This could be due to the higher aluminum content in the former and the least aluminum in the latter.

Table 4-3: Range of E_{corr} , steel weight, crack width for five replicate specimens.

Rebar grades	Transversely cracked			Longitudinally cracked			Sound	
	E_{corr} (mV vs SCE)	Steel weight (g)	Crack width (mm)	E_{corr} (mV vs SCE)	Steel weight (g)	Crack width (mm)	E_{corr} (mV vs SCE)	Steel weight (g)
C1	-408 -494	281 - 285	0.12 - 0.5	-415 -468	281 - 284	0.15 - 0.23	-457 -495	280 - 283
C2	-348 -448	277 - 279	0.13 - 0.25	-398 -442	278 - 279	0.14 - 0.25	-466 -511	276 - 278
C3	-511 -529	275 - 280	0.2 - 1.5	-526 -583	275 - 278	0.15 - 0.25	-535 -631	275 - 280
HDG	-230 -367	194 - 198	0.15 - 0.3	-266 -367	194 - 198	0.14 - 0.25	-409 -465	195 - 199
BLACK	-88 -183	244 - 247	0.13 - 0.26	-98 -200	242 - 247	0.12 - 0.25	-136 -206	244 - 246

4.1.3. Concrete properties

Table 4-4 shows the average values of the compressive strength at respective ages and, the individual values are presented in Appendix A. The table presents two sets of data, Cast 1 is used in casting all rebar samples except C3, which was obtained later and made with Cast 2.

Table 4-4: Average concrete compressive strength (MPa).

Age (Days)	Average Compressive Strength (MPa)	
	Cast 1	Cast 2
7	30.1	43.3
14	30.7	44.4
21	38.9	47.8
28	39.9	48.5
56	43.5	55.6

Regarding the 35 MPa set limit discussed in Chapter 3, the immediate observation from Table 4-4 is that at 28 days, both cast exceeded this limit. Furthermore, it can also be seen that both casts increased in a similar manner, but for the higher magnitude of increase observed from 14 to 21 days in Cast 1 and, the general higher strength values associated with cast 2. Since both concrete mixture designs were the same, this behaviour can be explained by the inhomogeneous nature of concrete and change in time/weather of casting. Also, it was possible that the composition of the cement could factor in such differences since Cast 1 was supplied as ready mix concrete from Dufferin Concrete and Cast 2 was made (with same mixture design) in the laboratory with cement supplied from Olsen cement.

These data help in understanding the properties and environment of the concrete the bars are embedded. For example, as strength increases, the resistivity of a concrete is known to increase and conductivity reduces. A lower conductivity means the ability for the concrete to transport ions needed to complete the electrochemical reaction is lower. That being said, it can be seen in Table 4-4 that there is little to no increase in compressive strength in the early days of cast (7 to 14 days), suggesting the concrete conductivity is not reducing.

4.2. Electrochemical Measurement Results

This section presents the electrochemical test results performed on: 25 bars embedded in sound concrete specimens, 25 bars in the transversely cracked specimens and, 25 bar in longitudinally cracked specimens, all exposed to 21% Cl⁻. In addition, three extra HDG bars were cast along with the C3 specimens using “Cast 2” concrete mixture for comparison purposes. However, data for these extra HDG bars are not discussed because their behaviour is very similar to the rest of

the HDG specimens made with “Cast 1”, Appendix C. The employed electrochemical technique was able to yield: corrosion potential (E_{corr}), corrosion current density (i_{corr}), and the concrete resistance (R_c) of the specimens. Note that only results from the GP test are shown here, while results from both the GP and LPR test are presented in Appendix C.

The most common method to qualitatively assess the corrosion condition of reinforcing bars in field concrete is through the measurement of their E_{corr} . This is largely due to the rapidity, ease and cheap cost associated in carrying out the measurement, as only a voltmeter and reference electrode are needed for testing. The collected E_{corr} values are then interpreted using the recommended ASTM C876 guideline (graphically depicted in Figure 1-1) in order to determine the possibilities of corrosion. However, these guidelines are applicable only to uncoated black steel reinforcing bars in concrete [51]. Consequently, the data for E_{corr} of the coated bars are presented with the goal of providing alternative guidelines for passive and active corrosion of these bars.

4.2.1. Sound Concrete

Figure 4-5 shows the average E_{corr} values of the sound beam specimens and, it can be seen that all curves remained approximately constant throughout the concrete exposure period. In relating the E_{corr} value of black steel (~ -100 mV vs SCE) to ASTM C876 (Figure 1-1), the curve falls in the low risk of corrosion region (more positive than -125 mV vs SCE). This indicates that the chlorides are yet to reach the passive film developed at early days on the rebar in sufficient quantity to de-passivate the steel. This emphasizes the importance of having little to no cracks in concretes to protect reinforcing steels. The galvanized steels, both HDG and CGR, were passively corroding.

A significant difference in E_{corr} values for the black steel and the galvanized steel specimens can also be seen, emphasising the need for a different guideline than ASTM C876 for assessing probability of corrosion of galvanized steels. The tested galvanized steel bars have similar potential values, but those of the HDG bars (approximately -300 mV) are -40 to 80 mV more positive than others. According to guideline provided by reference [51], shown in Table 2-5, there is 70% probability of passive corrosion for this potential value, which is more negative than the potential value (-260 mV vs SCE) for 90% probability of passive corrosion. Firstly, the

guideline needs to be carefully interpreted as it is nearly impossible for a potential value of -259 mV, regarded 90% passive corrosion, to reduce to 70% passive corrosion when it becomes -261 mV. Secondly, this is a guideline from a single author and cannot be considered absolute when predicting the conditions of the rebar. With support from the i_{corr} values (Figure 4-6), indicating that the HDG rebar is passively corroding ($\sim 0.2 \mu\text{m}/\text{yr.}$), again $>90\%$ probability of passive corrosion in fact begin from -300 mV vs SCE as opposed to the -260 mV vs SCE suggested by [51]. However, it should be mentioned that result from [51] was obtained for longer testing time, ~ 735 days, and with the HDG curve slightly becoming more positive over time, there is a chance that the potential value is reached overtime.

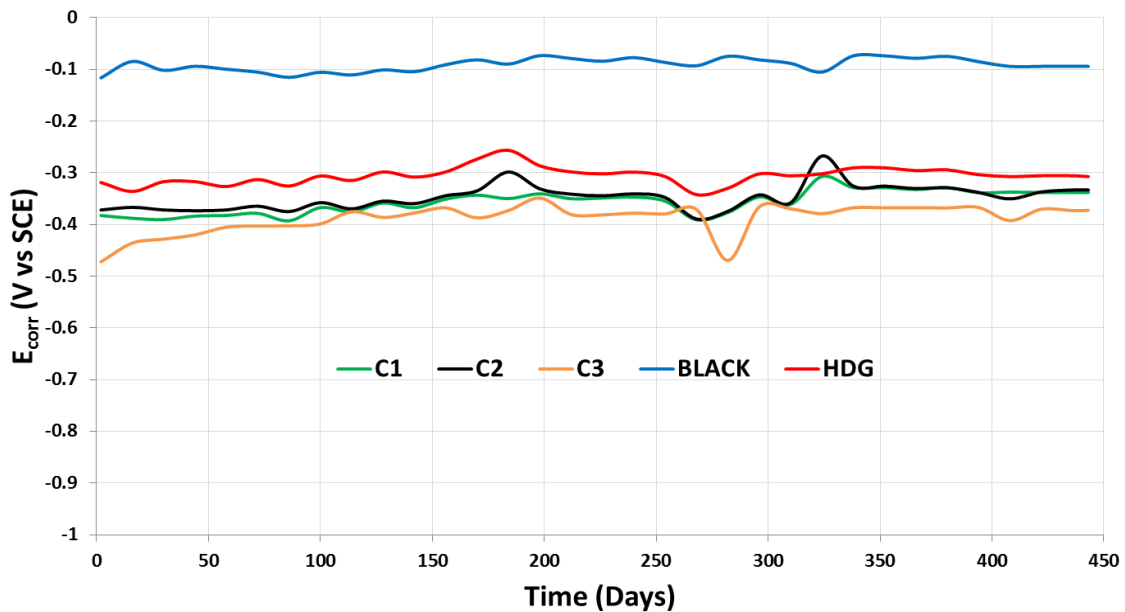


Figure 4-5: Average corrosion potential (E_{corr}) values of bars in sound concrete beam specimens.

The data for the HDG specimen in Figure 4-5 is in excellent agreement with those obtained in a previous study [63]. The C1 and C2 bars have very similar corrosion potential values, -340 mV, which is slightly more negative than the HDG specimen, but more positive than the C3 bars, -380mV. This could be due to the higher Al content in the C3 rebar and, since Al content in the coating increases from HDG to C3, these curves suggest that the higher the Al content, the more negative the potential. Thus, a different potential guideline may be needed in interpreting the potential of the high Al containing Zn coating. However, both values (-340 mV and -380 mV)

fall within the 70% probability of active corrosion region of the NRC guideline (Table 2-5) and, since it is expected that all of the bars are passively corroding similar to black steel in the same concrete beam, the NRC guideline cannot be taken as absolute for corrosion probability assessment.

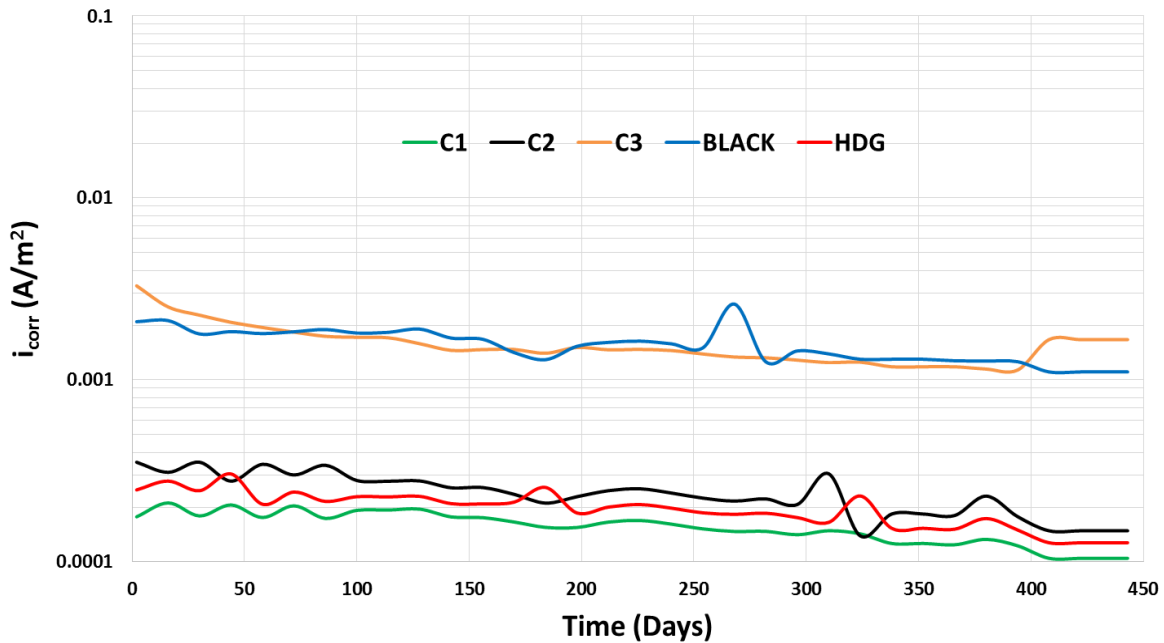


Figure 4-6: Average corrosion current density (i_{corr}) values of bars in sound concrete beam specimens.

Figure 4-6 shows the corrosion current density of the bars in the sound concrete beams and, an immediate observation is how the curves slightly decrease overtime, supported by the slight increase, more positive, in their E_{corr} values. Another very noticeable observation is the distinct and similar behaviour of the black steel and C3 specimens, starting with an average corrosion current density of ~ 0.002 and 0.003 A/m^2 respectively and decrease overtime to $\sim 0.0015 \text{ A/m}^2$. A corrosion current density value of 0.001 A/m^2 is equivalent to ~ 1 and 1.5 um/yr. for black and galvanized steel respectively and values in this range are typically regarded as passive corrosion. In Figure 4-5, the C3 specimen showed more negative passive potential value than the rest of the galvanized steel and the behaviour was attributed to the higher Al content. A corresponding higher passive corrosion current density value is also observed for the same rebar, Figure 4-6.

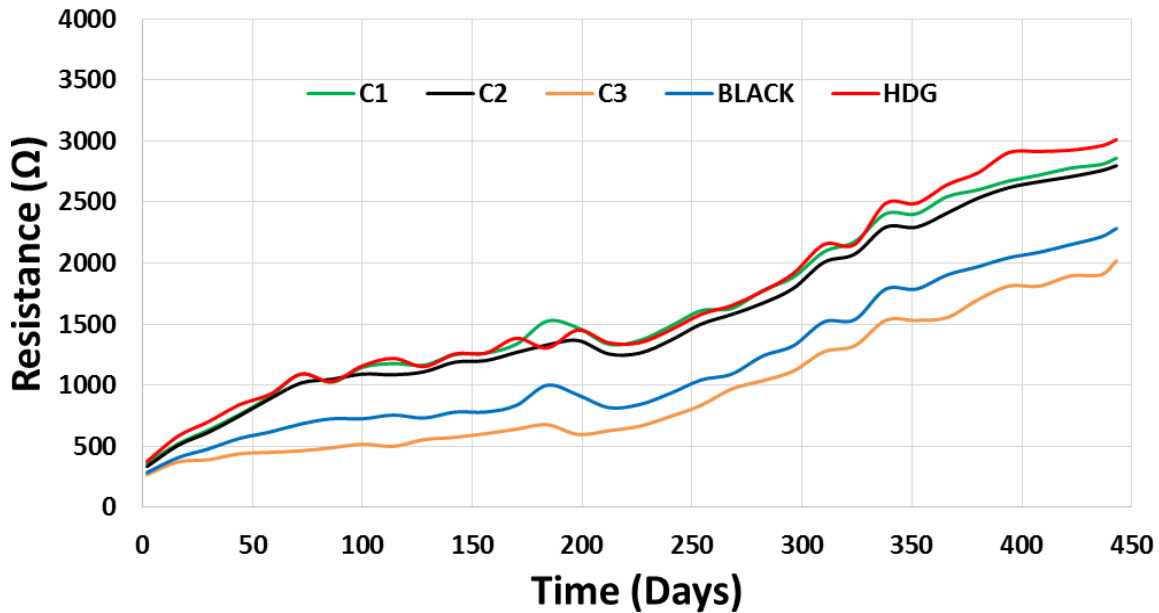


Figure 4-7: Average concrete resistance value of sound beam specimens.

Although it may not be a concern, since all bars are passively corroding, but an order of magnitude higher i_{corr} value suggests that aluminum addition in the range of the C3 sample to galvanized steels negatively (less corrosion resistance) affects corrosion performance. It is possible that during the initial corrosion of the galvanized bar, aluminum in the corrosion product causes the rebar to lose bond with the concrete. This claim is supported by the concrete electrical resistance values in Figure 4-7, which is interesting to see that even with no chloride, the resistance of the concrete around the C3 specimen (and black steel) is lower compared to the rest of the galvanized bar. Furthermore, the inferior passive behavior (i.e. higher passive current density) of the C3 bars relative to other galvanized bars was also observed by Cheng et al. [65]. They reported that “hot-dip coatings can be passivated, but the passivation current densities are much higher for Al-containing coatings than for galvanized pure zinc coatings”.

Apart from the distinct behaviour of the C3 specimen, the rest of the galvanized bars behaved in a similar manner, with an average corrosion current density in the range of 0.2 - 0.3 mA/m², which gradually decreases overtime. These values, in the range of 0.2-0.3 μm/yr., confirm the indication from the E_{corr} graph that the thinner Zn coating of C1 and C2 bars is as good as the significantly greater Zn thickness on the HDG steel in the passive condition. Furthermore, galvanized steels; HDG, C1 or C2, in a non-cracked concrete can offer protection of an order of

magnitude better than regular black steel (or Galvan). In comparing the i_{corr} curve of the HDG specimen from this experiment with those from [63] [Figure 4-6 insert], it can again be seen that the current densities are very similar, decreasing to about $\sim 0.2 \mu\text{m/yr.}$ over the 450-day period.

4.2.2. Transversely Cracked Concrete

Figure 4-8 shows the average corrosion potential of the transversely cracked specimens and, one of the first observations is how significantly more negative the curves are in comparison with the sound beam specimens. Having started at about -350 mV, the black rebar remained rather constant and slowly became more positive to a potential of approximately -320 mV. Judging by the recommendation in ASTM C876, a value of -320 mV vs SCE for black steel suggests 90% probability of active corrosion, emphasizing the detrimental effect of cracks in concretes. On the other hand, the galvanized bars started with a more negative potential, between -850 and -920 mV, significantly attained a more positive potential of about -410 mV, -520 mV, -470 mV, and -500 mV for the HDG, C1, C2 and C3 specimens respectively.

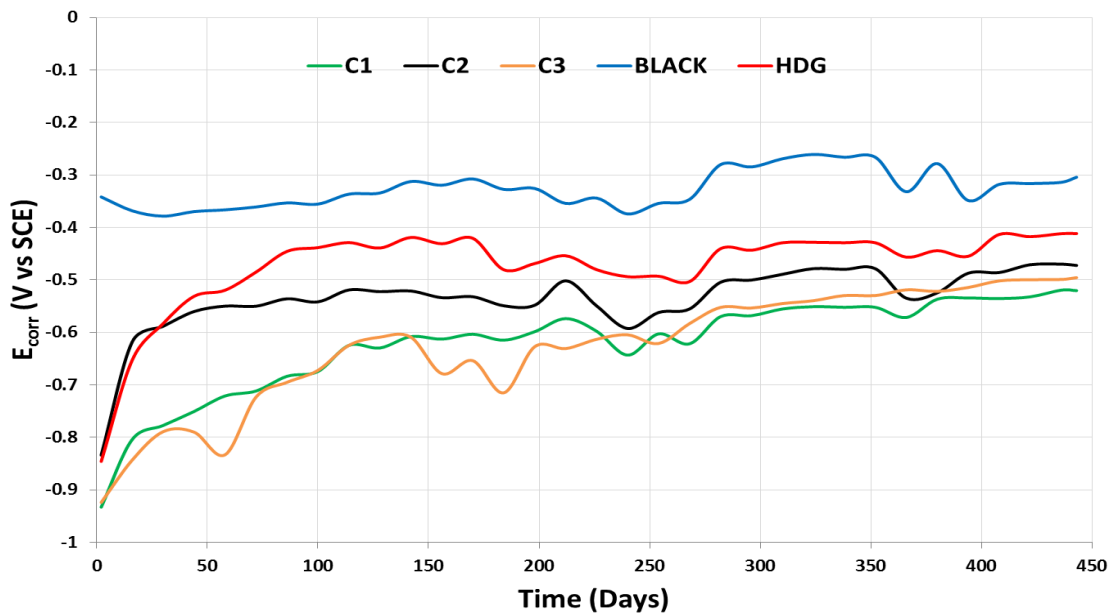


Figure 4-8: Average corrosion potential (E_{corr}) values of bars in transversely cracked concrete specimens.

As shown in Table 4-1, the potentials of the galvanized bars before exposure to brine solution were -480, -480, -570, and -440 mV for the C1, C2, C3, and HDG rebar respectively. When

exposed to brine solution (through the cracks), these potential immediately became more negative (between $-850 - -950$ mV), and over time, an increase, more positive, in potential is observed (significantly in the first 150 days). This significant more positive potential gain in the first 150 days, experienced only in the galvanized bar and not found in the sound beam specimens, is likened to the non-protective behaviour of the CHZ crystals when placed in neutral environment, as shown in the Figure 4-9 and 4-10. It was hypothesised, through a short (one week) test, that having formed a very compact CHZ crystal in the high pH environment of the concrete, when subsequently exposed to the 21% brine solution, some the crystals could fall off the rebar surface. In this short test, two bars, Bar 1 and Bar 2, were immersed in water so that their potential readings can be taken and were immediately taken out, Step A. Subsequently, both bars were placed in synthetic pore solution (composition provided in Appendix B) to passivate (i.e. form CHZ crystals) for five days, and their potential readings were monitored during those periods, Step B. Then, the passivated Bar 1 and Bar 2 were placed in water (Figure 4-9) and water containing 3% sodium chloride (Figure 4-10) respectively and, their potential values were monitored after 30 mins (Step C) and 24 hours (Step D). A similar change in potential and dropped CHZ crystals into the solution was observed. The huge more positive E_{corr} in the early days of exposure of the specimens to brine solution is expected to result in a corresponding drop in the corrosion current density values.

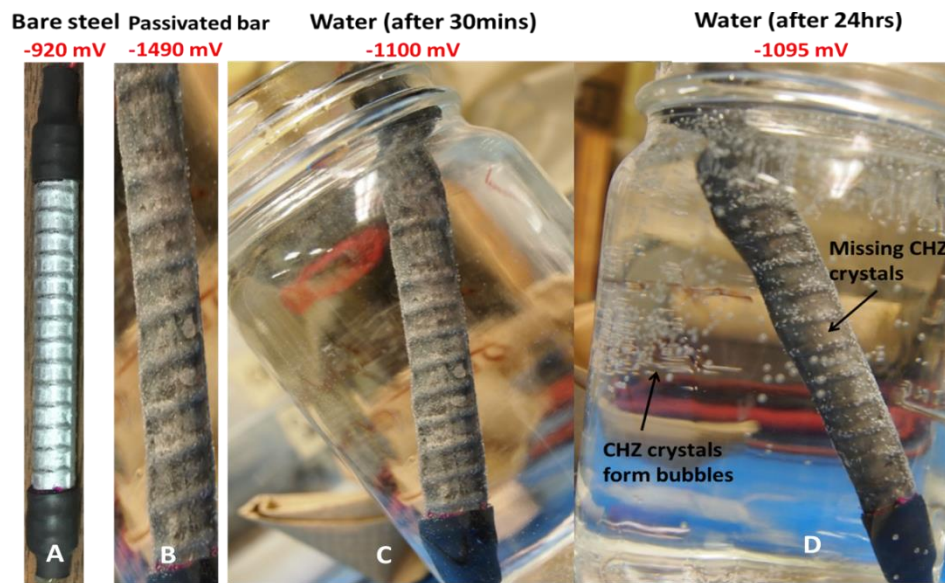


Figure 4-9: 1-week test showing the non-protective nature of CHZ crystals in water.

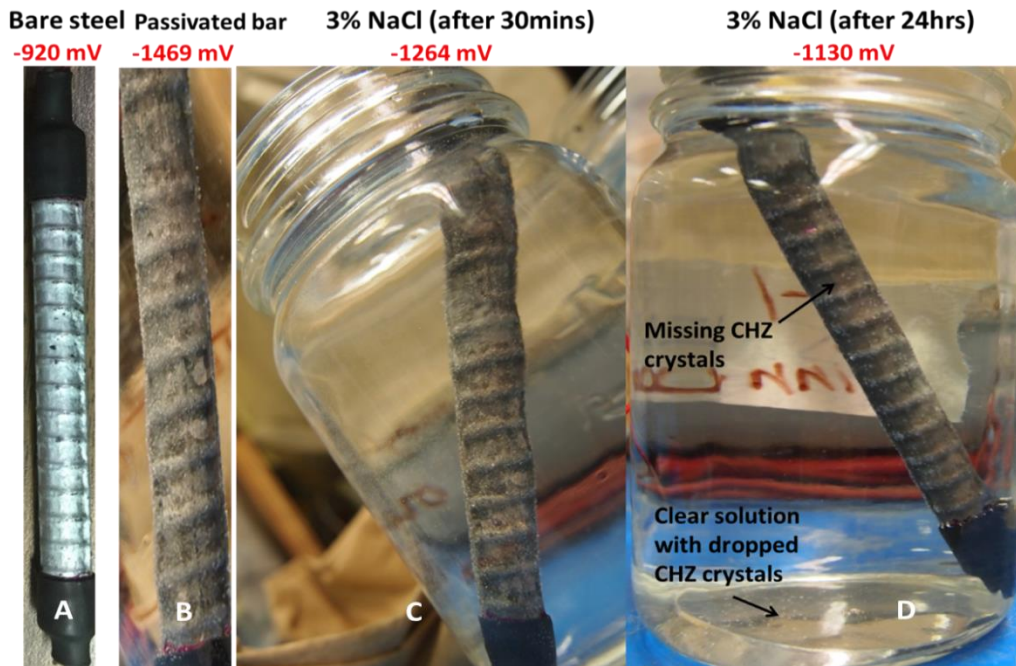


Figure 4-10: 1-week test showing the non-protective nature of CHZ crystals in 3% NaCl.

Judging by the NRC guideline in Table 2-5, it is no surprise that the potential values of the galvanized specimens in this cracked concrete condition fall in the region of 85-90% risk of active corrosion (i.e. between -425 – -535 mV vs SCE). Although there were significant differences in potential values between the HDG and C1, C2 and C3 samples, in the early days of exposure to the brine, the curves eventually attained similar potential value over time, with the HDG being about only ~90 mV more positive. The minor final difference again could be due to the insignificant Al content or the significantly higher Zn coating thickness in the HDG bars. An interesting observation is how the potential of C1 behaved similarly to that of C3 rather than C2 as observed in the sound beam. The reason for this behaviour is not clear, however, it should be noted that these are mixed potential values between the corroded and non-corroded areas on the bars, which may be different in terms of larger corrosion penetration into the Zn coating in the cracked region of the concrete. Also, it could be due to the varying crack width of the individual specimens, as shown in Figure 4-11.

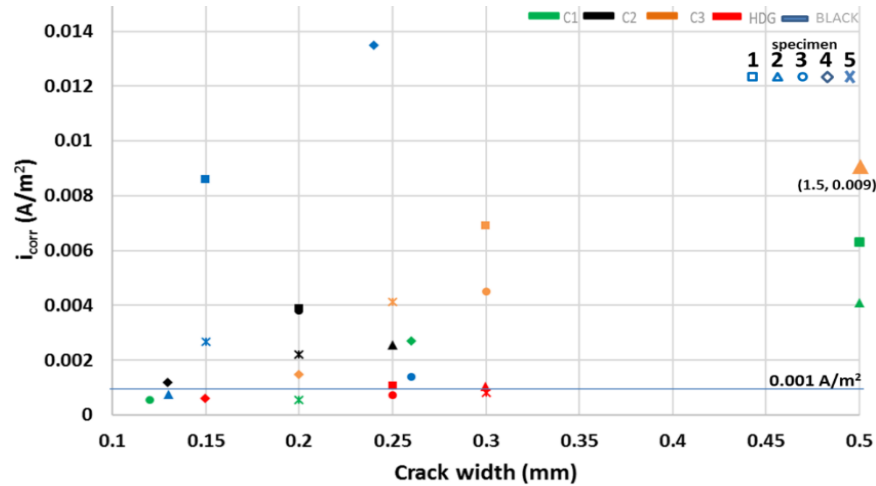


Figure 4-11: Correlation of crack width and corrosion current density of bars in the transversely cracked concrete specimens at 450 days of brine exposure.

It is important to consider the i_{corr} value of the bars to determine how significant 90 mV more positive potential of the HDG bars are relative to the C3 bars, since the same range of potential observed between both specimens in the sound beam result in an order of magnitude lower corrosion current density for the HDG specimens. It should also be added that the E_{corr} curve of the HDG specimen from this test is very similar and slightly more positive than those from [63].

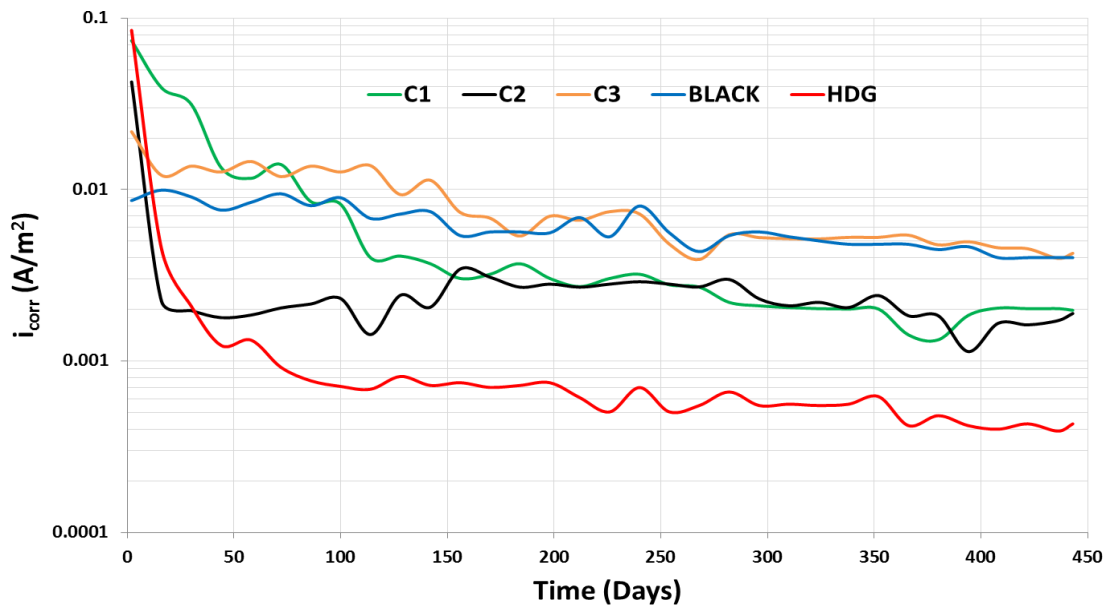


Figure 4-12: Average corrosion current density (i_{corr}) value of bars in transversely cracked concrete specimens.

Figure 4-12 shows the corrosion current density values of the transversely cracked specimens and, these curves showed significant initial decrease followed by a slight decrease over time corresponding to the initial increase and then gradual shift to more positive E_{corr} values in Figure 4-8. Furthermore, as observed in Figure 4-6 for the sound beam specimens, the behaviour of the C3 specimen in this concrete condition is similar to that of black steel, further suggesting the detrimental effect (in terms of corrosion resistance) of Al addition to galvanized steel coating. At this point (before autopsy), it is also possible to assume that all the thin (5 – 30 μm) Zn coating on the C3 bar is already lost through corrosion, causing the bar to behave like black steel. In addition, unlike the rest of the tested rebar sample, both the black bar and C3 specimen decreased at a rather consistent corrosion rate from 0.01 to 0.004 A/m^2 over time. Cheng et al. [65] reported the inferior behaviour of Al-containing galvanized steels in the active state, stating that “for Al-containing coatings, the coating thicknesses are greatly reduced and replaced by a layer of corrosion product mainly composed of $\text{Ca}_2\text{Al}(\text{OH})_7 \cdot 3\text{H}_2\text{O}$ ”.

A correspondingly lower corrosion current density of the galvanized bar is also observed in the first 150 days, following the huge increase, more positive, in potential experienced in the E_{corr} graph. Afterwards, the C1 and C2 samples behaved very similar with an average i_{corr} value of 0.002 A/m^2 at the end of ~450 days of testing, while the HDG steel is corroding at 0.0007 A/m^2 . As observed in the sound concrete specimens, the 90 mV more positive potential values observed in the HDG rebar relative to C3 result in an order of magnitude lower i_{corr} value for HDG. The same order of magnitude difference in i_{corr} is observed between HDG and black steel, supporting findings [51,48] that HDG steel gives 5-10 times extra corrosion protection than regular black steel. However, if the Zn coating is thinner and has a lower Al content (compared to C3), as in the C1 and C2 samples, the corrosion protection offered by the bars in a cracked concrete, such as this, exposed to ~21% chloride is between black steel and HDG. In other words, with reference to the behaviour of black steel (and galfan), C1 and C2 provide half the protection offered by HDG rebar.

4.2.3. Longitudinally cracked concrete

Figure 4-13 shows the average corrosion potentials of the longitudinally cracked specimens and, a comparison with data for the transversely cracked specimens in Figure 4-8 shows a

significantly more negative value for black steel (~-550 mV vs ~-350 mV), while the galvanized bars were only slightly more negative at the beginning, then later behaved similar to bars in the transversely cracked specimens. For the black bars, the potential value, -550 mV rising to -450 mV over time, according to ASTM C876 falls in the 90% probability of active corrosion similar to the -350 mV of the transversely cracked specimen. The more negative potentials of the bars in the longitudinally cracked concrete are indicative of the higher corrosion rate because of the larger cracked area. For the galvanized bars, since the potentials in both types of cracked concrete are similar at the end of the testing period, it can be concluded that, as long as galvanized steel is exposed to chlorides, the potential value is about the same regardless of the extent of crack. Again, the increase, more positive, in potential values of the galvanized specimens in the first 150 days, is similar to that found for the transversely cracked specimens. The similar rise in potential at ~50 – 100 days and, similar potential values at 450 days between the transversely- and longitudinally- cracked HDG specimens was also observed by Van Niejenhuis [63].

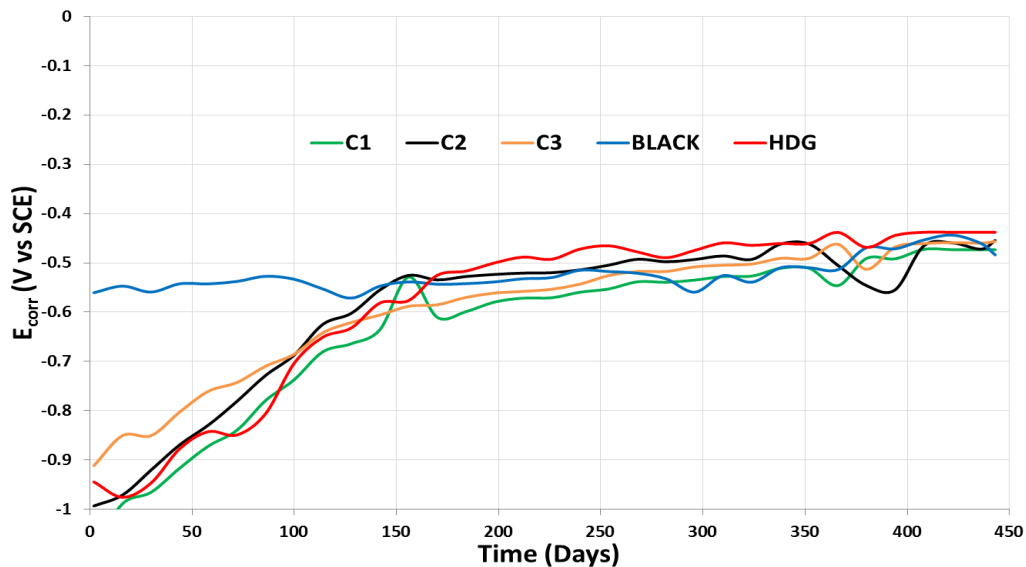


Figure 4-13: Average corrosion potential (E_{corr}) values of bars in longitudinally cracked concrete specimens.

Furthermore, although the potentials of the galvanized specimen are similar, there still exist about 50mV more positive potential in the HDG steel relative to C3, which can also prove to be significant in the i_{corr} value as observed in the previous concrete conditions. In addition, if the

galvanized steels potential values were to be interpreted by the NRC guideline, > 90% probability of corrosion is predicted, which may not be surprising considering the transversely cracked specimens, with more positive potentials, were already in the 85-90% probability of active corrosion range. One should not, at this point, draw conclusions (in terms of corrosion performance) from the similar range of potential values at the end of testing of the galvanized and black bars in this concrete condition.

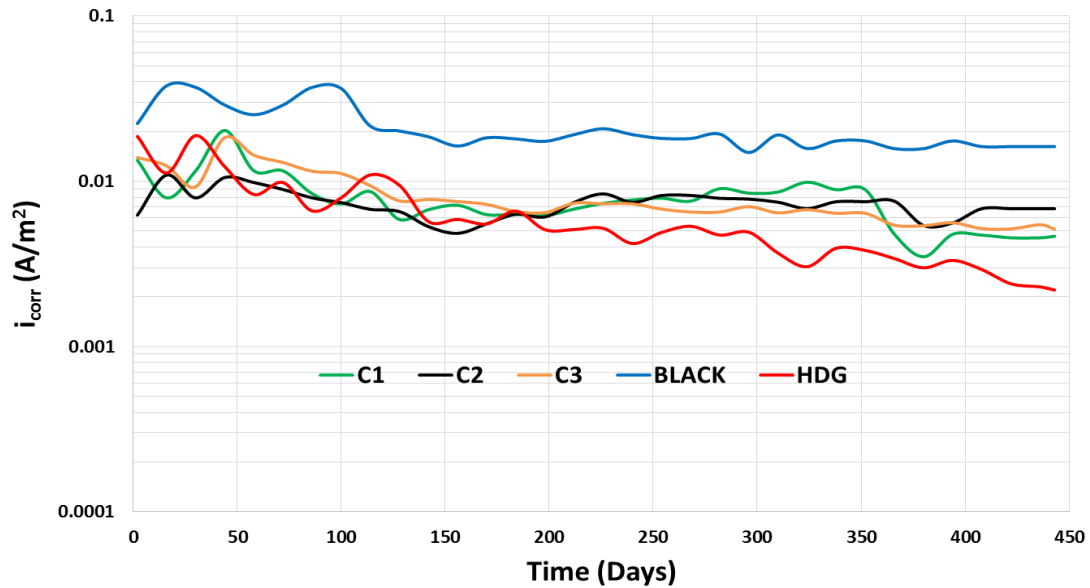


Figure 4-14: Average corrosion current density (i_{corr}) values of bars in longitudinally cracked concrete specimens.

Figure 4-14 shows the average corrosion current density of bars in the longitudinally cracked concrete and, it can be seen that all curves slightly decrease over time, corresponding to the slight positive shift in their E_{corr} values. The black steel specimens started with an average corrosion current density value of $\sim 0.03 \text{ A/m}^2$ and slightly reduced to $\sim 0.01 \text{ A/m}^2$. All the galvanized steel specimens started at $\sim 0.01\text{-}0.02 \text{ A/m}^2$ and the current densities of the C1, C2 and C3 specimens decreased over the test period to $\sim 0.004\text{-}0.007 \text{ A/m}^2$, while the HDG specimens decreased to $\sim 0.002 \text{ A/m}^2$. The general decrease in corrosion current densities of these specimens could be due to the precipitation of salt crystals in the cracks, blocking further ingress of chloride, Figure 4-15. However, the much lower decrease experienced in the HDG specimens could be that its corrosion product bonds well with the concrete, further blocking the ingress of chloride.



Figure 4-15: Salt crystals on the surface and in the cracked region. Such crystals in the crack could block further ingress of salt.

The difference in i_{corr} value observed between black steel (0.004 A/m^2) and HDG bars (0.0008 A/m^2) suggest 5 times better corrosion performance from the HDG steel. This again supports previous observations [51] that HDG rebar is able to give about 5-10 extra corrosion protection than black steel. Furthermore, the C3 specimen, rather than behaving like black steel as observed in the sound and transversely cracked specimens, performed like the C1 and C2 bars, by showing ~5 times lower corrosion rate than black steel, which is half of that offered by HDG and relates to their coating thicknesses. It should also be mentioned that the i_{corr} values of the HDG samples obtained from this test are also an order of magnitude lower than those from [63]. This is due to a larger ($> 0.2 \text{ mm}$ on average) crack width in the concrete specimens used in reference [63].

4.3. Autopsy Results

After a year of exposing the reinforced concretes to multi-chloride brine solution and electrochemical testing, one specimen of the five replicates of each rebar grade in the transversely- and longitudinally- cracked concrete was autopsied. The specimen in each set of five that exhibited the highest corrosion current density was chosen for confirmation of its corrosion initiation. Also, the other objective for autopsying was to determine the corroded area, so that an actual, or more specific, corrosion current density value may be obtained. Once the specimens were removed from brine solution, they were photographed to document any corrosion staining (although not expected in the galvanized specimens because of its soluble corrosion products) outside of the concrete.

4.3.1. Concrete and rebar analysis for corrosion product

The specimens were autopsied by dry cutting the concrete on both sides to a depth near the rebar surface (approximately the concrete cover) without touching with the corroded surface or the corrosion product. Figure 4-16 is an example of autopsied transversely cracked concrete specimen, and it is apparent from the figure that corrosion is initiated in the cracked region. Note that the picture shows the same rebar with the exposed (top) and unexposed (bottom) side.



Figure 4-16: Concrete specimen of autopsied transversely cracked C2 specimen.

Figures 4-17 and 4-18 show the side of the bars exposed to the crack and the reverse side of the bars (non-exposed surface) of the five replicates of HDG rebar placed in both the transversely- and longitudinally- cracked concrete, respectively. The photographs of the C1, C2 and C3 are given in Appendix E. It is clear from these photographs that it is predominantly the exposed surfaces of the bars in longitudinally cracked concrete that suffered from corrosion, whereas the corrosion extends around the whole circumference in the transversely cracked concrete. As a result, the adjusted i_{corr} values of the transversely cracked specimens were calculated for the 1.5 inches (38.1mm) corroded length, and, for the longitudinally cracked specimens, the corroded area was taken as half of the circumference but the whole exposed length.



Figure 4-17: Exposed surface (to concrete crack) of bars in transversely- (left) and longitudinally- (right) cracked HDG steel specimen 1 to 5.

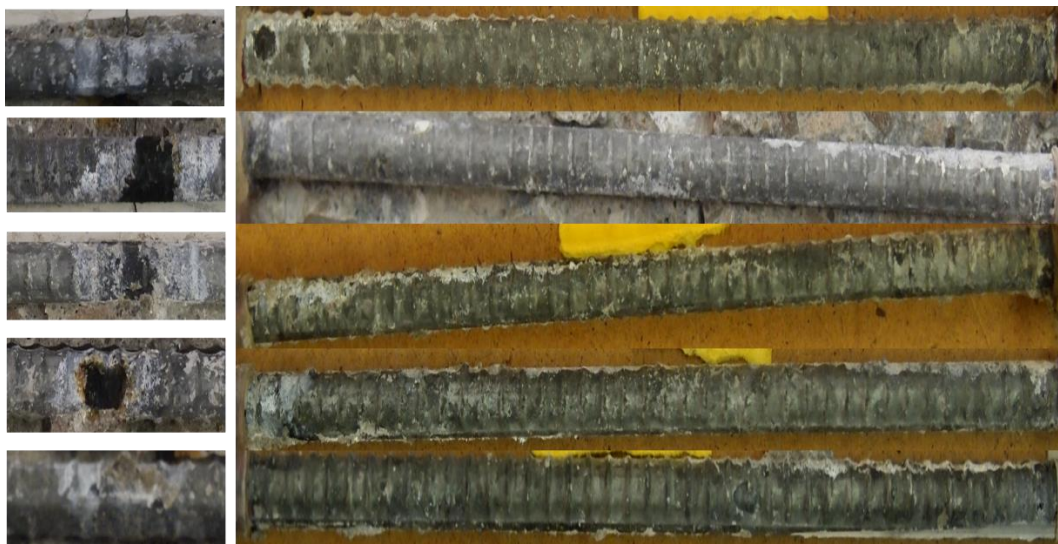


Figure 4-18: Non-exposed surface (to concrete crack) of bars in transversely- (left) and longitudinally- (right) cracked HDG steel specimen 1 to 5.

Cutting the concrete on both sides to within 38.1mm of the rebar also allowed for examination of the concrete adjacent to the rebar surface for corrosion product. This examination was achieved using XRF, and it was performed on two replicates of all rebar grades in both types of cracked concrete and the photographs are presented in Appendix E. Figure 4-19 is an example of analysis

performed on an autopsied transversely cracked concrete specimen housing a C3 rebar and, it can be seen that significant amount of Zn was detected in the concrete. The specimen exhibited the highest amount of Zn detected in the specimens. Another feature of the corrosion product of the C3 rebar was that it was very wet compared to that of the other galvanized bars, and as a result, it flowed from the cracked region to cover more of the rebar surface adjacent to the crack, up to 40 – 50 mm on either side of the black corroded area. This supports the earlier suggestion that the significantly higher Al in the C3 specimen causes it to debond from its concrete due to the build-up of corrosion product.

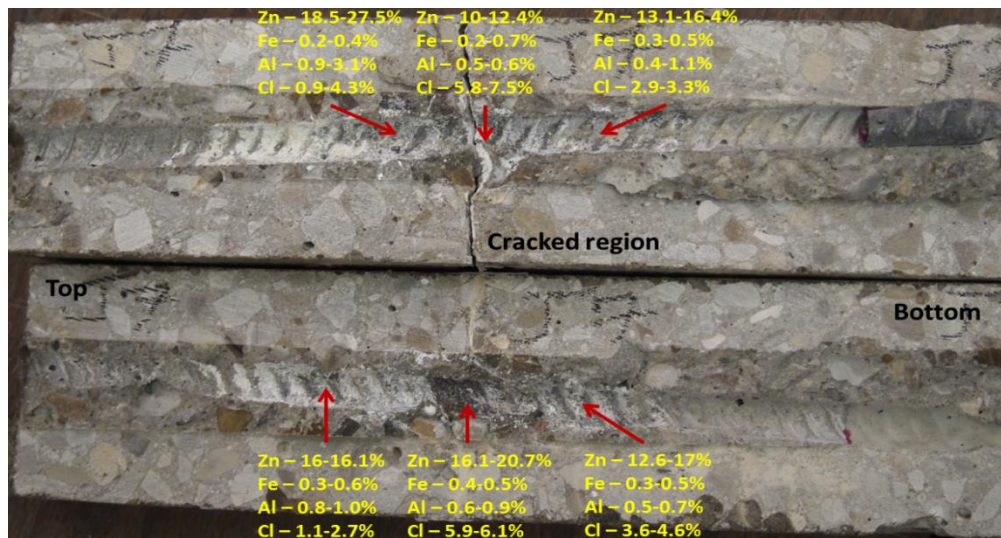


Figure 4-19: XRF analysis of autopsied transversely cracked C3 concrete specimen. The detection of aluminum in the autopsied concrete confirms the $\text{Ca}_2\text{Al}(\text{OH})_7 \cdot 3\text{H}_2\text{O}$ product suggested by [65].

4.3.2. Recalculated electrochemical result of the cracked specimens

Among the five replicates of a type of reinforced concrete specimen, varying level of corrosion products were observed because of the varying crack widths from a specimen to another, which served the purpose of having several replicate specimens to determine such variability. The corrosion products decrease from the cracked region to adjacent areas on the rebar surface where the corrosion product had travelled, except for the cases like that of Figure 4-19.

An adjusted current density estimated from the corroded area of each rebar for the transversely- and longitudinally- cracked specimens, respectively, is plotted in Figure 4-20 and 4-21. For the

transversely cracked specimens, these values approximately an order of magnitude higher than those calculated using the exposed area on the bar, while the longitudinally cracked specimens showed slightly higher values.

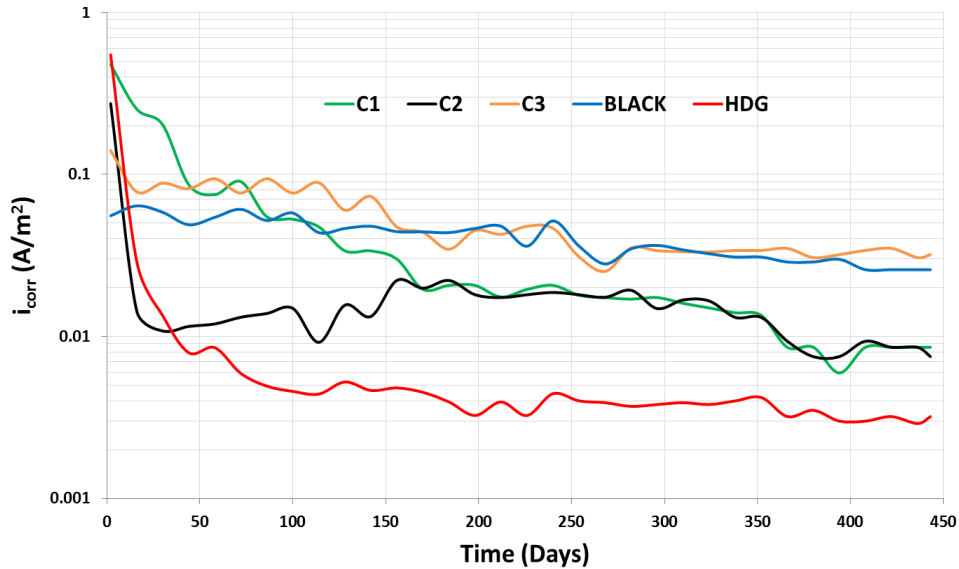


Figure 4-20: Average corrosion current density (i_{corr}) in the corroded area of transversely cracked specimens. Insert are the i_{corr} values averaged over the exposed surface.

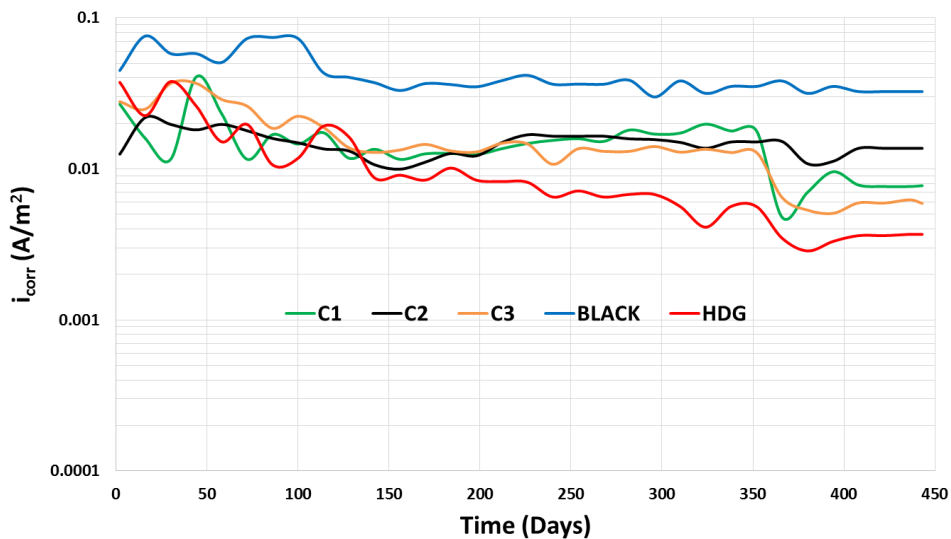


Figure 4-21: Average corrosion current density (i_{corr}) in the corroded area of longitudinally cracked specimens. Insert are the i_{corr} values averaged over the exposed surface.

4.4. General discussions

The electrochemical results and observations of the rebar surface after autopsy of the sound concrete specimens showed that active corrosion was not initiated on any of the reinforced bars, including the black bars. Also, on analysing the concrete adjacent to the rebar surface, no chloride was detected by the XRF, indicating that, after 450 days of concrete exposure to brine solution, there is little chloride diffusion into the concrete in the absence of cracks. In contrast, significant chloride concentrations were detected in, and adjacent to, the cracked region of the two sets of specimens. Moreover, the potential and current density values indicate that the black bars in cracked concrete started to corrode within few days of exposure to the brine solution. These data further emphasise the need for minimizing cracks in concrete to protect reinforcing steel.

At the end of ~450 days of exposure to 21% chloride solution, the HDG bars showed better, by an order of magnitude, average passive and active corrosion current densities, than black bars, suggesting ten times better “corrosion performance”. Since time to corrosion initiation was not determined for any of the bars – because of the huge amount of chloride the bars were exposed to, “corrosion performance” is defined as the active corrosion rate after initiation, Figure 4-22.

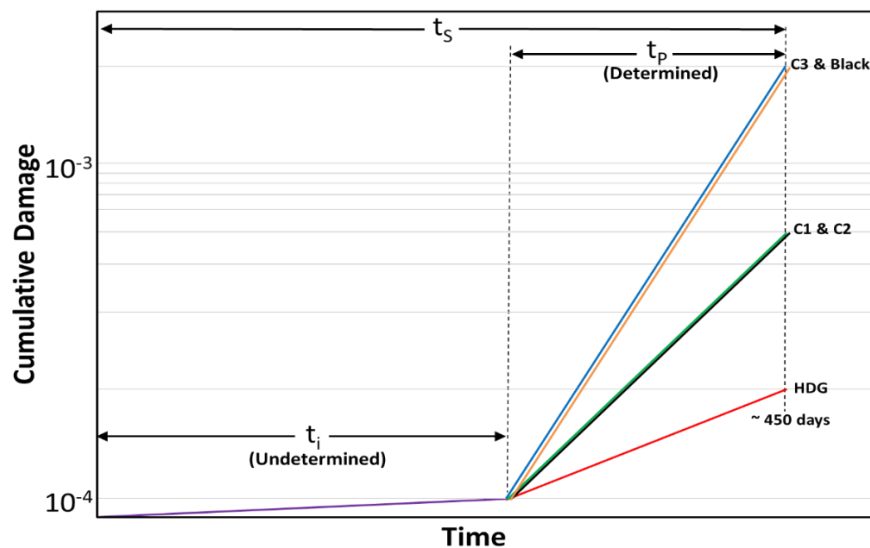


Figure 4-22: Definition of “corrosion performance”. t_i = corrosion initiation time, t_p = corrosion propagation time, t_s = service life time.

To compare with others, the passive corrosion current density values of the HDG bars from the present work (0.0002 A/m^2) are in agreement with those obtained by NRC [51] at 455 days on 100% R.H. concrete (0.0005 A/m^2), Figure 4-26. In the active state, at the end of ~450 days of testing, the current density values of HDG specimens from the present work were 0.0005 and 0.002 A/m^2 for transversely- and longitudinally- cracked specimens respectively. To compare with the work by Bautista and Gonzalez [45] where they submerge non-cracked concretes reinforced with HDG in artificial sea water ($\sim 3.5\% \text{ Cl}^-$) prepared according to ASTM D1141. After 365 days, the bars displayed active average corrosion current density values, 0.005 - 0.05 A/m^2 , which were higher than those from the present work, Figure 4-23.

Furthermore, average current density values from the present work are slightly lower in range than those from NRC ($0.002 - 0.01 \text{ A/m}^2$) obtained on their 100% R.H. concretes, Figure 4-23. This difference could be because the specimens from NRC contained cast-in chlorides between 1- 2% by mass of cementitious material, as opposed to those from the present work that were cast two months before exposure to 21% multi-chloride solution. For the specimens used by NRC, the bars will not be allowed to form stable CHZ crystals before being attacked by the admixed chloride, resulting in higher current density values.

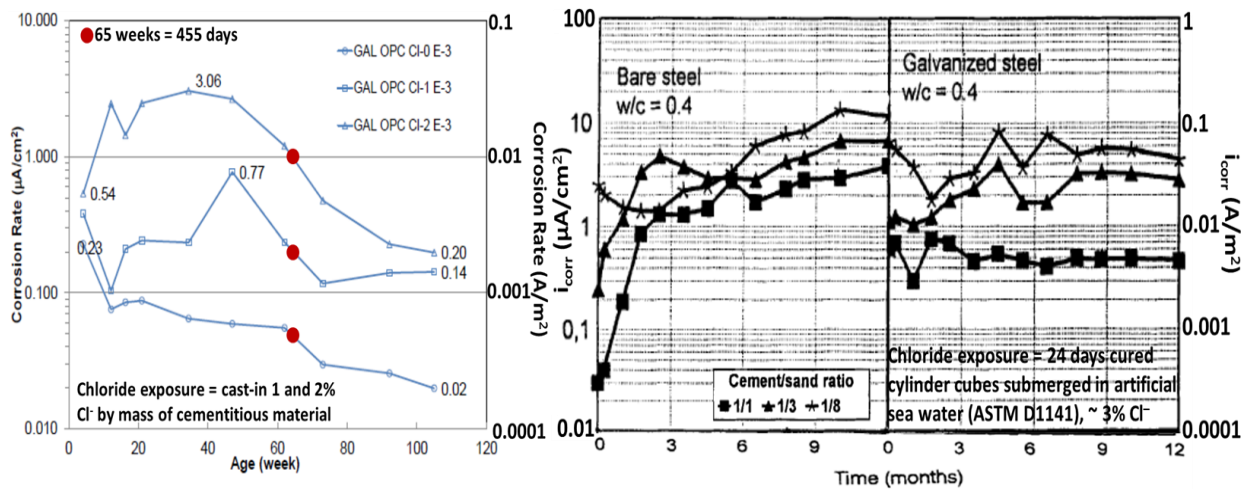


Figure 4-23: Corrosion current density (i_{corr}) of galvanized steel in OPC concrete with cast in chloride kept at 100% R.H. [51] (left) and OPC concrete submerged in artificial sea water [45] (right). Note: cement/sand ratio of 1/3 is similar to one used in the present work.

The NRC concluded from their laboratory exercises that 5-10 times better “corrosion protection” is offered by using HDG rebar. In contrast, field evaluation by corrosion- potentials and currents, chloride analysis, visual survey and degree of delamination, from the MTO on 30-year old Ontario highway structure [48] stated that “galvanized steel was marginally better than conventional black reinforcement”. The bridge was cast in 1975 and, 20 years later, a measured chloride threshold of black steel (0.025% by mass of concrete) was reported to have caused an average i_{corr} values an order of magnitude higher than those from the present work, 0.01 A/m^2 . “For conventional black reinforcement, a corrosion current in the range of 1.0 to $10 \mu\text{A/cm}^2$ (0.01 to 0.001 A/m^2) corrosion damage is expected in 2 to 10 years based on data from National Bureau of Standards 3LP equipment manufacture’s data”. This implies that the HDG rebar only improved the performance by a factor of two compared with black steel. The MTO further stated that “Galvanized reinforcing bars are not recommended as the primary or sole means of corrosion protection for structures exposed in the Ontario highway environment. Based on the findings of this study, they do not provide effective long-term protection from corrosion”.

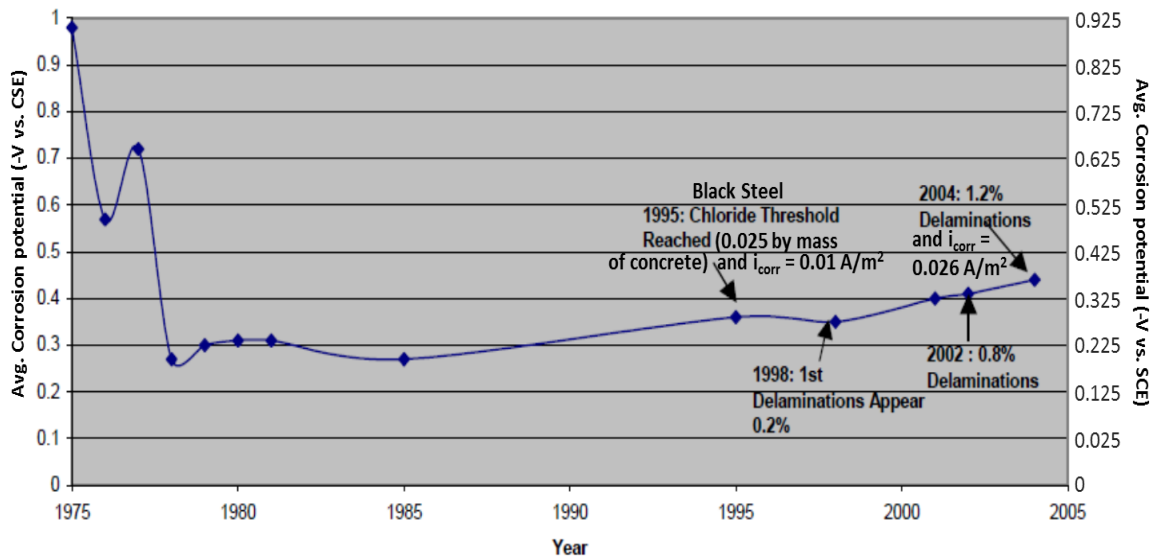


Figure 4-24: Average corrosion potential (E_{corr}) values on a 30 years old bridge deck reinforced with HDG steel [48]. The figure also shows the corrosion current density values and degree of delamination found at years where the E_{corr} values began to rise again.

Furthermore, some delamination was reported by the MTO: “approximately 10% of the deck had deteriorated and required rehabilitation before achieving even a twenty-year service life” [48].

Since the average corrosion current density values of galvanized reinforced structure after 20 years were inferred to be similar to that of black bar, it is possible that the delamination was caused by corrosion of the base steel. This difference points out the gap in laboratory experiment performed at steady temperature and R.H. and field structures affected by varying weather conditions. For the CGR prototypes, the C1 and C2 bars containing aluminum and thinner Zn coatings behaved very similar with average current density values of $\sim 0.0002 \text{ A/m}^2$ in the passive state and average current density values of $0.002 - 0.008 \text{ A/m}^2$ in the active state. With respect to the tested black bars, these bars performed approximately three to five times better when attacked by 21% chloride. The C3 specimens, containing the highest amount of aluminum and thinnest coating, exhibited i_{corr} values similar to those of black steel in the sound and transversely cracked concrete and, approximately five times lower i_{corr} values in the longitudinally cracked concrete specimens. The difference in behaviour in both active state for the C3 bars is not completely understood, however the regions with the thinnest coatings on the bars may have been exposed to the smaller cracked area of the transversely cracked specimens. As a result, chloride attack is more severe than in a larger cracked area of the longitudinally cracked specimens where the effect of sacrificial anode of Zn may have offered more protection.

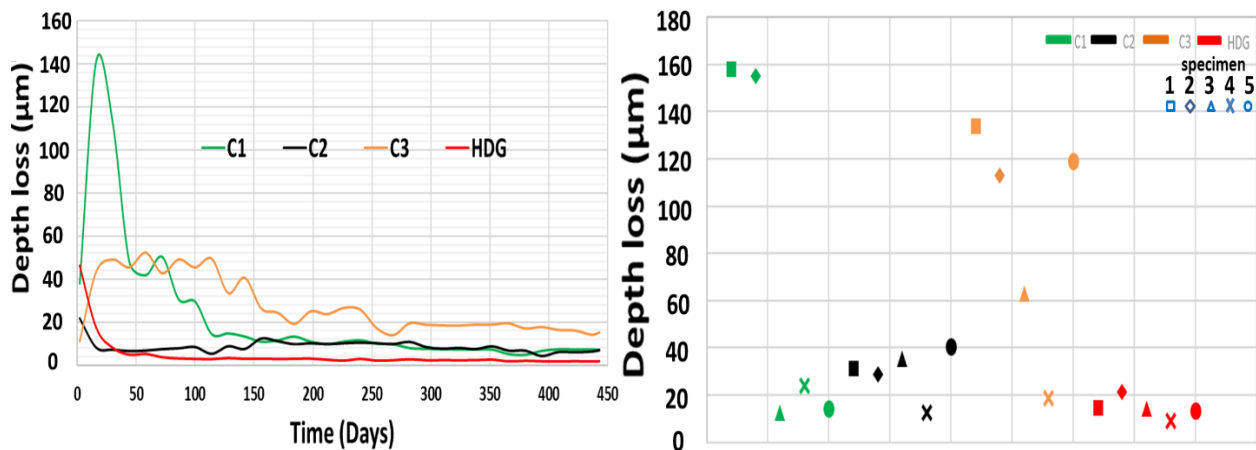


Figure 4-25: Average depth loss over time of the corroded area on all galvanized bars (left) and total depth loss (at the end of 64 weeks' exposure to brine) of the corroded area on each of the 5 replicate bars (right), both in the transversely cracked concrete specimens.

In general, the corrosion performance of the galvanized bars was shown to be dependent on the coating thickness – the thicker the Zn coating, the better the corrosion performance. In addition,

the result also suggested that the higher the Al content in the coatings, the lower the corrosion performance. Figure 4-25 (left) shows that the depth loss for bars in the transversely cracked specimens was higher at the beginning of testing and decreased over time to less than 20 μm . However, the total depth loss of the 1 – 1.5 inches corroded area at the end of 450 days testing showed that up to 160 μm was loss, Figure 4-25 (right). The CGR bars have Zn thickness less than this, and regions around the bars with lesser coating will be more affected by this zinc loss.

In terms of corrosion potentials, the galvanized specimens showed similar range of values which were far more negative than those of black bars, emphasising the need for a different potential guideline than ASTM C876. To characterize the corrosion potential of the galvanized specimens, the passive potential values are in the range of -300 – -380 mV vs SCE, with the HDG bars being at the more positive end. These values are far more positive than those observed by both Moreno and Sagues [64], which is between -425 – -525 mV vs SCE, and Bautista and Gonzalez [45], which is between -535 – -675mV vs SCE (Figure 4-26). Furthermore, the values are also more positive than those from the NRC [51] test at 65 weeks for the 100% R.H concrete specimens (Figure 4-26).

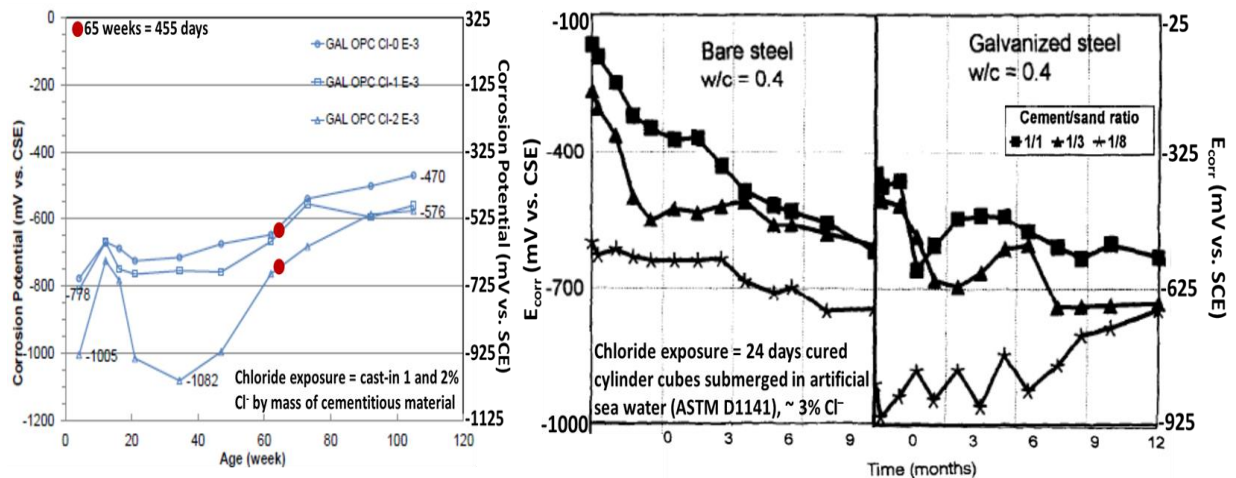


Figure 4-26: Corrosion potential (E_{corr}) of galvanized steel in OPC concrete with cast in chloride kept at 100% R.H. [51] (left) and OPC concrete submerged in artificial sea water [45] (right). Note: cement/sand ratio of 1/3 is similar to one used in the present work.

There are two important things to note about the potential values reported above: the values from the present test are averages from five replicates (individual values summarized in Table 4-5),

while the above values from NRC are different (more negative) from those stated in their potential guideline, Table 2-5, for 90% probability of passive corrosion. This is because the potential guideline recommended by [51] is developed from statistics carried out on potential values obtained from 50 to 100% R.H and 25 to 40°C temperature concrete conditions. In other words, the potential values obtained from the 100% R.H. concrete is specific to that exposure condition which is similar to the saturated concrete conditions in the current project. On the other hand, the potential values in the guideline are more general and considers lower R.H. concrete, in which case will result in more positive potential values as reported.

Table 4-5: Corrosion potential values of the bars in cracked and non-cracked concrete after 450 days' exposure to brine containing 21% Cl⁻.

Specimen (vs SCE)	Sound		Transverse		Longitudinal	
	potential range (mV)		potential range (mV)		potential range (mV)	
C1	-313	-357	-445	-686	-443	-647
C2	-299	-379	-440	-534	-381	-488
C3	-266	-382	-389	-670	-415	-471
HDG	-264	-353	-345	-449	-371	-529
Black	-67.1	-97.1	-241	-346	-451	-511

Furthermore, in the active state, i.e. both the transversely- and longitudinally- cracked concrete, the average potential values after 450 days are in the range of -320 to -520 mV vs SCE. The ranges of individual specimens are also shown in Table 4-5. These potential values, even with 21% chloride exposed to the crack, are more positive than those obtained on 100% R.H. concrete from NRC, which were between -550 and -650 mV vs SCE at 455 days for the 1 and 2% admixed chloride respectively, Figure 4-28. Even if potential values in Figure 4-26 [45] were considered active, the values from the present work are still more positive than those reported, despite being in cracked concretes exposed to higher chloride.

In general, if the average potential values measured from the present work were to be interpreted with the potential guideline 1 and 2 developed by NRC, one can see that even the non-corroded bars in the sound beam concretes showed more negative potential values than the suggested -260 mV vs SCE for > 90% probability of passive corrosion. Since this was not the case when the potentials were compared with similar concrete conditions from NRC test, it means that

potential guidelines for assessing galvanized steel should be related to concrete exposure condition (e.g. similar degree of saturation of the concrete). As such, a new potential guideline is recommended, Figure 4-27. In developing this guideline, as observed in the black bars (Table 4-5), some of the potentials from the cracked specimens fall in the uncertain region (between -125 and -275 mV vs SCE) of the ASTM C876 (Figure 1-1), despite visually observing corrosion on the bars. Similarly, in the galvanized bars, some of the potentials from bars in the cracked specimens are similar to those passive bars in the sound beam specimens, despite visually observing corrosion on the bars. As a result, the regions where they overlap is used to generate the “uncertain region” in Figure 4-27.

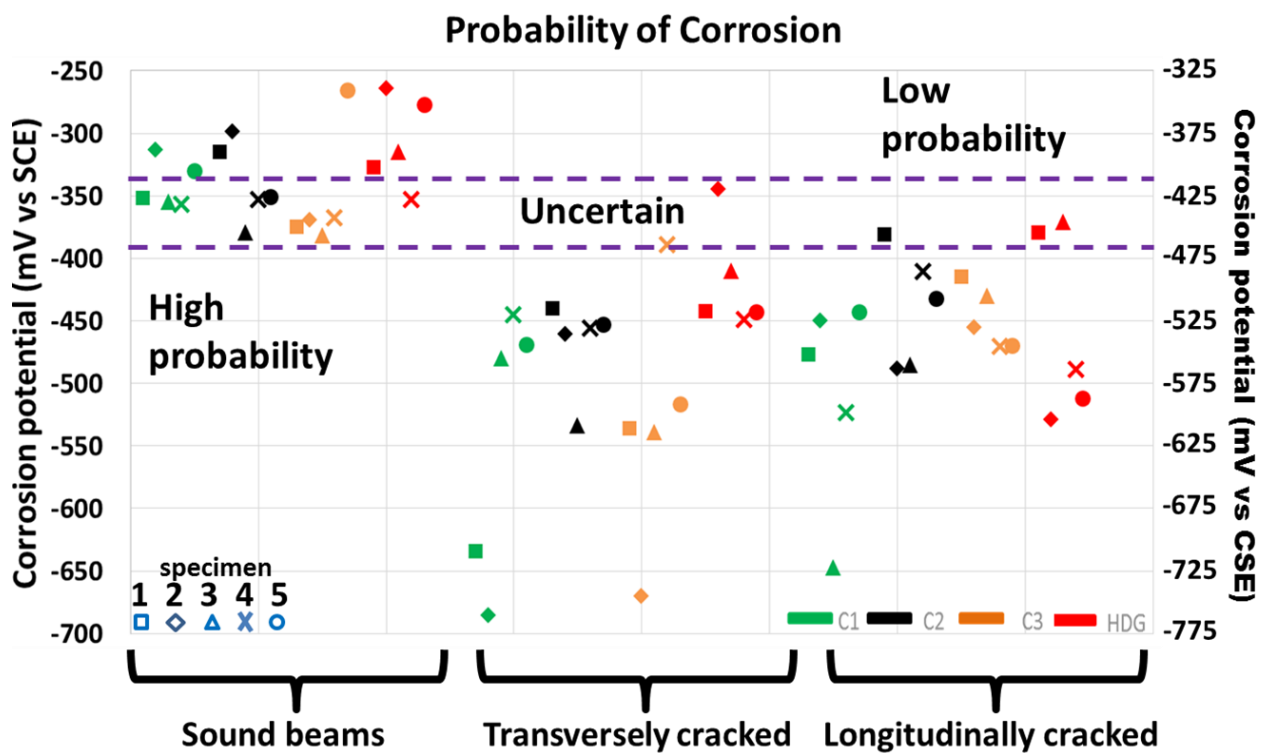


Figure 4-27: Potential guideline for assessing the probability of corrosion of galvanized steels in concrete.

In terms of exposure conditions, on comparing the potential values from the current work with those from the MTO [48] obtained on a ~30-year old bridge deck reinforced with galvanized steels, the influence of varying weather conditions (e.g. degree of saturation) of the field concretes on the corrosion potential values of the embedded bar is apparent. The potential values

measured by the MTO (Figure 4-24) were significantly more positive than those observed from both the current work (Figure 4-27) and even the NRC [51] (Figure 4-26). It is also interesting to see that even after delamination of the concrete and chloride threshold of black steel was reached, the potential values were still more positive than those observed in the present work. The author did not specify the relative humidity of the environment and degree of saturation of the concrete at the time of collection of these potential values.

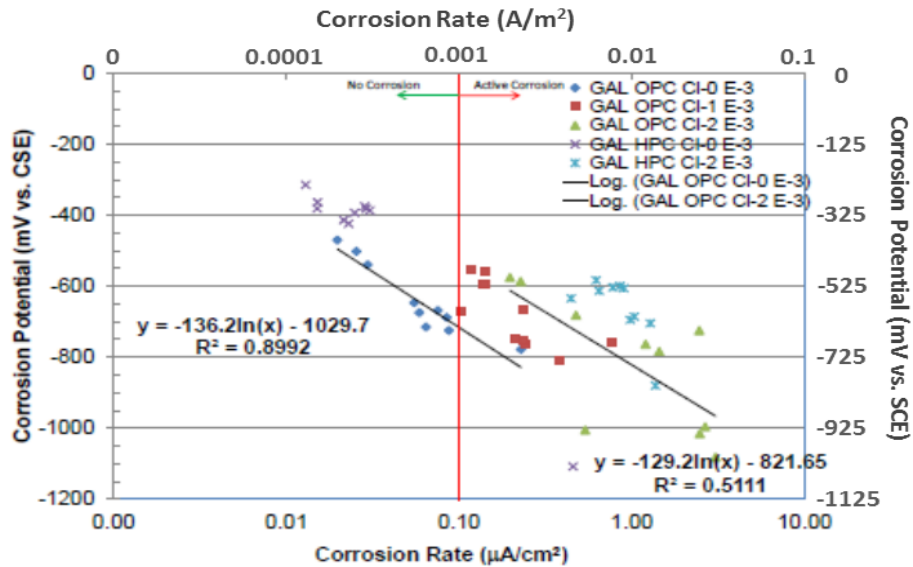


Figure 4-28: Correlation of corrosion- potential and rate of 100% R.H concrete [51].

Figure 4-28 is a scatter of the passive and active E_{corr} versus i_{corr} values from the NRC test obtained on the 100% R.H. concrete condition from week 1 to 105. One can see there is a general trend of more positive potential and lower corrosion rate over time in the passive state. The passive state values from the present work (Figure 4-29) compares very well with those in HPC concrete without chlorides in Figure 4-28. Again supporting the observations that chlorides had not reached the surface of the bars in sound concrete specimens. In the active state, no general trend is found in both Figure 4-28 and Figure 4-29; however lower i_{corr} values and more positive potentials can be seen in the latter. When the corrosion current values were divided by the corroded area (Figure 4-30), the i_{corr} range is similar to those of Figure 4-28.

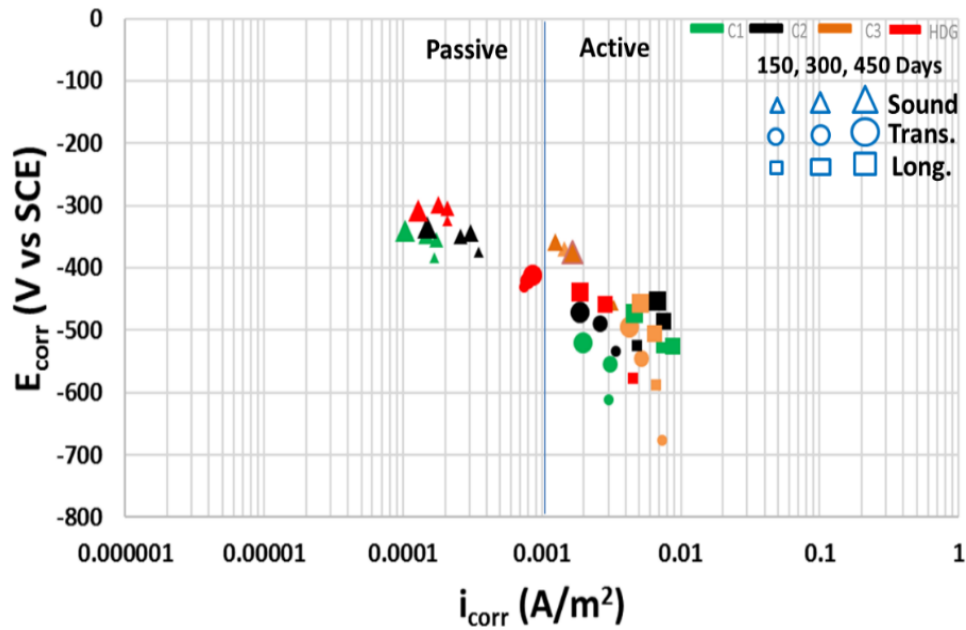


Figure 4-29: Correlation of corrosion- potential and current density (averaged over the entire exposed rebar area) at 150, 300 and 450 days of exposure to brine solution.

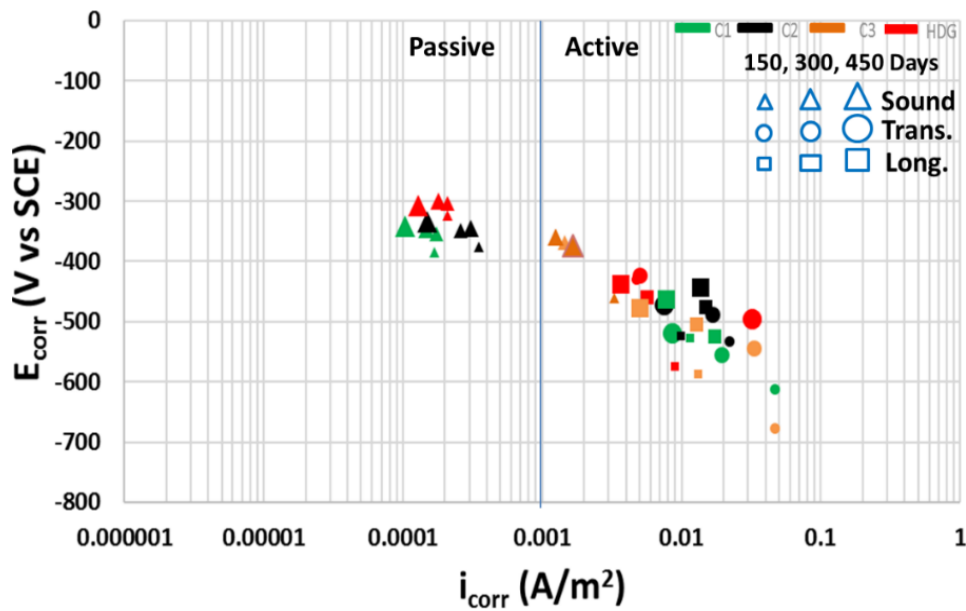


Figure 4-30: Correlation of corrosion- potential and current density (averaged over the entire corroded rebar area) at 150, 300 and 450 days of exposure to brine solution.

4.5. Observations during electrochemical testing

The galvanostatic pulse (GP) and linear polarization resistance (LPR) techniques, being among the most widely used electrochemical techniques for assessing reinforced concrete, can determine the resistance of the concrete specimen. However, the GP technique can easily determine the concrete resistance because it employs transient response in the system. This may largely be due to the fact that recovery of current (applied by GP) is faster after breakdown/drop when compared with voltage. Marcotte [66] found when passivated stainless steels (304L, 316L and 2205) surface were scratched while immersed in synthetic pore solution, there was an almost immediate recovery of the corrosion current, while it took longer time for the potential to recover, Figure 4-31.

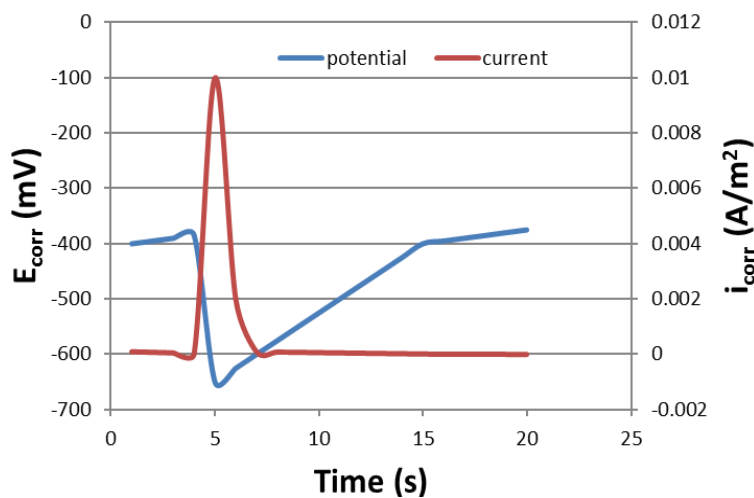


Figure 4-31: Recovery time for potential and current controlled system [66].

However, the concrete resistance obtained from this test may be semi-quantitative, especially in concretes containing macro-cracks. For example, when concrete resistance was measured in a particular type of cracked specimen (e.g. transversely cracked) cast with the same concrete mixture design, the values were found to be within a range. The inhomogeneity of concrete may be insufficient in explaining this behaviour, therefore it is suggested that the side of the cracked concrete being measured is a major influence. In other words, when running a test for sets of reinforced concrete specimens, the system can take a measurement from the cracked section (where the rebar is directly exposed) of one replicate specimen, and measure from behind, where there is no crack, for another replicate specimen. In the former, concrete resistance will be lower

compared to the latter with a significantly higher value. It is also possible for this behaviour to occur in a single specimen type (e.g. replicate number 2 of HDG reinforced concrete). That is, if previous measurements on that specimen are taken from the non-cracked region and, a new measurement is taken from the region containing the macro-crack, the concrete resistance over time will show significant drop. Thus, concrete resistance values obtained from a GP test on cracked concretes should be carefully interpreted.

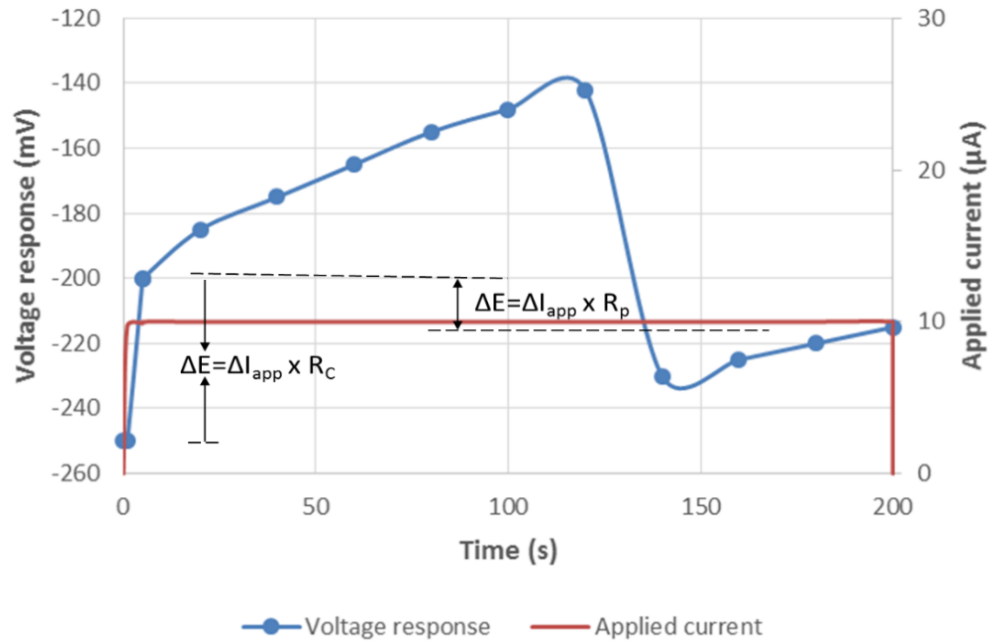


Figure 4-32: Outlier in a galvanostatic pulse weekly test.

The side of a cracked concrete measured can sometimes also result in outlier in polarization curves obtained from the GP measurements. For example, if electrons/ions from the C.E travels through the non-cracked region in the concrete specimen to polarize the rebar, and then suddenly finds a shorter path (i.e. cracked region) to the rebar, the polarization value will drop drastically, having being significantly higher. This drop will result in a negative polarization resistance value when calculated, further resulting a negative I_{corr} value, Figure 4-32. This behaviour could be managed by plotting the individual graphs at the end of the test to determine where the drop is experienced. The points at the end of the curve, after attaining steady state and before the drop, can then be picked for calculation.

Chapter 5 Summary and Conclusion

5.1. Influence of cracks in concrete

The sound (non-cracked) concrete beams have yet, after 450 days of exposure to brine, to produce any electrochemical data that indicates initiation of corrosion. This was also confirmed from the two of the five replicate specimens autopsied after a year. This indicates there is slow chloride diffusion through the concrete beams so that even the low chloride threshold of black steel has not been surpassed. Such low chloride diffusion behaviour can be attributed to the excellent quality of the concrete due to both the controlled casting conditions and increased curing time which limits the number of interconnected pores through which chlorides travel from the concrete ponding well.

To emphasize the influence of cracks, the transversely- and longitudinally- cracked specimens were continuously exposed to brine solution. The effect of the cracks was clearly evident, as the electrochemical results suggest all specimens under both crack conditions started to actively corrode almost immediately. After specimens were autopsied, the direct effect of the crack could be physically seen as corrosion initiated only in the cracked regions, but propagated laterally along the rebar surface for a few cm. However, in some cases, transversely cracked specimens, corrosion also propagated around the circumference of the bar, probably due to the crack extending beyond the bar. In the longitudinally cracked specimens, more of the Zn coating is lost through corrosion in the wider cracked area of the concrete prism than in the sections adjacent to narrower cracks. In general, the influence of cracks in concrete should not be overlooked when developing a life cycle cost or service life model for any structure.

5.2. Behaviour of the coatings

From this laboratory assessment, HDG coating provided approximately ten times better “corrosion performance” than conventional black steel in the cracked concrete exposed to 21% chloride, which agrees with the laboratory examination from NRC [51]. Although field evaluation from MTO [48] also showed “marginally” better performance of the HDG rebar relative to black steel and, some delamination in an HDG reinforced concrete structure. Corrosion performance in the present work has been defined to exclude time to corrosion initiation on the tested rebar.

Furthermore, the thinner Zn coated bars, C1 and C2, provided approximately three to five times better corrosion performance than conventional black steel in the active state, but showed similar behaviour as HDG in the passive state. These galvanized bars may be considered the next option after HDG steel for reinforcement, but provide an advantage during forming (e.g. bending) because of their ductile coating.

Unfortunately, coatings similar to the C3 bar do not seem to provide significant advantage over conventional black steel in both passive and active state. In fact, the rebar displayed an order of magnitude higher passive corrosion current density value than other galvanized steels, which was similar to black steel. In the active state, the behaviour of the bar was suggested (from the concrete resistance values, wet and overflowed corrosion products observed in the autopsied concrete) to be affected by the higher aluminum content in the coating, as its corrosion products causes the rebar to lose bond with adjacent concrete. In the long term, a bonding problem of the bar may result in delamination of the concrete, which is often the problem associated with using conventional black steel. Thus, when considering a type of galvanized bar for reinforcement, one similar to C3 may not be the best option judging by its behaviour in 21% chloride environment.

In general, coating thicknesses of all tested galvanized bars were highly non-uniform and, in worse cases; the coatings were so thin in some regions of the bar that it was not detectable. The regions with less coating loses the zinc faster and, as mentioned by [45], once corrosion is initiated on galvanized steel, all of the Zn can be lost in five years, but in the case of non-uniformity of the coating, perhaps less. Thus, coating uniformity in all of the galvanized bars is essential for better and consistent performance of galvanized steel in concrete.

5.3. Corrosion potential characterization

To characterize the potential values for the galvanized steels, the passive potential for all galvanized rebar grades at the end of the present test were between -266 and -382 mV, with HDG and C3 bar at opposite end respectively. This falls in the “uncertain and 70% probability of passive corrosion” region of the potential guidelines from NRC, but all bars showed no active corrosion from the electrochemical result and autopsy. On the other hand, the active potential values for all tested galvanized rebar from the present work is between -345 and -686 mV, with HDG and C3 bar again at opposite end respectively. These lie in the “uncertain and 70%

Summary and Conclusion

probability of active corrosion” regions, respectively of the NRC guidelines, but all bars showed (after autopsy) active corrosion. Thus, a different potential guideline is generated from this study.

Despite the attempt to replicate field scenario in this laboratory test by using similar salt solution and considering cracks, there is still gap in assessment due to more stable and varying weather condition of the laboratory and field atmosphere, respectively. Nonetheless, with respect to other corrosion resistance rebar like stainless steels, galvanized steel is better for reinforcement in concrete exposed to moderate chloride environment and/or subject to carbonation because of its price point and durability provided due to its soluble corrosion products.

Chapter 6 Recommendation

6.1. Recommendations for application of the experimental results

The experimental results have demonstrated that galvanized reinforcing bars performed better than the conventional black steel. The extent to which they outperform black steel in this work is dependent upon their coating composition, coating thickness and uniformity, and concrete quality (cracked or non-cracked). As a result, the author recommends to the producer of the bars that thicker and more uniform coating should be added to the CGR, to at least stand a chance to show similar performance as the conventionally hot-dipped galvanized steels. Furthermore, the aluminum content in the coating should be sufficient enough to produce a continuous and crack-free inhibition layer in the coating. That being said, processing parameters should also be optimized to prevent the outburst of this layer. In addition, since the values from the present work are mostly lower than those found by other authors, despite exposing the bars to significantly higher chlorides, additional service life can be obtained from a CGR if used in a moderate to less severe chloride environment and in concrete containing lesser cracks. In general, optimum quality control in the production of any of the galvanized coatings is recommended to ensure better performance.

As a result of the gap between the potential values from a specific concrete exposure condition and a general potential guideline, a more realistic guideline is recommended. At the very least, more test needs to be performed on different exposure conditions to examine the ranges of passive and active potential values. Furthermore, Zn coatings containing significant amount of other elements, such as aluminum, may require separate potential guidelines for assessment. This is because the potential values of the C3 specimens were mostly found to be more negative compared with HDG steel containing little to no Al. With respect to the use of guideline 2 developed by NRC, the age of the structure may affect the middle range of potential values developed in the guideline.

6.2. Recommendations for Future Research

The present work could be improved upon to enhance the value of results obtained from this relatively long term testing. For the most part, the experimental design set up parameters like wet

curing time and concrete crack width, and the use of lower chloride content to obtain time to corrosion initiation are the major highlights worth mentioning.

The tested concrete specimens were wet cured (with daily soaked burlap) for 14 days and subsequently exposed to laboratory atmosphere for another 45 days before exposure to brine solution. Compared with the 4 days minimum wet curing adopted in the field for roads and bridges, specified by clause 904.07.10 of the Ontario Provincial Standard and Specifications for, the extended concrete cure time would have exaggerated the corrosion performance of the reinforced bars. In other words, it may have also been possible to get the non-cracked concrete beams to corrode had the increased cure time not decrease the chloride diffusivity into the concrete.

The concrete specimens had large variance in crack width due to the brittle nature of concrete. However, with better control of the equipment and limiting the loading rate based on crack displacement, a more uniform and consistent crack width can be achieved in a specimen and across replicate specimens respectively.

Time to corrosion initiation was not estimated in the present work because of the high percentage of chloride solution the specimens were exposed to. Although the objectives of using the brine solution employed in the present work were very clear, a relatively smaller experimental setup that uses lower chloride content is recommended to be included in future test to obtain a time to corrosion initiation on the bars. This will enable one to know the corrosion resistance of the bars, so that an actual “service life of the bar” may be estimated.

References

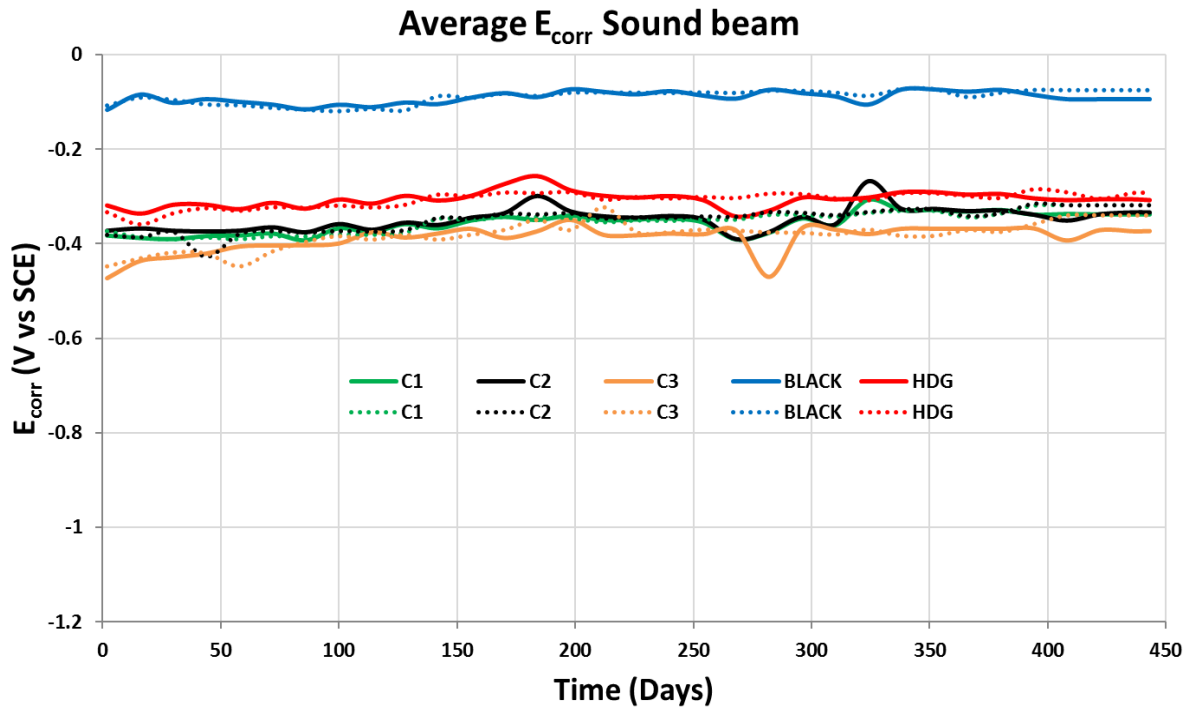
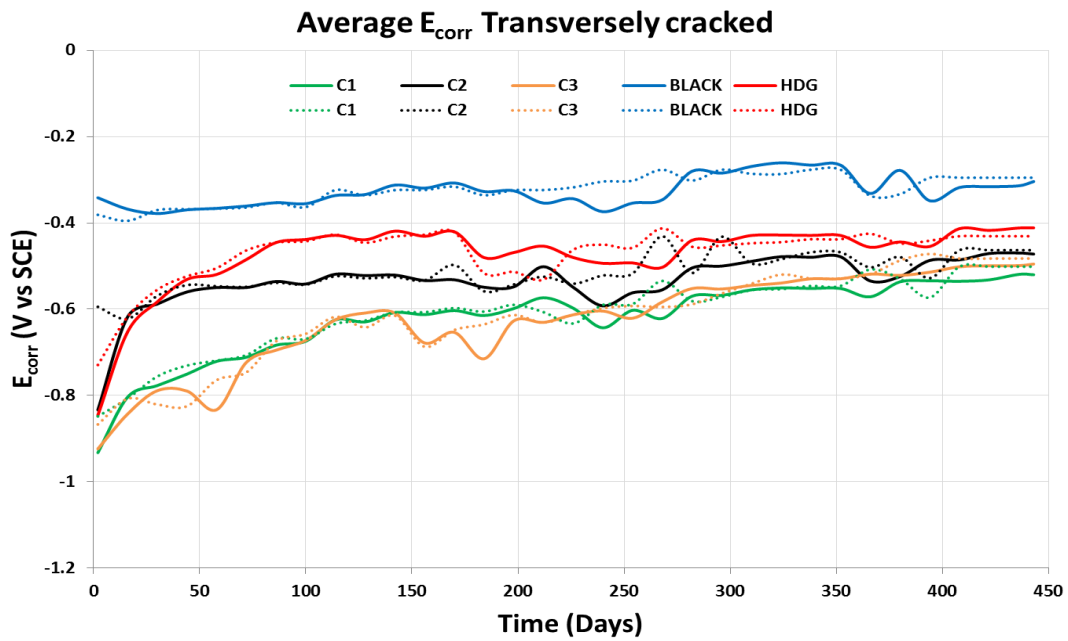
1. C.M. Hansson, B. Sørensen, The Threshold Concentration of Chloride in Concrete for the Initiation of Reinforcement Corrosion. *Corrosion Rates of Steel in Concrete*, 1990, ASTM, Philadelphia, PA: pp. 3-16.
2. C.M. Hansson, Comments on Electrochemical Measurements of the Rate of Corrosion of Steel in Concrete. *Cement and Concrete Research*, 1984, 14(4): pp. 574-584.
3. T.P. Hoar, The Production and Breakdown of the Passivity of Metals. *Corrosion Science*, 1967, 7: pp. 341-355.
4. M. Pourbaix, *Atlas of Electrochemical Equilibria in Aqueous Solutions*. NACE: Houston, TX, 1984.
5. C.M. Hansson, A. Poursaei and S. J. Jaffer, "Corrosion of Reinforcing Bars in Concrete," Waterloo, 2007 PCA R&D Serial No. 3013
6. C. M. Hansson, A. Poursaei, et al. (2006). "Macrocell and microcell corrosion of steel in ordinary Portland cement and high performance concretes." *Cement and Concrete Research* **36**(11): pp. 2098-2102.
7. Marcus et al., Localized corrosion (pitting): "A model of passivity breakdown including the role of the oxide layer nanostructure." *Corrosion science*, Volume 50, Issue 9, September 2008, pp. 2698–2704.
8. T.D. Marcotte, Characterization of Chloride-Induced Corrosion Products that Form in Steel-Reinforcement Cementitious Materials. PhD Thesis in Dept. of Mechanical Engineering, 2001, University of Waterloo: Waterloo, ON, Canada: p. 330.
9. M. Yunovich, N. G. Thompson, et al. (2001). Appendix D - Highway Bridges. *Corrosion Costs and Preventive Strategies in the United States*. G. H. Koch, M. P.H.Brongers, N. G. Thompson, Y. P. Virmani and P. D. Joe H. Payer. CC Technologies Laboratories Inc, Dublin, Ohio, Federal Highway Administration.
10. O. Kayali, S.R. Yeomans, Bond of galvanized steel in concrete. *Cement and Concrete Composites*, 2000. **22**(6): pp. 459-467.
11. K. Basham, "Choices in Corrosion-Resistant Rebar: A Comparison of the Features, Performance, and Costs of Five Rebar Options," *Concrete Construction*, 1 October 1999.
12. Galvanizing, C. Custom Hot Dip Galvanizing. 2003 [cited 2014 March 13].
13. S. R. Yeomans, Galvanized Steel in Concrete, in *Galvanized Steel Reinforcement in Concrete*, S. R. Yeomans, Ed., Elsevier, 2004, pp. 8.
14. Macias, A. and C. Andrade, Corrosion of galvanized steel in dilute Ca(OH)₂ solutions (pH 11.1–12.6). *British Corrosion Journal*, 1987. **22**(3): pp. 162-171.
15. C. Andrade and C. Alonso, Electrochemical Aspects of Galvanized Reinforcement Corrosion, in *Galvanized Steel Reinforcement in Concrete*, S. R. Yeomans, Ed., Oxford, 2004, pp. 111-144.
16. Z. Q. Tan and C. M. Hansson, "Effect of Surface Condition on the Initial Corrosion of Galvanized Steel Embedded in Concrete," *Corrosion Science*, vol. 59 (9), pp. 2512-2522, 2008.
17. S.R. Yeomans, *Applications of Galvanized Rebar in Reinforced Concrete Structures*. 2001, National Association of Corrosion Engineers; Houston, TX, USA.

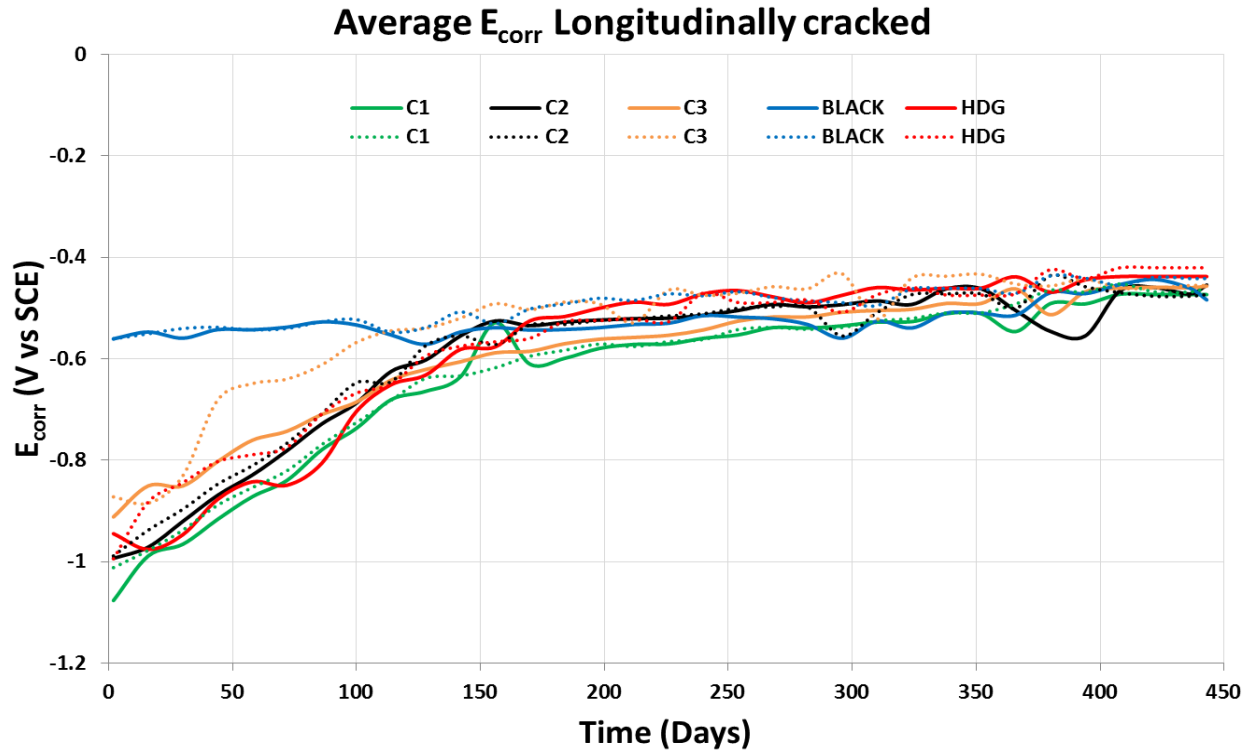
18. A.R. Marder, The metallurgy of zinc-coated steel. *Progress in Materials Science*, 2000 (45): pp. 191-271.
19. Z.Q. Tan, The Effect of Galvanized Steel Corrosion on the Integrity of Concrete, in *Mechanical and Mechatronics Engineering*. 2007, University of Waterloo: Waterloo, Ontario.
20. Z.Q. Tan and C.M. Hansson, Effect of surface condition on the initial corrosion of galvanized steel embedded in concrete, *Corrosion Science*, 2008, 59(9), pp. 2512-2522.
21. C.E. Jordan, Marder AR. Fe-Zn phase formation in interstitial-free steels hot-dip galvanized at 450°C, Part I 0.00 wt% Al±Zn baths. *J Mater Sci* 1997; pp. 32:5593.
22. D. Horstman, Formation and growth of iron±zinc alloy layers. In: *Proceedings of 14th International Hot Dip Galvanization Conference*. London: Zinc Development Association, 1986. pp. 61.
23. J. Mackowiak, Short NR. Metallurgy of galvanized coatings. *Int Met Reviews* 1979;1.
24. C. Allen, Mackowiak J. *J Inst Met* 1962: 3 pp. 91:369.
25. M. Onishi, Y. Wakamatsu, H. Miura, Formation and growth kinetics of intermediate phases in Fe-Zn diffusion couples. *Trans JIM* 1974; pp. 15:331.
26. Y. Hisamatsu, Science and technology of zinc and zinc alloy coated steel sheet. In: *GALVATECH '89*, Tokyo: The iron and Steel Institute of Japan (ISIJ). 1989. p. 3.
27. J.J. Sebesty, G.E. Ruddle, Hydrogen-atmosphere galvanizing of iron-base alloys, Research Report No. R 255. Ottawa: DOE, Mines Branch, 1972.
28. J.A. Elias, R.E. Hook, Interstitial free sheet steel applications and performance, SAE Paper No. 720018, 1972.
29. A.R. Marder, Zinc coating of interstitial-free steel sheet. In: *Proceedings of Conference on Interstitial-Free Steel Sheet: Processing, Fabrication and Properties*. Ottawa: Metallurgical Society of CIM, 1991. Pp. 157.
30. T.J. Langill, B. Dugan, Zinc Materials for Use in Concrete, in *Galvanized Steel Reinforcement in Concrete*, S.R. Yeomans, Editor. 2004, Elsevier. pp. 87-109.
31. M. Guttman, Y. Lepretre, A. Aubry, M-J. Roche, T. Moreau, P. Drillet, J.M. Maigne, H. Baudin, Mechanism of the galvanizing reaction. Influence of Ti and P contents in steel and of its surface microstructure after annealing. In: *GALVATECH '95*. Chicago, IL: Iron and Steel Society, 1995. pp. 295.
32. K. Osinski, The influence of aluminum and silicon on the reaction between iron and zinc. Doctoral Thesis. Technical University, Eindhoven, 1983.
33. P. Perrot, J-C. Tissier, J-Y. Dauphin, Stable and metastable equilibria in the Fe-Zn-Al system at. *Z Metallkde* 1992; pp. 83:111
34. N-Y. Tang, G.R. Adams, P.S. Kolisnyk, On determining effective aluminum in continuous galvanizing baths. *GALVATECH '95*. Chicago, IL: Iron and Steel Society, 1995. pp. 777.
35. N-Y. Tang, Thermodynamics and kinetics of alloy formation in galvanized coatings. In: *Zinc-based steel coating systems: production and performance*. Goodwin FE, editor, Warrendale, PA:TMS, 1998. pp. 3.
36. J. Faderl, M. Pimminger, L. Schonberger, Influence of steel grade and surface topography on the galvannealing reaction. *GALVATECH '92*. Amsterdam: Stahl and Eisen, 1992. pp. 194.

37. N.Y. Tang, Modeling of enrichment in galvanized coatings. *Met Mater Trans* 1995; 26A: pp.1669.
38. C. Andrade, C. Alonzo, Electrochemical Aspects of Galvanized Steel, in *Galvanized Steel Reinforcement in Concrete*, Yeomans S.R., Editor. 2004, Elsevier. pp. 111-143.
39. M. Isobe, Initial alloying behavior in galvannealing process. *CAMP-ISIJ* 1992; 5: pp. 1629.
40. T. Kato, K. Nunome, Y. Morimoto, K. Nishimura, N. Kato, H. Saka, In situ TEM observations of reaction between Fe and molten Zn(Al). *GALVATECH '98*. Tokyo: The Iron and Steel Institute of Japan, 1999. pp. 803.
41. C.E. Jordan, A.R. Marder, Effect of phosphorous surface segregation on iron±zinc reaction kinetics during hot-dip galvanizing. *Met. Mater. Trans.* 1997;28A: pp. 2695.
42. C.E. Jordan, A.R. Marder, The effect of substrate grain size on Fe-Zn reactions during hot-dip galvanizing. *Met. Mater. Trans.* 1997;28A: pp. 2683.
43. C.E. Jordan, A.R. Marder, Inhibition layer break down and outburst Fe-Zn alloy formation during galvanizing. In: Goodwin FE, editor. *Zinc-based steel coating systems: production and performance*. Warrendale, PA: TMS, 1998. pp. 115.
44. J.P. Broomfield, "Corrosion of Steel in Concrete Understanding, Investigation and Repair.", E & FN Spon, London and New York, (1998).
45. A. Bautista, and J.A. González, Analysis of the protective efficiency of galvanizing against corrosion of reinforcements embedded in chloride contaminated concrete. *Cement and Concrete Research*, 1996. **26**(2): pp. 215-224.
46. E.F. Goodwin, New Solution/Application Continuous Galvanized Rebar, IZA International Galvanizing Conference and Exhibition, Delhi, India, 2014.
47. International Zinc Association (IZA), Continuous Galvanized Rebar Brochure, Second Revision, 2015.
48. F. Pianca and H. Schell, "The Long Term Performance of Three Ontario Bridges Constructed with Galvanized Reinforcement", International Bridge Conference, Pittsburgh, PA, USA. 2005.
49. J.L. Kepler, D. Darwin, C.E Locke Jr., "Evaluation of corrosion protection methods for reinforced concrete highway structures", Structural Engineering and Engineering Materials SM Report No. 58, 2000.
50. T. Rezanoff and D. Stot, "Durability of concrete containing chloride-based accelerating admixtures, *Can. J. Civ. Eng.* 17, 102- 112 (1990).
51. J. Zhang and B. Baldock, Condition Assessment and Corrosion Mitigation of Galvanized Steel Reinforcement in Concrete Structures, National research council of Canada (NRC), Report No. A1-000339.2, 2015.
52. M. Stern, and A.L. Geary, Electrochemical Polarization – A Theoretical Analysis of the Shape of Polarization Curves. *Journal of the Electrochemical Society*, 1957. 104(1): pp. 56-63.
53. C.J. Newton, and J.M. Sykes, A galvanostatic pulse technique for investigation of steel corrosion in concrete. *Corrosion Science*, 1988. 28(11): pp. 1051-1074.
54. C. Andrade and C. Alonso, Corrosion rate monitoring in the laboratory and on-site, *Construction and Building Materials*, 1996, vol. 10, pp. 315-328.
55. J.E.B. Randles, "Kinetics of Rapid Electrode Reactions", *Discussions of the Faraday Society*, 1947, vol. 1, pp. 11-19.

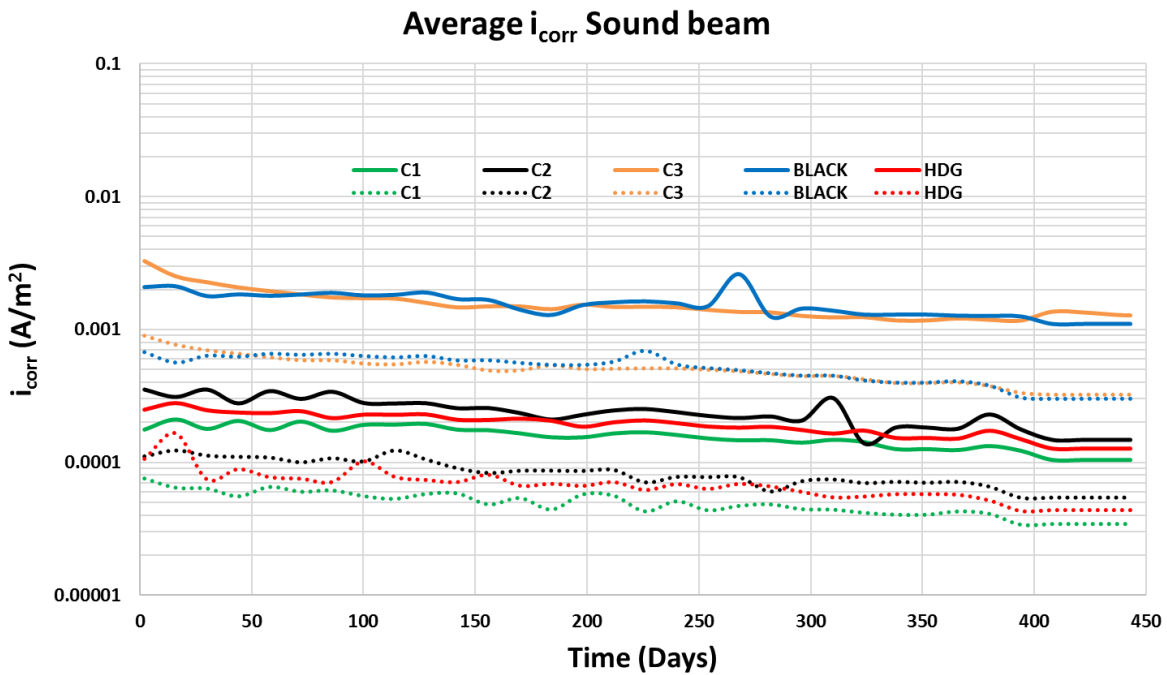
56. D.A. Jones, Principles and Prevention of Corrosion, second edition, Prentice Hall, Englewood Cliffs, NJ (1996).
57. R. Scholtz and S. Uhlig, Introduction to X-Ray Fluorescence (XRF), Madison, Wisconsin: Bruker AXS GmbH, Karlsruhe, West Germany, 2006, pp. 10-11.
58. Ontario Provincial Standard Specification Provision 902, Construction Specification for Deck Joint Assemblies, Preformed Seals, Joint Fillers, Joint Seals, Joint Sealing Compounds, and Waterstops – Structures. 2008, OPSS.
59. Ontario Provincial Standard Specification Provision 904, Construction Specification for Concrete Structures. 2012, Ontario Provincial Standard Specification.
60. Ontario Provincial Standard Specification Provision 1002, Material Specification for Aggregates in Concrete. 2013, Ontario Provincial Standard Specification.
61. J. Goldstein. Scanning Electron Microscopy and X-Ray Microanalysis. Springer (2003): pp. 297-300.
62. <http://automotive.arcelormittal.com/europe/products/coatings/galfan/EN> [Accessed April 20, 2016].
63. C.B. Van Niejenhuis, The Case for Stainless Steel Reinforcing Bars, in Civil and Environmental Engineering. 2015, University of Waterloo: Waterloo, Ontario.
64. E.I. Moreno and A.A. Sagüés (1996). “Performance of plain and galvanized reinforcing steel during the initiation stage of corrosion in concrete with pozzolanic additions.” Paper 326 Corrosion 96, NACE International Annual Conference and Exposition.
65. T.P. Cheng, J.T. Lee, K.L. Lin, and W.T. Tsai, Electrochemical Behavior of Galvanized Al—Zn Coatings in Saturated Ca(OH)₂ Solution, CORROSION—Vol. 47, No. 6, 1991, pp. 436 – 442.
66. T.D. Marcotte, Characterization of Chloride-Induced Corrosion Products that form in Steel-Reinforced Cementitious Materials, in Mechanical Engineering. 2001, University of Waterloo: Waterloo, Ontario.

Appendix A – Specimen averages for both GP and LPR

A1. Corrosion potential (E_{corr})Figure A1.1: Average E_{corr} Sound (non-cracked) concrete specimen.Figure A1.2: Average E_{corr} transversely cracked concrete specimen.



A2. Corrosion current density (i_{corr})



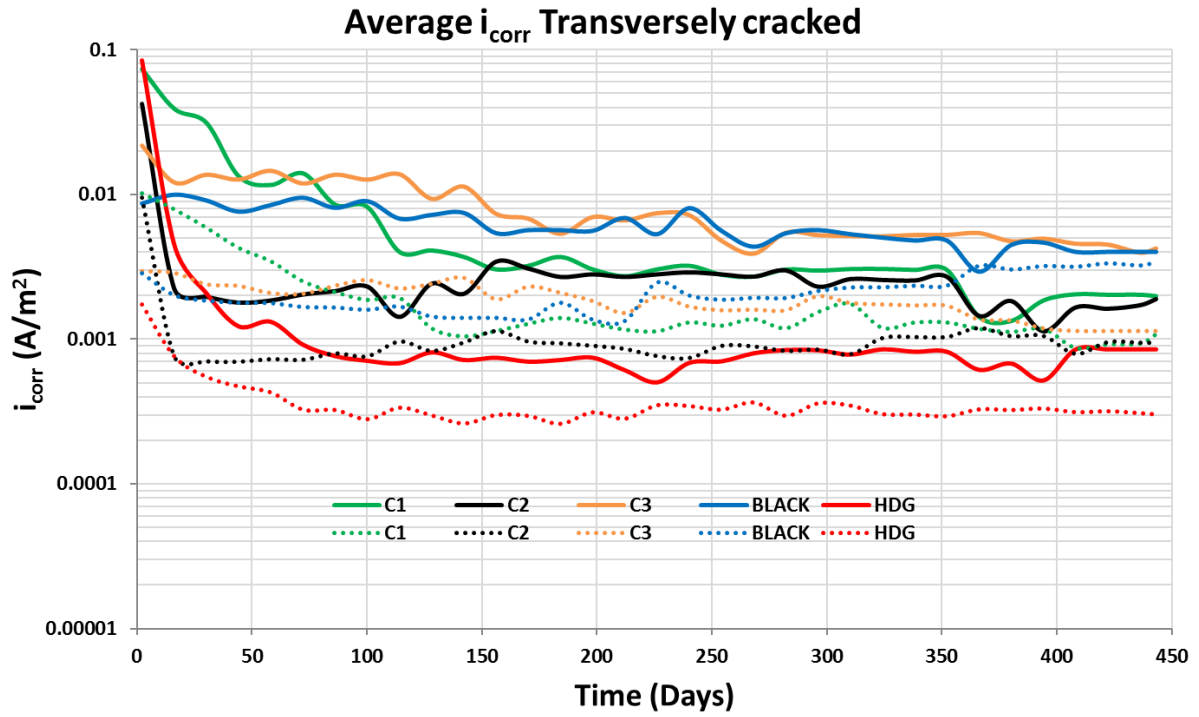


Figure A2.2: Average i_{corr} transversely cracked concrete specimen.

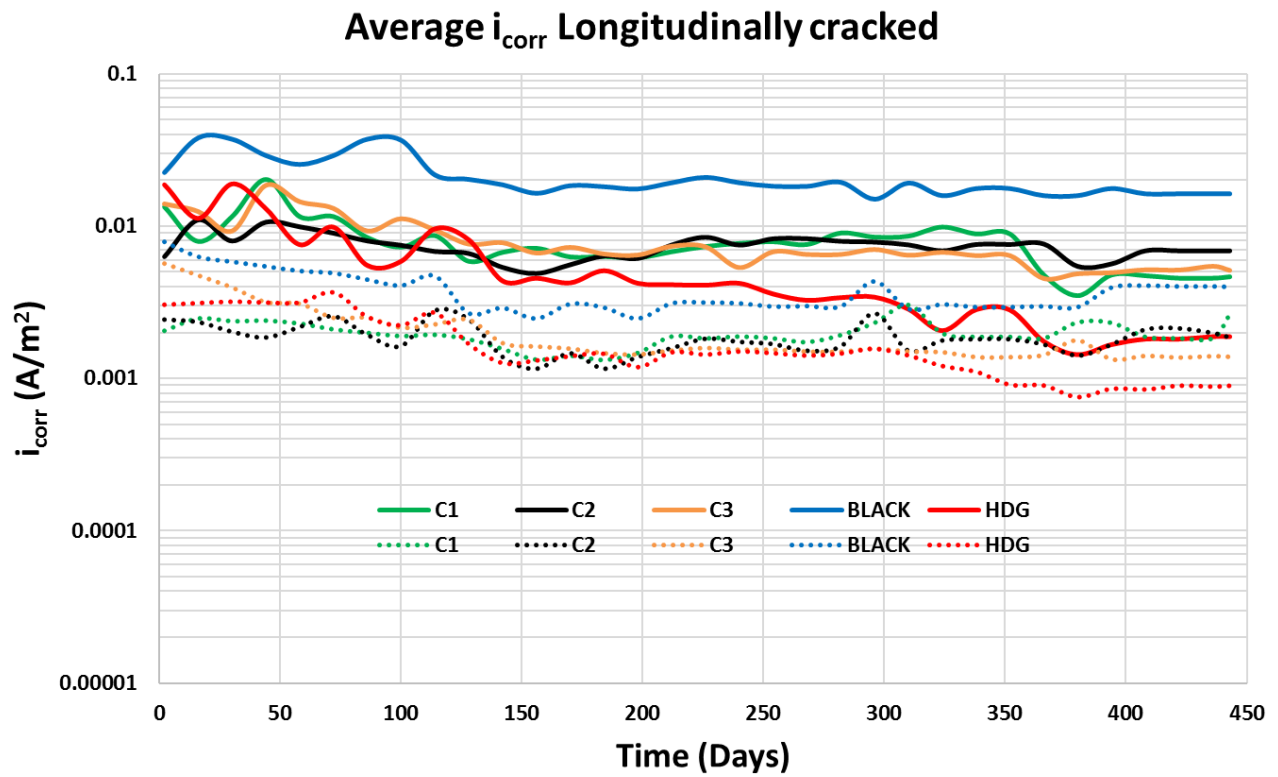


Figure A2.3: Average i_{corr} longitudinally cracked concrete specimen.

A3. Concrete resistance

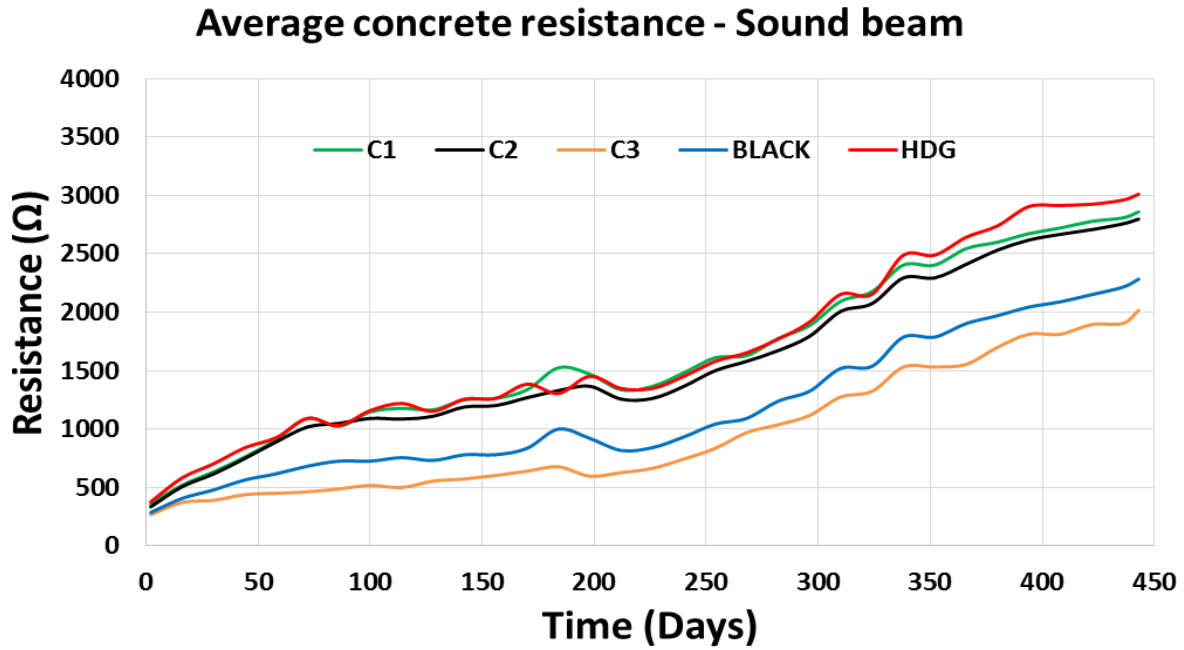


Figure A3.1: Average concrete resistance for Sound (non-cracked) concrete specimen.

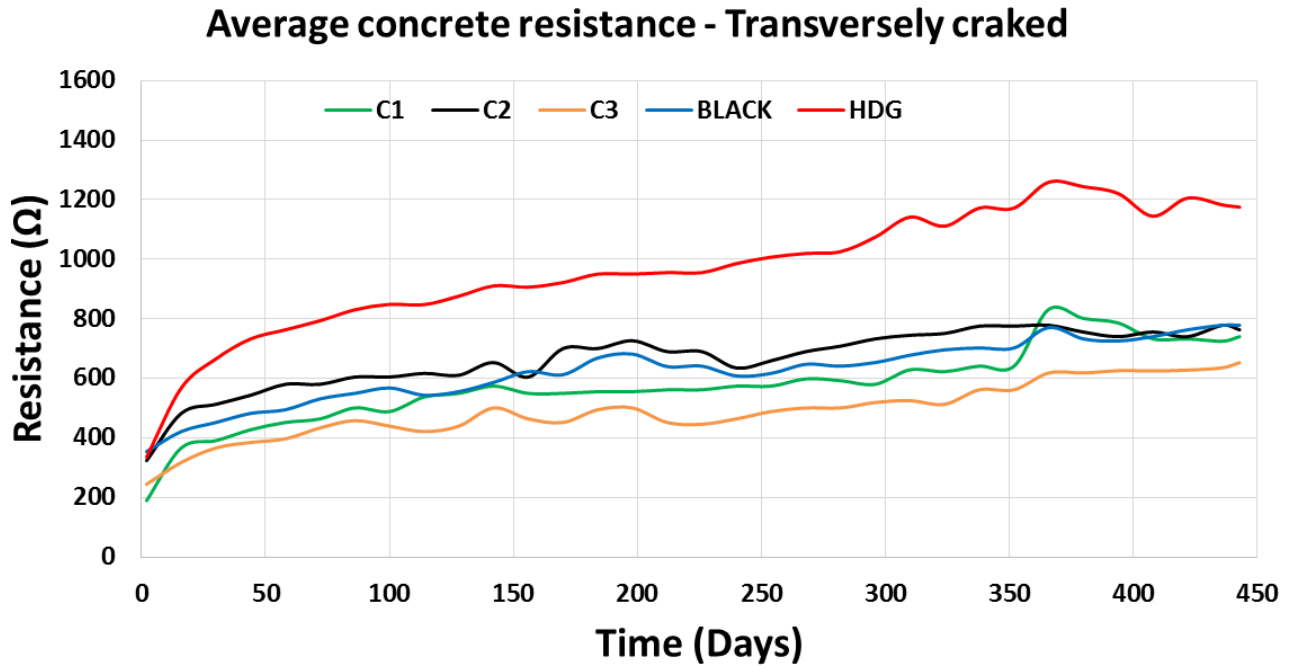


Figure A3.2: Average concrete resistance for transversely cracked concrete specimen.

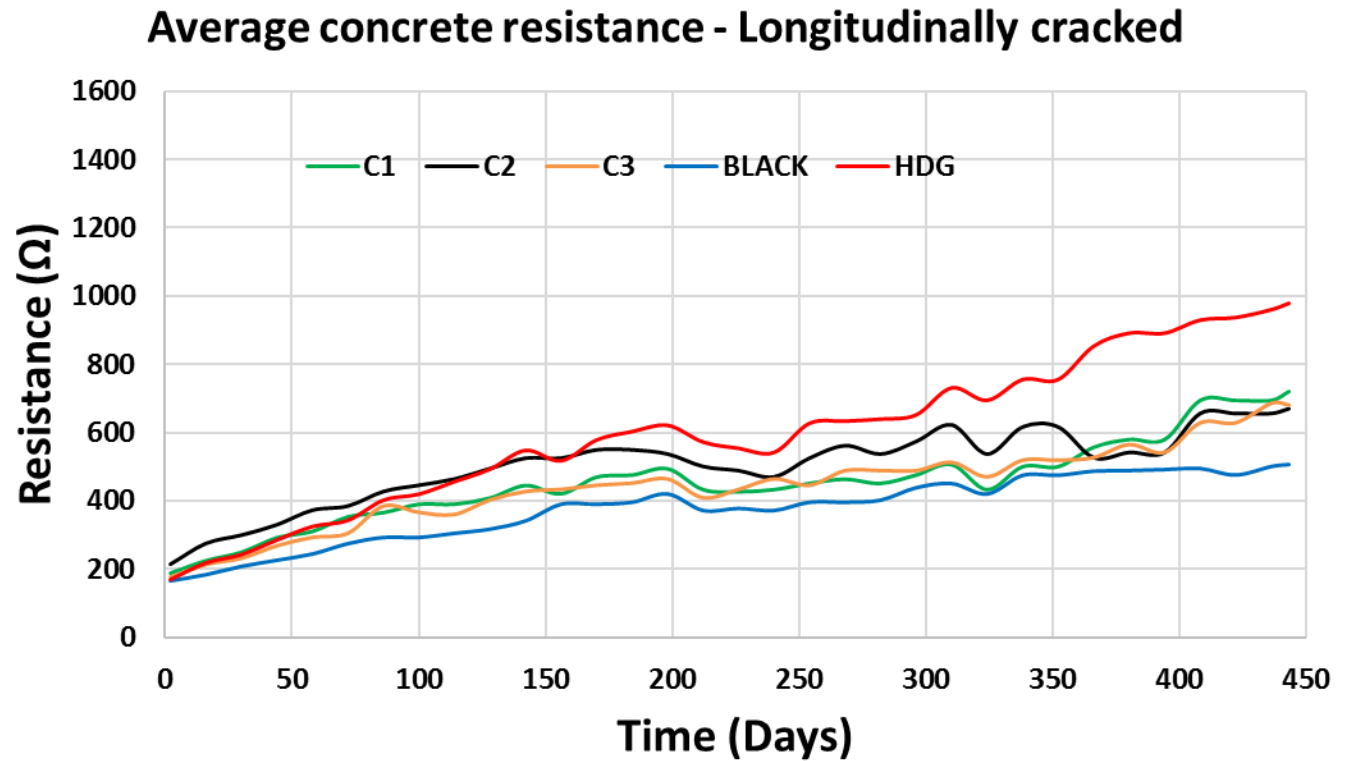


Figure A3.3: Average concrete resistance for longitudinally cracked concrete specimen.

Appendix B – Steel and concrete properties

B1. Steel weight, crack peak load, and crack width

Table B1.1: C1 steel weight, crack peak load, and crack width

C1	Transversely cracked			Longitudinally cracked			Sound
	Steel weight (kg)	Crack peak load (kN)	Crack width (mm)	Steel weight (kg)	Crack peak load (kN)	Crack width (mm)	Steel weight (kg)
1	282.25	25	0.5	284.91	51.4	0.2	280.43
2	283.91	36	0.5	281.52	53.01	0.15	282.87
3	285.24	16.1	0.12	281.6	49.99	0.18	279.73
4	280.67	15.4	0.26	279.3	52.6	0.23	283.33
5	283.26	18.1	0.2	282.1	41.9	0.2	282.82

Table B1.2: C2 steel weight, crack peak load, and crack width

C2	Transversely cracked			Longitudinally cracked			Sound
	Steel weight (kg)	Crack peak load (kN)	Crack width (mm)	Steel weight (kg)	Crack peak load (kN)	Crack width (mm)	Steel weight (kg)
1	279.17	17.8	0.2	279.43	51.7	0.14	276.97
2	276.84	17.7	0.25	279.72	47.6	0.25	276.25
3	279.33	15	0.2	278.89	63.5	0.14	275.43
4	279.02	15.5	0.13	277.56	51.7	0.2	277.53
5	278.55	16.6	0.2	277.59	51	0.2	276.37

Table B1.3: C3 steel weight, crack peak load, and crack width

C3	Transversely cracked			Longitudinally cracked			Sound
	Steel weight (kg)	Crack peak load (kN)	Crack width (mm)	Steel weight (kg)	Crack peak load (kN)	Crack width (mm)	Steel weight (kg)
1	278.81	6.07	0.3	277.67	89	0.25	280.25
2	274.62	7.92	1.5	277.07	55	0.2	275.23
3	277.17	6.55	0.3	274.96	59	0.15	276.74
4	280.31	10.5	0.2	277.8	53	0.15	279.64
5	277.87	6.49	0.25	276.4	87	0.2	277.72

Table B1.4: HDG steel weight, crack peak load, and crack width

HDG	Transversely cracked			Longitudinally cracked			Sound
	Steel weight (kg)	Crack peak load (kN)	Crack width (mm)	Steel weight (kg)	Crack peak load (kN)	Crack width (mm)	Steel weight (kg)
1	198.37	13	0.25	195.1	52.2	0.15	198.31
2	194.9	14.97	0.3	193.9	50.9	0.25	199.54
3	194	17.8	0.25	197.12	52.5	0.14	197.4
4	195.21	15	0.15	196.81	61.9	0.15	195.4
5	197.62	13.7	0.3	197.64	52.1	0.2	196.38
HDG new (Cast with C3 specimens)							
1	200.78	16.44	0.3	199.87	52	0.15	200.67
2	198.64	11.45	0.2	199.38	54	0.15	201.23
3	200.01	8.19	0.15	202.03	52	0.12	203.92

Table B1.5: Black steel weight, crack peak load, and crack width

Black	Transversely cracked			Longitudinally cracked			Sound
	Steel weight (kg)	Crack peak load (kN)	Crack width (mm)	Steel weight (kg)	Crack peak load (kN)	Crack width (mm)	Steel weight (kg)
1	244.55	13.6	0.15	243.72	49.3	0.25	243.89
2	247.12	14.2	0.13	247.32	50.8	0.2	245.64
3	245.18	15.4	0.26	244.3	61.4	0.14	245.44
4	244.18	20.7	0.24	243.68	54.5	0.12	246.02
5	244.02	13.35	0.15	242.82	45.8	0.25	243.05

B2. Compressive strength – individual concrete cylinder**Table B2.1: Compressive strength – individual concrete cylinder**

Days	Cylinder sample	Cast 1		Cast 2	
		Compressive strength (Mpa)	Average	Compressive strength (Mpa)	Average
7	1	29.5	30.1	43.57	43.3
	2	29.73		42.64	
	3	31.13		43.62	
14	1	29.9	30.7	47.52	44.4
	2	30.1		40.6	
	3	32.1		45.1	
21	1	39.83	38.9	47.16	47.8
	2	39.68		47.67	
	3	37.09		48.67	
28	1	40.5	40.0	49.88	48.5
	2	40.25		47.02	
	3	39.18		48.56	
56	1	42.12	43.4	56.63	55.6
	2	43.52		54.43	
	3	44.7		55.64	

B3. Pore solution recipe

Table B3.1: Simulated concrete pore solution

Compound	standard	To prepare	Unit
NaOH	12.8	5.27	g
KOH	44.9	18.48	g
CaSO4 * 2 H2O	1.38	0.57	g
Ca(OH)2 (excess amount)	5.71	2.35	g
H2O	2.43	1000	L
Mass of solution		1026.66	g

Appendix C – Electrochemical results

C1. E_{corr} for individual specimens

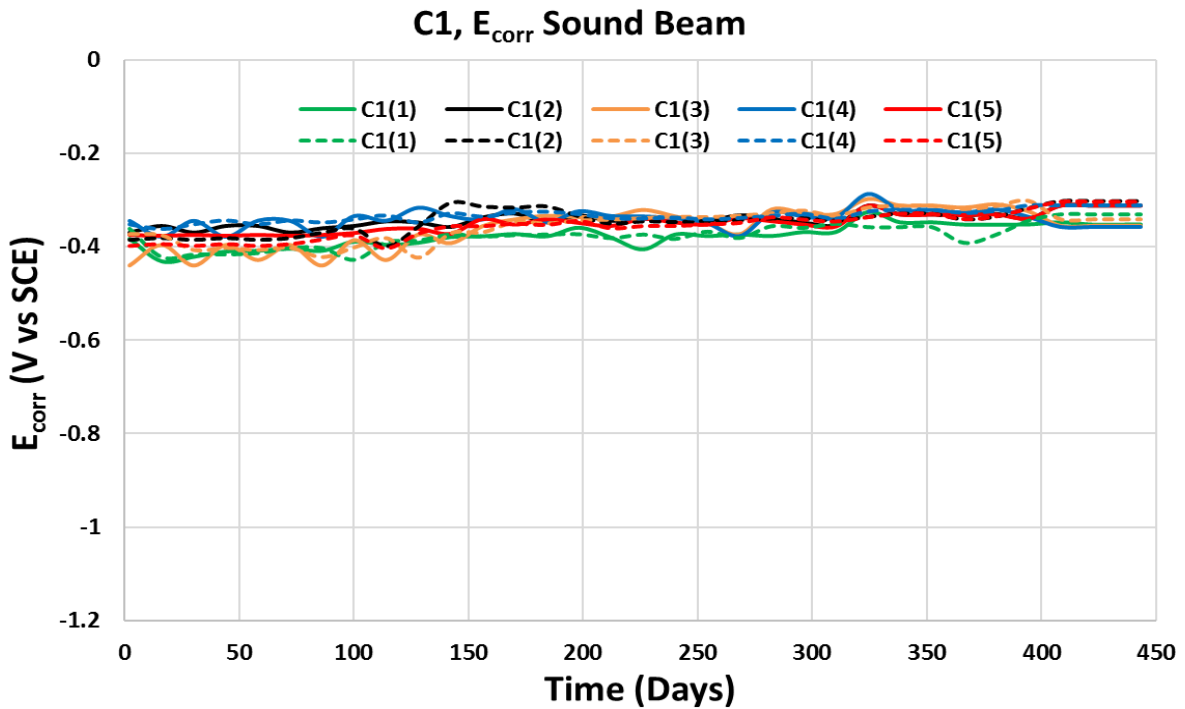


Figure C1.1: Sound (non-cracked) concrete beam.

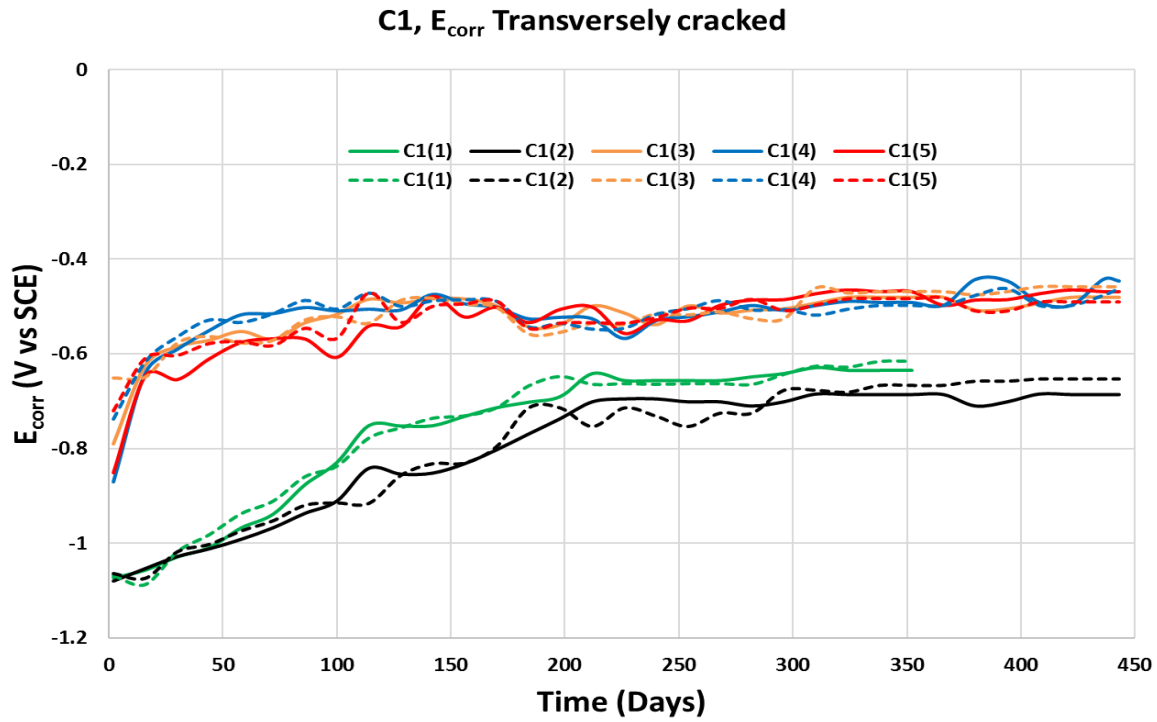


Figure C1.2: Crack width \rightarrow C1(1) = 0.5, C1(2) = 0.5, C1(3) = 0.13, C1(4) = 0.26, C1(5) = 0.2.

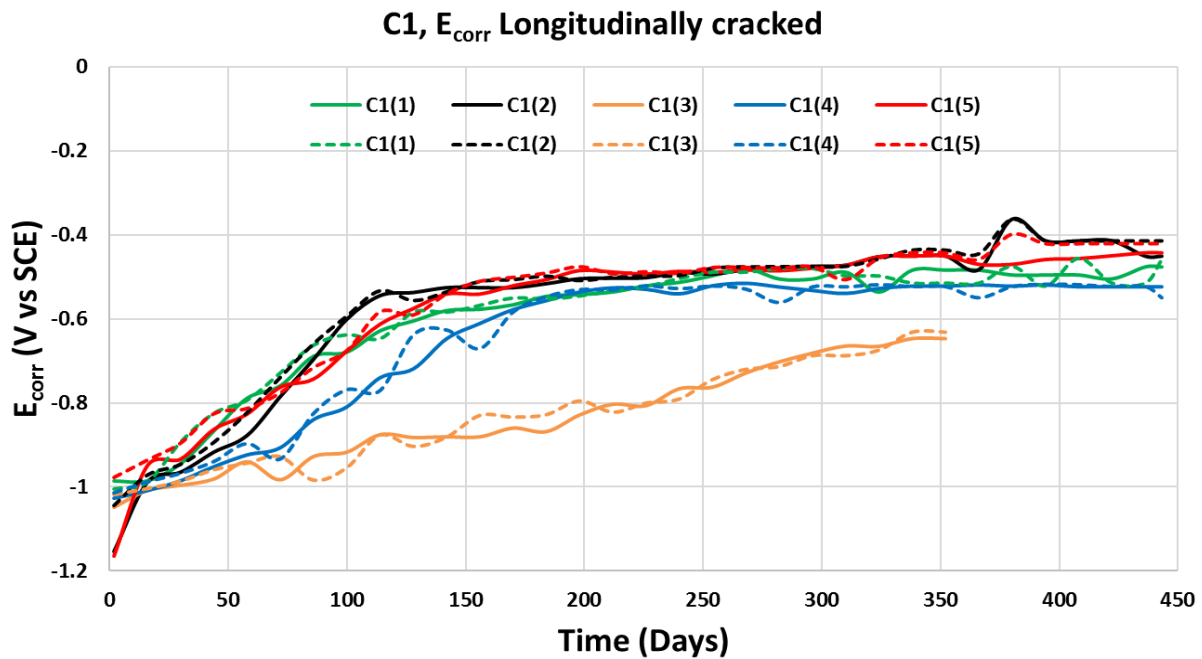


Figure C1.3: Crack width \rightarrow C1(1) = 0.2, C1(2) = 0.15, C1(3) = 0.18, C1(4) = 0.23, C1(5) = 0.2.

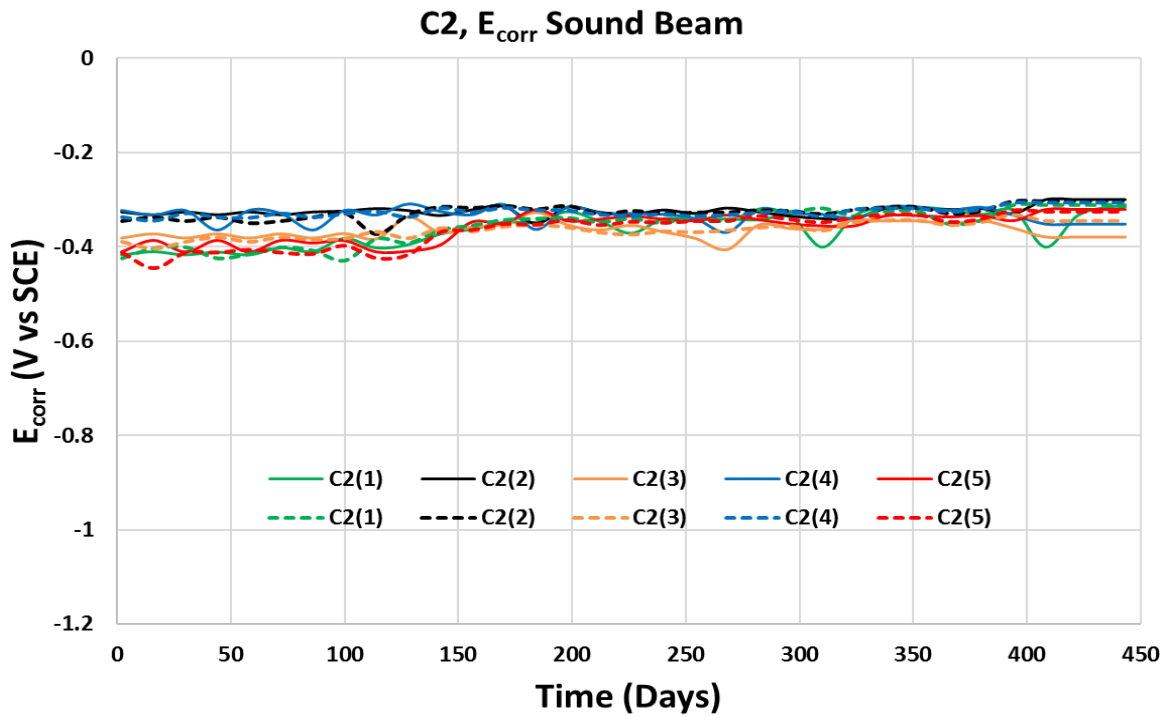


Figure C1.4: Sound (non-cracked) concrete beam.

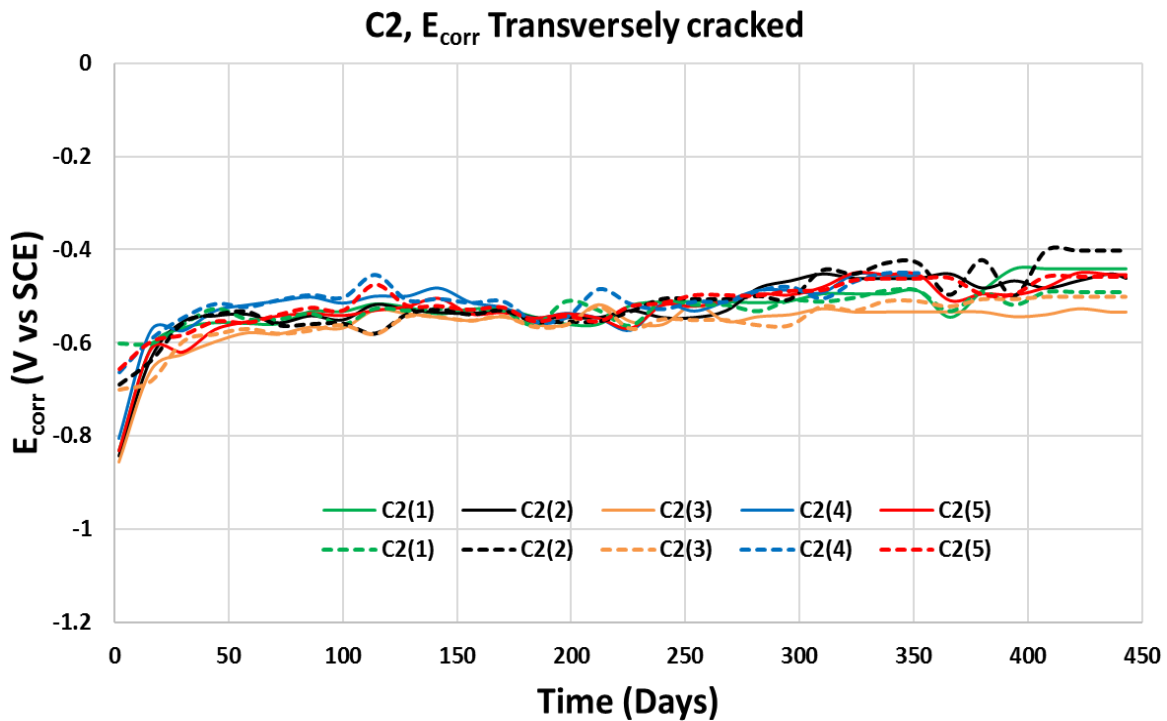


Figure C1.5: Crack width \rightarrow C2(1) = 0.2, C2(2) = 0.25, C2(3) = 0.2, C2(4) = 0.13, C2(5) =

0.2.

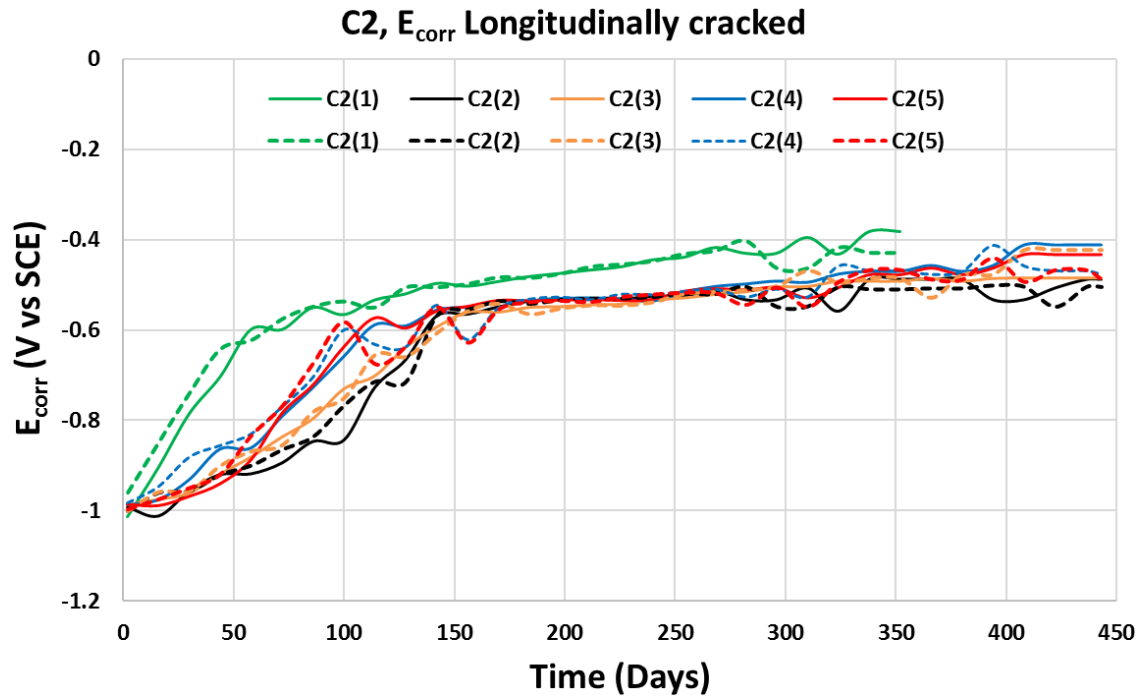


Figure C1.6: Crack width \rightarrow C2(1) = 0.14, C2(2) = 0.25, C2(3) = 0.14, C2(4) = 0.2, C2(5) = 0.2.

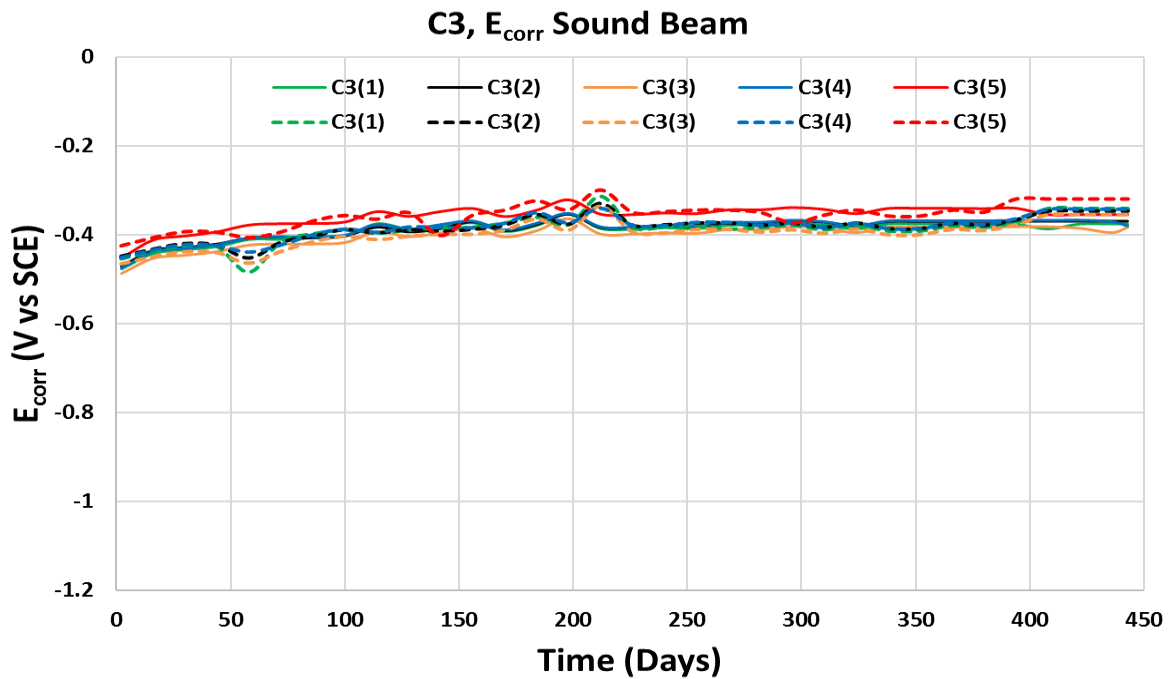


Figure C1.7: Sound (non-cracked) concrete beam.

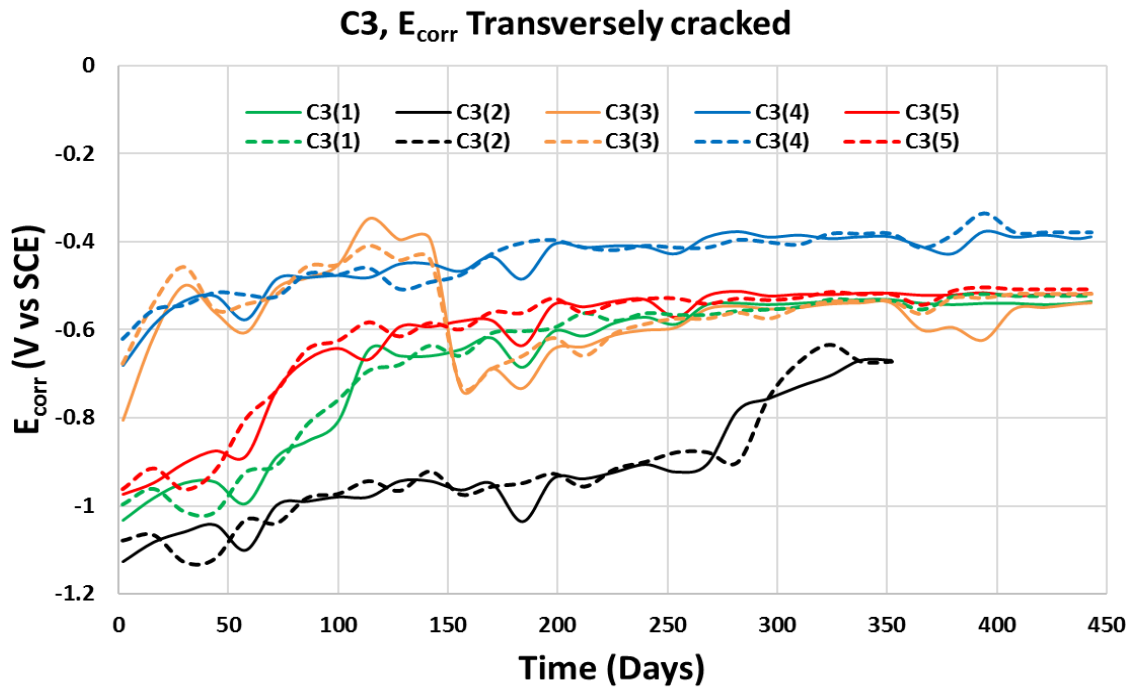


Figure C1.8: Crack width \rightarrow C3(1) = 0.3, C3(2) = 1.5, C3(3) = 0.3, C3(4) = 0.2, C3(5) = 0.25.

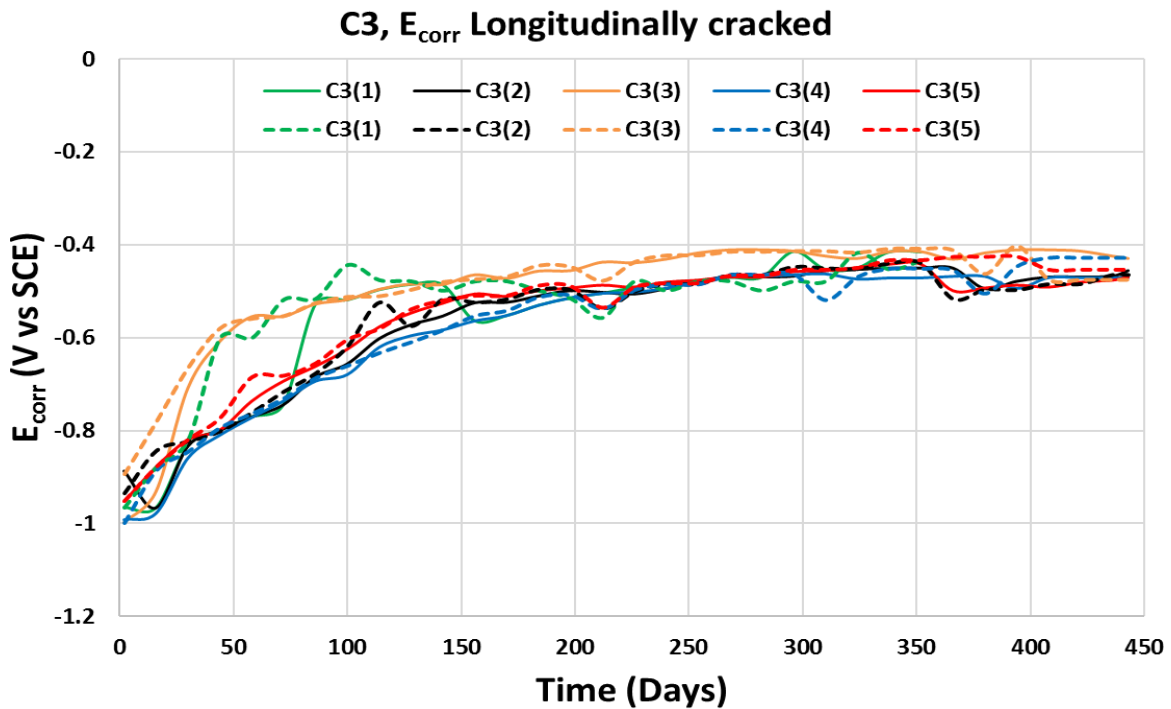


Figure C1.9: Crack width \rightarrow C3(1) = 0.25, C3(2) = 0.2, C3(3) = 0.15, C3(4) = 0.15, C3(5) = 0.2.

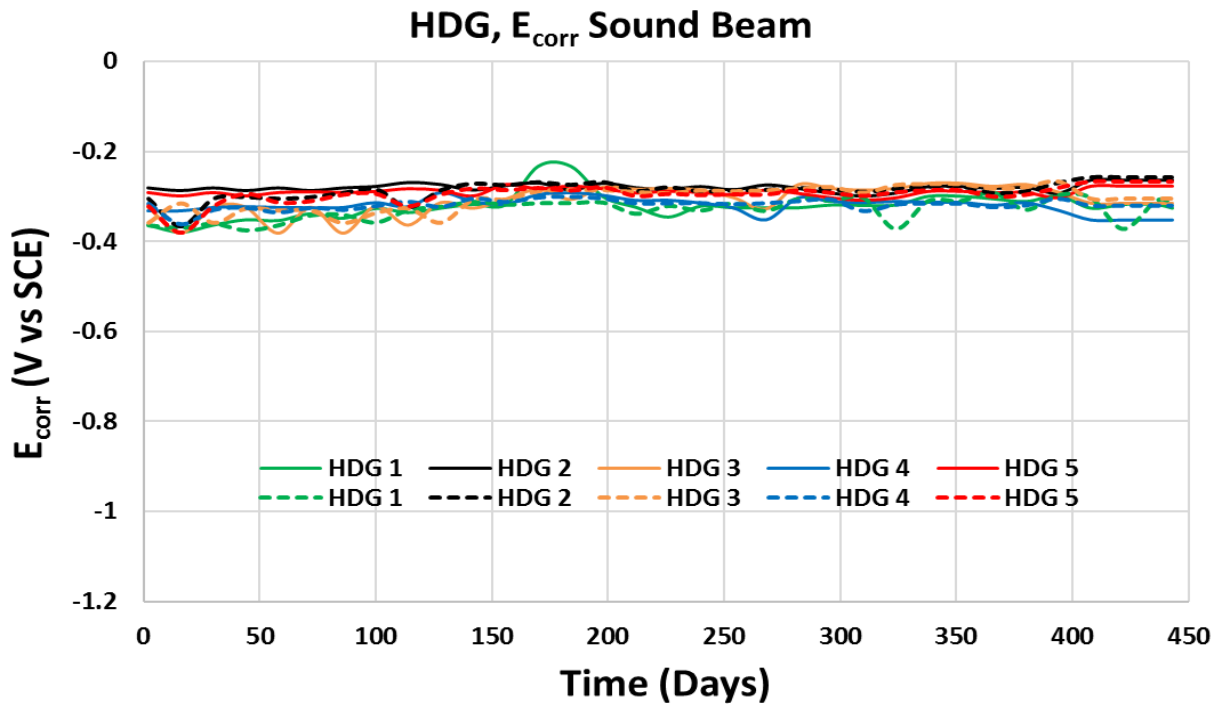


Figure C1.10: Sound (non-cracked) concrete beam.

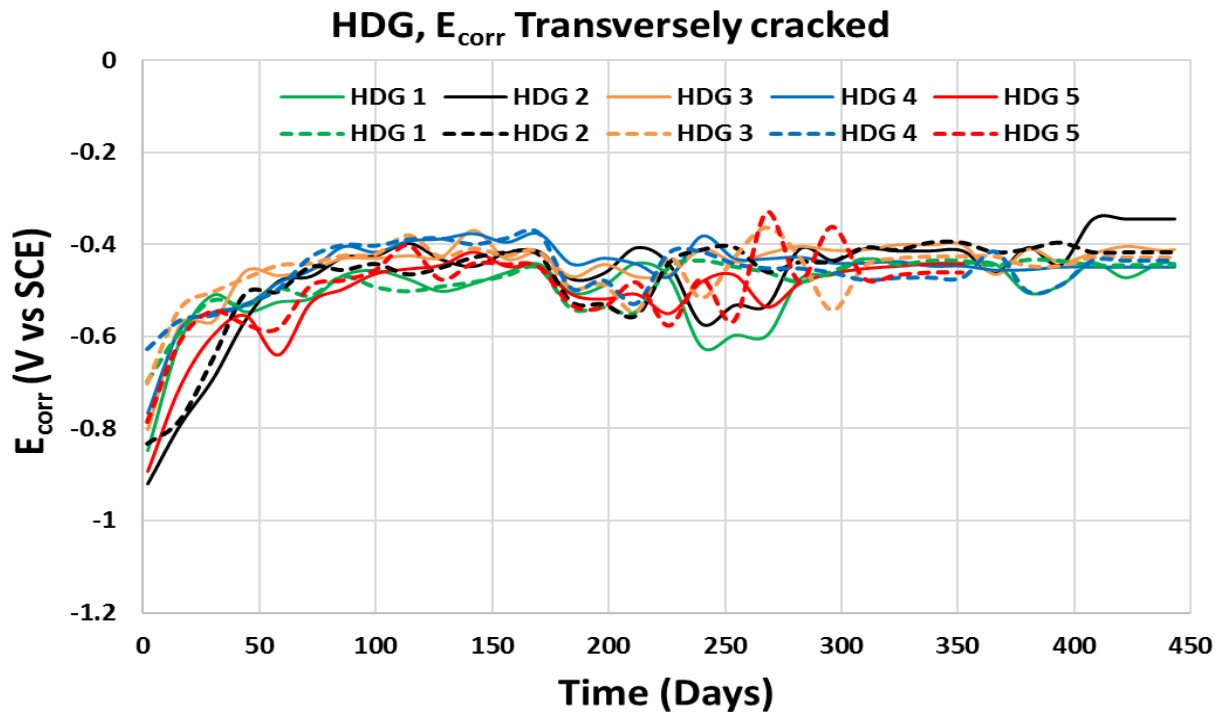


Figure C1.11: Crack width \rightarrow HDG1 = 0.25, HDG2 = 0.3, HDG3 = 0.25, HDG4 = 0.15, HDG5 = 0.3.

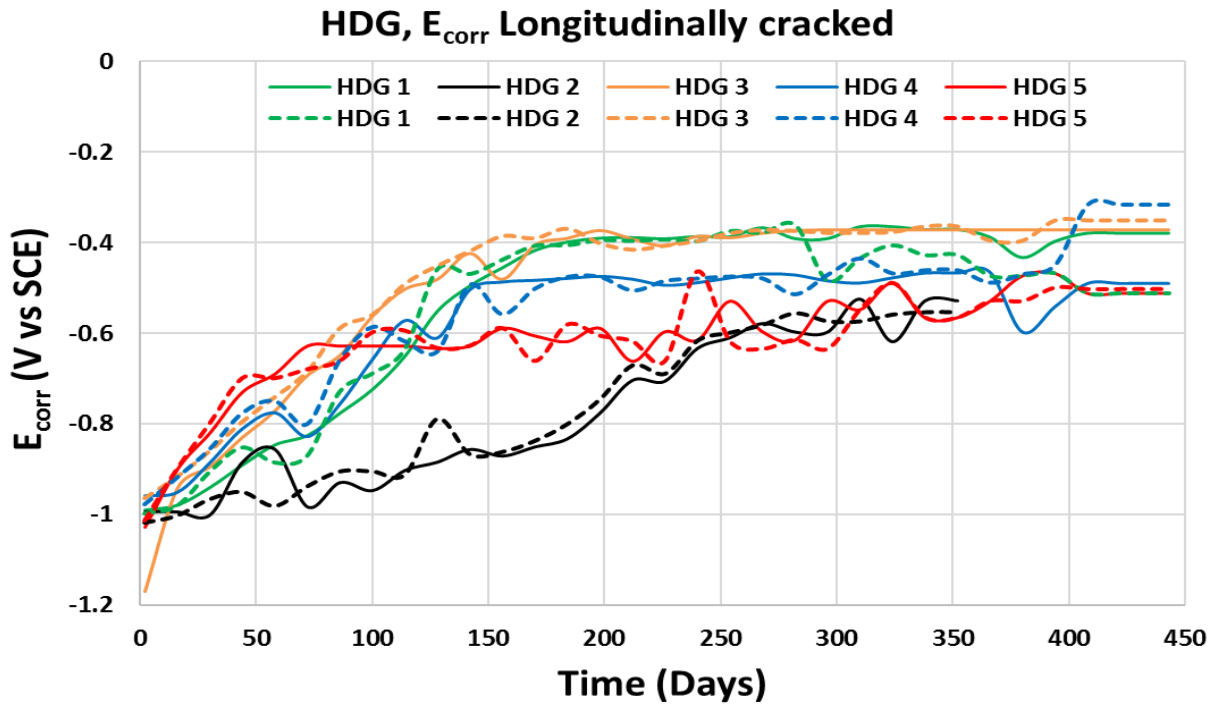


Figure C1.12: Crack width \rightarrow HDG1 = 0.15, HDG2 = 0.25, HDG3 = 0.14, HDG4 = 0.15, HDG5 = 0.2.

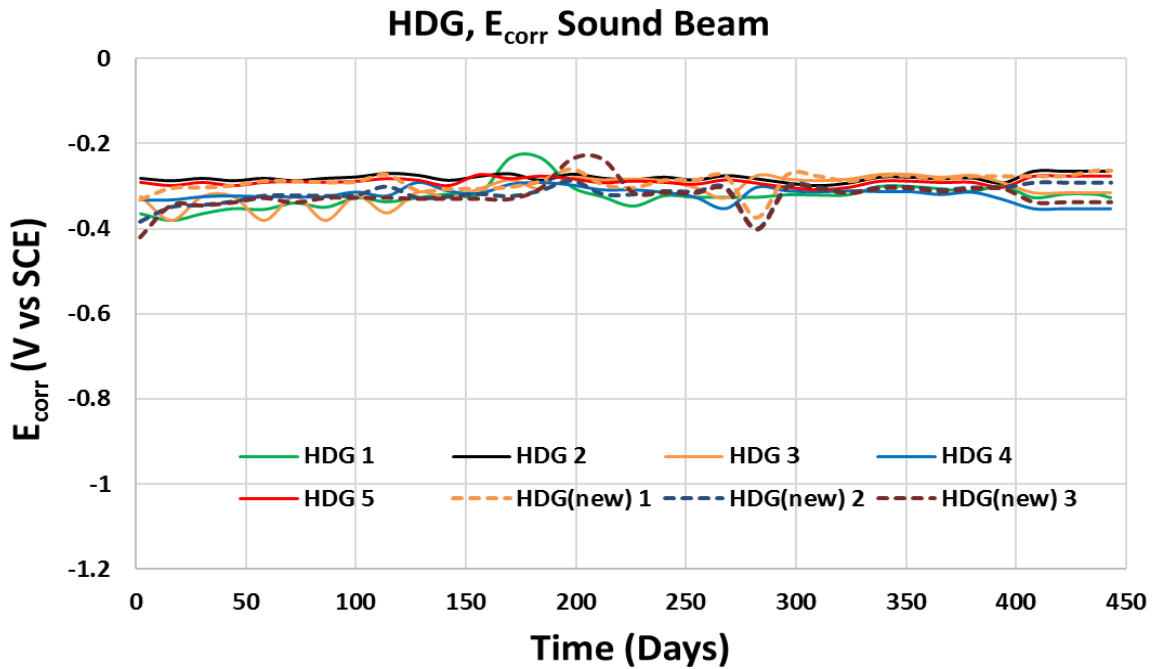


Figure C1.13: GP result of sound (non-cracked) concrete specimen from Cast 1 and Cast 2.

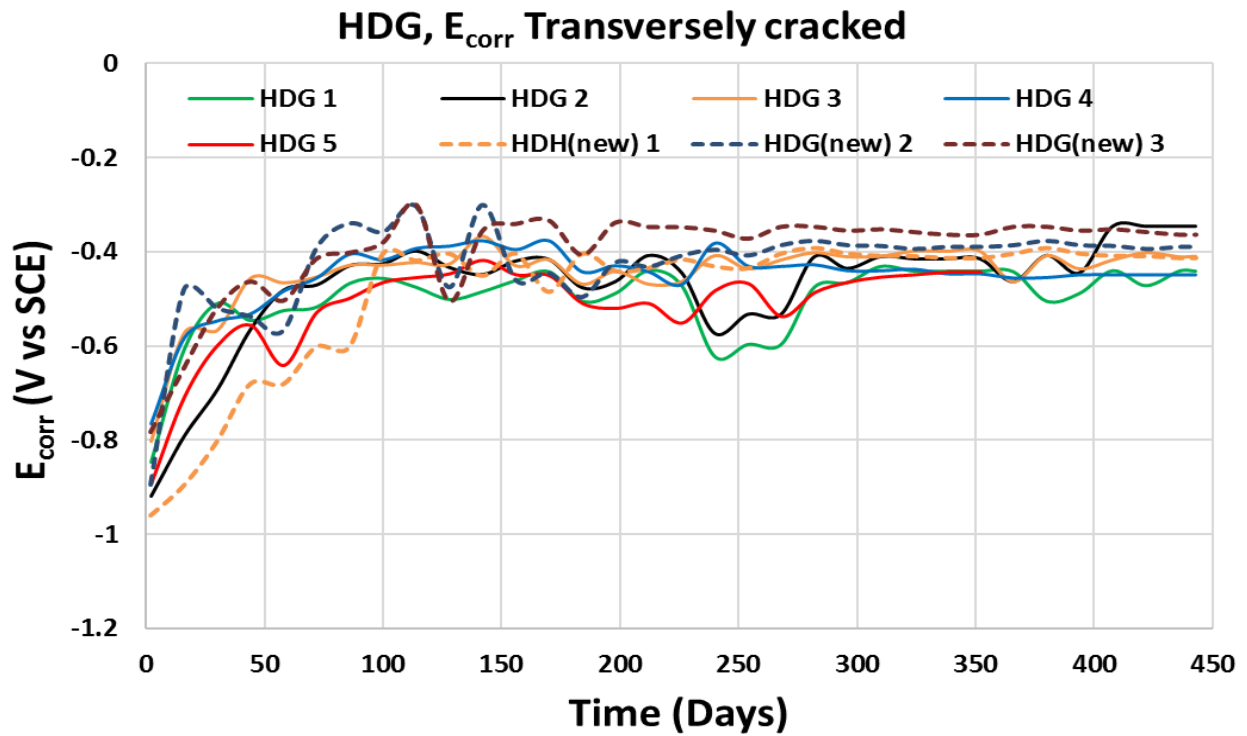


Figure C1.14: GP result of transversely cracked specimens from Cast 1 and 2.

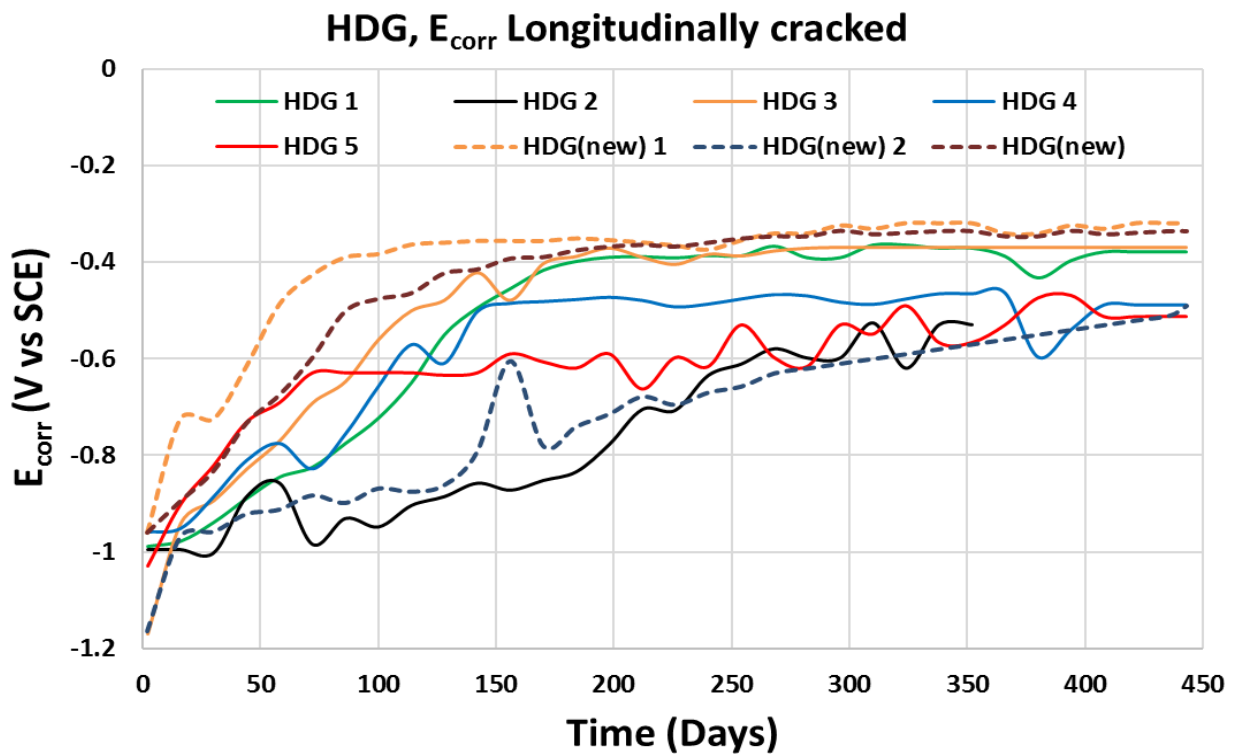


Figure C1.15: GP result of longitudinally cracked specimens from Cast 1 and 2.

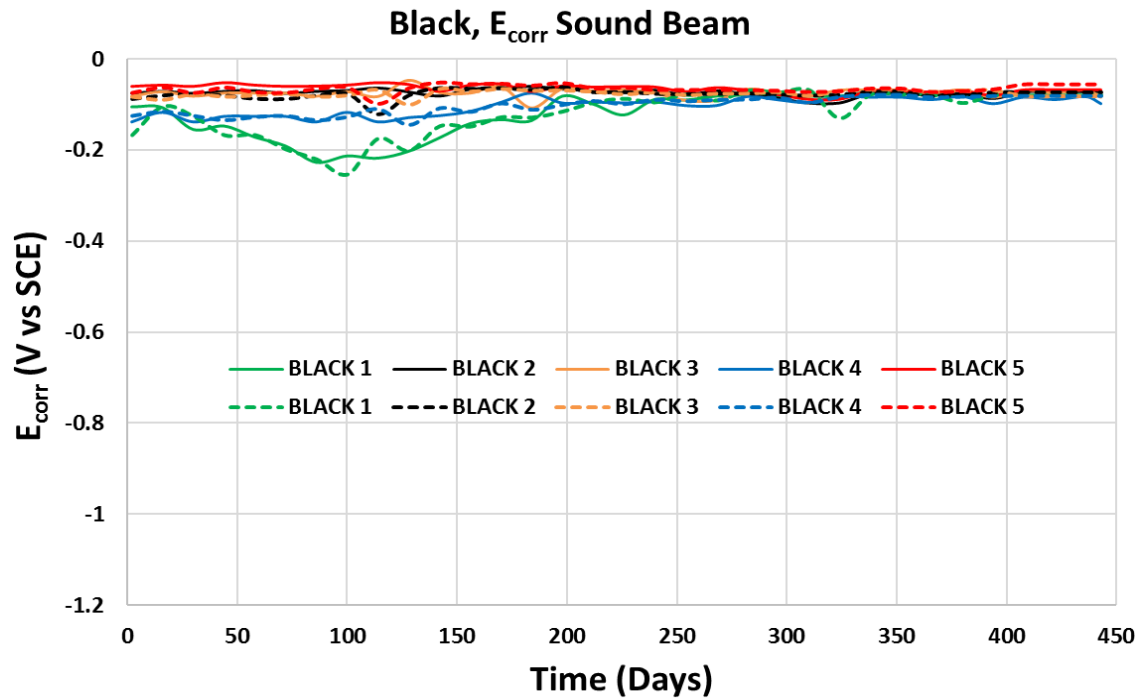


Figure C1.16: Sound (non-cracked) concrete beam.

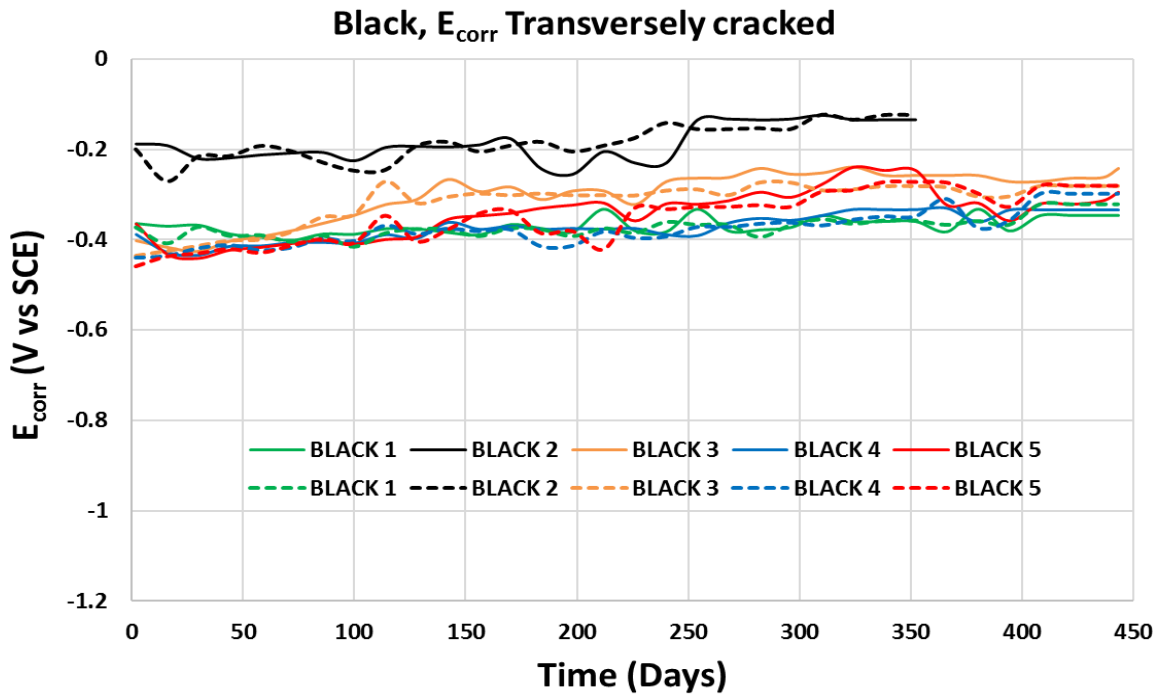


Figure C1.17: Crack width → BLK1 = 0.15, BLK2 = 0.13, BLK3 = 0.26, BLK4 = 0.24, BLK5 = 0.15.

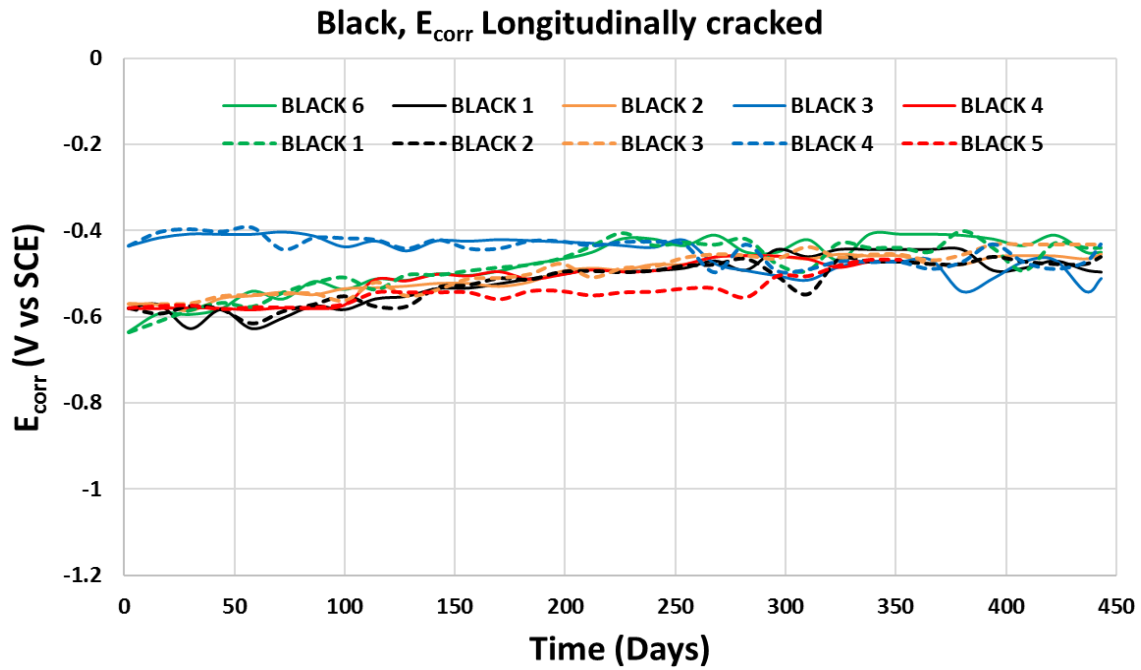


Figure C1.18: Crack width \rightarrow BLK1 = 0.25, BLK2 = 0.2, BLK3 = 0.14, BLK4 = 0.12, BLK5 = 0.25.

C2. i_{corr} for individual specimens

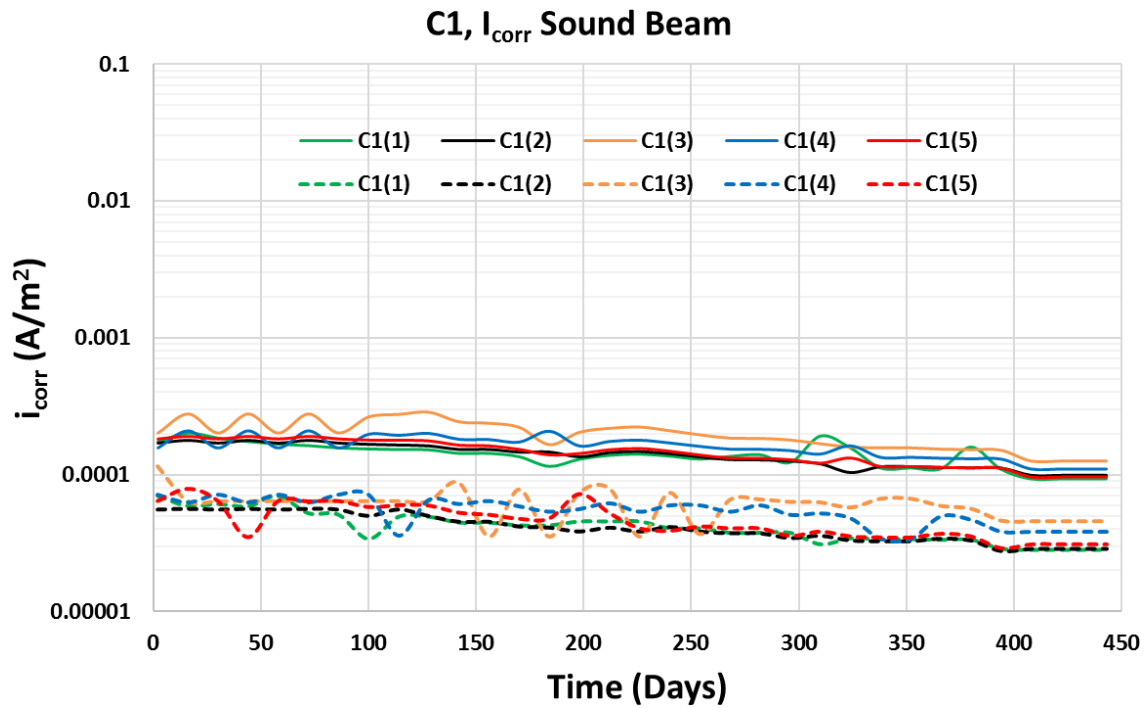


Figure C2.1: Sound (non-cracked) beam.

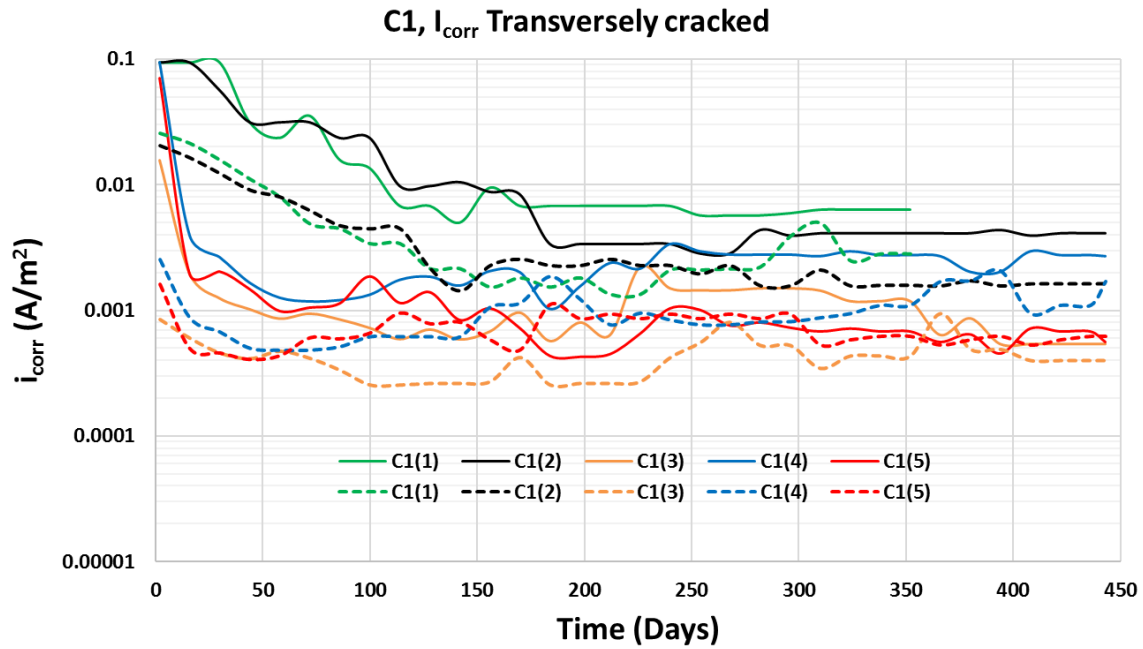


Figure C2.2: Crack width \rightarrow C1(1) = 0.5, C1(2) = 0.5, C1(3) = 0.13, C1(4) = 0.26, C1(5) = 0.2.

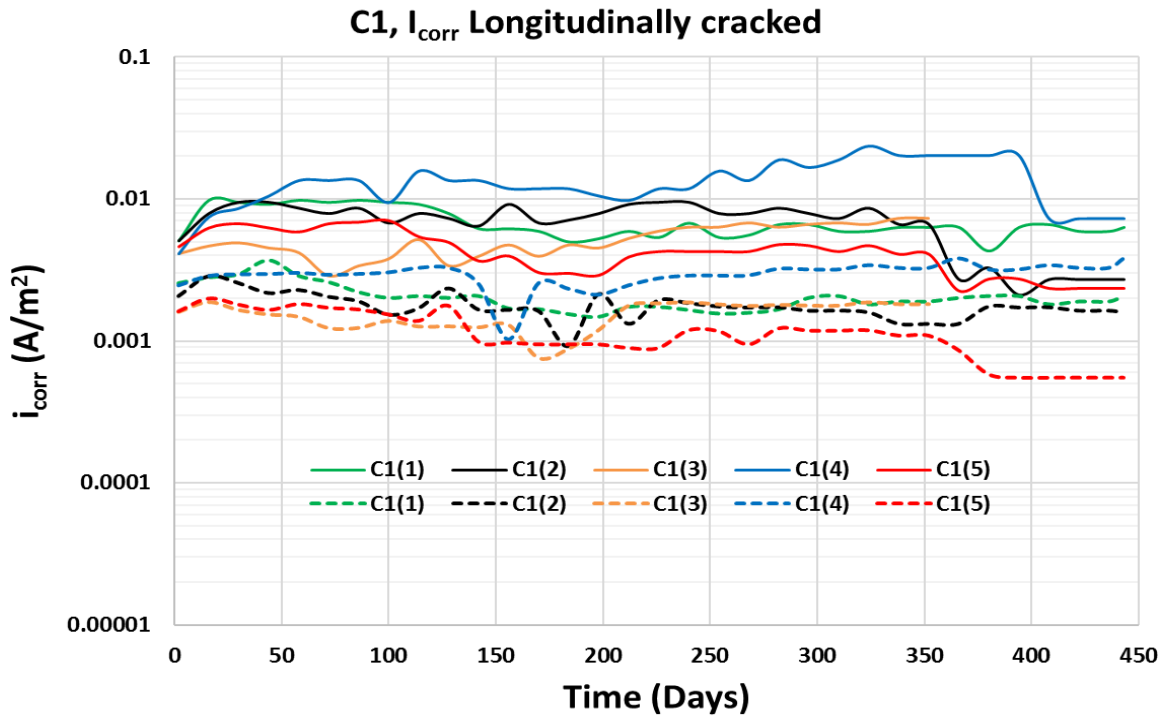


Figure C2.3: Crack width \rightarrow C1(1) = 0.2, C1(2) = 0.15, C1(3) = 0.18, C1(4) = 0.23, C1(5) = 0.2.

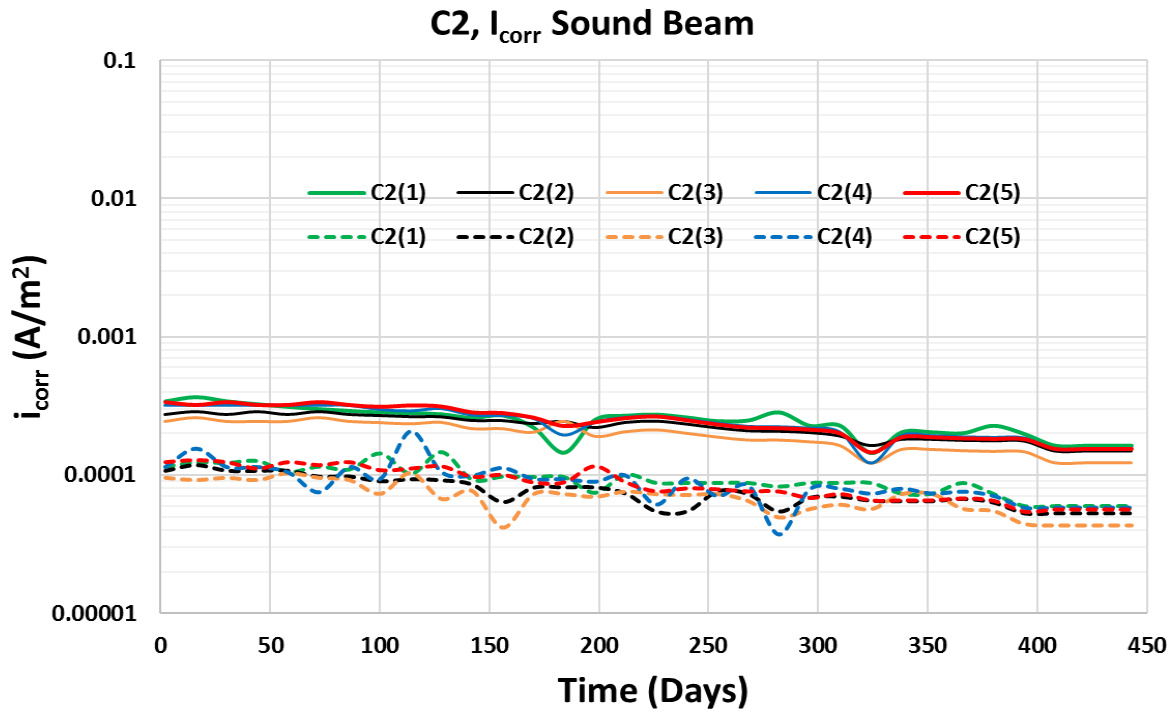


Figure C2.4: Sound (non-cracked) concrete beam.

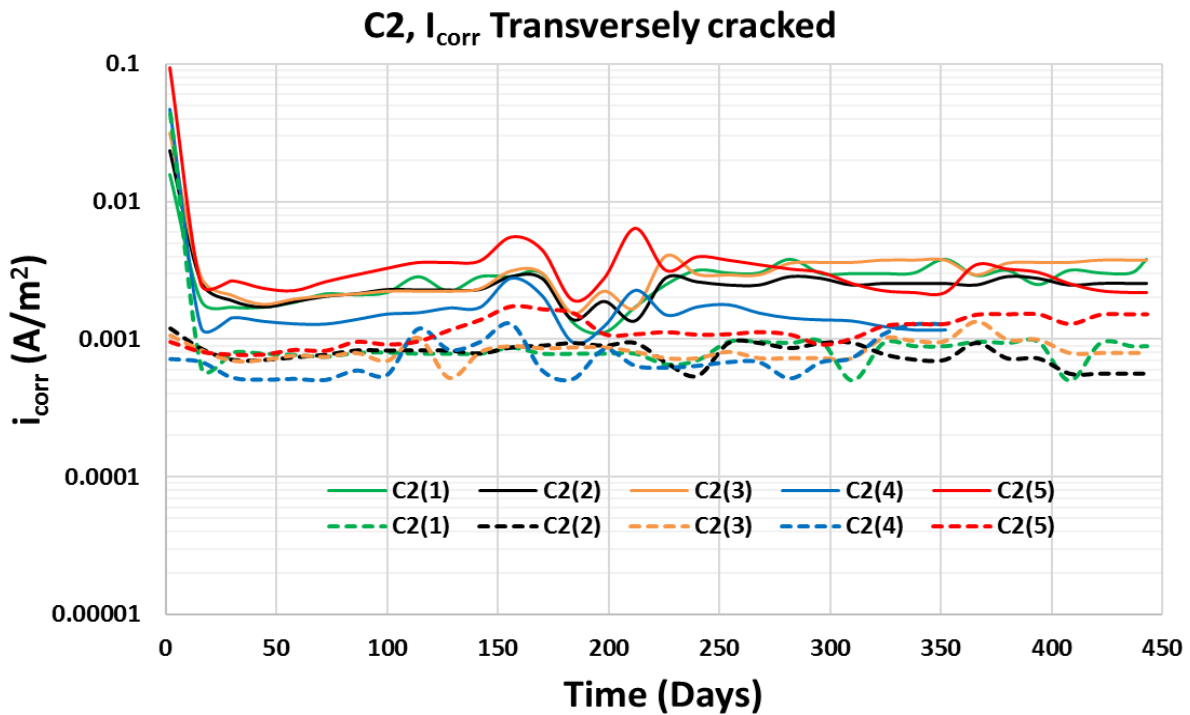


Figure C2.5: Crack width \rightarrow C2(1) = 0.2, C2(2) = 0.25, C2(3) = 0.2, C2(4) = 0.13, C2(5) = 0.2.

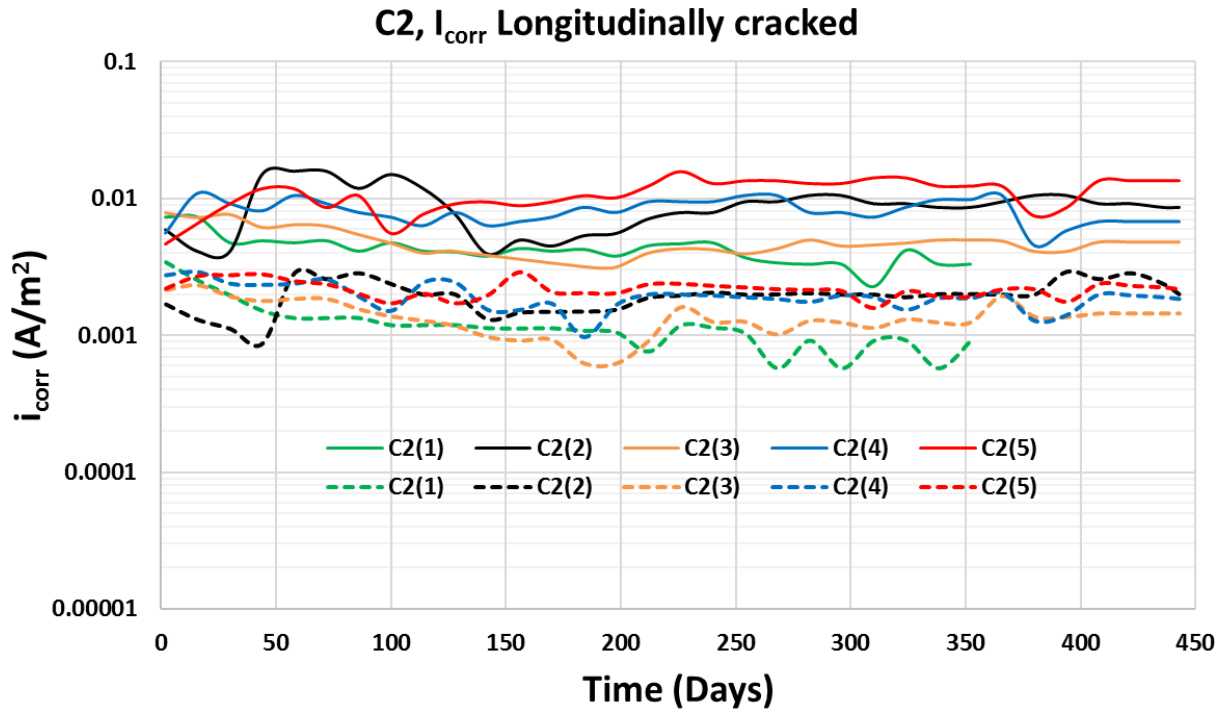


Figure C2.6: Crack width \rightarrow C2(1) = 0.14, C2(2) = 0.25, C2(3) = 0.14, C2(4) = 0.2, C2(5) = 0.2.

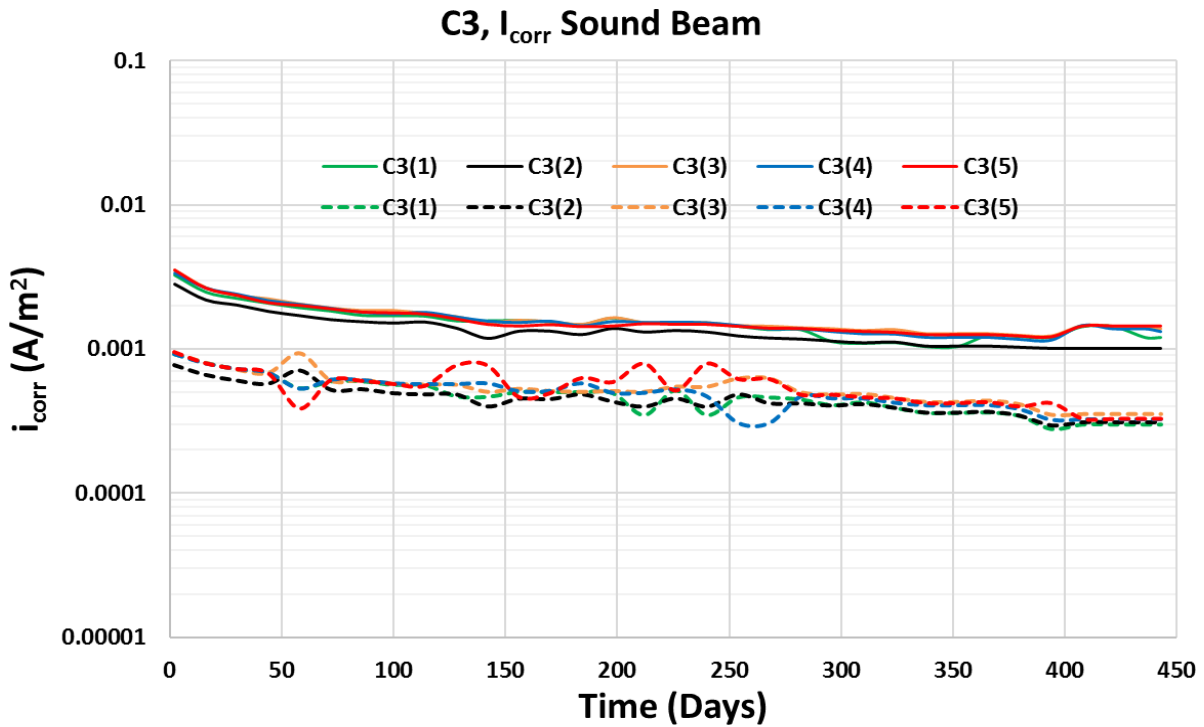


Figure C2.7: Sound (non-cracked) concrete beam.

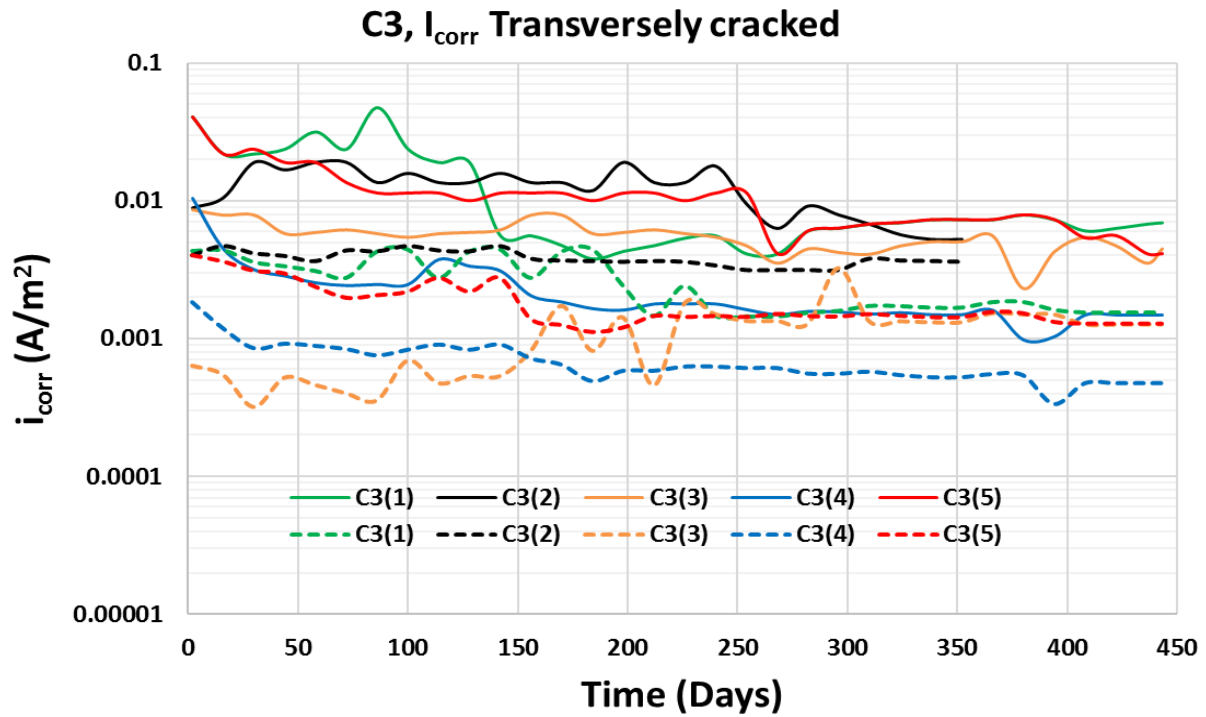


Figure C2.8: Crack width \rightarrow C3(1) = 0.3, C3(2) = 1.5, C3(3) = 0.3, C3(4) = 0.2, C3(5) = 0.25.

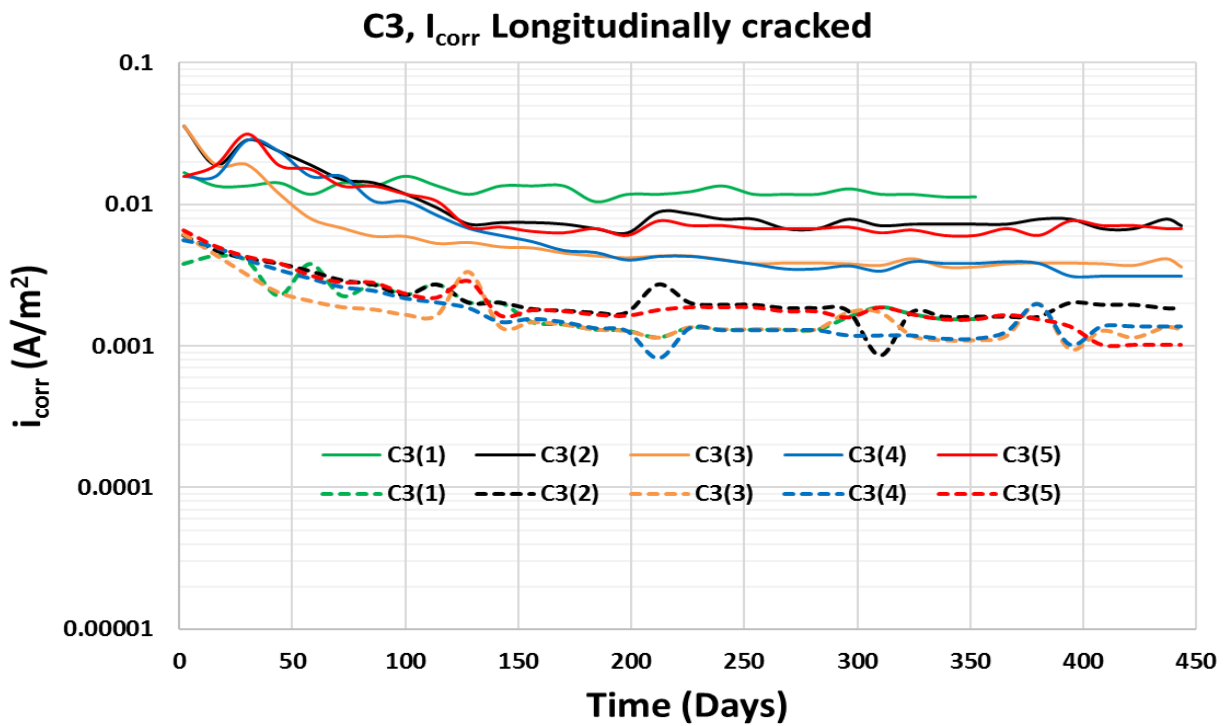


Figure C2.9: Crack width \rightarrow C3(1) = 0.25, C3(2) = 0.2, C3(3) = 0.15, C3(4) = 0.15, C3(5) =

0.2.

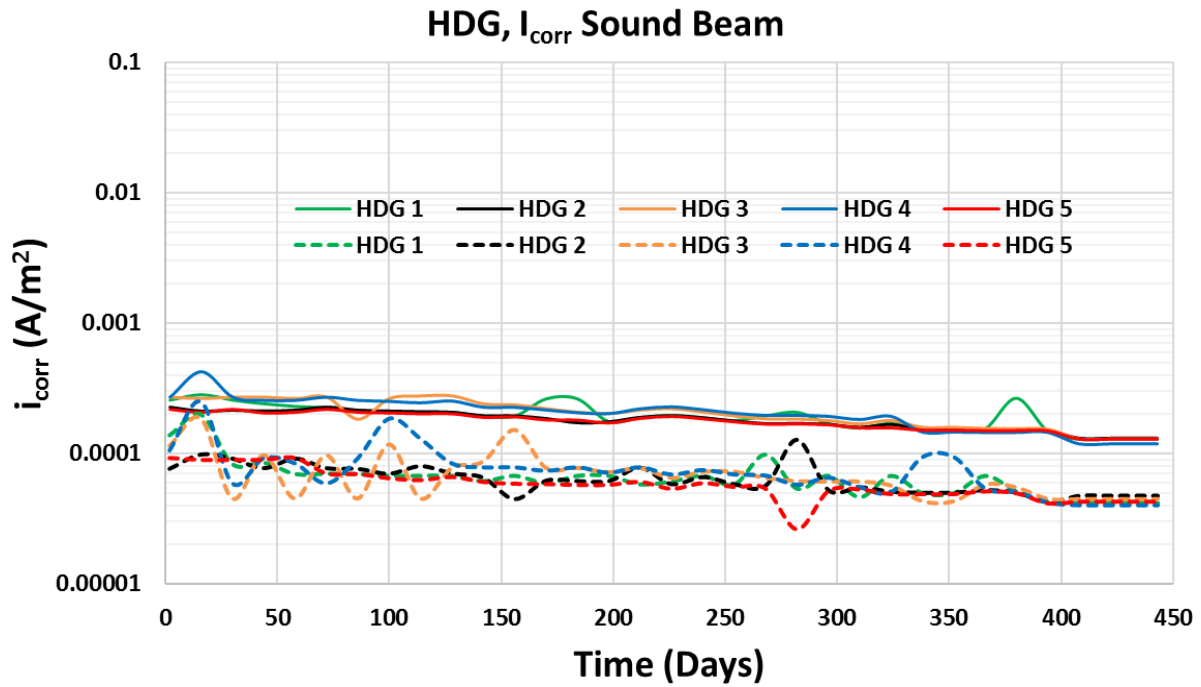


Figure C2.10 – Sound (non-cracked) concrete beam.

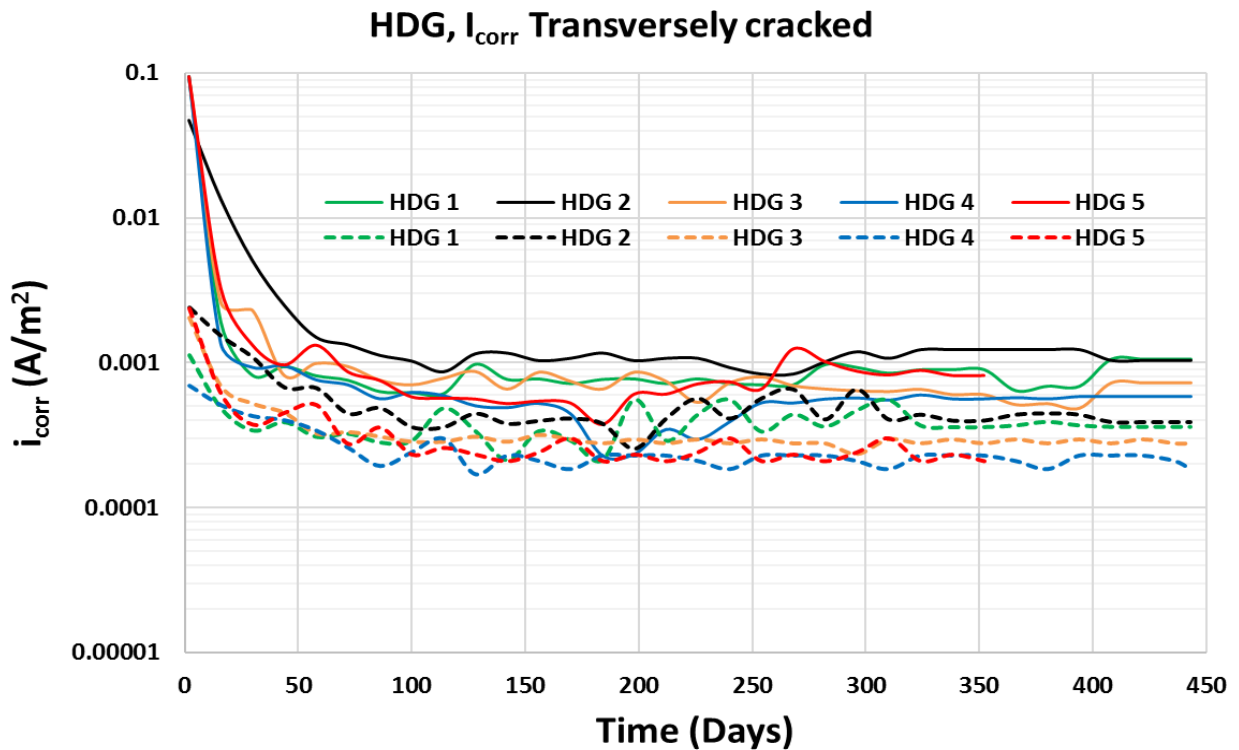


Figure C2.11: Crack width \rightarrow HDG1 = 0.25, HDG2 = 0.3, HDG3 = 0.25, HDG4 = 0.15, HDG5 = 0.3.

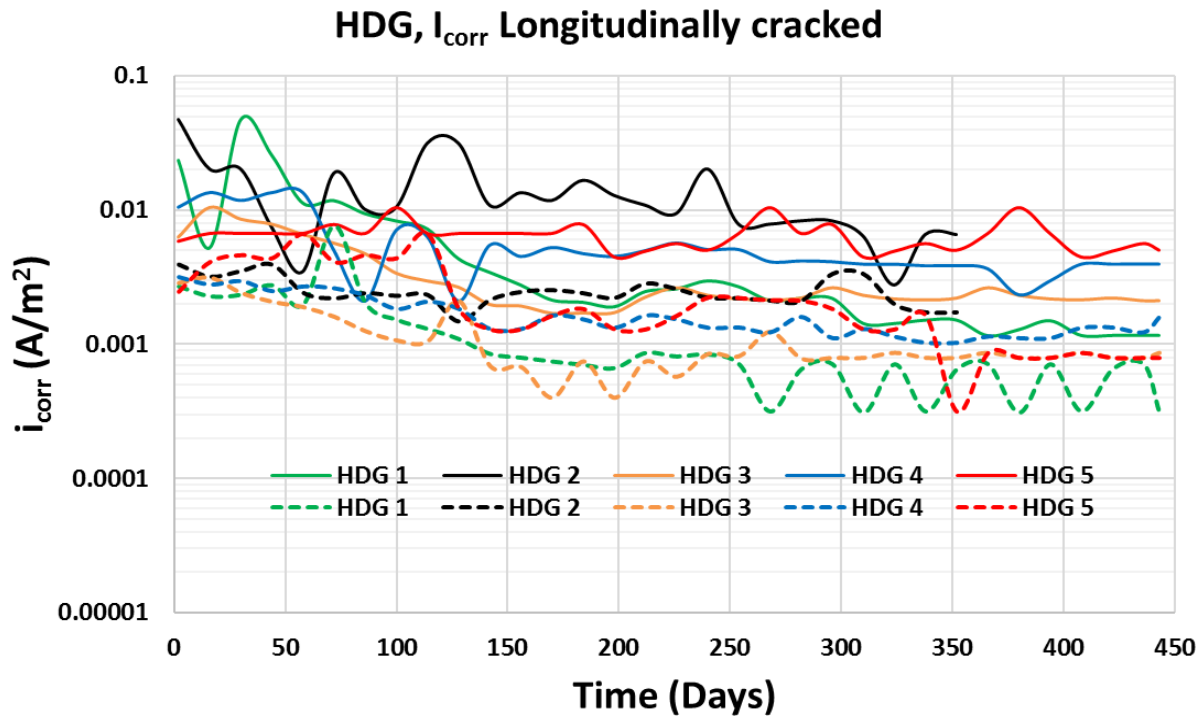


Figure C2.12: Crack width - HDG1 = 0.15, HDG2 = 0.25, HDG3 = 0.14, HDG4 = 0.15, HDG5 = 0.2.

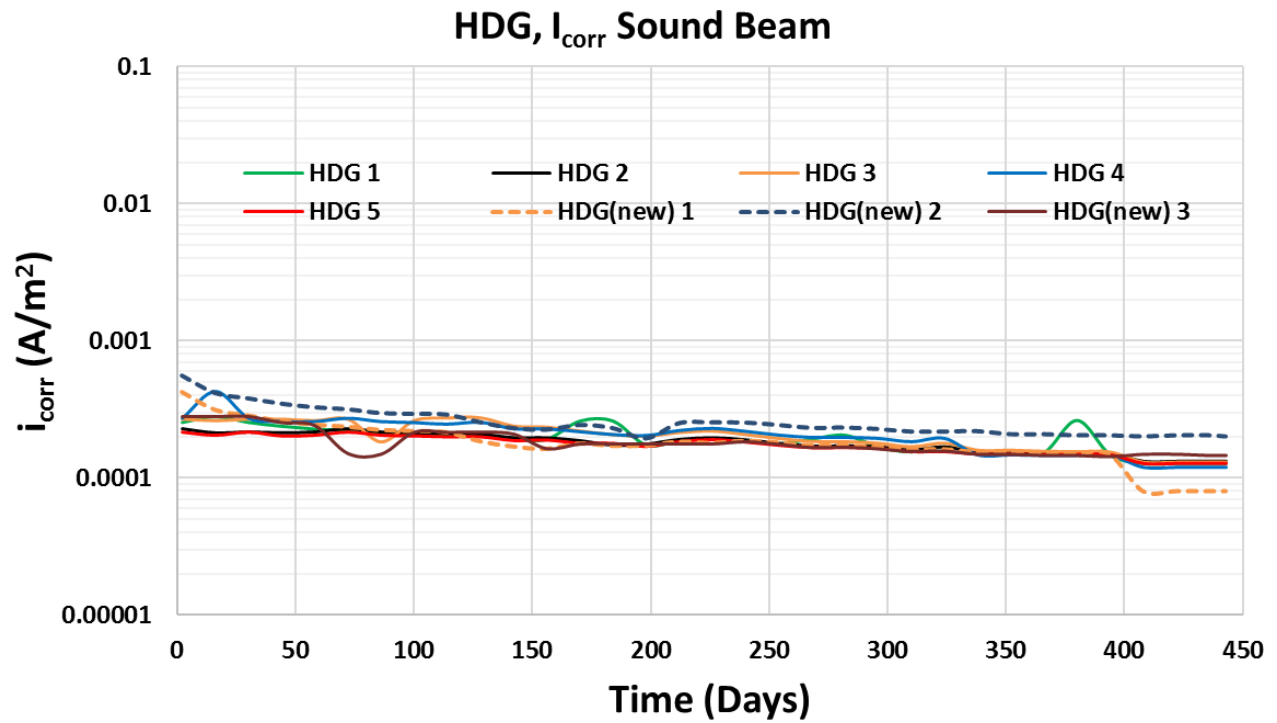


Figure C2.13 – Sound (non-cracked) concrete specimens from Cast 1 and 2.

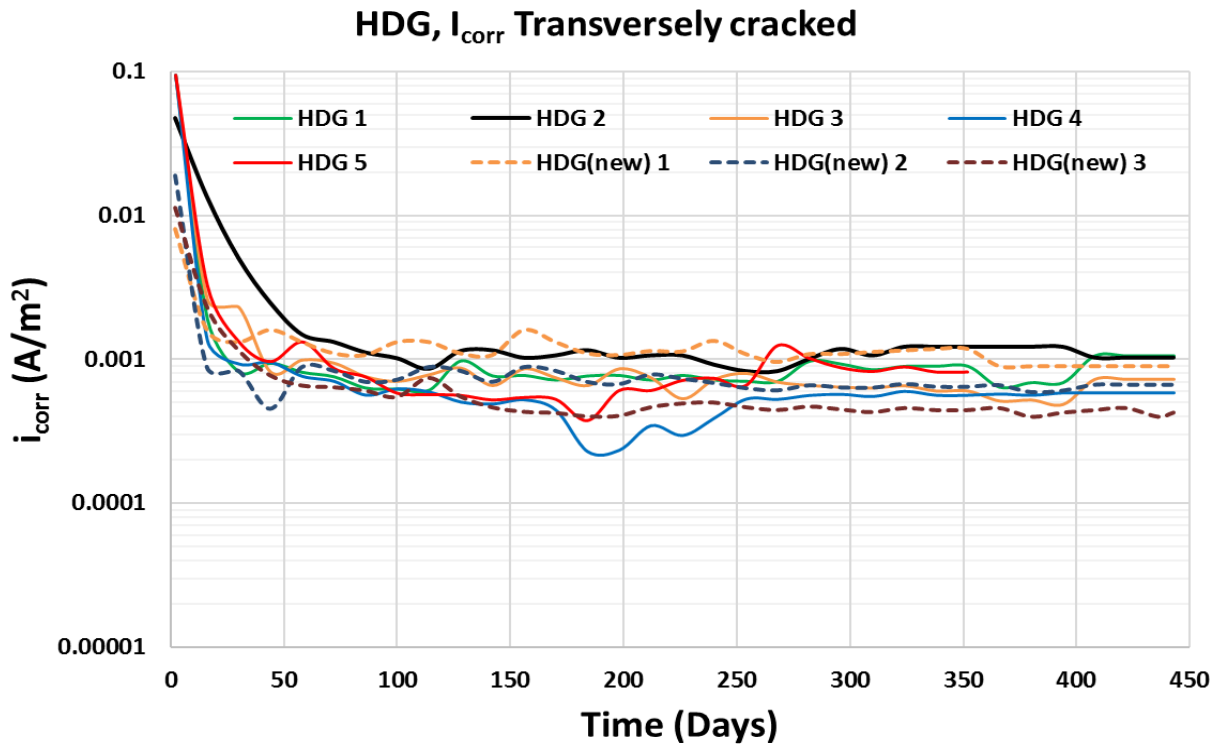


Figure C2.14 – GP result for transversely cracked specimens from Cast 1 and 2.

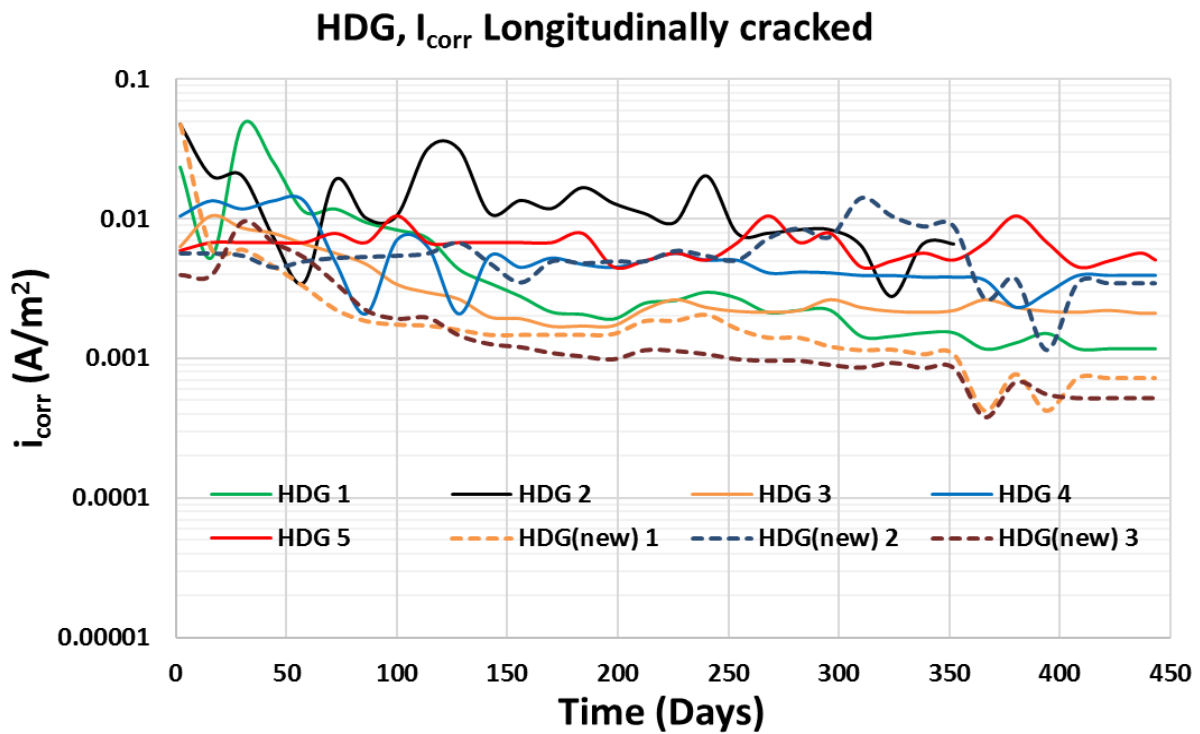


Figure C2.15 – GP result for longitudinally cracked specimens from Cast 1 and 2.

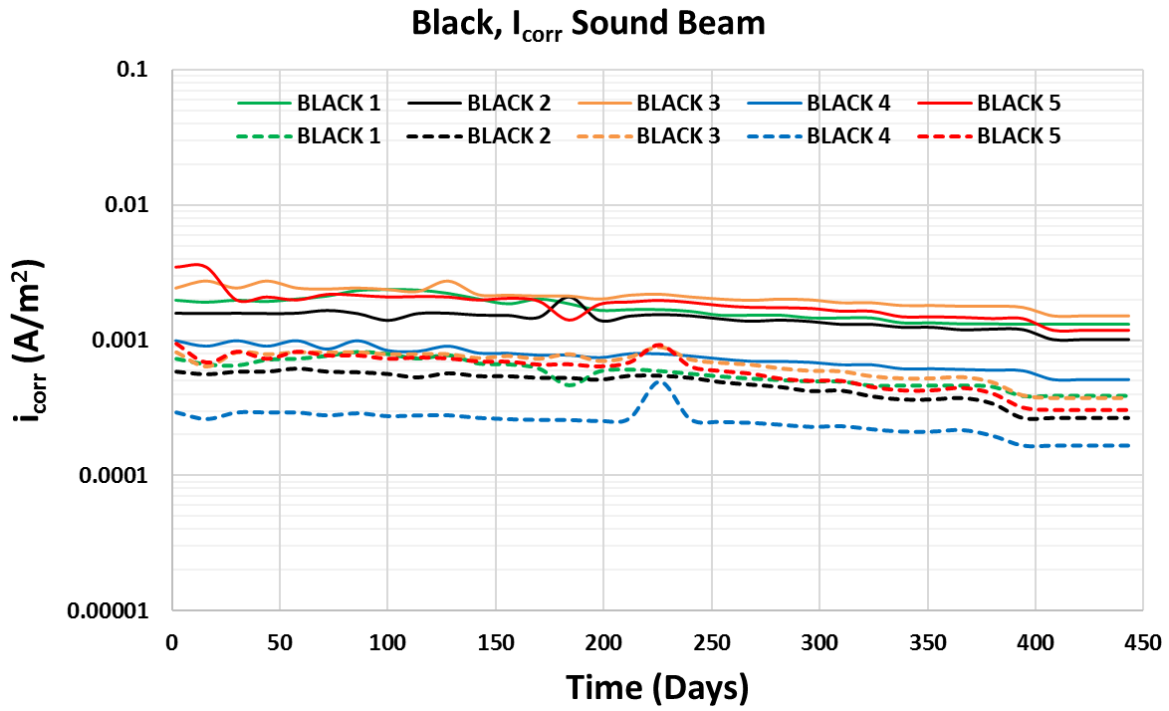


Figure C2.16 – Sound (non-cracked) concrete beam.

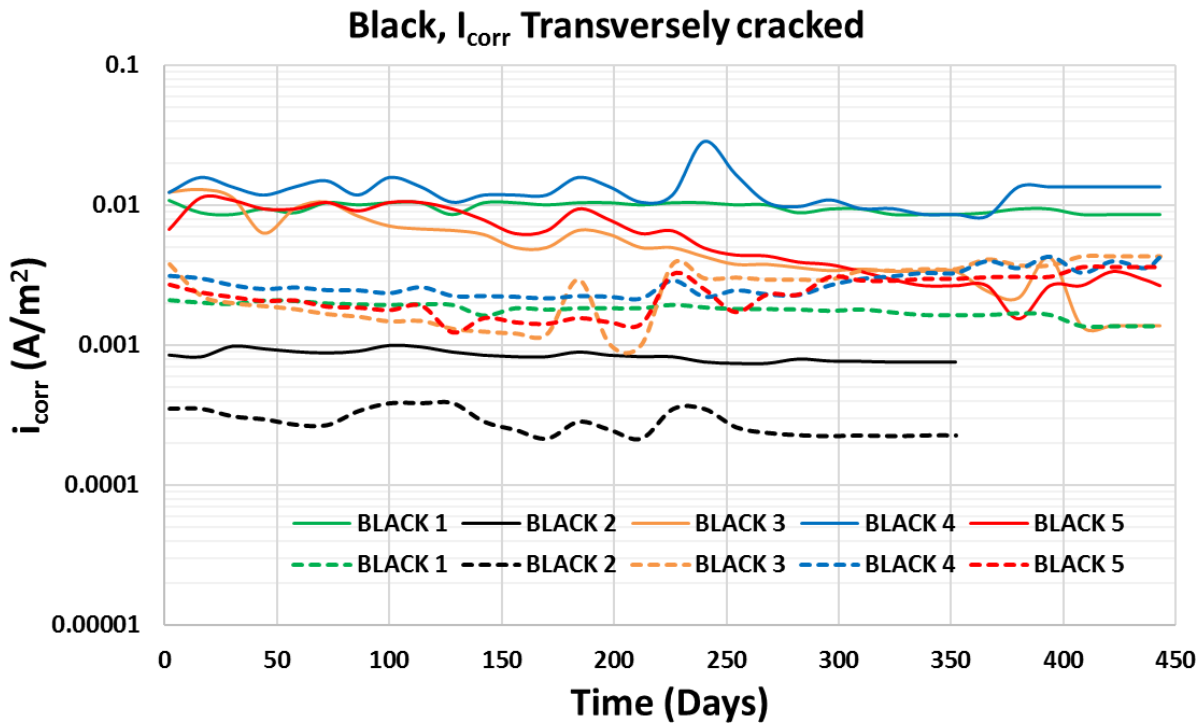


Figure C2.17 – Crack width \rightarrow BLK1 = 0.15, BLK2 = 0.13, BLK3 = 0.26, BLK4 = 0.24, BLK5 = 0.15.

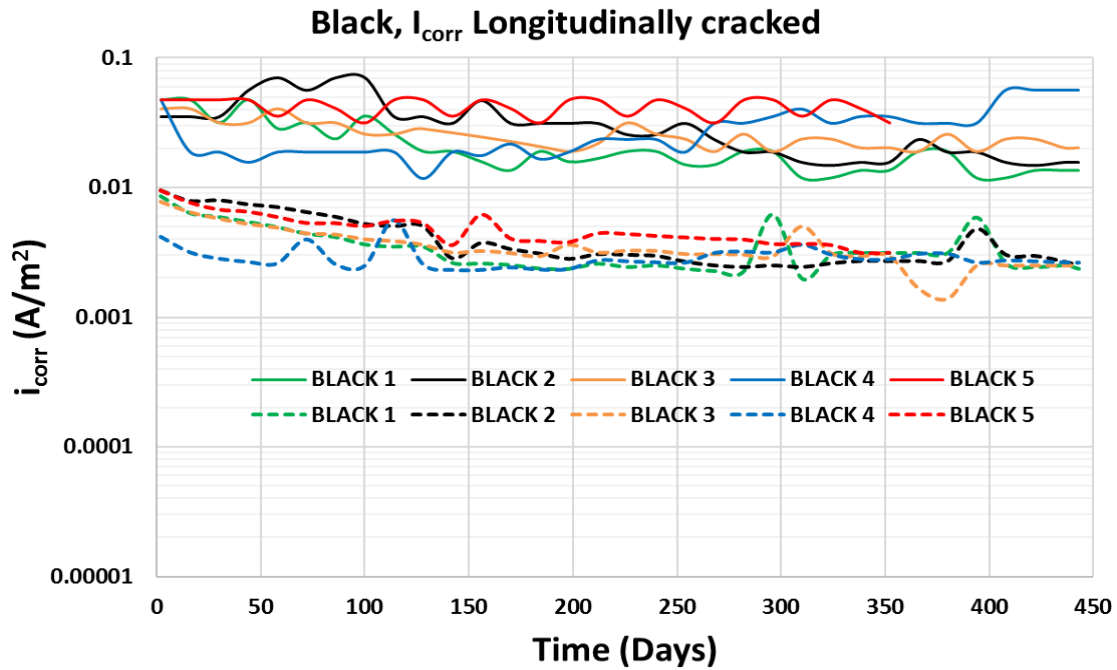


Figure C2.18 – Crack width → BLK1 = 0.25, BLK2 = 0.2, BLK3 = 0.14, BLK4 = 0.12, BLK5 = 0.25.

C3. Concrete resistance for individual

Concrete resistance - Sound beam, C1

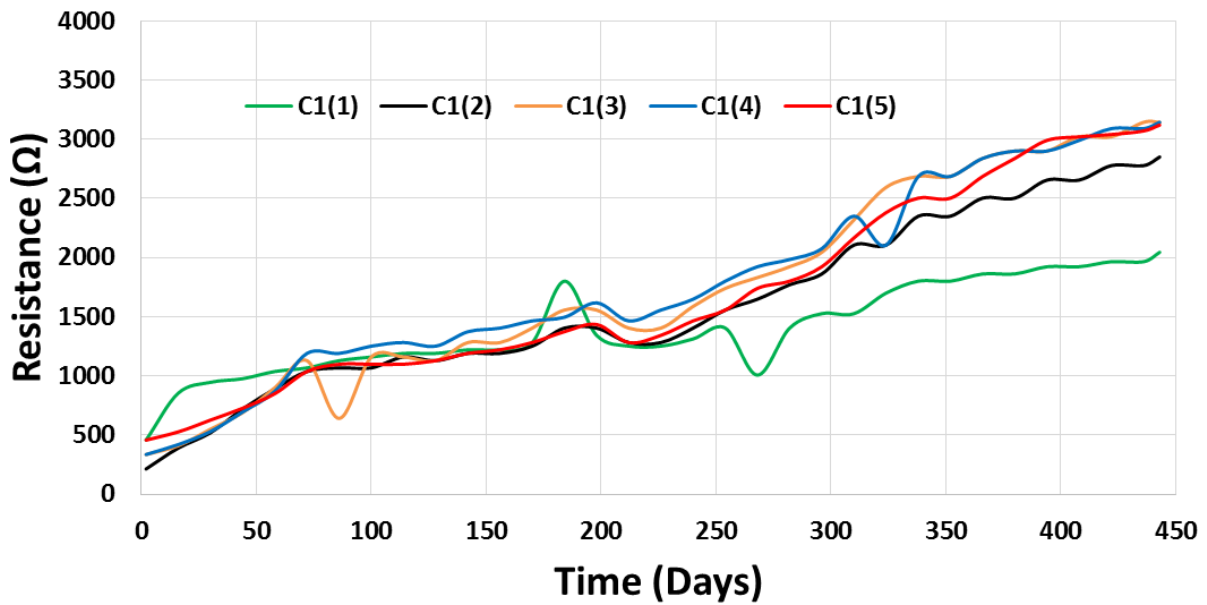


Figure C3.1: Sound (non-cracked) beam.

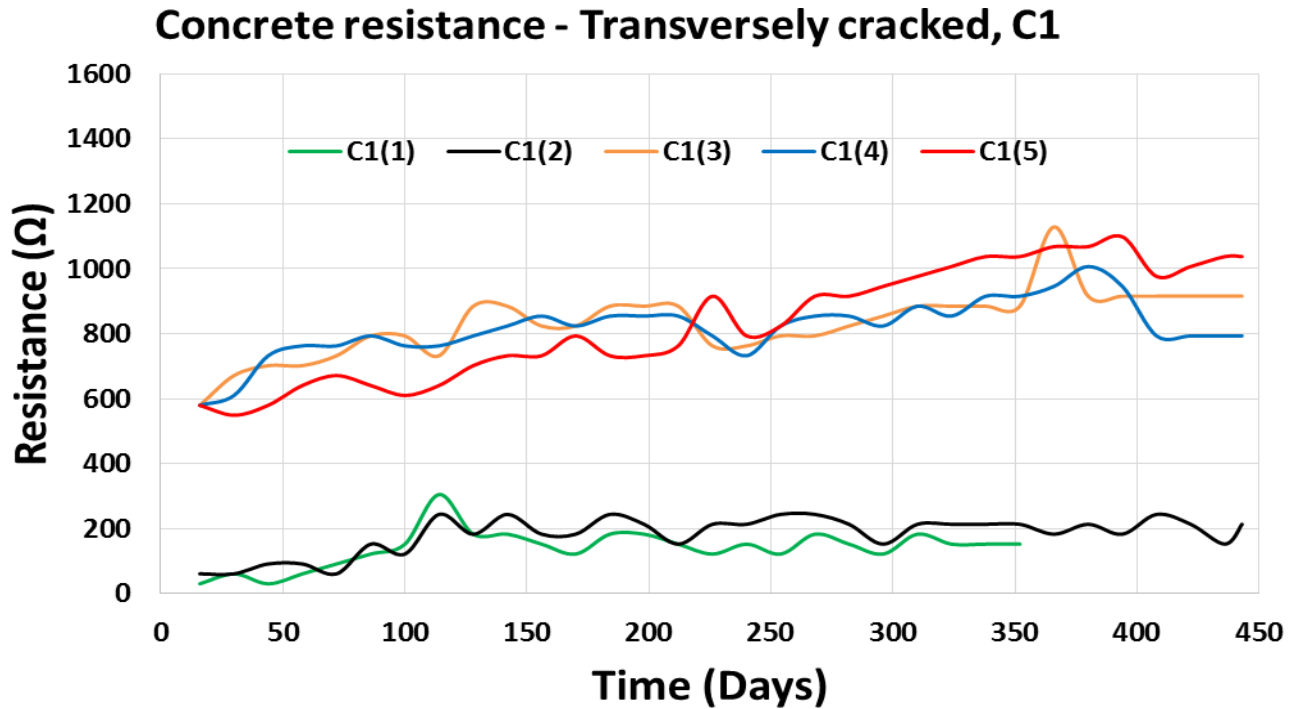


Figure C3.2: Crack width → C1(1) = 0.5, C1(2) = 0.5, C1(3) = 0.13, C1(4) = 0.26, C1(5) = 0.2.

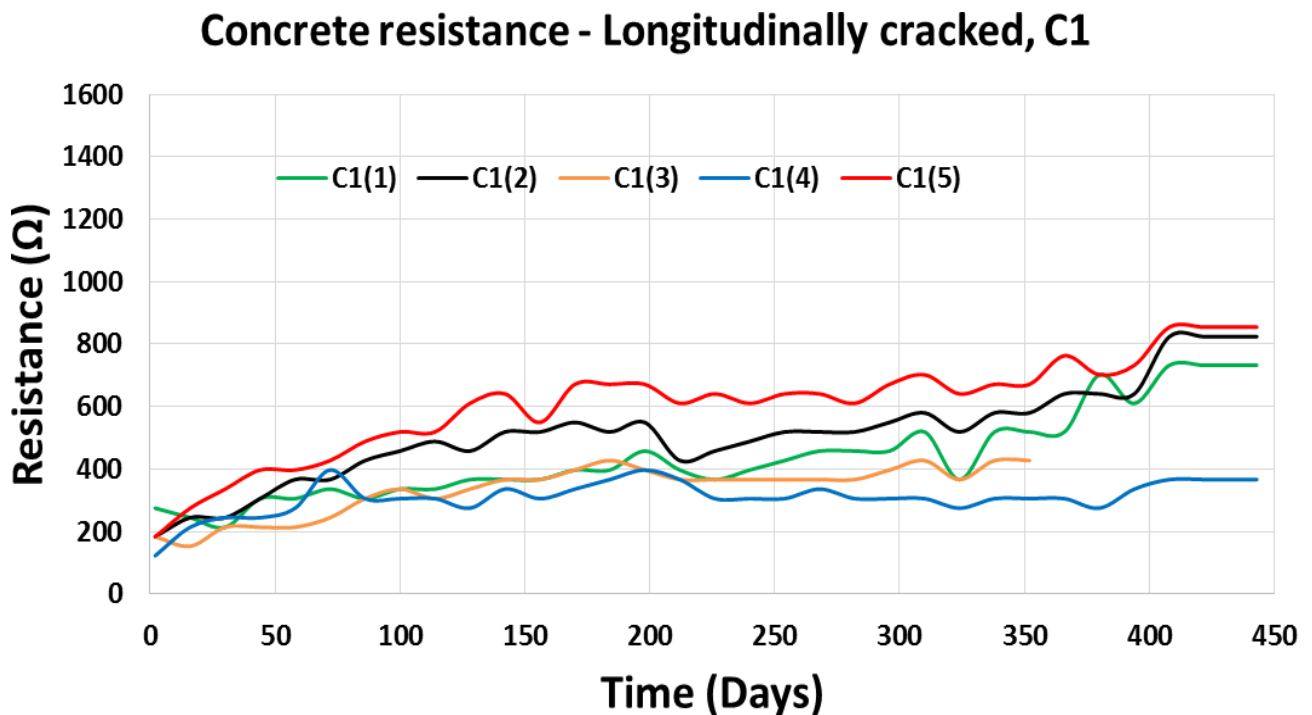


Figure C3.3: Crack width → C1(1) = 0.2, C1(2) = 0.15, C1(3) = 0.18, C1(4) = 0.23, C1(5) = 0.2.

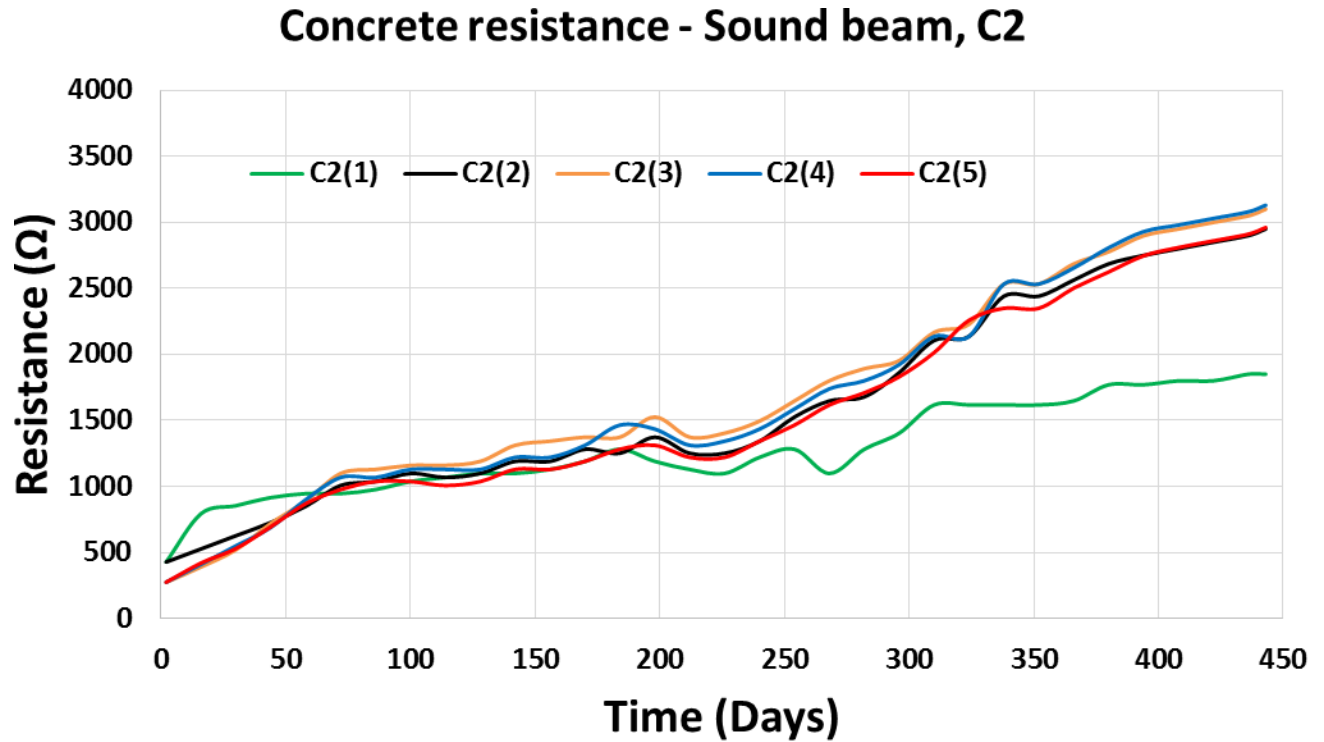


Figure C3.4: Sound (non-cracked) concrete beam.

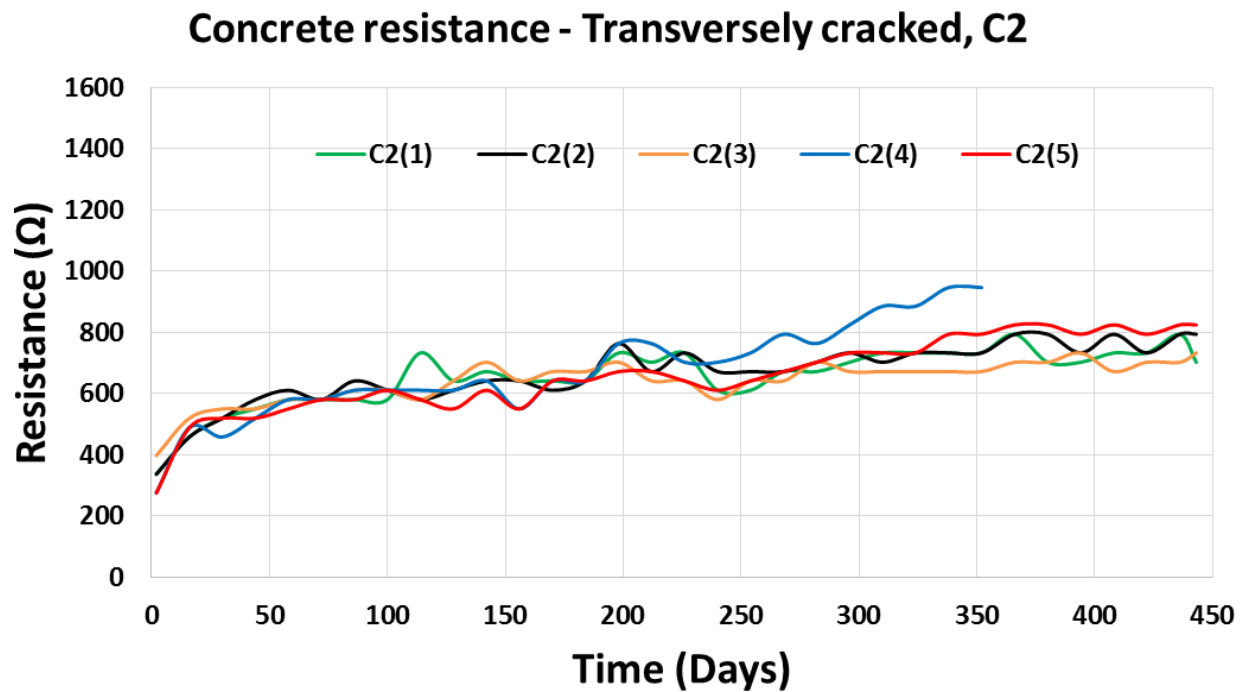


Figure C3.5: Crack width \rightarrow C2(1) = 0.2, C2(2) = 0.25, C2(3) = 0.2, C2(4) = 0.13, C2(5) = 0.2.

Concrete resistance - Longitudinally cracked, C2

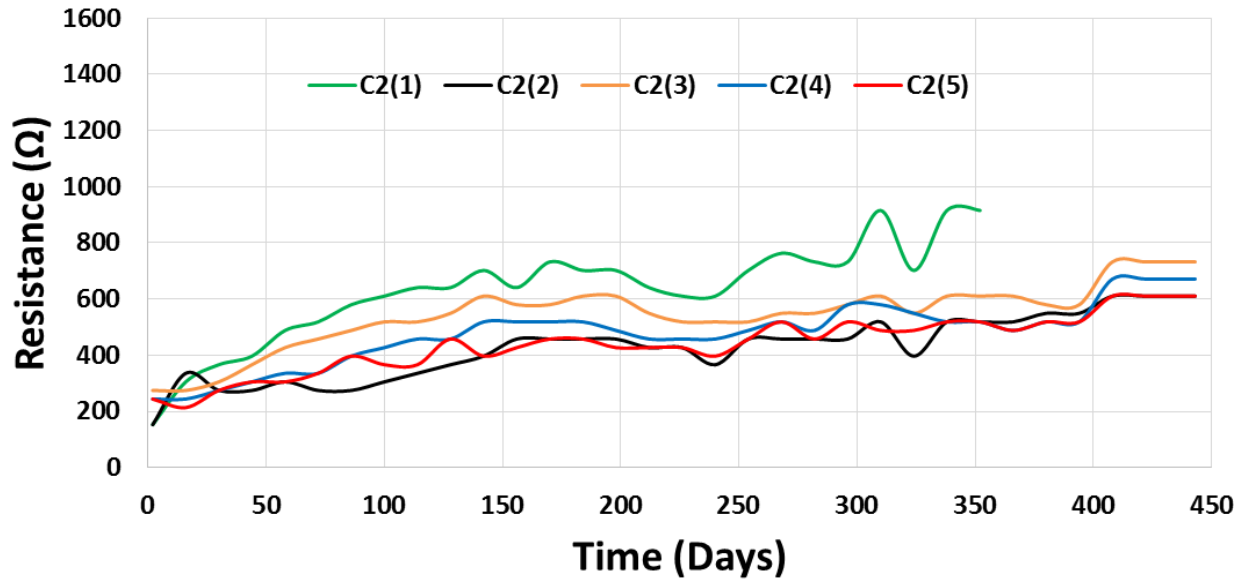


Figure C3.6: Crack width → C2(1) = 0.14, C2(2) = 0.25, C2(3) = 0.14, C2(4) = 0.2, C2(5) = 0.2.

Concrete resistance - Sound beam, C3

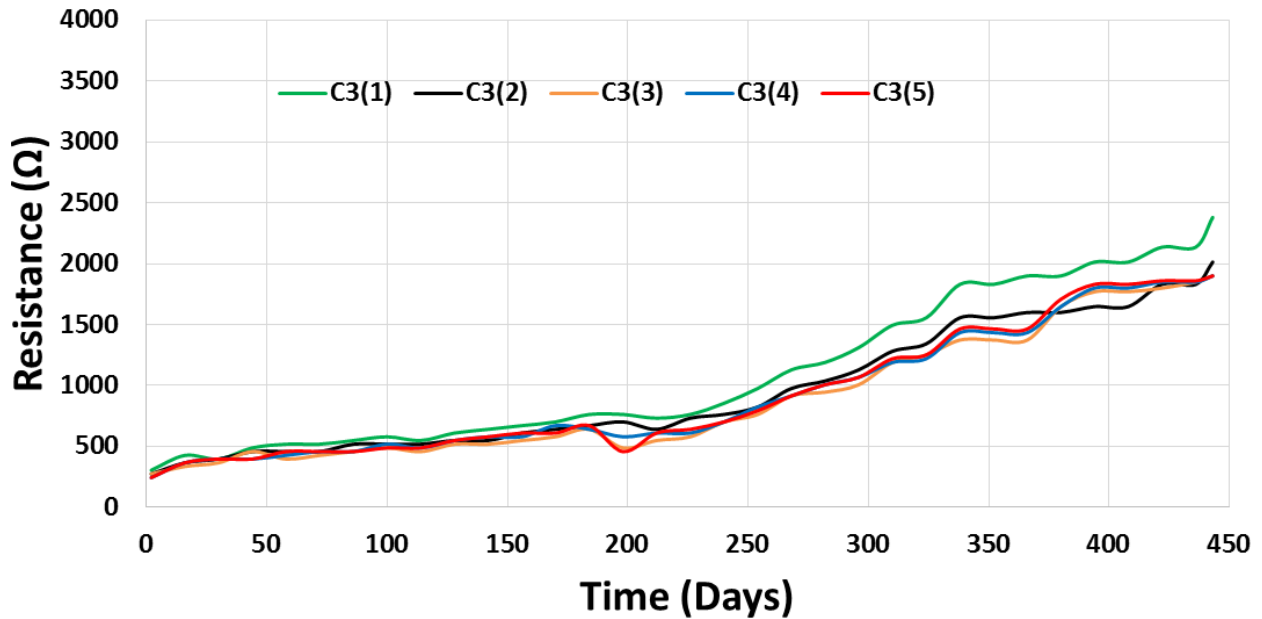


Figure C3.7: Sound (non-cracked) concrete beam.

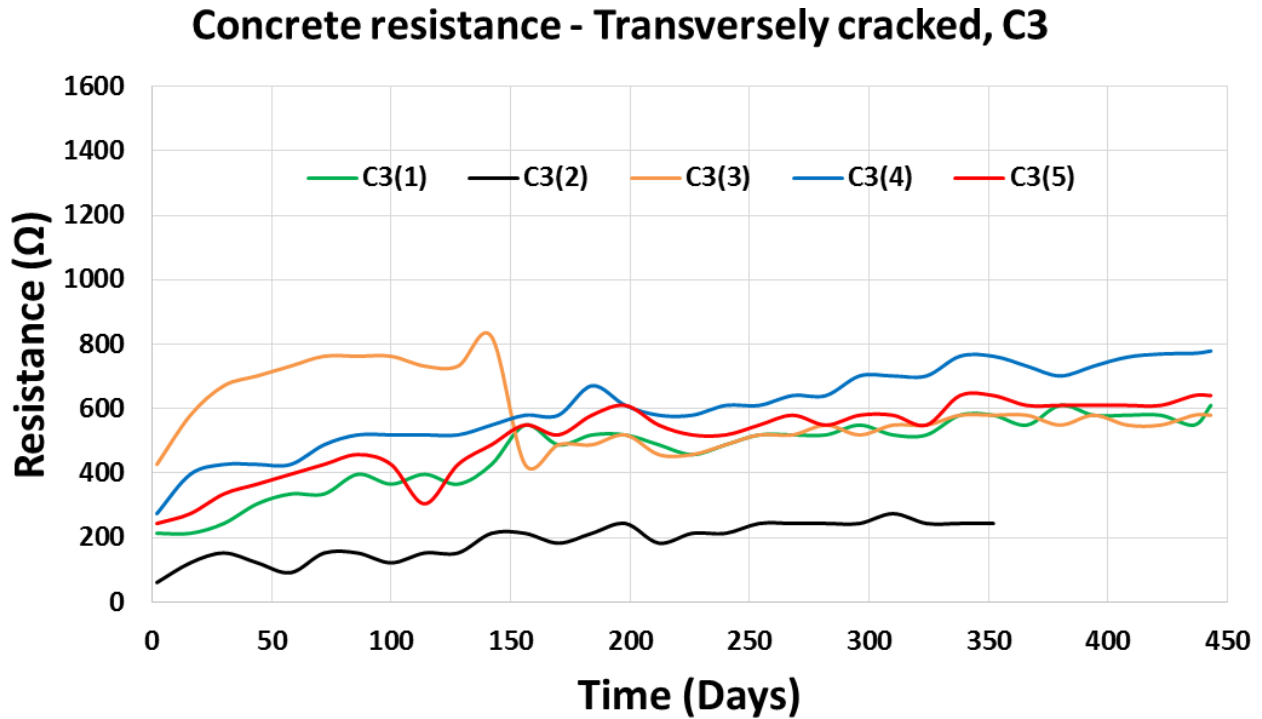


Figure C3.8: Crack width → C3(1) = 0.3, C3(2) = 1.5, C3(3) = 0.3, C3(4) = 0.2, C3(5) = 0.25.

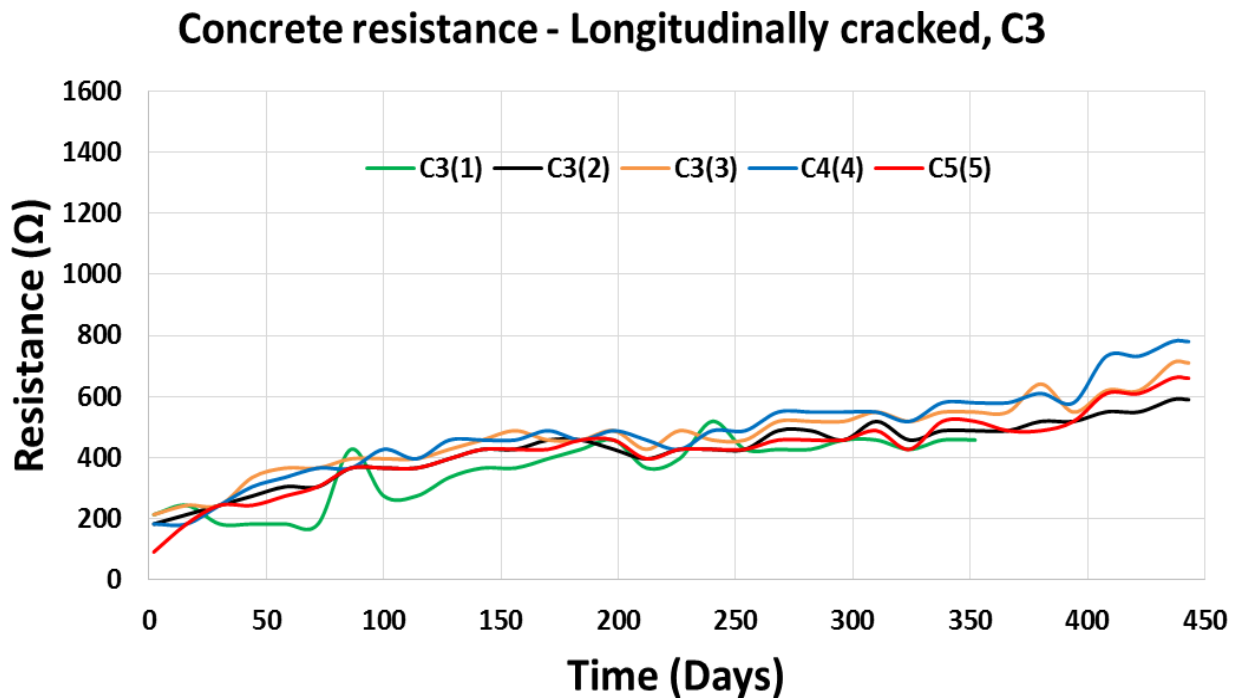


Figure C3.9: Crack width → C3(1) = 0.25, C3(2) = 0.2, C3(3) = 0.15, C3(4) = 0.15, C3(5) = 0.2.

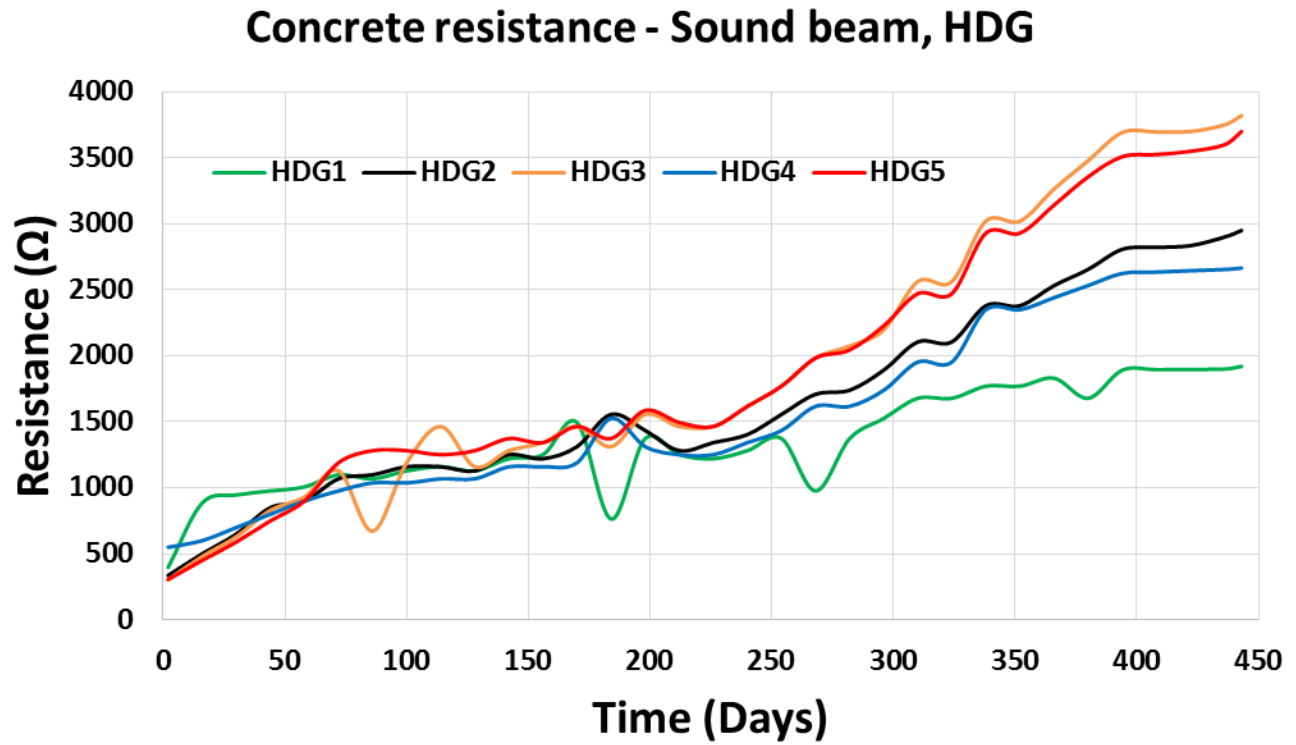


Figure C3.10 – Sound (non-cracked) concrete beam.

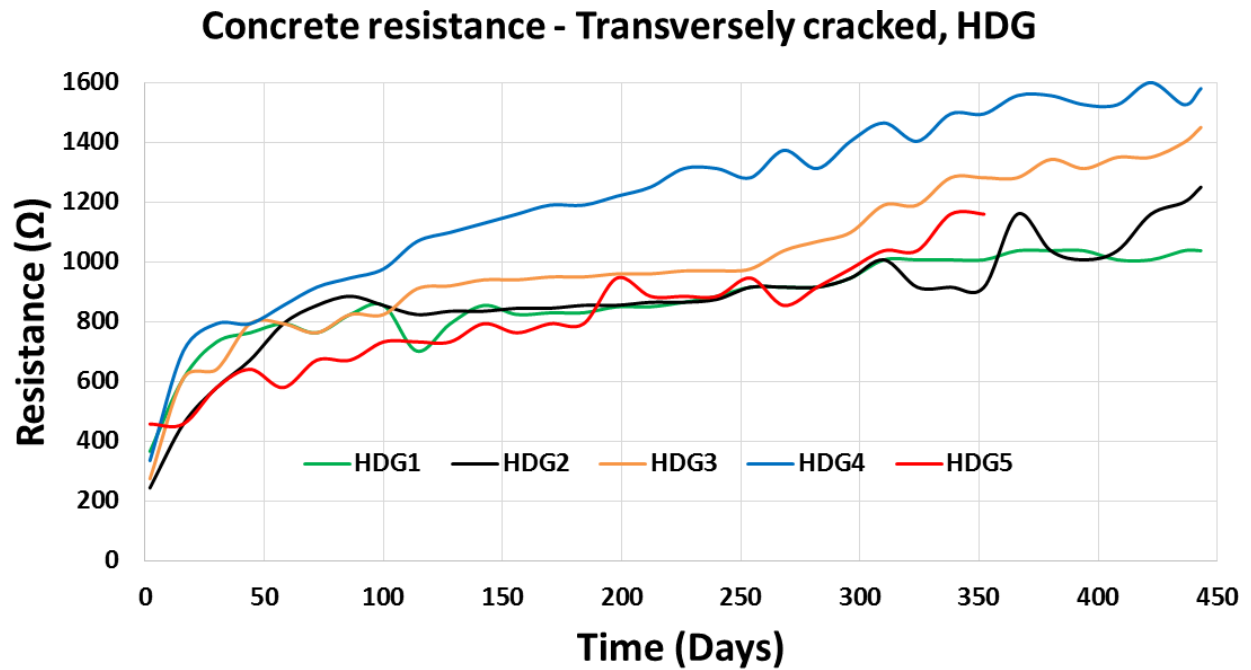


Figure C3.11: Crack width → HDG1 = 0.25, HDG2 = 0.3, HDG3 = 0.25, HDG4 = 0.15, HDG5 = 0.3.

Concrete resistance - Longitudinally cracked, HDG

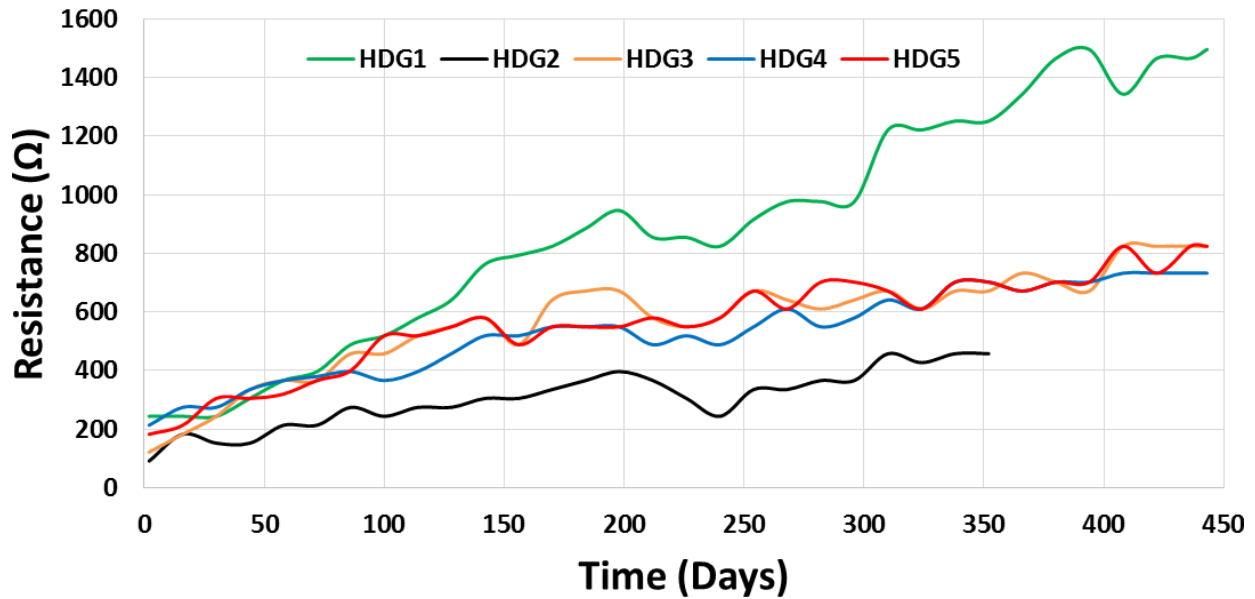


Figure C3.12: Crack width - HDG1 = 0.15, HDG2 = 0.25, HDG3 = 0.14, HDG4 = 0.15, HDG5 = 0.2.

Concrete resistance - Sound beam, Black

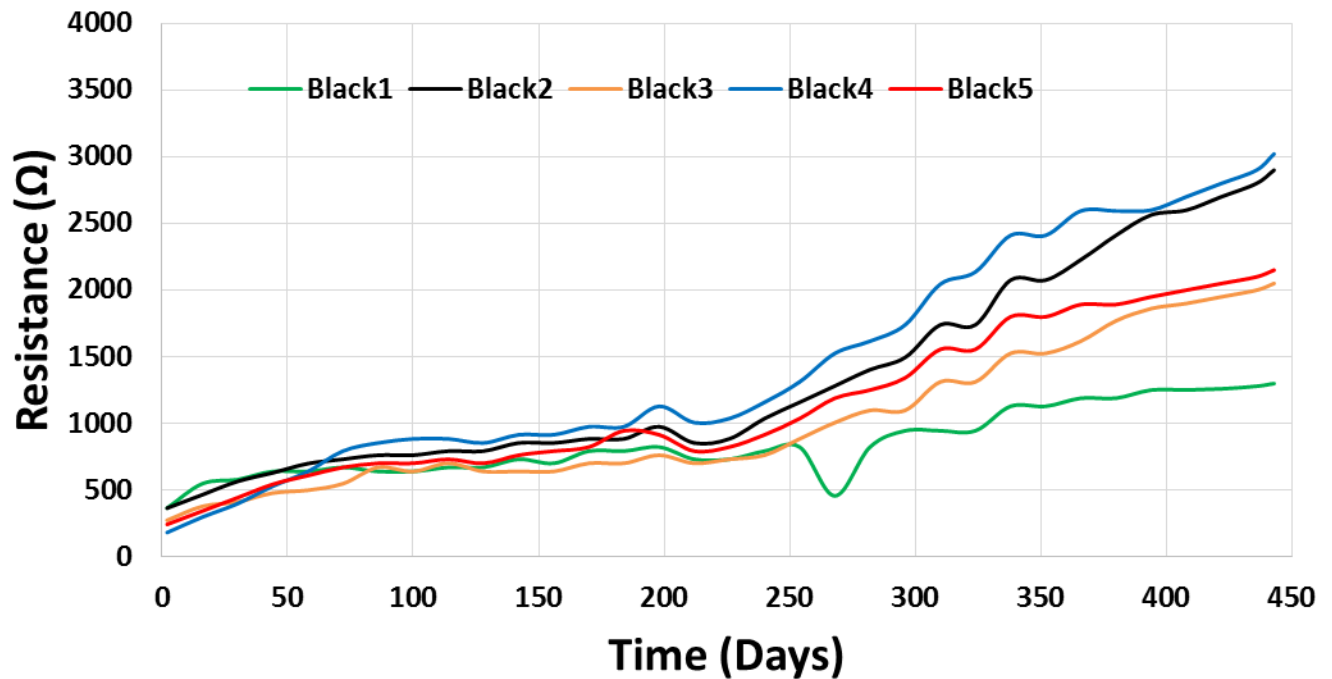


Figure C3.13: Sound (non-cracked) beam.

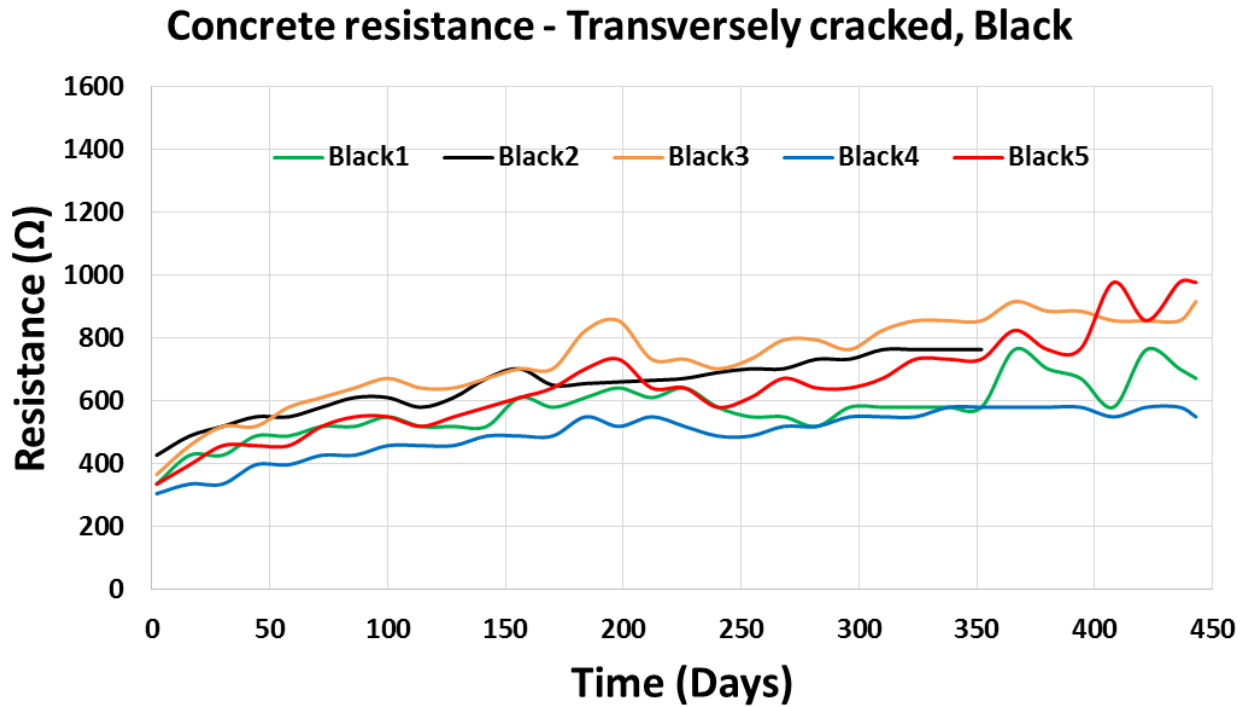


Figure C3.14 – Crack width → BLK1 = 0.15, BLK2 = 0.13, BLK3 = 0.26, BLK4 = 0.24, BLK5 = 0.15.

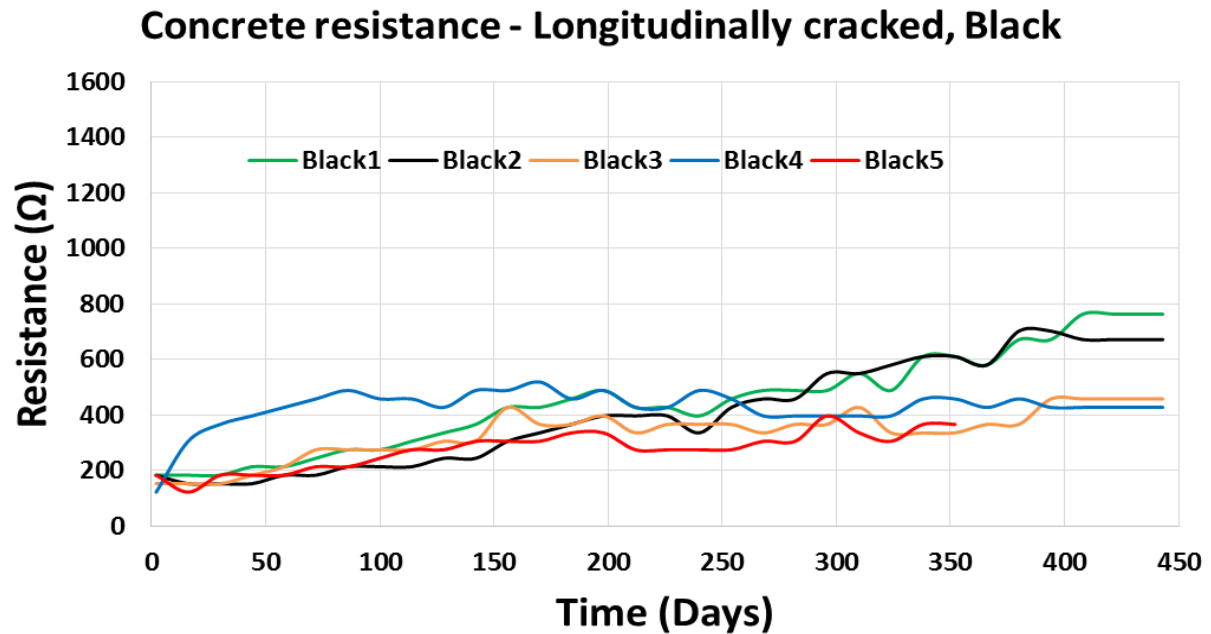


Figure C3.15 – Crack width → BLK1 = 0.25, BLK2 = 0.2, BLK3 = 0.14, BLK4 = 0.12, BLK5 = 0.25.

Appendix D– Micrographs

D1. Micrograph of specimen C1.

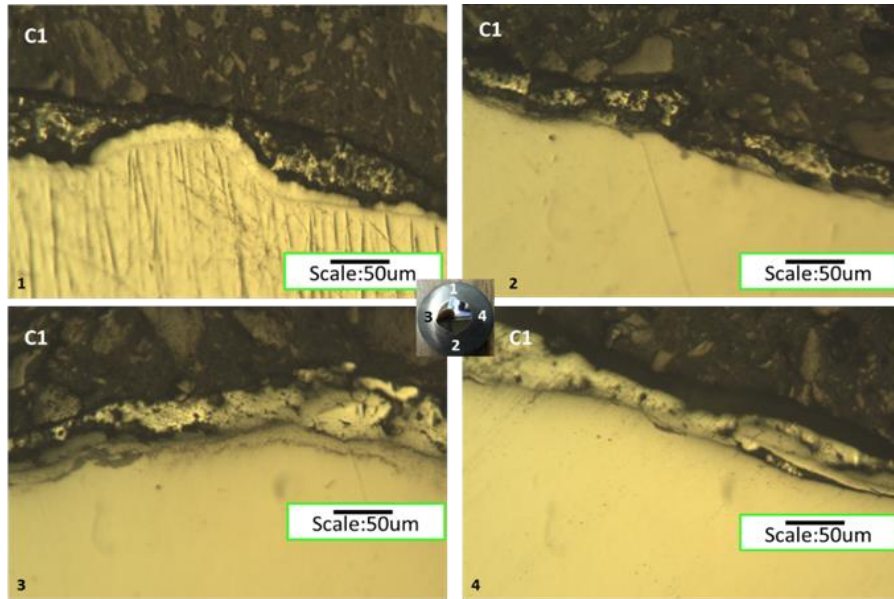


Figure D1.1: Optical microscopy image of polished C1 specimen.

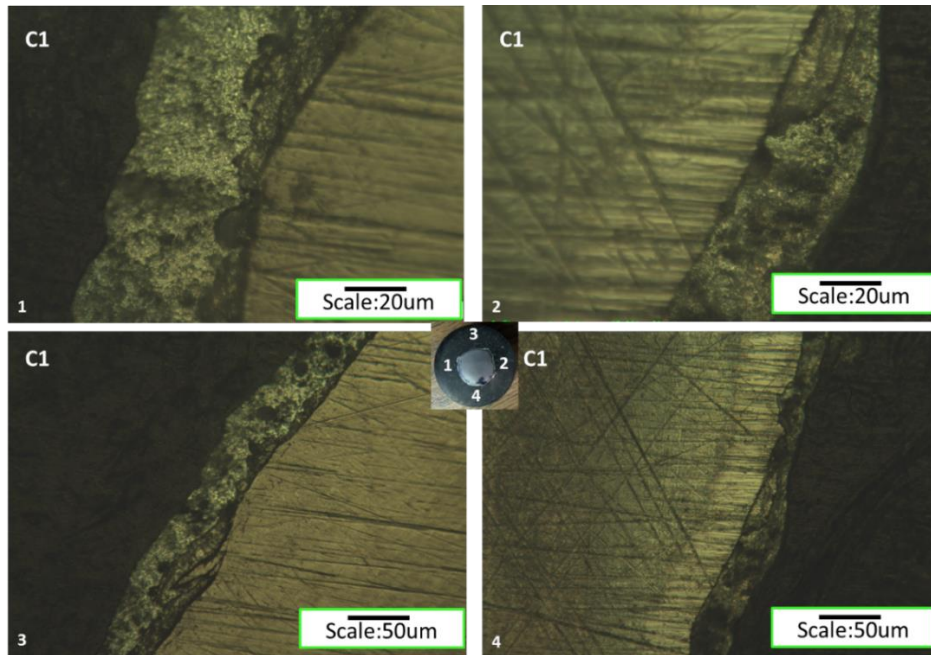


Figure D1.2: Optical microscopy image of etched C1 specimen.

D2. Micrograph of specimen C2

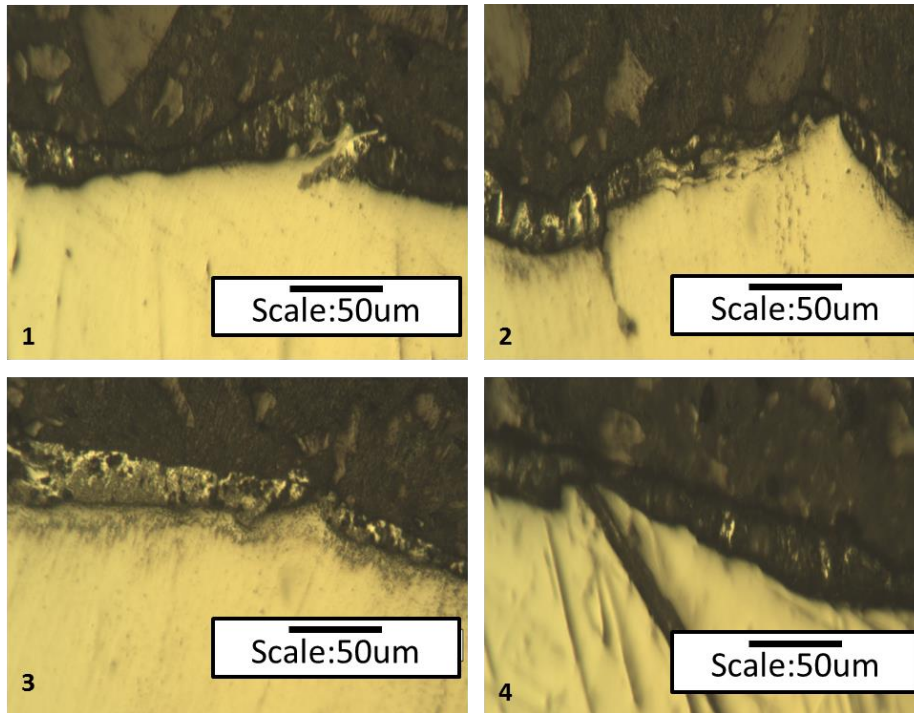


Figure D2.1: Optical microscopy image of polished C2 specimen

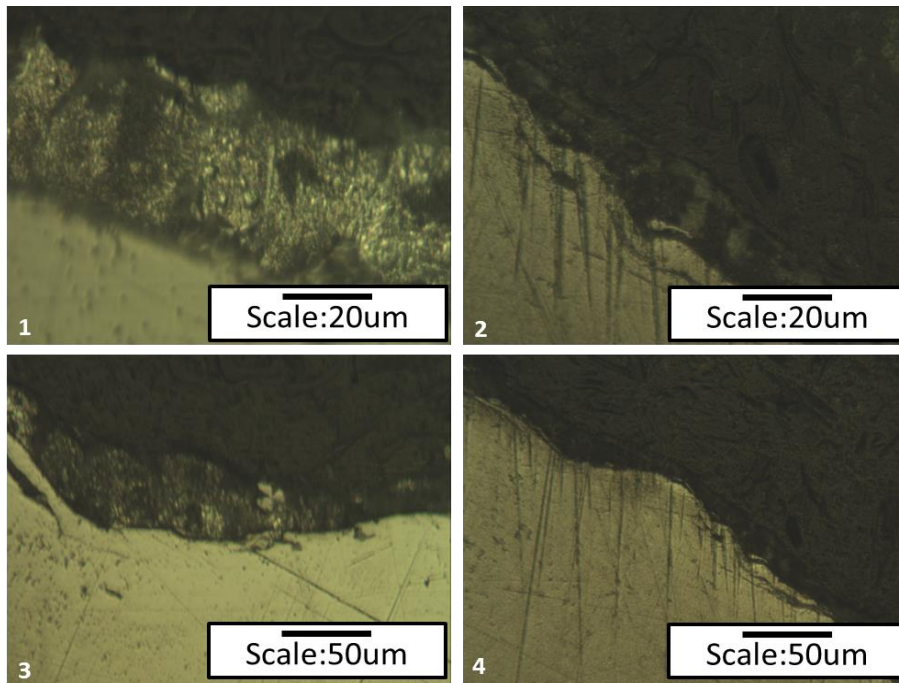


Figure D2.2: Optical microscopy image of etched C2 specimen

D3. Micrograph of specimen C3

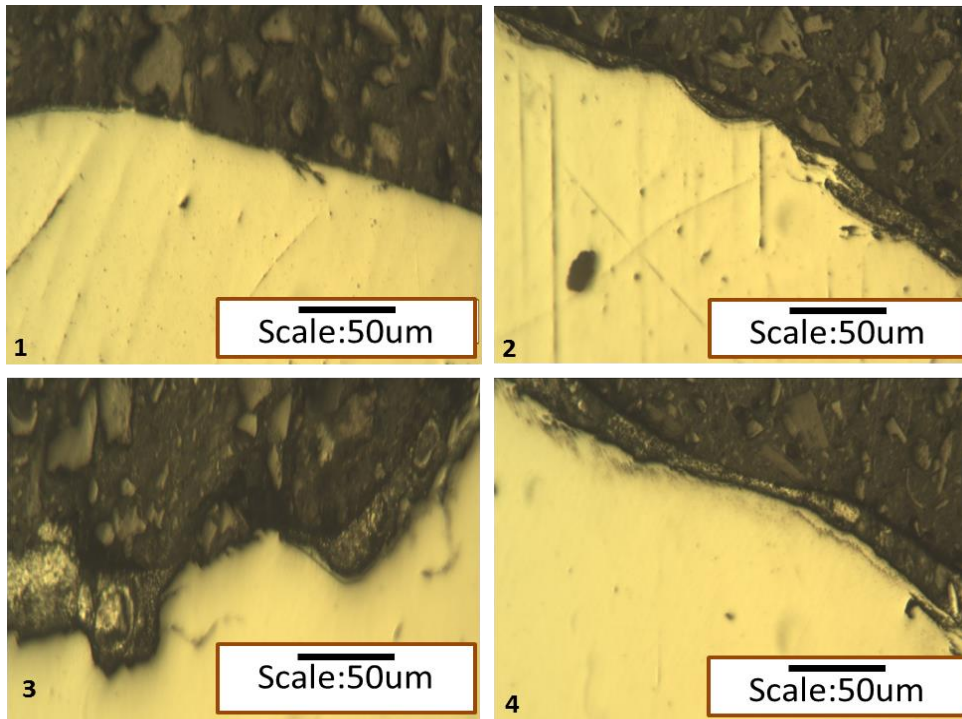


Figure D3.1: Optical microscopy image of polished C3 specimen

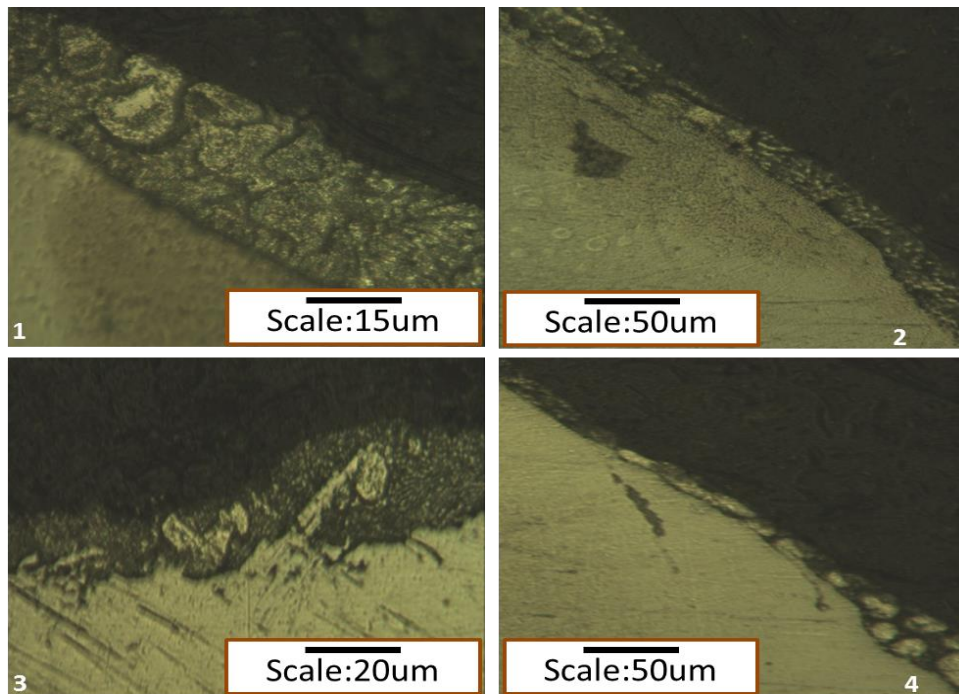


Figure D3.2: Optical microscopy image of etched C3 specimen.

D4. Micrograph of specimen HDG

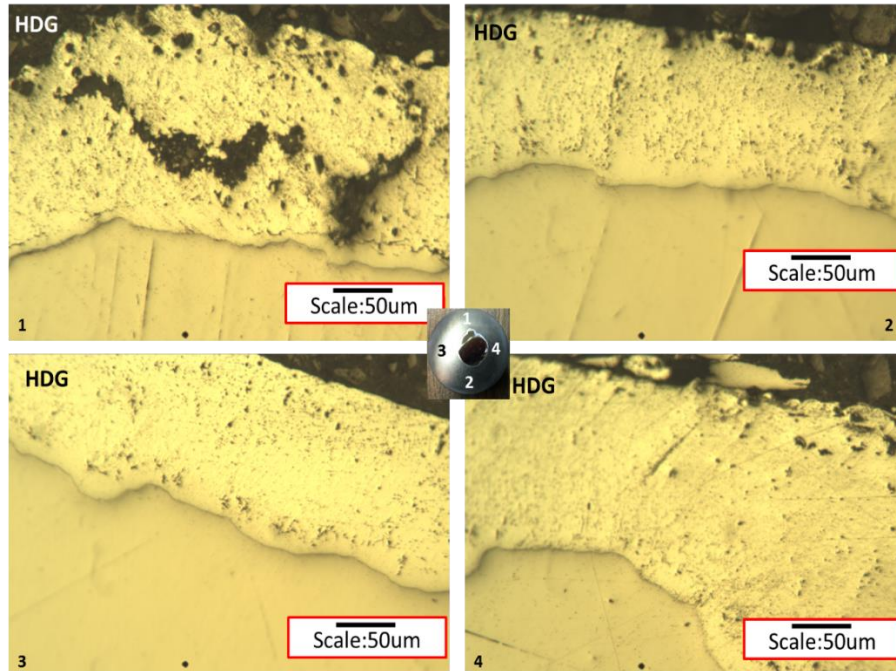


Figure D4.1: Optical microscopy image of polished HDG specimen

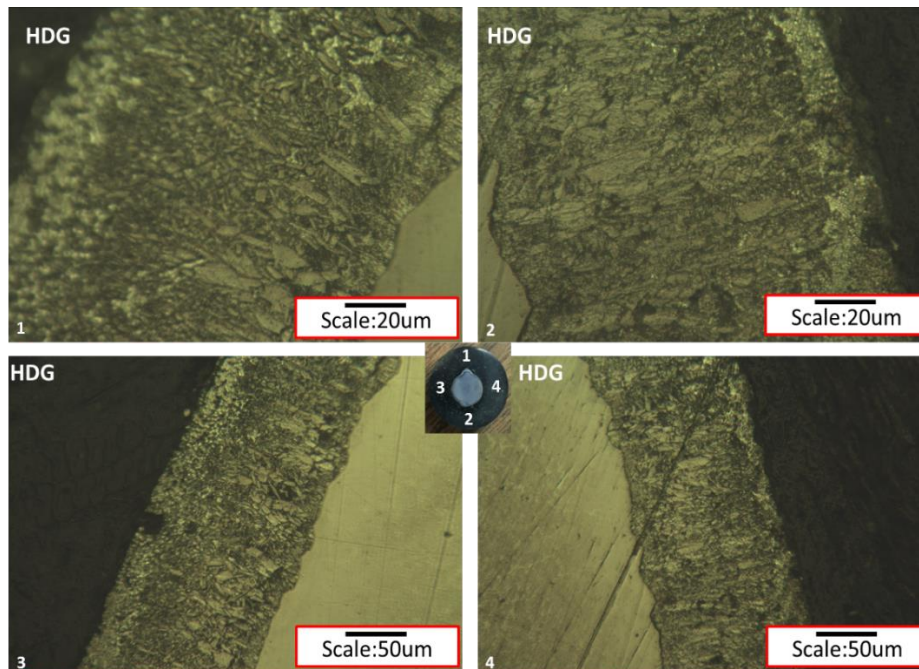


Figure D4.2: Optical microscopy image of etched HDG specimen

D5. Micrograph of galvanized specimen

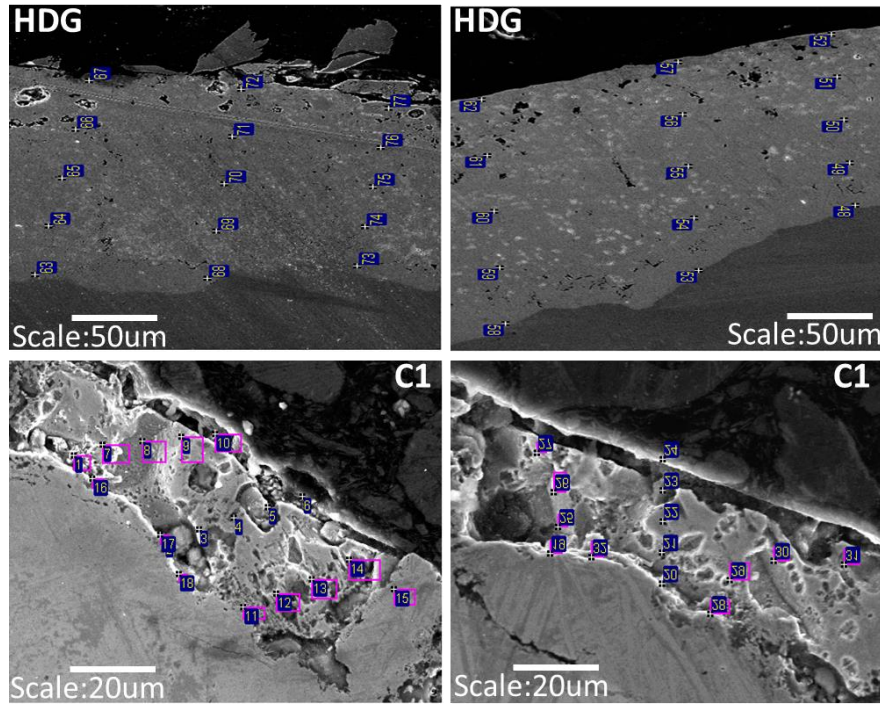


Figure D5.1: Scanning electron microscopy image of polished bar

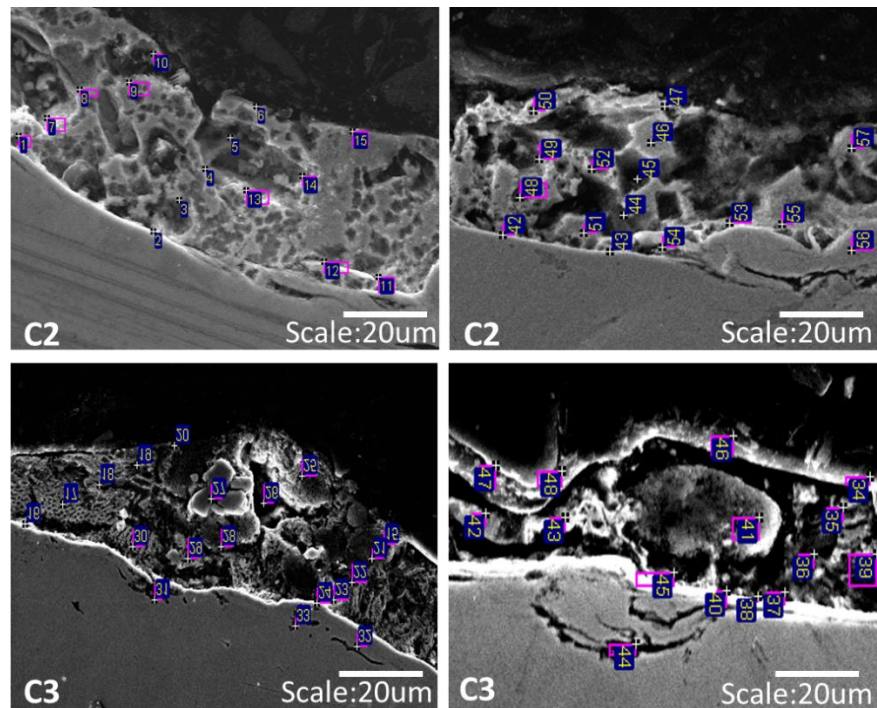


Figure D5.2: Scanning electron microscopy image of polished bar.

Appendix E – Autopsy specimens

E1. Initial autopsy

C1

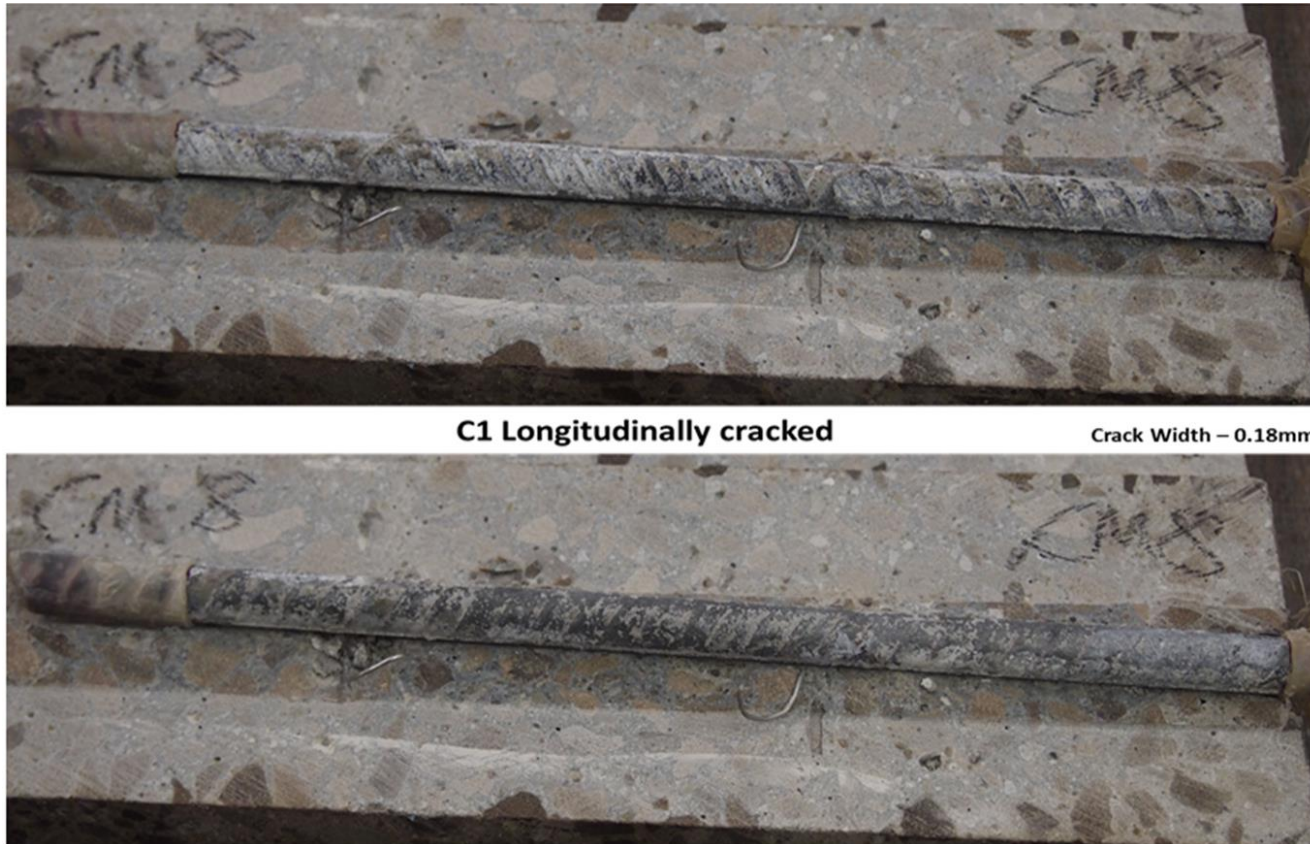


Figure E1.1.1: Concrete specimen of autopsied longitudinally cracked C1 specimen

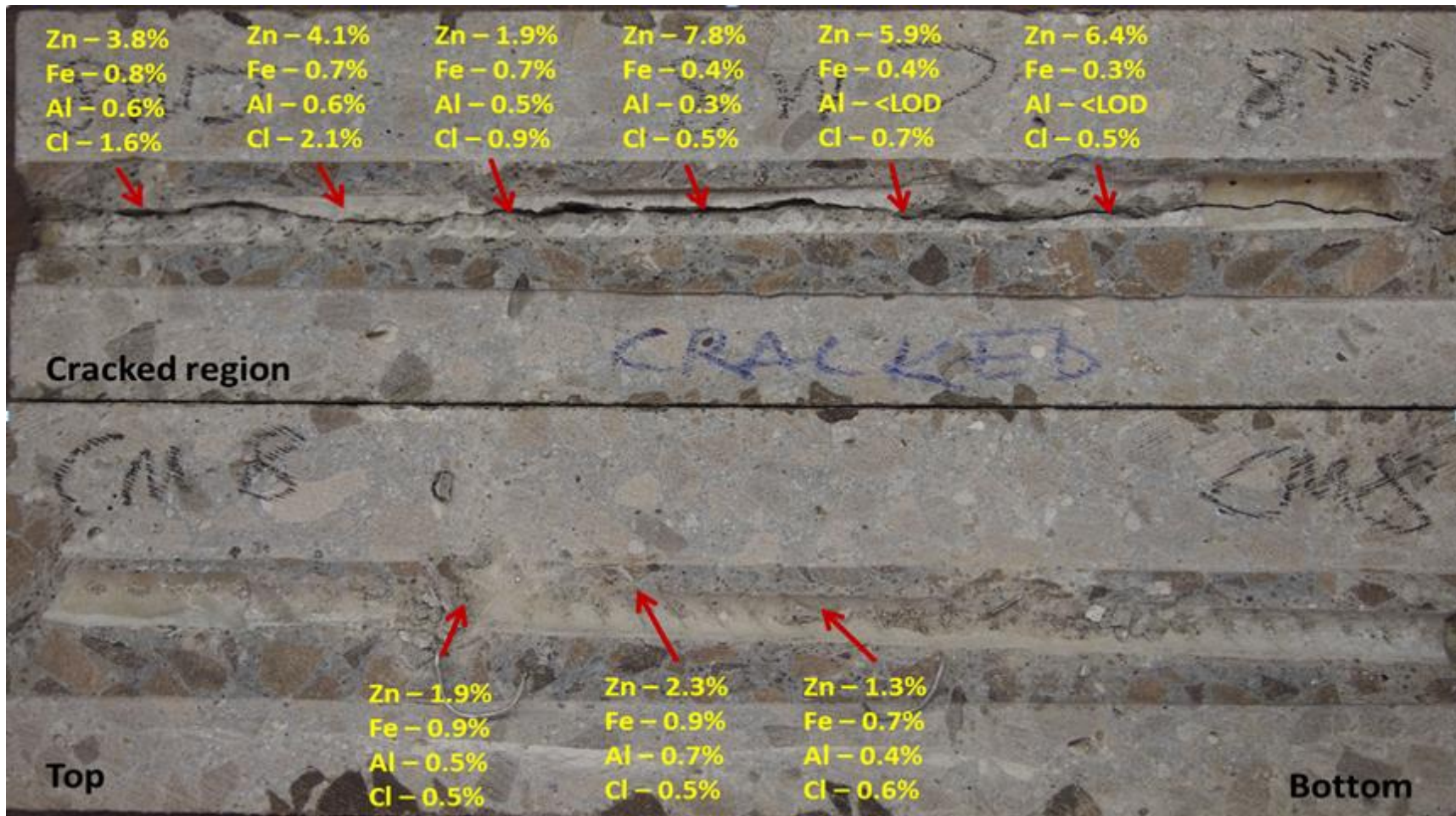


Figure E1.1.2: XRF analysis of autopsied longitudinally cracked C1 concrete specimen

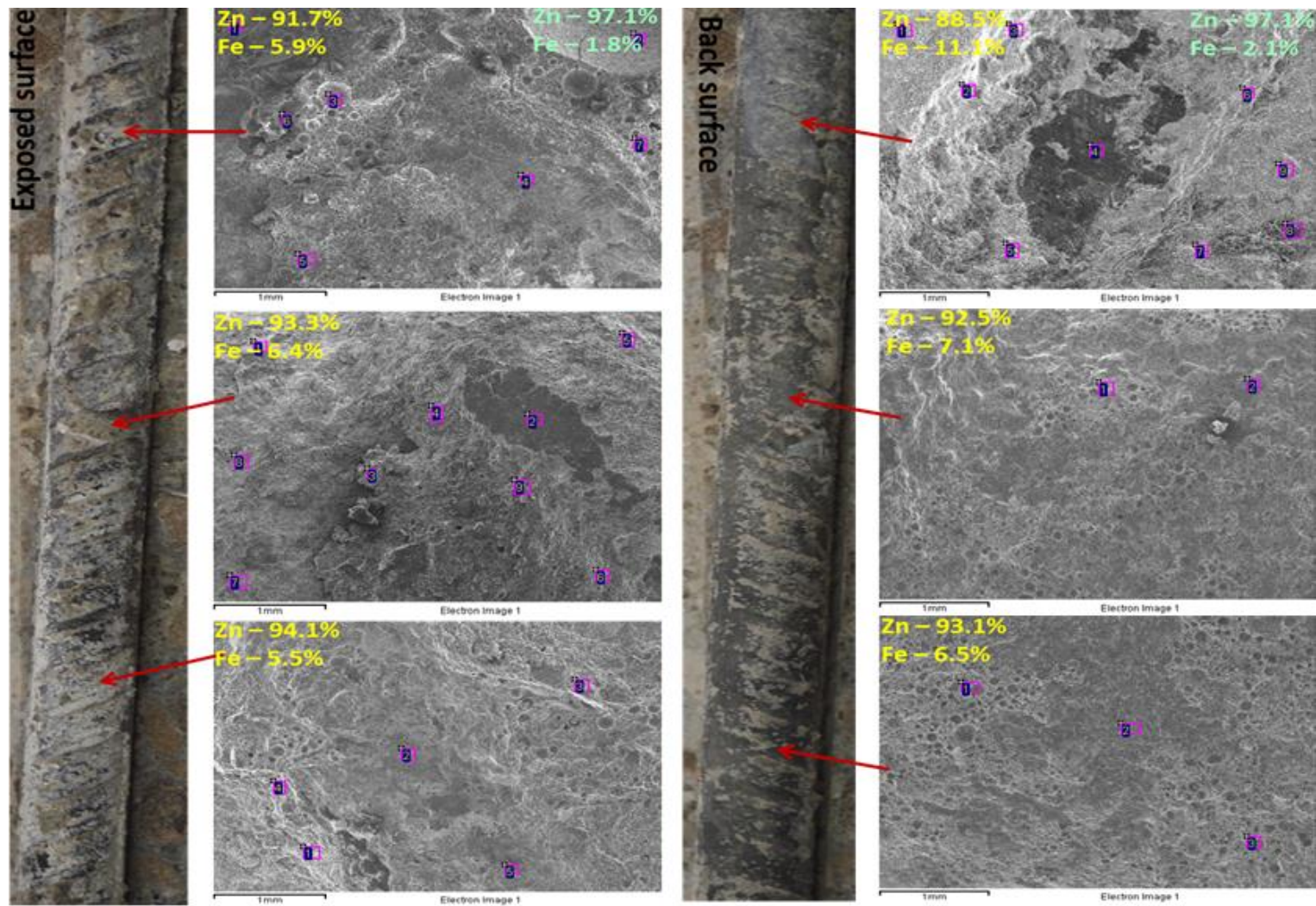


Figure E1.1.3: XRF analysis of autopsied C1 steel specimen. Note: values in green and yellow are before and after corrosion testing.

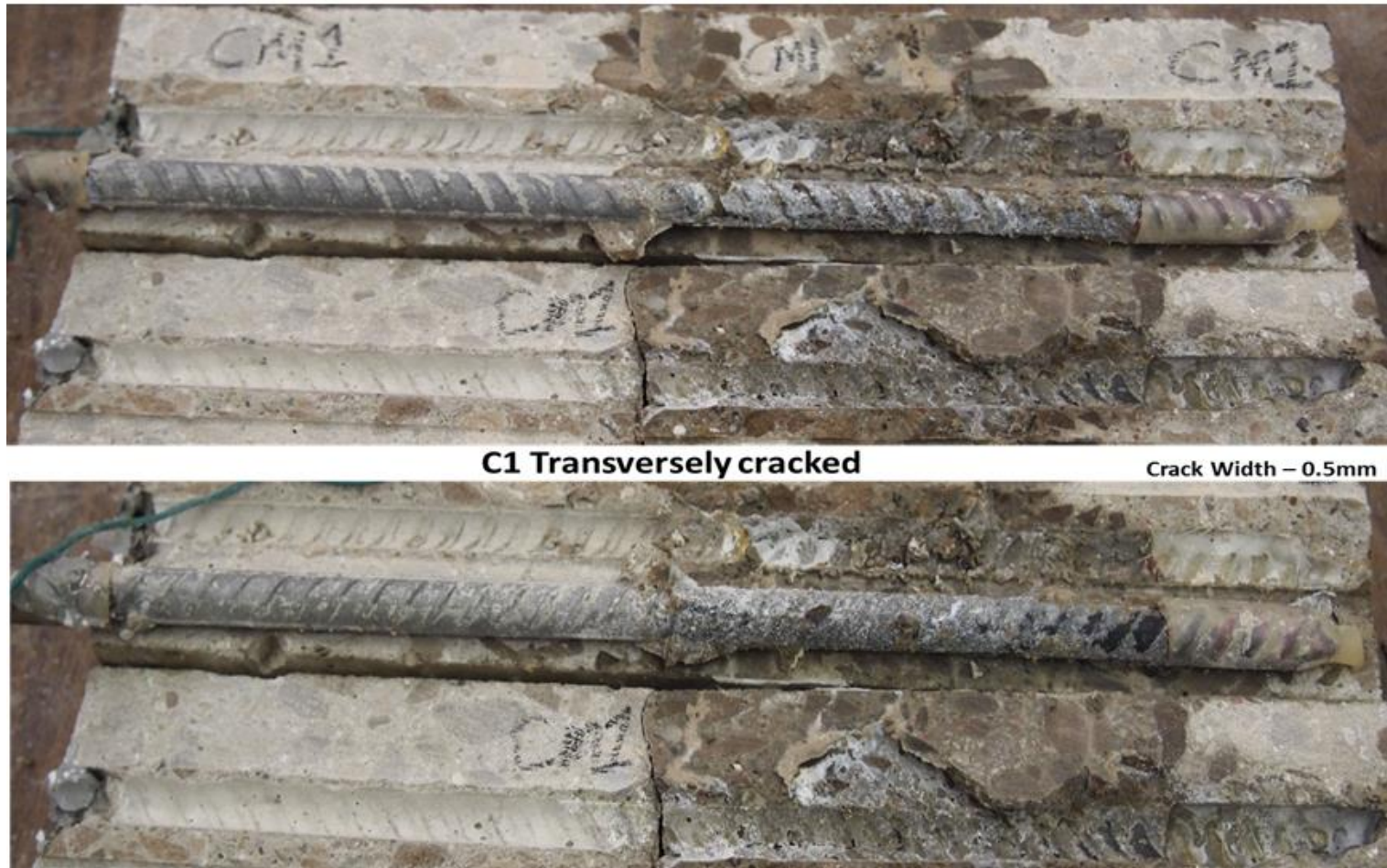


Figure E1.1.4: Concrete specimen of autopsied transversely cracked C1 specimen

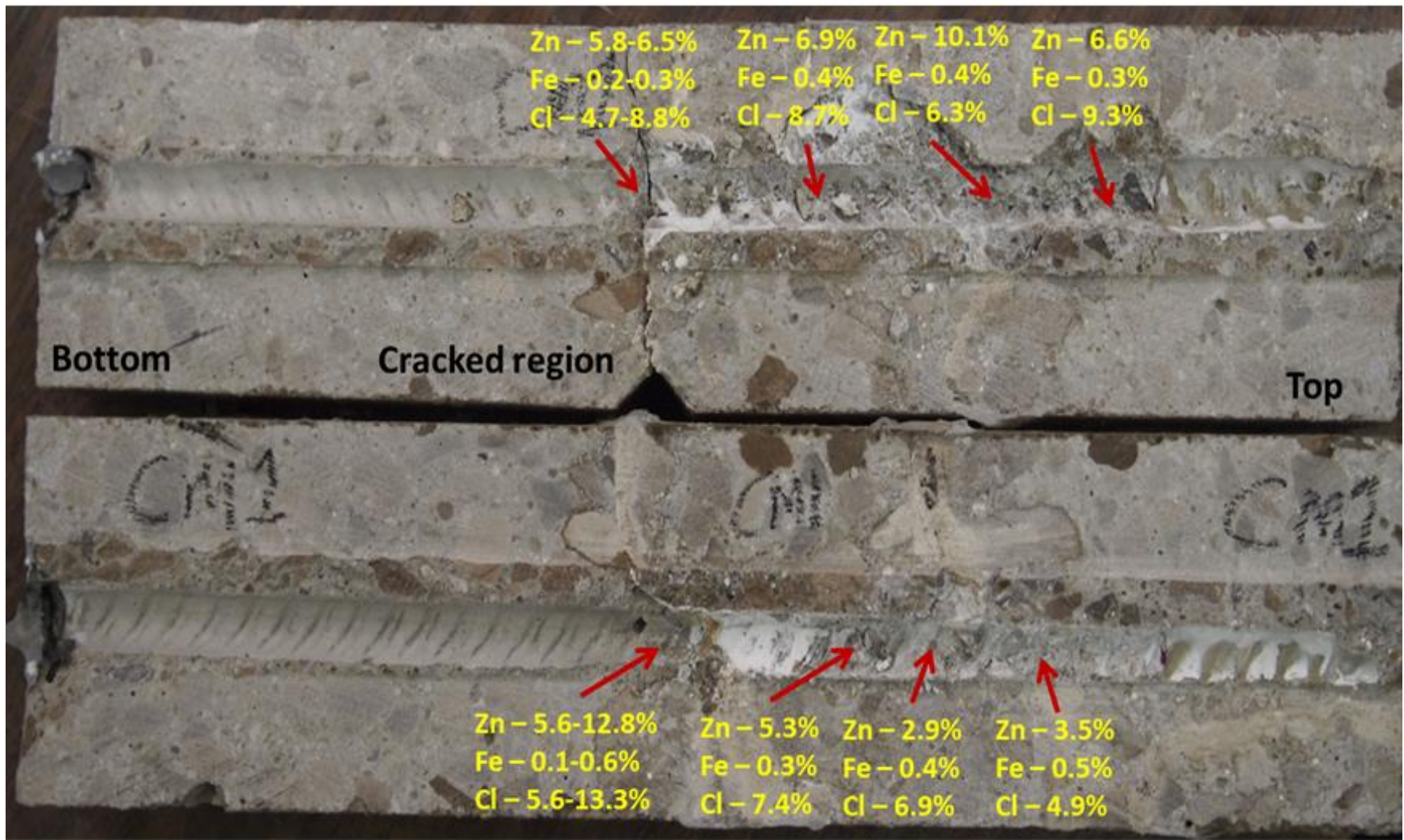


Figure E1.1.5: XRF analysis of autopsied transversely cracked C1 concrete specimen

C2



C2 Longitudinally cracked

Crack Width – 0.14mm



Figure E1.2.1: Concrete specimen of autopsied longitudinally cracked C2 specimen

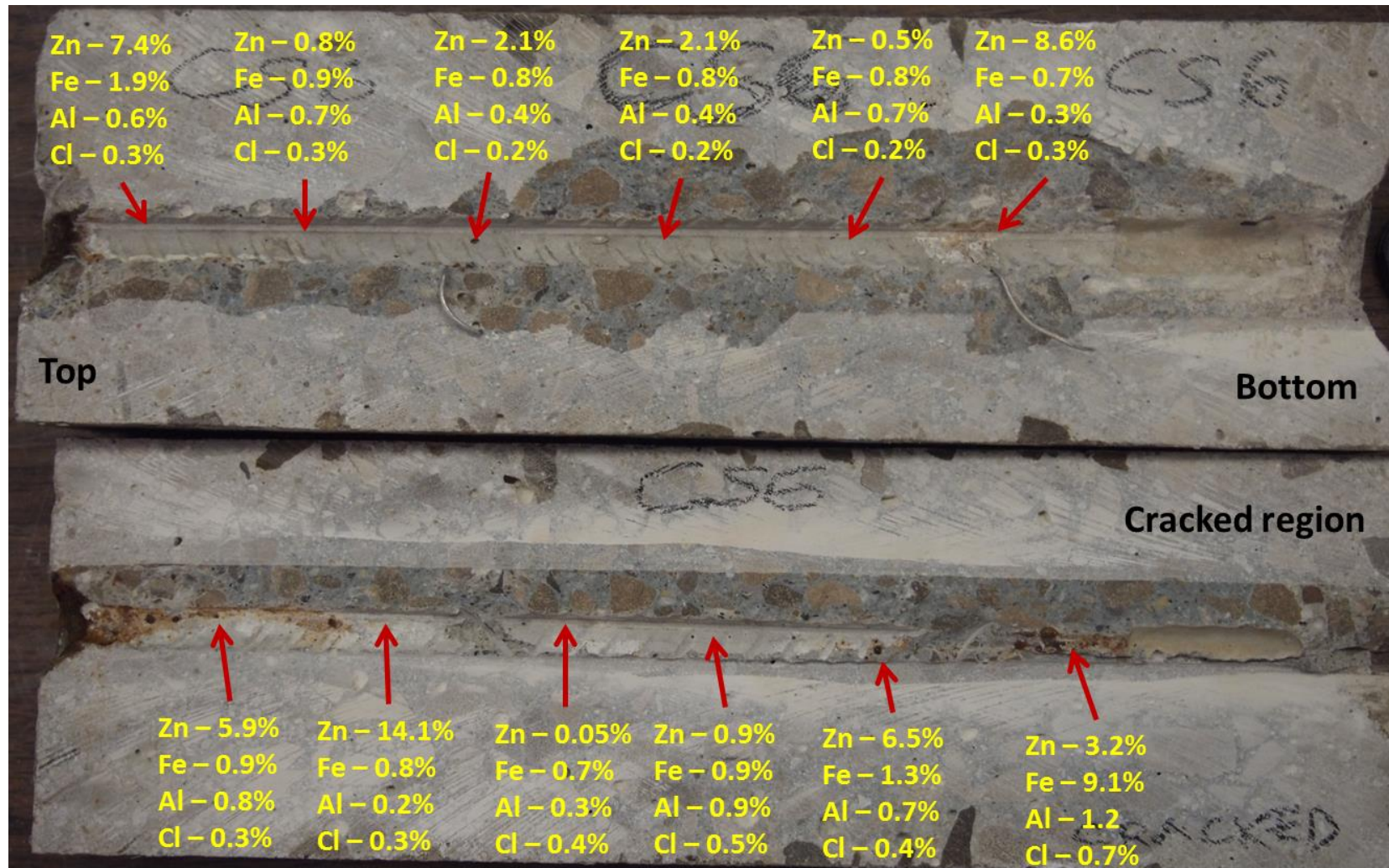


Figure E1.2.2: XRF analysis of autopsied longitudinally cracked C2 concrete specimen

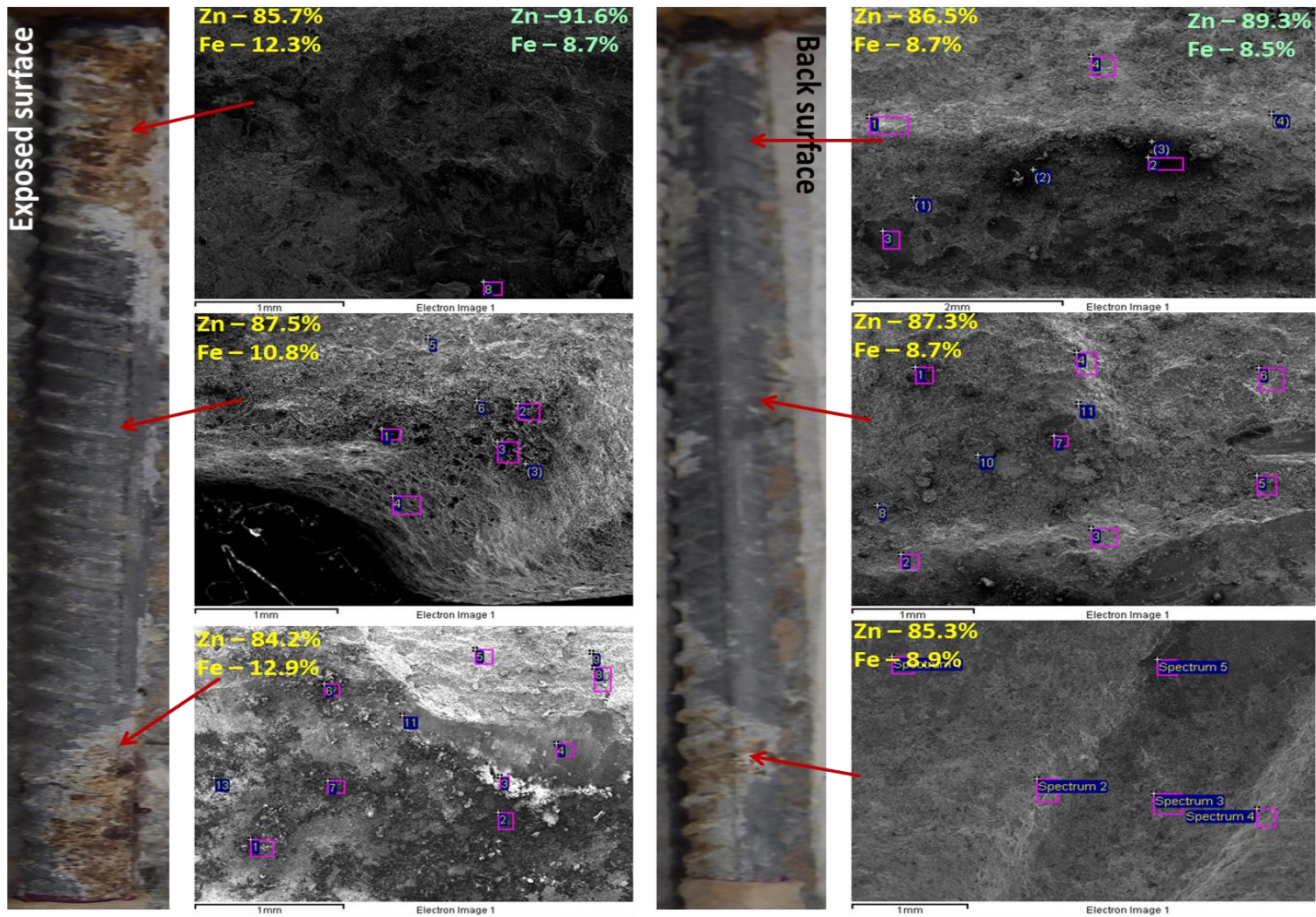


Figure E1.2.3: XRF analysis of autopsy C2 steel specimen. Note: values in green and yellow are before and after corrosion testing.



C2 Transversely cracked

Crack Width – 0.13mm



Figure E1.2.4: Concrete specimen of autopsied transversely cracked C2 specimen.

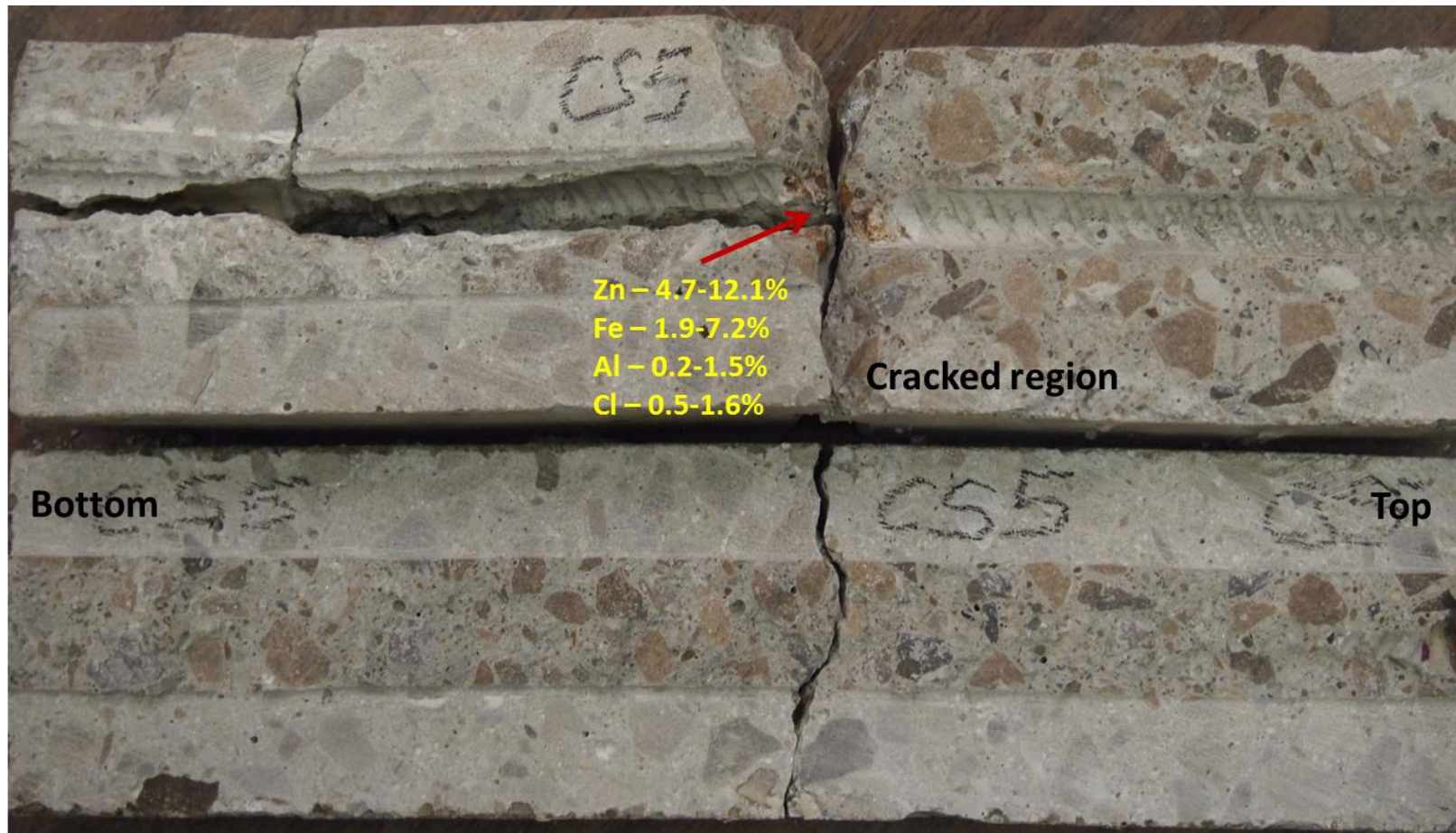


Figure E1.2.5: XRF analysis of autopsied transversely cracked C2 concrete specimen

C3



C3 Longitudinally cracked

Crack Width – 0.25mm



Figure E1.3.1: Concrete specimen of autopsied longitudinally cracked C3 specimen

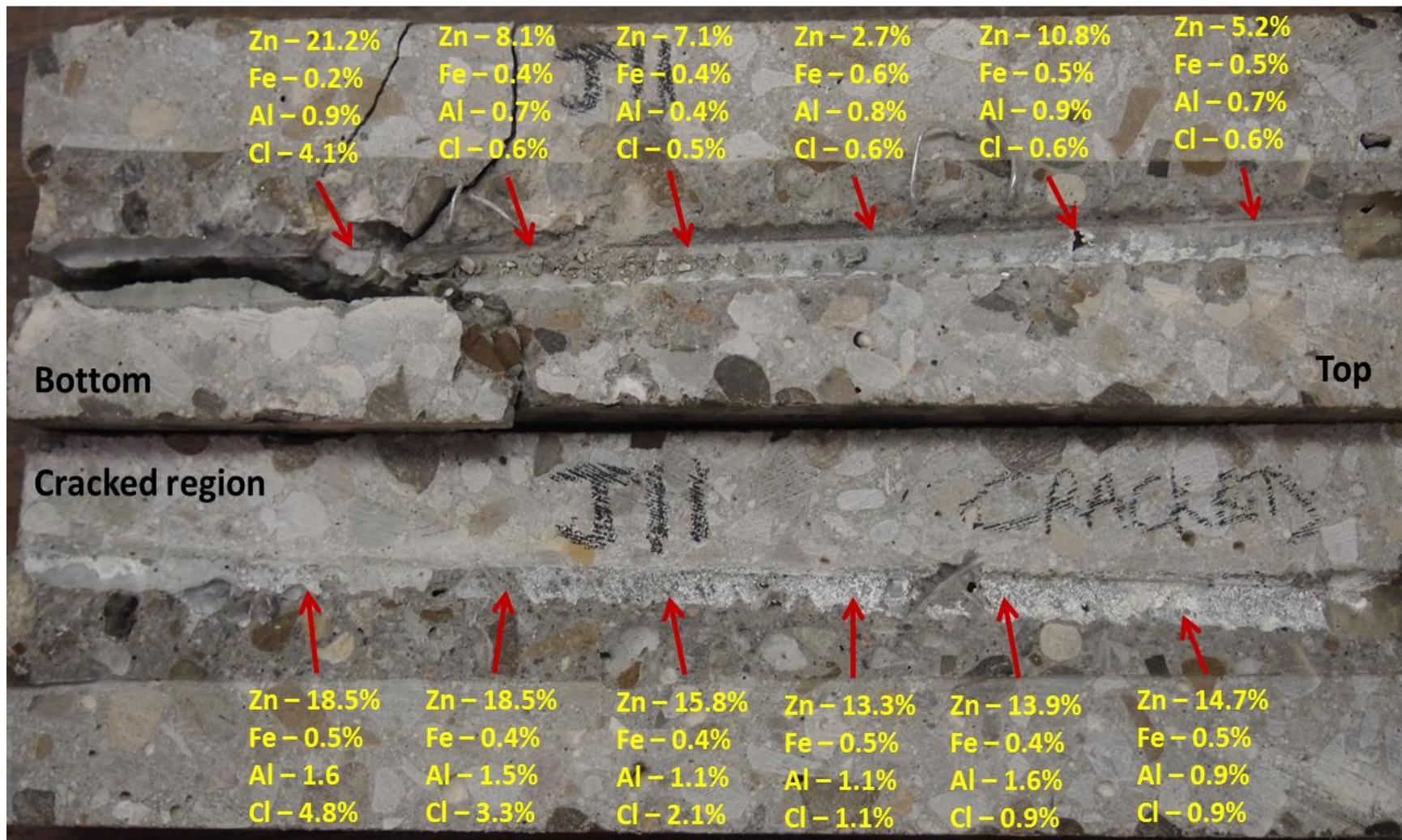


Figure E1.3.2: XRF analysis of autopsied longitudinally cracked C3 concrete specimen

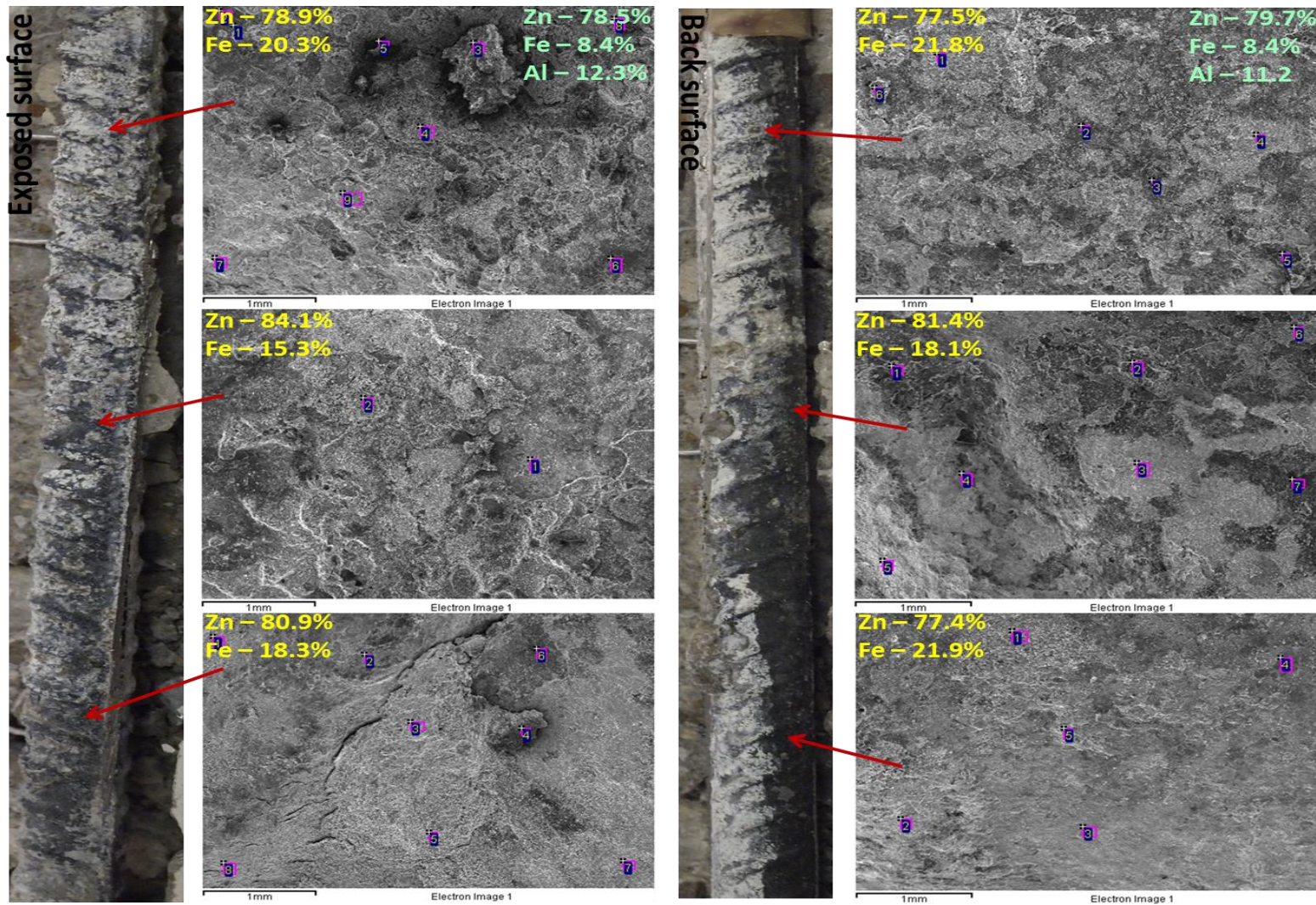


Figure E1.3.3: XRF analysis of autopsied C3 steel specimen. Note: values in green and yellow are before and after corrosion testing.



C3 Transversely cracked

Crack Width – 1.5mm



Figure E1.3.4: Concrete specimen of autopsied transversely cracked C3 specimen.

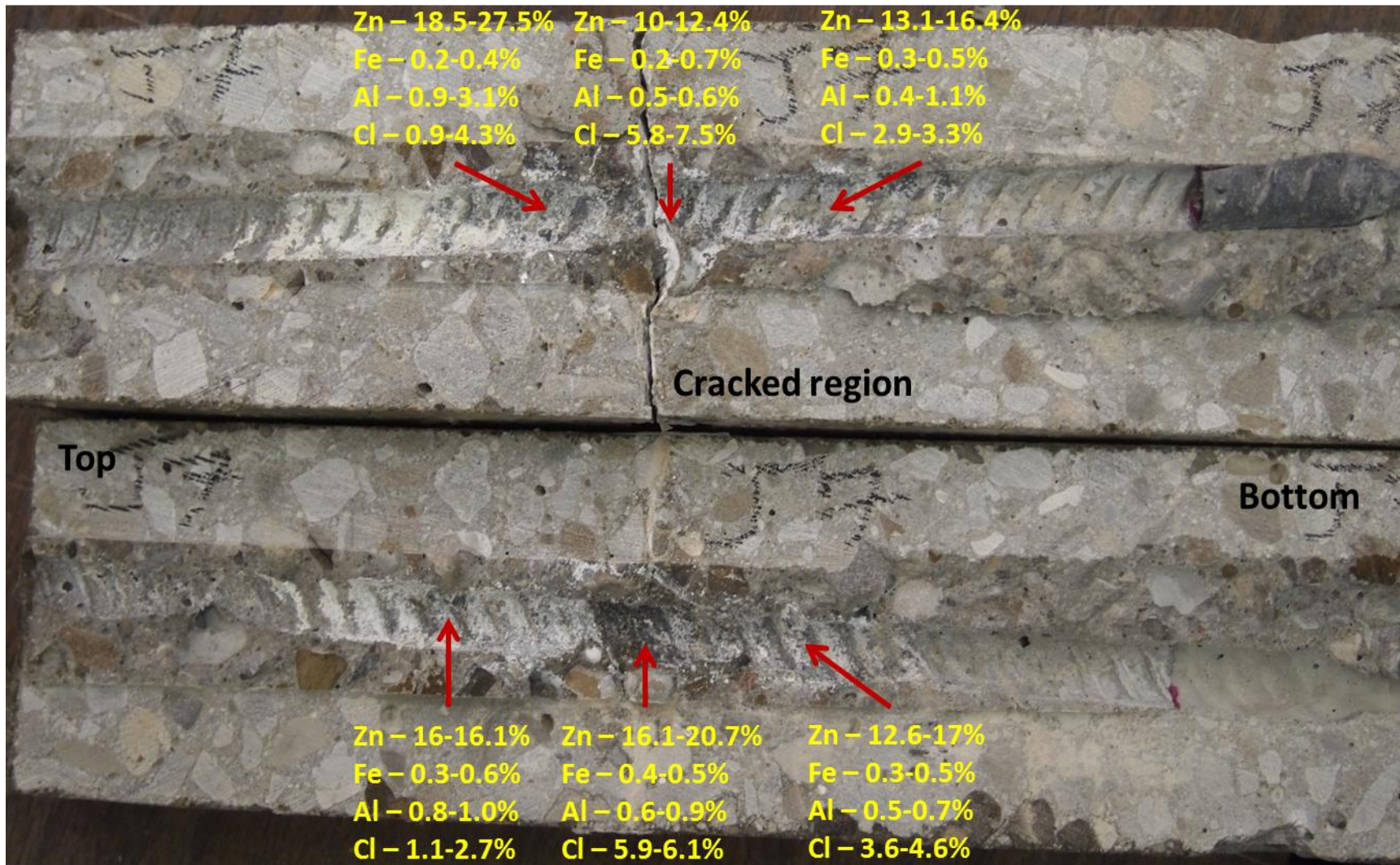


Figure E1.3.5: XRF analysis of autopsied transversely cracked C3 concrete specimen

HDG



HDG Longitudinally cracked

Crack Width – 0.25mm



Figure E1.4.1: Concrete specimen of autopsied longitudinally cracked HDG specimen.

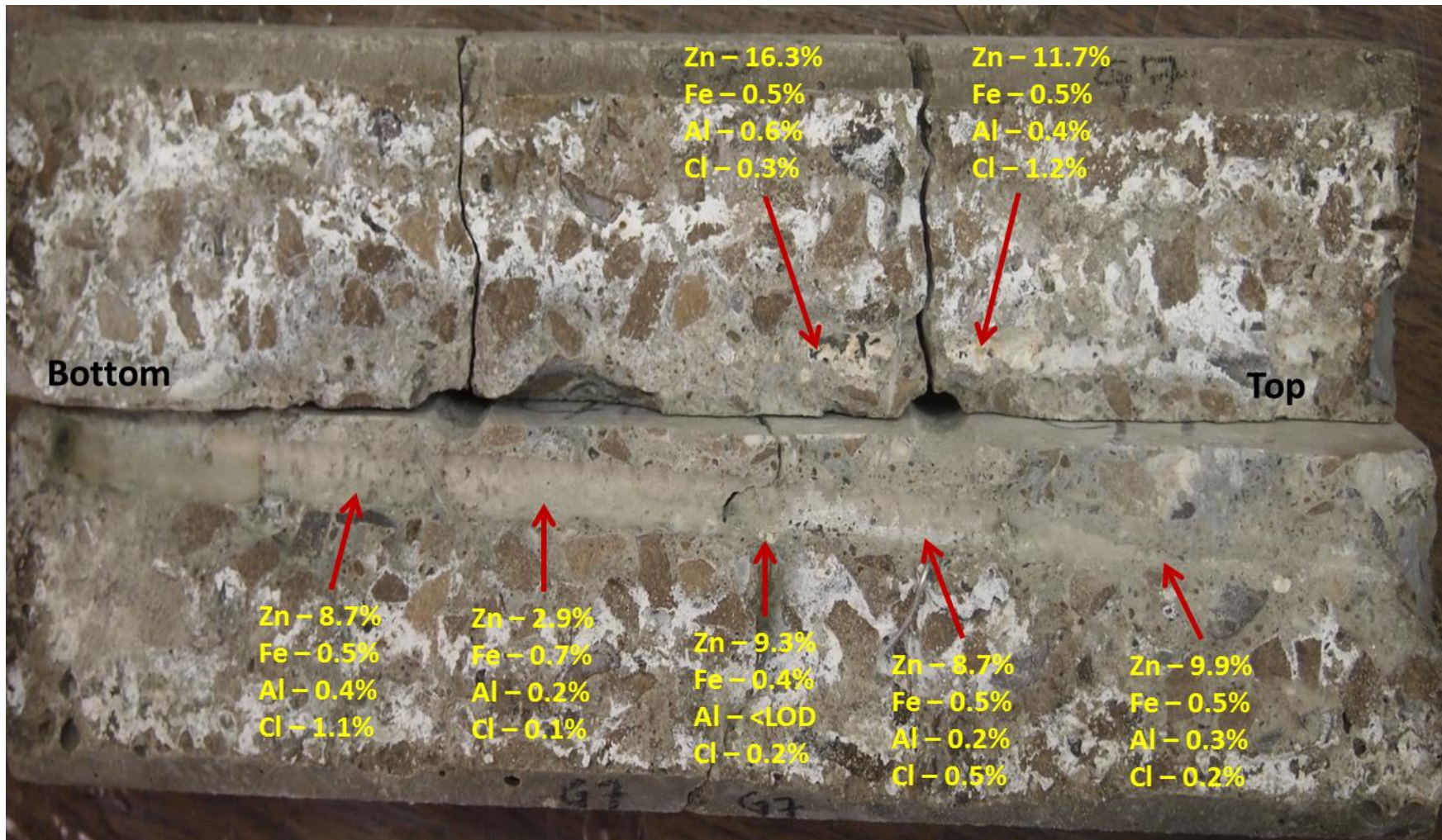


Figure E1.4.2: XRF analysis of autopsied longitudinally cracked HDG concrete specimen.

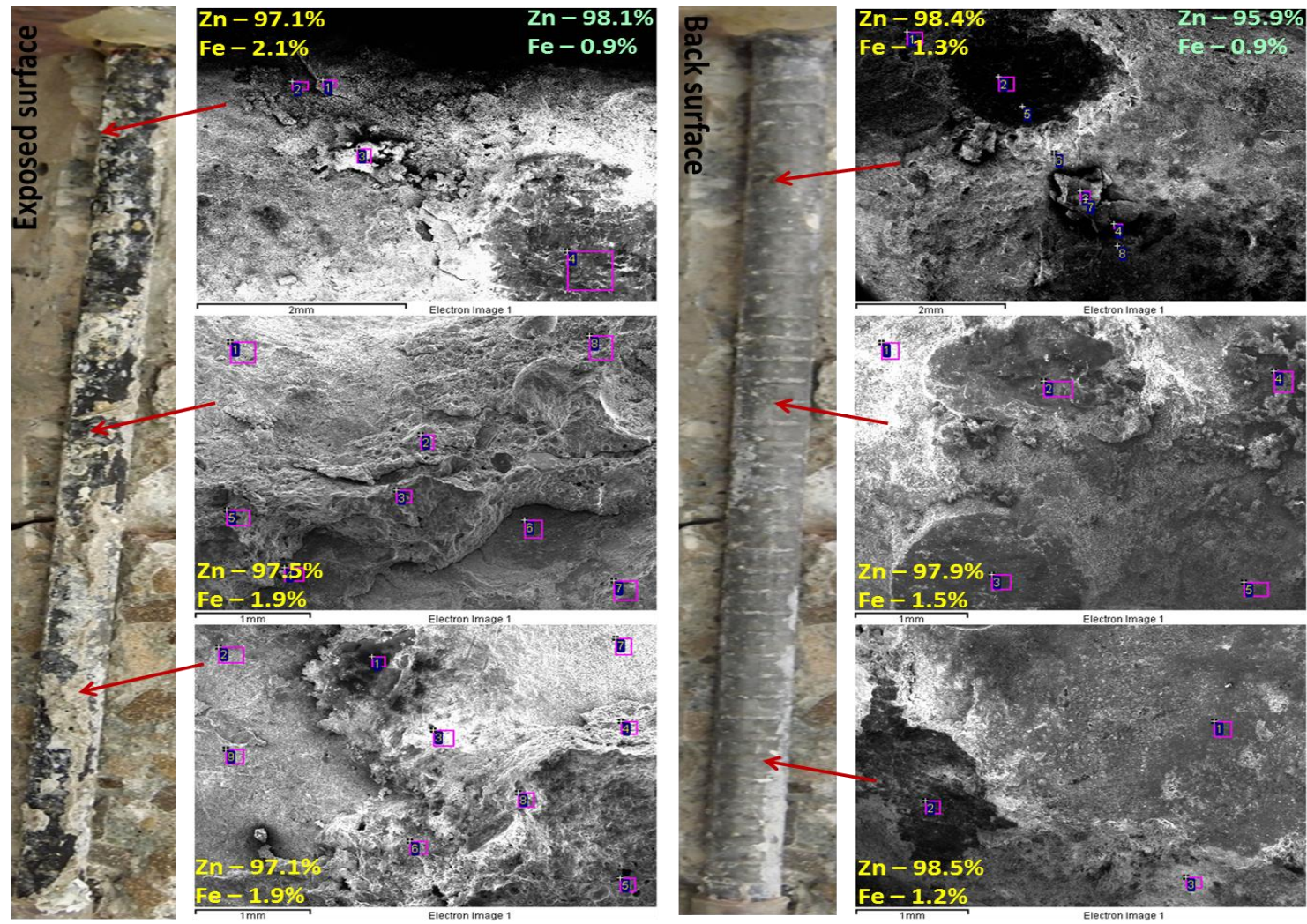


Figure E1.4.3: XRF analysis of autopsied HDG steel specimen. Note: values in green and yellow are before and after corrosion testing.



HDG Transversely cracked

Crack Width – 0.3mm



Figure E1.4.4: Concrete specimen of autopsied transversely cracked HDG specimen.

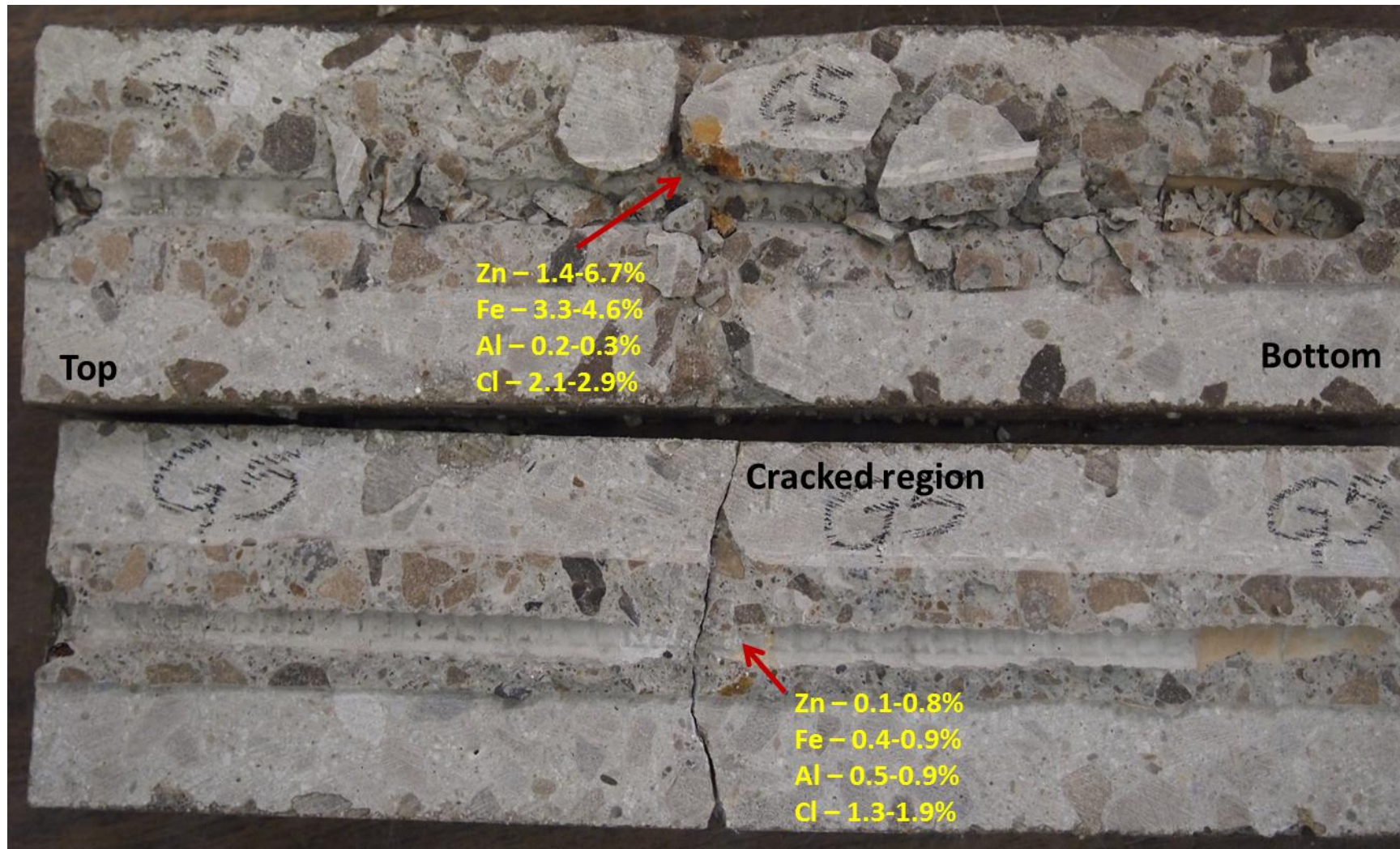


Figure E1.4.5: XRF analysis of autopsied transversely cracked HDG concrete specimen.

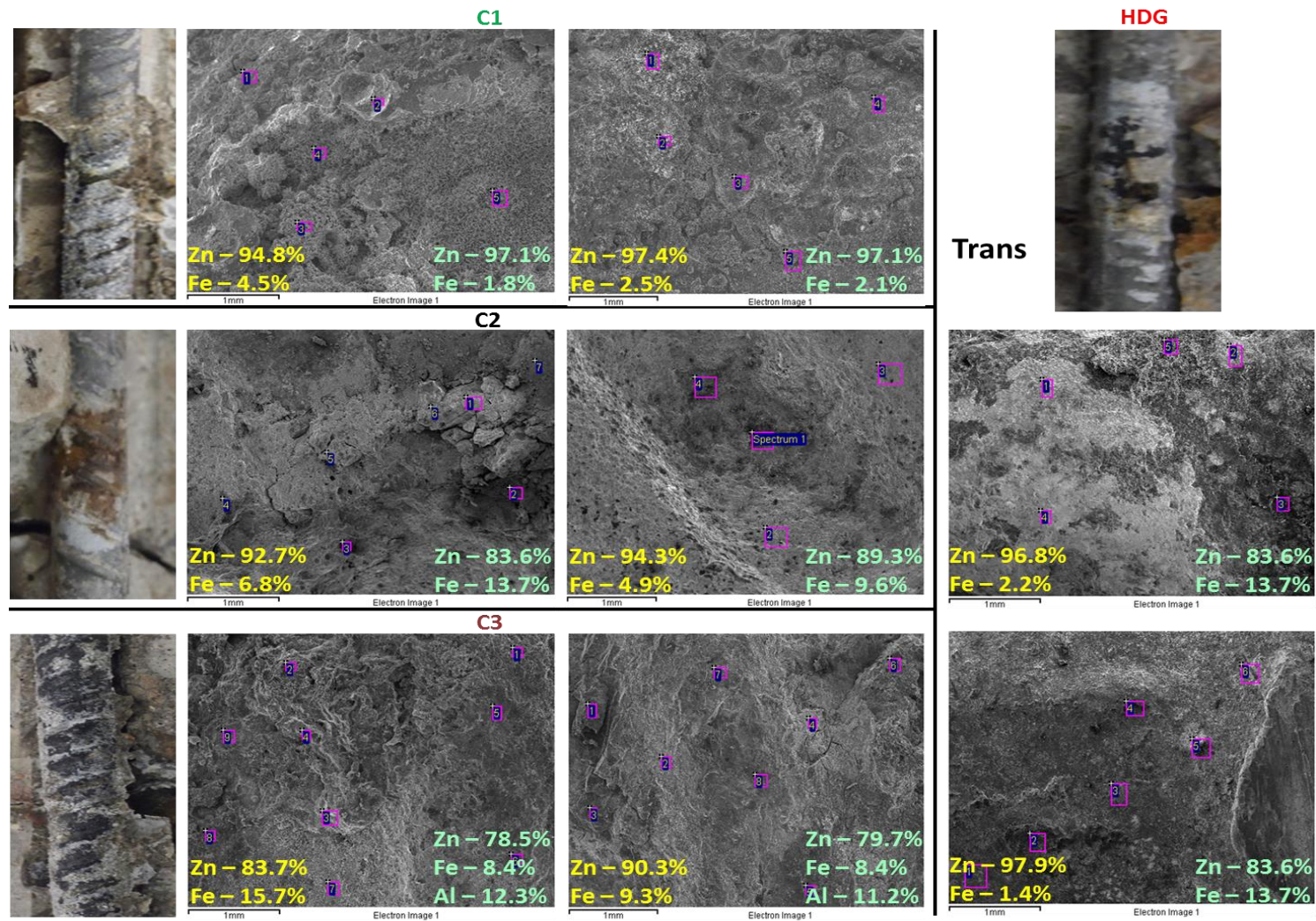


Figure E1.4.6: XRF analysis of autopsied transversely cracked steels. Note: values in green and yellow are before and after corrosion testing

E2. Final autopsy

C1



Figure E2.1.1: Exposed surface (to concrete crack) of transversely- (left) and longitudinally- (right) cracked C1 steel specimen

1 to 5.

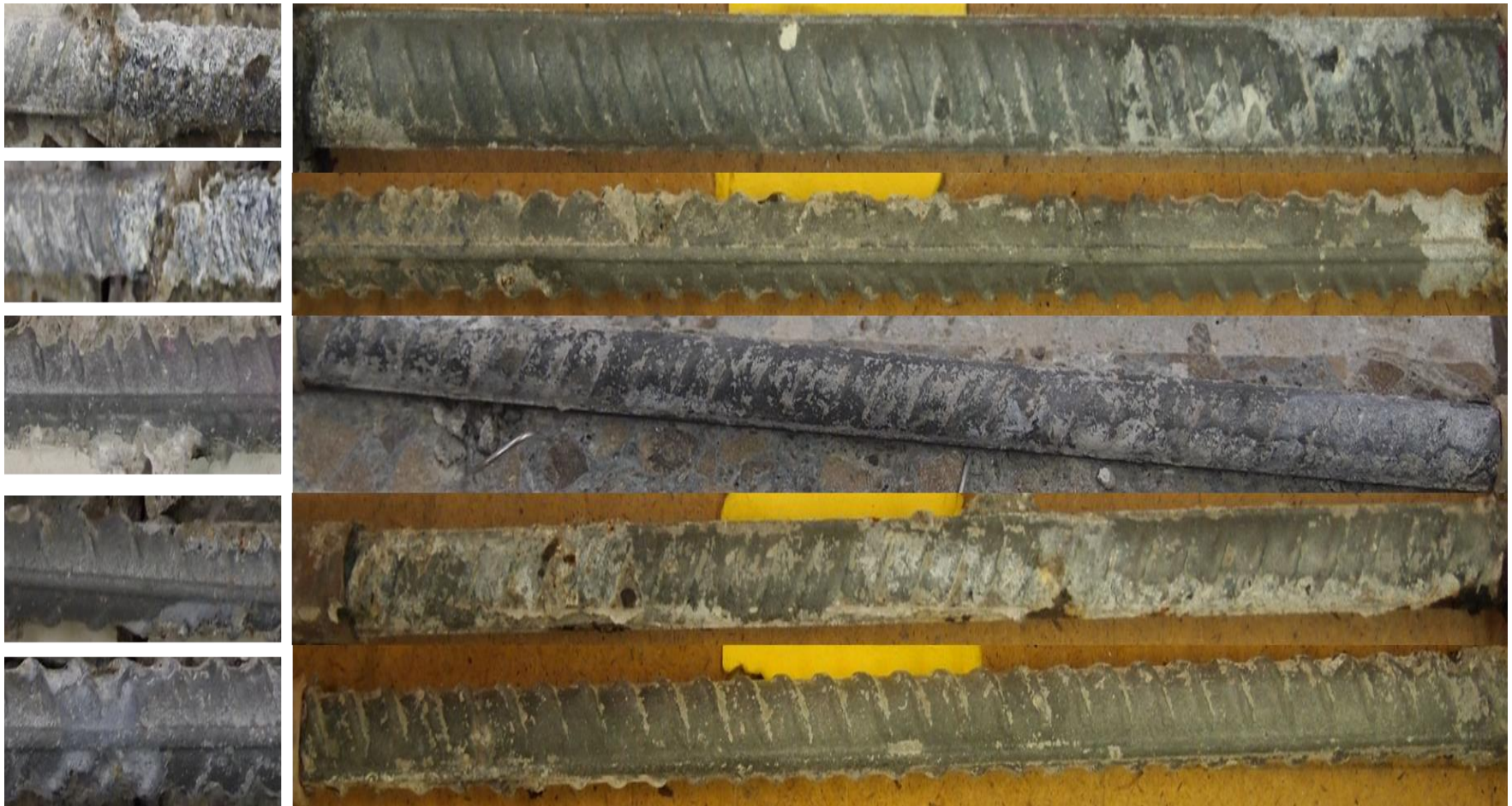


Figure E2.1.2: Non-exposed surface (to concrete crack) of transversely- (left) and longitudinally- (right) cracked C1 steel specimen 1 to 5.

C2



Figure E2.2.1: Exposed surface (to concrete crack) of transversely- (left) and longitudinally- (right) cracked C2 steel specimen

1 to 5.



Figure E2.2.2: Non-exposed surface (to concrete crack) of transversely- (left) and longitudinally- (right) cracked C2 steel specimen 1 to 5.

C3



Figure E2.3.1: Exposed surface (to concrete crack) of transversely- (left) and longitudinally- (right) cracked C3 steel specimen 1 to 5.

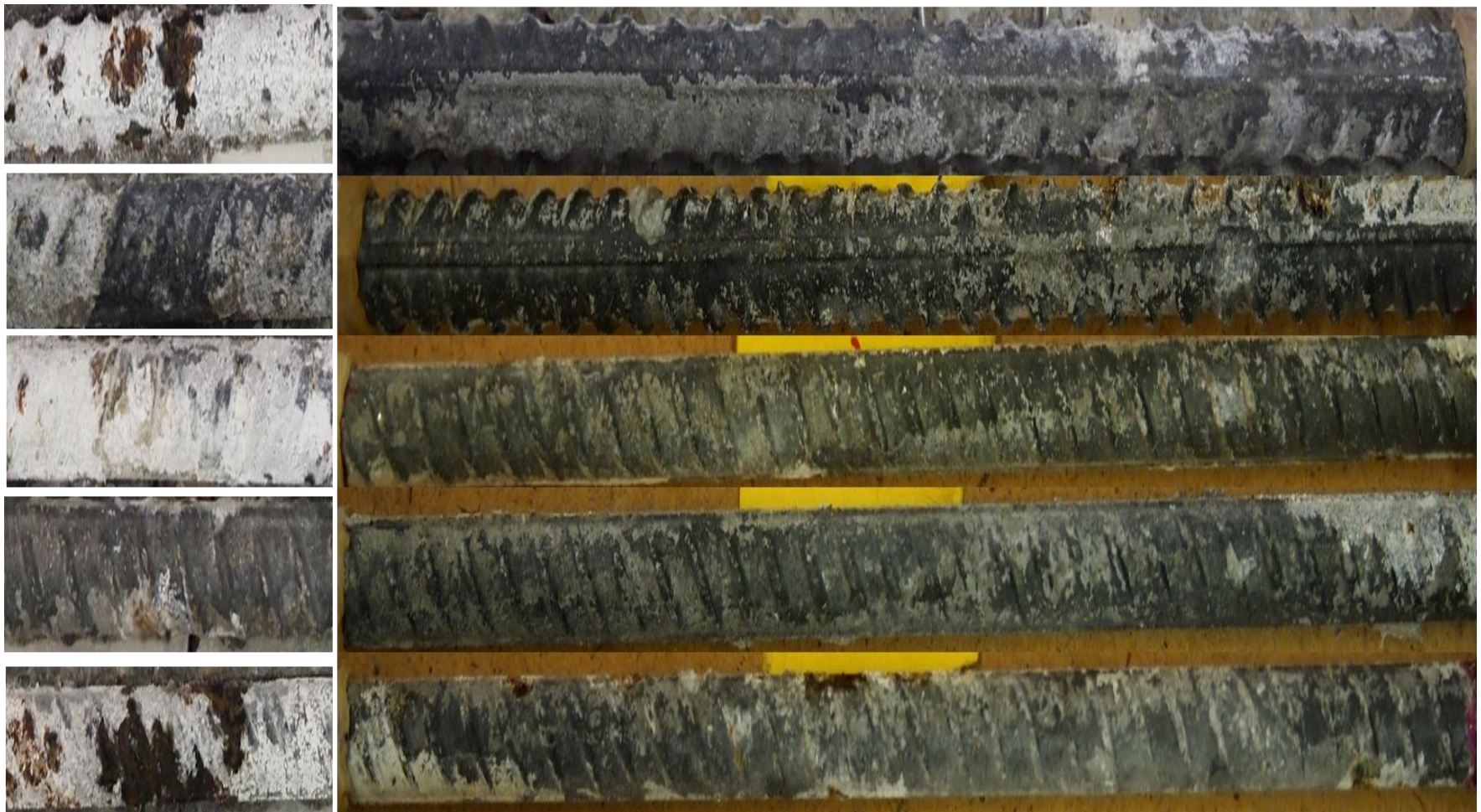


Figure E2.3.2: Non-exposed surface (to concrete crack) of transversely- (left) and longitudinally- (right) cracked C3 steel specimen 1 to 5.

HDG



Figure E2.4.1: Exposed surface (to concrete crack) of transversely- (left) and longitudinally- (right) cracked HDG steel specimen 1 to 5.



Figure E2.5.2: Non-exposed surface (to concrete crack) of transversely- (left) and longitudinally- (right) cracked C1 steel specimen 1 to 5.